Title

Epitaxial growth, surface, and electronic properties of unconventional semiconductors: RE-V/III-V nanocomposites and semiconducting Half Heusler alloys

Author

Kawasaki, Jason Ken

Publication Date

2014

UNIVERSITY of CALIFORNIA
Santa Barbara

Epitaxial growth, surface, and electronic properties of unconventional semiconductors: RE-V/III-V nanocomposites and semiconducting Half Heusler alloys

A Dissertation submitted in partial satisfaction of the
requirements for the degree

Doctor of Philosophy
in
Materials

by

Jason Ken Kawasaki

Committee in charge:

Professor Chris J. Palmstrøm, Chair
Professor Arthur C. Gossard
Professor Chris G. Van de Walle
Professor Anders Mikkelsen, Lund University

September 2014

The dissertation of Jason Ken Kawasaki is approved.

Arthur C. Gossard

Chris G. Van de Walle

Anders Mikkelsen, Lund University

Chris J. Palmstrøm, Chair

June 2014

Epitaxial growth, surface, and electronic properties of unconventional semiconductors: RE-V/III-V nanocomposites and semiconducting Half Heusler alloys

by

Jason Ken Kawasaki

Acknowledgements

This dissertation could not have been completed without the help and support of a number of people. First of all I would like to thank my adviser, Professor Chris Palmstrøm. Chris has an amazing depth of knowledge in the science and technology of MBE and all things related to UHV. I joined Chris's lab in the summer of 2009, a year after the group moved from Minnesota. Much of the heavy lifting had been done by the older students and postdocs (including Qi Hu, Paul Simmonds, Masahiko Hashimoto, Trevor Buehl, Erik Berg, Erdem Arkun, Darby Feldwinn, and others), but as a new student it was a great time to learn by helping to rebuild the lab. Chris has a great mantra of "learning by doing," which entails learning by diving head first into the lab, building equipment, troubleshooting, and generally learning the "pulse" of the machines. For me this sometimes turned into "learning by breaking things," for example overbaking a cryopump within my first month of joining the group. Fortunately as a teacher and mentor Chris has a great deal of patience and, as I soon discovered, making mistakes is one of the best ways to learn. Chris taught me to be ambitious in experiments, to be creative, and to look for those problems that no one else can tackle.

I also owe a great deal of thanks to Professor Anders Mikkelsen. Anders has effectively served as my second adviser overseas, first hosting me on a visit to Lund to learn STM and then on subsequent visits to MAX-lab. Anders has been a great resource for learning surface science and how to design experiments. I also thank Professor Art Gossard for being a great collaborator and role model. I am constantly impressed by his depth of knowledge, humility, and work-life balance. I hope that late into my career I will also

be able to ride my bicycle into work. Thank you to Professor Chris van de Walle for encouraging me to seek a greater theoretical understanding of the materials I was growing and for being a great teacher. Also Professor Ram Seshadri for discussions on Heuslers and for advice throughout the academic job search.

To Brian Schultz and John English, thank you for keeping things running smoothly, both in the Palmstrøm lab and in the MBE lab in general. I don't know where we'd be without Brian's help and direction in getting the lab up and running again. Brian has a great skill for explaining things coupled with a great deal of patience. We must have asked Brian hundreds of dumb questions, but Brian always made sure that we left the conversation with a better understanding than when it began. Brian has also been instrumental in developing the scientific part of our research efforts: much of the growth studies on ErSb nanostructures resulted from conversations with Brian, as well as many other projects.

I have also had the privilege of working with a number of great staff scientists and postdocs. Thank you to Rainer Timm for hosting me the first summer in Lund and teaching me STM, Hong Lu for many great conversations about rare earths and inspiring the ErSb nanorod work, Kris Delaney for helping me to understand bandstructures more intuitively, Anderson Janotti and Anindya Roy calculations on Half Heuslers. Thank you to Jörg Buschbeck for teaching me about shape memory alloys and also for being a great lab partner, office mate, and friend.

Thank you to fellow Palmstrøm and MBE group members past and present for your friendship and for making the lab a fun place to work: Sahil Patel, Borzoyeh Shojaei, Rachel Koltun, Trevor Buehl, Peter Burke, Qi Hu, Rick Liptack, Ludwig Feigl, Alex Kozhanov, Javad Shabani, Shinobu Ohya, Xiang Liu, Jacqueline Hall, Erik Berg, Alex Young, Anthony Megrant, Ken Ohno, Anthony Rice, Nate Wilson, Mihir Pendharkar, Anisa Myzaferi, Tony McFadden, Alan Liu, Steven Brown, Thomas Neulinger, Linda Johansson, Sean Harrington, Mitchell Maier, Jay Logan, Ryan Need, Dan Pennachio, and Tobias Brown-Heft. Despite our best efforts the MBE monkey keeps on attacking, but I think we're getting better at responding in the aftermath. To the first wave of students and postdocs who moved from Minnesota, we are in your debt for laying the groundwork.

Thank you Martin Hjort, Rainer Timm, and Sahil Patel for many fun evenings at MAX-Lab, and Balasubramanian Thiagrajan and Johan Adell for teaching me ARPES and maintaining an excellent i4 beamline. Thank you to my undergraduate thesis adviser Professor Craig Arnold, for setting me free in the lab and sharing his enthusiasm for materials science.

I would also like to thank my family: my parents Alan and Elaine, and brother David, for providing unwavering support through the years. Finally I would like to thank my wife Kate for her love, care, and support, especially during the writing of this dissertation.

Curriculum Vitæ

Jason Ken Kawasaki

EDUCATION

Ph.D. in Materials, 2014

University of California, Santa Barbara

Adviser: Professor Chris J. Palmstrøm

B.S.E. in Mechanical Engineering, 2009

Princeton University, Princeton NJ

Certificate in Materials Science & Engineering

Certificate in Applied & Computational Mathematics

PUBLICATIONS INCLUDED IN THIS DISSERTATION

1. **J. K. Kawasaki**, L. I. M. Johansson, B. D. Schultz, and C. J. Palmstrøm. Growth and transport properties of epitaxial lattice matched Half Heusler CoTiSb/InAlAs/InP(001) heterostructures. *Appl. Phys. Lett.*, **104**, 2 (2014).
2. **J. K. Kawasaki**, T. Neulinger, R. Timm, M. Hjort, A. A. Zakharov, A. Mikkelsen, B. D. Schultz, and C. J. Palmstrøm. Epitaxial growth and surface studies of the Half Heusler compound NiTiSn (001). *J. Vac. Sci. Technol. B.*, **31**, 04D106 (2013).
3. **J. K. Kawasaki**, B. D. Schultz, H. Lu, A. C. Gossard, and C. J. Palmstrøm. Surface Mediated Tunable Self-Assembly of Single Crystal Semimetallic ErSb/GaSb

Nanocomposite Structures. *Nano Lett.*, **13**, 6 (2013).

4. **J. K. Kawasaki**, B. D. Schultz, and C. J. Palmstrøm. Size effects on the electronic structure of ErSb nanoparticles embedded in the GaSb(001) surface. *Phys. Rev. B.*, **87**, 035419 (2013).

5. **J. K. Kawasaki**, R. Timm, K. T. Delaney, E. Lundgren, A. Mikkelson, and C. J. Palmstrøm. Local Density of States and Interface Effects in Semimetallic Rare Earth-V Nanostructures Embedded in a Semiconducting Matrix. *Phys. Rev. Lett.* (Editors' Suggestion), **107**, 036806 (2011).

6. **J. K. Kawasaki**, R. Timm, T. Buehl, E. Lundgren, A. Mikkelson, A. C. Gossard, and C. J. Palmstrøm. Cross Sectional Scanning Tunneling Microscopy and Spectroscopy of ErAs Nanostructures Embedded in GaAs. *J. Vac. Sci. Tech. B*, **29**, 3 (2011). (featured in Virt. J. Nan. Sci. & Tech.)

OTHER PUBLICATIONS

1. S. J. Patel, **J. K. Kawasaki**, J. A. Logan, B. D. Schultz, J. Adell, B. Thiagarajan, A, Mikkelsen, and C. J. Palmstrøm. Surface and Electronic Structure of Epitaxial LuPtSb (001) Thin Films. *Appl. Phys. Lett.*, **104**, 201603 (2014).

2. J. Buschbeck, **J. K. Kawasaki**, A. Kozhanov, R. D. James and C. J. Palmstrøm. Martensite transformation of epitaxial Ni-Ti films. *Appl. Phys. Lett.*, **98**, 19 (2011).

3. J. Buschbeck, **J. K. Kawasaki**, T. Buehl, A. C. Gossard, and C. J. Palmstrøm. Growth of epitaxial NiTi shape memory alloy films on GaAs (001) and evidence

of martensitic transformation. *J. Vac. Sci. Tech. B*, **29**, 3 (2011).

4. **J. K. Kawasaki** and C. B. Arnold. Synthesis of platinum dendrites and nanowires via directed electrochemical nanowire assembly. *Nano Lett.*, **11**, 191901 (2011).
5. N. Ferralis, **J. K. Kawasaki**, R. Maboudian, and C. Carraro. Evolution in surface morphology of epitaxial graphene layers on SiC induced by controlled structural strain. *Appl. Phys. Lett*, **93**, 191916 (2008).

AWARDS

- Kavli Postdoctoral Fellowship, Kavli Institute at Cornell, 2014
- Russell and Sigurd Varian Student Award, American Vacuum Society, 2013
- Iris Ovshinsky Student Award, Div. Materials Physics, American Physical Society, 2013
- Graduate Student Gold Award, Materials Research Society, 2012
- Distinguished Scholar Award, Microanalysis Society, 2012
- Best Student Oral Presentation, North American Molecular Beam Epitaxy Conference, 2011 and 2012
- Young Scientist Award, Physics and Chemistry of Surfaces and Interfaces Conference, 2011 and 2013
- National Science Foundation Nordic Research Opportunity Award, 2011
- National Defense Science and Engineering Graduate Fellowship, 2010
- National Science Foundation Graduate Research Fellowship, 2010
- Donald Janssen Dike Award for Excellence in Undergraduate Research, Princeton

University, 2009

Abstract

Epitaxial growth, surface, and electronic properties of unconventional semiconductors:
RE-V/III-V nanocomposites and semiconducting Half Heusler alloys

by

Jason Ken Kawasaki

This dissertation explores how modifications to and within a parent zincblende lattice, chemical composition and reduced dimensionality, can be used to engineer materials with functionality beyond that of conventional III-V semiconductors.

The first part explores the use of dimensionality to control the electronic properties. Here we examine the growth mechanisms and properties of semimetallic rare earth monopnictide (RE-V) nanostructures embedded coherently within a semiconducting III-V matrix. While previous work has focused primarily on the growth of embedded RE-V nanoparticles (e.g. ErAs or ErSb) for applications in thermoelectrics, here we show that by increasing the Er composition during simultaneous growth with GaSb, a wide range of new nanostructures form including nanorods, branched nanotrees, and lamellar nanosheets. These ErSb nanostructures form simultaneously with the GaSb matrix, and by combining molecular beam epitaxy (MBE) with in-situ scanning tunneling microscopy (STM), we image the growth surfaces one atomic layer at a time and show that the nanostructured composites form via a surface-mediate self assembly mechanisms that is controlled entirely at the growth front and is not a product of bulk segregation. Using angle resolved photoemission spectroscopy (ARPES) and scanning tunneling spectroscopy (STS), we measure the momentum (k-) and spatially- resolved electronic structure of the embedded RE-V nanostructures and show that despite the predictions of simple quantum confinement models, they remain semimetallic down to their smallest dimensions. These nanostructured composites show great promise for applications in thermoelectrics, tunnel diodes, and fully epitaxial polarization filters.

The second part focuses on Half Heusler alloys, which are a ternary analogue to the zincblende III-Vs. The Full and Half Heusler alloys are an attractive family of multifunctional materials with tunable electronic and magnetic properties. These include both semiconducting and metallic behavior as well as magnetism, half metallic ferromagnetism, superconductivity, topological insulator behavior, and the shape memory effect. In this dissertation we demonstrate the MBE growth of NiTiSn and CoTiSb, two prototypical semiconducting Half Heusler compounds. The films are epitaxial, single crystalline, and show semiconducting-like transport properties with higher electron mobilities and lower electron densities than their bulk counterparts. We also show that both CoTiSb(001) and NiTiSn(001) exhibit a number of different surface reconstructions with phase behavior similar to that of III-V semiconductors, and we propose atomic models for these reconstructions. Using angle resolved photoemission spectroscopy (ARPES) we report the first direct measurement of the surface and bulk electronic bandstructure of semiconducting Half Heuslers and show that these compounds are semiconductors with a bulk bandgap, but with metallic surface states within the gap. These studies lay the groundwork for

future studies on all-Heusler heterostructures.

Contents

Contents **xvii**

1 Introduction **1**

1.1 RE-V/III-V nanocomposites 7

1.2 Semiconducting Half Heusler alloys 9

2 MBE growth and in-situ surface characterization **12**

2.1 Introduction 12

2.2 Scanning tunneling microscopy and spectroscopy 15

2.2.1 Theory of STM 16

2.2.2 Imaging 21

2.2.3 Scanning tunneling spectroscopy 22

2.2.4 Tip shape and tip-induced band bending 25

2.2.5 Plan-view and cross-sectional STM 28

2.3 Photoemission spectroscopy 31

2.3.1 The three step model 34

2.3.2 Core level energy shifts 38

2.3.3 Band mapping 39

2.3.4 Experiments and sample preparation 45

3 Growth Mechanisms and Structure of RE-V/III-V nanocomposites **51**

3.1 Introduction to rare earth monopnictides 51

3.2 Nucleation of ErSb on GaSb 56

3.3 Codeposition of $Ga_{1-x}Er_xSb$: nanoparticles, rods, trees, and lamellae . . 67

3.4 Cross sectional STM of ErAs nanoparticles 90
3.5 Conclusions 99

4 Electronic Properties of low dimensional RE-V/III-V nanocomposites 103
4.1 Introduction: quantum confinement and interface effects 103
4.2 ARPES of ErAs and ErSb films 108
4.3 Scanning tunneling spectroscopy of ErSb and ErAs nanoparticles and nanorods 124
  4.3.1 Effect of ErAs/GaAs interfaces 129
4.4 Conclusions 136

5 Growth of Semiconducting Half Heuslers 140
5.1 Introduction to Heuslers 140
  5.1.1 Why semiconducting Half Heuslers? 145
5.2 MBE growth of NiTiSn and CoTiSb 150
  5.2.1 Choice of substrate 150
  5.2.2 Controlling the composition 154
  5.2.3 Growth of CoTiSb on InAlAs/InP(001) 159
  5.2.4 Growth of NiTiSn on MgO (001) 166
5.3 Transport 174
  5.3.1 CoTiSb 174
  5.3.2 NiTiSn 181
5.4 Conclusions 184

6 Half Heusler Surfaces 187
6.1 Why surfaces 187
6.2 Bonding and crystal structure at (001) Half Heusler surfaces 191
6.3 CoTiSb(001) surfaces 193
  6.3.1 RHEED and LEED: periodicity of the reconstructions 196
  6.3.2 XPS: bonding and stoichiometry 201
  6.3.3 STM and surface reconstruction models 207
6.4 NiTiSn(001) surfaces 216
  6.4.1 Surface structure by LEED and STM 216

6.4.2 Challenges of capping and decapping for high resolution photoemission spectroscopy . . . 221
6.5 Conclusions . . . 229

7 Electronic structure of CoTiSb 233
7.1 Introduction . . . 233
7.2 Normal emission for (001): Bulk $\Gamma - X$ . . . 235
7.3 Surface states for the $c(2 \times 4)$ reconstruction . . . 240
7.4 Normal emission for (111): bulk $\Gamma - L$ . . . 242
7.5 Conclusions . . . 244

8 Ni_2TiSn/NiTiSn nanocomposites for potential thermoelectric applications 246
8.1 Introduction to Half Heusler thermoelectrics . . . 246
8.2 MBE growth of $Ni_{1+\delta}TiSn$ nanocomposites . . . 250
8.3 Transport of $Ni_{1+\delta}TiSn$ nanocomposites . . . 260
8.4 Conclusions . . . 261

9 Conclusions and Outlook 265
9.1 Embedded RE-V / III-V nanocomposites . . . 265
9.2 Semiconducting Half Heusler compounds . . . 269

A XPS layer intensity modeling 275

B NiTi shape memory alloys 280

C MATLAB code for ARPES bulk dispersions using free electron like final states 289

D MATLAB code numerical solutions to the Schrödinger equation 292

Chapter 1

Introduction

The ability to grow high quality crystals and engineer them in artificially layered heterostructures is a key driving force for both improved technology and the discovery of fundamentally new physics. Consider the example of the two dimensional electron gas (2DEG) formed in group IV or group III-V compound semiconductor materials such as Si and GaAs. These 2DEGs form not only the central component in modern semiconductor transistors, but they also directly led to the discovery of the integer and fractional quantum Hall effects [1, 2]. But as Si- and GaAs-based technology begins to mature, there emerges a need to identify and develop materials with functionality beyond that of conventional semiconductors.

For the above mentioned III-V semiconductors, molecular beam epitaxy (MBE) has been a key enabling technology. MBE is a method for the controlled growth of high crystal quality, low defect density thin films and heterostructures with near atomic level precision. Here, high purity elements are evaporated from individual effusion cells (or gas sources) onto a substrate in ultrahigh vacuum (10^{-10} mbar) (Figure 1.1). The mean free paths for the impinging atomic or molecular species are on the order of several hundred kilometers ($\lambda = k_B T/\sqrt{2}\pi d^2 p$, where k_B is the Boltzmann constant, d is the particle diameter, and p is the pressure), such that the reactions occur primarily at the growth surface rather than in the atomic/molecular beam. Furthermore the thermally evaporated species have much lower energies than species produced by other processes such as sputtering or pulsed laser ablation. Thus MBE is a comparatively gentle growth technique that does not produce ablation or radiation damage in the resulting films. Under certain conditions the depositing film adopts the crystal structure of the underlying substrate and hence the process is termed epitaxy. Finally the growth is performed at relatively low temperatures and the rate is slow, on the order of one atomic layer per second. Thus by opening and closing individual shutters the growth can be controlled at near atomic precision. For these reasons it is sometimes likened to “atomic spray painting” [3]. This ability to precisely engineer III-V heterostructures by MBE has led to important concepts such as band engineering [4], modulation doping [5], and fundamental insights into the transport behavior of high mobility two dimensional electron and hole systems, as well as applications in devices such as high electron mobility transistors, photodetectors, lasers, and many others.

Thus in the search and development of new electronic materials, MBE is a very promising technique. Indeed, since the initial development of MBE in the 1960s for the growth of III-Vs, this technique has been expanded to the growth of group IV-IV, II-VI and III-nitride semiconductors as well as epitaxial metals. In the past 25 years MBE has

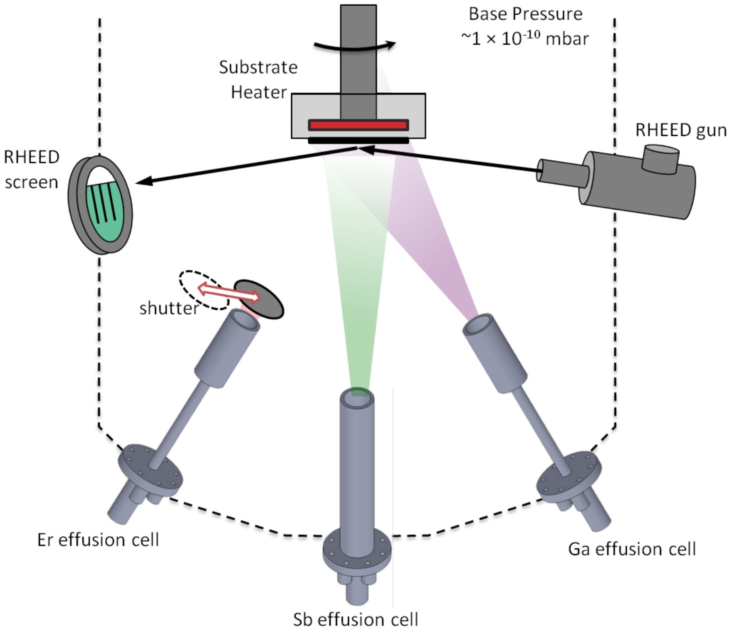

Figure 1.1. Schematic of a molecular beam epitaxy (MBE) system.

also shown great success in the growth and enhancing the understanding of complex oxide materials [3]. The complex oxides, which typically adopt the perovskite crystal structure, are often called "multifunctional materials" due to their wide range of properties that include both metallic and insulating behavior, superconductivity, magnetism, and strong electron-electron correlations. But as we search for new multifunctional materials, an added criteria is that we would like to be able to integrate them epitaxially with existing group IV or III-V substrates. This means identifying multifunctional materials that have crystal structures very closely related to the diamond or zincblende structures found in group IV or III-V semiconductors.

This dissertation explores the epitaxial growth, surface, and electronic properties of two novel materials systems that are closely related to a parent zincblende lattice [Figure 1.2(a)]. Two approaches are taken. The first approach is to start with a zincblende com-

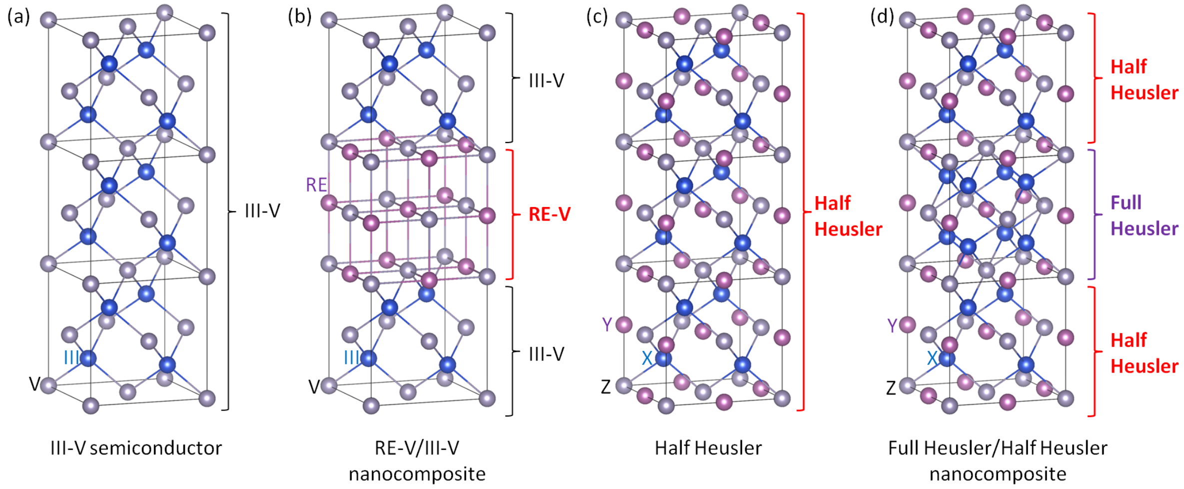

Figure 1.2. Schematic crystal structures for the samples grown in this dissertation. (a) The parent zincblende lattice found in many of the III-V compound semiconductors, e.g. GaSb and GaAs. (b) Precipitation of a secondary rare earth monopnictide (RE-V) metallic phase, e.g. ErSb or ErAs, which adopt rocksalt structure. (c) The Half Heusler structure (composition XYZ) which is related to the parent XZ zincblende lattice by addition of a third element Y at (1/2, 0, 0). X and Y are transition metals or rare earth metals, while Z is typically a group III, IV, or V metalloid. Many of the Half Heuslers with 18 valence electrons per formula unit are semiconducting. Examples include CoTiSb and NiTiSn. (d) Precipitation of a metallic Full Heusler phase (X_2YZ) from the Half Heusler matrix. The Full Heusler is related to the Half Heusler by the addition of a second X' sublattice at (3/4, 1/4, 1/4). Here the example of Ni_2TiSn/NiTiSn is shown.

pound semiconductor (e.g. GaSb, GaAs) and controllably precipitate metallic nanostructures (e.g. ErAs, ErSb) from the semiconducting matrix [Figure 1.2(b)]. The size, shape, and distribution of the nanostructures can be used to tune properties of the composite. We discuss this approach in the rare earth monopnictide (RE-V) / III-V semiconductor system.

The second approach is to identify entire materials families with new functionality that are structurally and chemically compatible with III-Vs. This approach will be demonstrated with Half Heusler alloys [Figure 1.2(c,d)]. The Half Heusler alloys are a family of ternary intermetallic compounds with composition XYZ, where X and Y are transition or rare earth metals and Z is a group III, IV, or V metalloid. Structurally these compounds are closely related to the zincblende compound semiconductors in that elements X and Z of the Half Heusler form a zincblende sublattice, with Y atoms stuffed at the (1/2, 0, 0) sites. They also have very similar lattice parameters as the III-V compound semiconductors, and hence many Half Heuslers can be grown epitaxially on III-V substrates. But unlike the compound semiconductors, Half Heuslers adopt a wide range of properties including both metallic and insulating behavior, magnetism, superconductivity, and topological insulator behavior.

In the growth of these unconventional materials we have paid special attention to the atomic and electronic structure at the surfaces and interfaces. Due to surface relaxations and reconstructions, the properties at surfaces can be very different than the properties in the bulk. These effects become especially important for thin films and for embedded nanoparticles and nanorods. Methods for characterizing these surfaces are described in

Chapter 2.

1.1 RE-V/III-V nanocomposites

Metal-semiconductor nanocomposites are of great interest for applications in thermoelectrics, plasmonics, enhanced tunneling across semiconductor junctions, and many others. A number of years ago it was found that the simultaneous growth of GaAs with Er just beyond the solubility limit yields metallic ErAs nanoparticles precipitated from a semiconducting GaAs matrix. Due to the similarities in crystal structure and the thermodynamic stability of the rocksalt ErAs with zincblende GaAs [Figure 1.2(b)] the resulting nanocomposites have atomically sharp ErAs/GaAs interfaces with no defects as observed by TEM. Similar behavior is observed for many other combinations of RE-V with III-V. Thus it is possible to introduce these metallic nanostructures without seriously disrupting the quality of the semiconducting matrix.

While the embedded RE-V nanoparticles grown in the dilute RE regime are now well studied for applications in thermoelectrics, the growth mechanisms are still not well understood. This is especially important as the properties of the resulting nanocomposite are dependent on the size, shape, and distribution of the RE-V nanoparticles. In this dissertation we use the combination of MBE growth with *in-situ* scanning tunneling microscopy and other tools to study the growth mechanisms for embedded RE-V nanoparticles in III-Vs (Chapter 3). Along the way, we also discover a wide range of new embedded RE-V/III-V nanostructures, including nanorods, branched nanotrees, and lamellae. Using angle-resolved photoemission spectroscopy (ARPES) and scanning tunneling spectroscopy (STS) we measure the momentum (**k**-) and spatially resolved electronic structure of these RE-V nanostructures as a function of reduced dimensionality (Chapter 4).

1.2 Semiconducting Half Heusler alloys

The Heusler alloys offer the promise of an extremely wide range of properties not observed in compound semiconductors, including both metallic and semiconducting behavior [6], half metallic ferromagnetism [7], superconductivity [8], heavy fermion behavior [9], shape memory effect [10], and topological insulator behavior [11, 12]. These properties make the Heuslers an exciting playground for investigating novel phenomena, and when combined with atomically precise growth by molecular beam epitaxy (MBE), they provide a unique platform for engineering combinations of functionalities in heterostructures and exploring new physics that may emerge at their interfaces. However beyond their magnetic properties [13], experimentally many of the other properties of Full (composition X_2YZ) and Half Heuslers (composition XYZ) remain under-explored. This is due largely to challenges in achieving high quality crystals, which have typically been grown by bulk methods or by sputtering [14, 15]. For example, although Half Heuslers with 18 valence electrons per formula unit (filled s, p, and d shells) are predicted to be semiconducting, experimentally most bulk grown samples have shown metallic behavior with a high density of defect states near the Fermi level [16].

MBE offers the possibility of growing very high quality single crystalline thin films and heterostructures of Heuslers. This dissertation develops the epitaxial growth, surface, and electronic properties of two of the prototypical semiconducting Half Heuslers: CoTiSb and NiTiSn (Chapters 5, 6, and 7). Additionally some of the semiconducting Half Heusler compounds (e.g. NiTiSn) show a coexistence with a metallic Full Heusler phase (e.g. Ni_2TiSn). Thus it may be possible to grow Full Heusler / Half Heusler nanocomposites (Chapter 8 and Figure 1.2(d)), similar to the RE-V/III-V nanocomposites from Chapters 3 and 4.

However, one of the challenges to applying MBE to the growth of intermetallics and other new compounds is the difficulties in controlling composition. One of reasons for the particular success of III-V materials growth by MBE is the existence of a group-V adsorption limited growth window. Due to the high volatility of the group-V species (e.g. As or Sb), stoichiometric films of III-V are easily grown while supplying an excess of group-V to the surface [17, 18]. Only the stoichiometric amount of group V will be incorporated into the film. This self-limited regime occurs over a finite range of growth temperatures and group-V overpressures and is often called the “growth window.” Growth windows also exist for the rare earth monopnictides (RE-V) and for some of the complex oxides. However, for many Heusler compounds (and intermetallics in general) a growth window does not necessarily exist. This issue is addressed in further detail in Chapter 5.

Chapter 2

MBE growth and in-situ surface characterization

2.1 Introduction

All samples in this dissertation were grown by molecular beam epitaxy (MBE). Beyond the ability to grow high quality epitaxial films with atomic control, one of the advantages of MBE is that it can be readily integrated with a variety of surface sensitive analysis tools. At surfaces the breaking of bonds and change of symmetry often produce relaxations or reconstructions of the atomic positions. Thus the atomic structure at surfaces, as well as the resulting electronic properties, can be very different at surfaces than in the bulk. These surface considerations become increasingly important for nanostructures or heterostructured thin films.

Samples were grown at the University of California Santa Barbara in an integrated

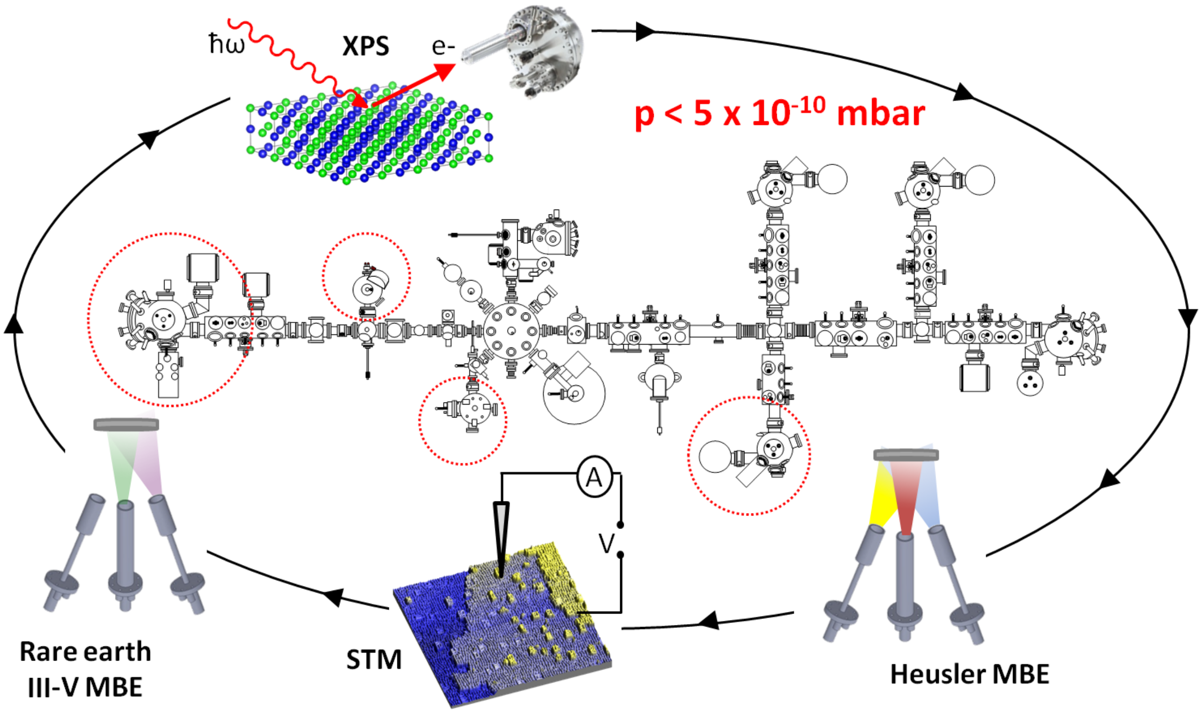

Figure 2.1. Schematic of the interconnected MBE growth - UHV surface analysis system. III-V and rare earth doped materials such as GaAs, InAlAs, ErAs, ErSb, etc were grown in a VG V80H III-V MBE system (circled, far left). Heusler alloys were grown in a VG V80 MBE system that is dedicated for Heusler and other metals growth (circled, bottom right). Primary surface characterization was performed using X-ray photoemission spectroscopy (XPS) and scanning tunneling microscopy (STM).

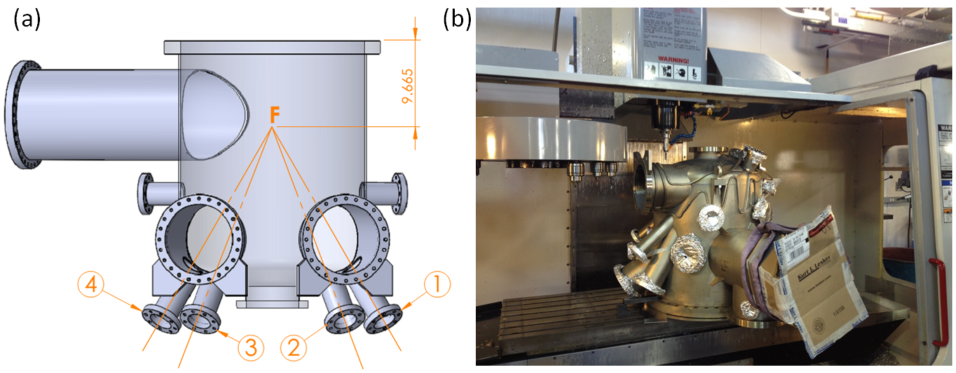

Figure 2.2. (a) Drawing of the VG V80 system used for Heusler and metals growth. In Winter 2012/2013 we added 4 additional effusion cell ports (labelled 1-4) to expand the total number of ports to 8. (b) The metals VG V80 detached from the main lab and disassembled, flipped upside down, and ready to be CNC'd at the UCSB Physics Machine Shop.

surface analysis system that combines several MBE growth chambers with scanning tunneling microscopy (STM), x-ray photoemission spectroscopy (XPS), reflection high energy electron diffraction (RHEED), low energy electron diffraction (LEED), and other surface analysis tools (Figure 2.1). Although at times challenging to maintain, the advantage of this approach is that it allows samples to be grown and measured without removal from ultrahigh vacuum. This enables fundamental studies of the surface atomic structure, bonding, and electronic structure, as well as studies of growth mechanisms as films are grown one atomic layer at a time.

Some samples have also been characterized by high resolution core level photoemission and angle resolved photoemission (ARPES). These studies necessitate the use of synchrotron light, for which we used beamlines I311 and I4 of MAX-Lab synchrotron at Lund University, Sweden. Thus we have developed capping methods to protect sample surfaces during transfer through air from UCSB to Lund, to be described later in this chapter and subsequent chapters.

Here we briefly review the theory and experimental considerations for two of the primary surface characterization methods used in this dissertation: scanning tunneling microscopy/spectroscopy (STM/STS), and angle-resolved photoemission spectroscopy (ARPES). More detailed reviews of MBE can be found in Refs. [19, 20, 21, 22].

2.2 Scanning tunneling microscopy and spectroscopy

Scanning tunneling microscopy, developed in the early 1980's by Binnig, Rohrer, Gerber, and Weibel [23, 24, 25], is a powerful method for both imaging and measuring the electronic structure of surfaces with atomic resolution. STM can also be used as a method for single atom manipulation and assembling artificial structures. This section briefly reviews the theory and practical aspects of STM as a method for studying the growth and electronic properties of MBE-grown films. More detailed treatments can be found in Refs. [26, 27, 28, 29].

2.2.1 Theory of STM

STM is based on the principle of quantum tunneling. A sharp metallic tip is brought within several Angstrom of a conductive sample (but not in contact) and when a bias is applied electrons tunnel from sample to tip or vice versa, with typical tunneling currents on the order of pA to nA. By rastering this tip across the sample surface, the topography can be imaged as well local variations in the electronic structure (Figure 2.3).

We first consider tunneling in a one-dimensional model of tunneling across a vacuum

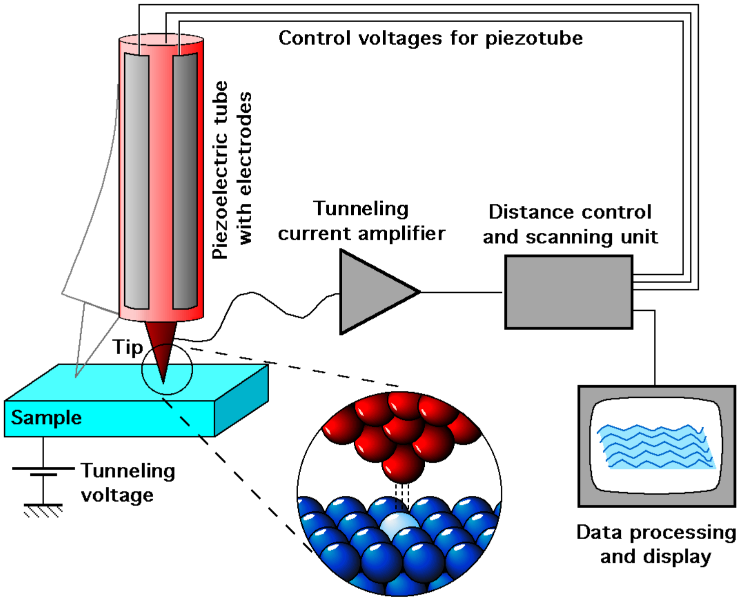

Figure 2.3. Schematic of an STM. From Ref [30]

barrier with height V_0 and width z (corresponding to the tip-sample separation). From a calculation of the transmission coefficient through the barrier [31], the tunneling current is given by

$$I \propto exp\left(-2\kappa z\right) \tag{2.1}$$

where $\kappa = \sqrt{2m\left(V_0 - \epsilon\right)}/\hbar$. Here the tunneling current decays exponentially with distance, but the model encodes no information about the particular material or its electronic structure (other than the barrier height), and it does not account for the rate at which electrons tunnel through the barrier.

A more advanced treatment follows from time dependent perturbation theory. This tunneling formalism was first developed by Bardeen [32] and later adapted to the STM problem by Tersoff and Hamann [33, 34]. Here the tip and sample are considered as two independent subsystems and the tunneling current corresponds to a transition of a charge carrier from a state in the tip to a state in the sample (or vice versa). For the unperturbed tip and sample states ψ_μ^t and ψ_ν^s, with corresponding energies E_μ^t and E_ν^s, the tunneling current under an applied bias V is given by

$$I = \frac{4\pi e}{\hbar} \sum_{\mu,\nu} f(E_\mu^t) \left[1 - f(E_\nu^s + eV)\right] \left|M_{\mu\nu}\right|^2 \delta(E_\mu^t - E_\nu^s) \tag{2.2}$$

where the sum is over all tip and sample states (μ and ν) and the matrix elements $M_{\mu\nu}$ are given by

$$M_{\mu\nu} = -\frac{\hbar}{2m} \int \left(\psi_\mu^{t*} \nabla \psi_\nu^s - \psi_\nu^{s*} \nabla \psi_\mu^t\right) \cdot d\mathbf{S} \tag{2.3}$$

Here the integral is over an arbitrary surface $\mathbf{S}$ between the two subsystems. The appearance of the Fermi-Dirac function $f(E)$ in Equation 2.2 implies that tunneling occurs from occupied states into unoccupied states, and the delta function restricts the problem to elastic tunneling only. At reasonably low temperatures the Fermi-Dirac function can be approximated as a Heaviside step function. Then by converting the sum in Equation 2.2 to an integral, the tunneling current becomes

$$I = \frac{4\pi e}{\hbar} \int_0^{eV} \rho_s(\epsilon - eV, \mathbf{R}) \rho_t(\epsilon) \left|M\right|^2 d\epsilon \tag{2.4}$$

where we now have an expression that depends on real materials parameters, namely ρ_t the density of states of the tip and $\rho_s(\epsilon, \mathbf{R})$ the spatially varying local density of states (LDOS) of the sample. The zero in energy is referenced to the Fermi level.

Following Tersoff and Hamann [33, 34], several approximations can be made. The tip is modeled as a spherical potential well, and the matrix elements are assumed to be

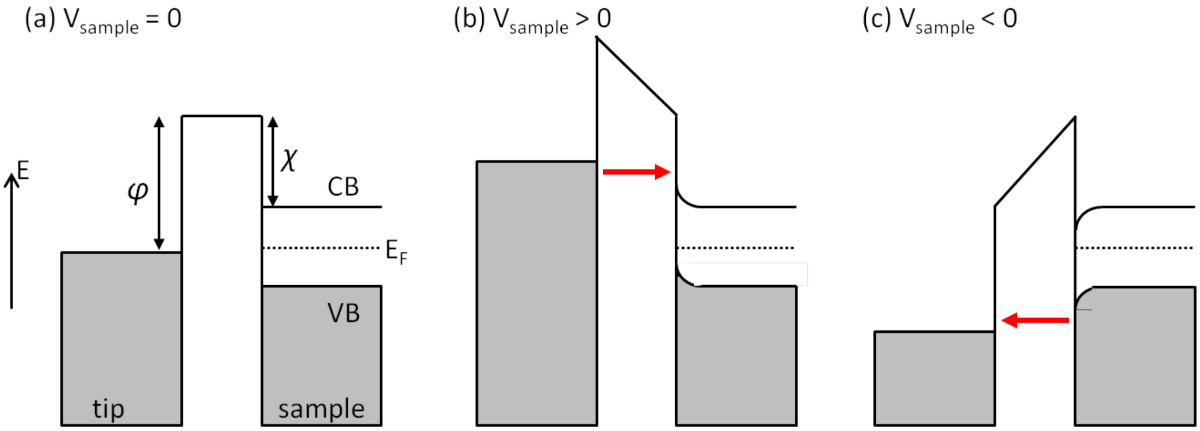

Figure 2.4. Schematic illustrating the tunneling under various biases for a semiconducting sample. Positive sample bias ($V_{sample} > 0$) corresponds to electrons tunneling from the tip to empty states in the sample valence band, while negative sample bias corresponds to electrons tunneling from filled states in the valence band to the tip. In real samples the tip induces band bending, resulting in some of the voltage being dropped across the vacuum barrier and some dropped across the sample itself. This leads to depletion for positive sample biases and accumulation for negative sample biases.

constant with energy. Since the probe tips are metallic, the density of states of the tip is also assumed to be roughly constant with energy (or at least much more slowly varying than for a semiconducting or semimetallic sample). This gives

$$I \propto |M|^2 \rho_t(0) \int_0^{eV} \rho_s(\epsilon, \mathbf{R}) d\epsilon \tag{2.5}$$

where we see that the tunneling current is proportional to the LDOS of the sample, integrated from the Fermi level to the external bias eV.

Further approximations recover the explicit dependence on tip-sample separation z. If the energy height of the barrier, given by the average of the tip and sample workfunctions, is slowly varying, then the matrix element can be treated with a WKB approximation. This gives $|M|^2 = exp\left(-2\gamma\right)$, where $\gamma = \int_0^z (\sqrt{2m\phi}/\hbar) dz' = \sqrt{2m\phi}z/\hbar$, and ϕ is the average workfunction [27, 29, 32]. Hence the expression for tunneling current becomes

$$I(eV,\mathbf{R}) \propto exp\left(-z\sqrt{\frac{8m\phi}{\hbar^2}}\right)\rho_t(0)\int_0^{eV}\rho_s(eV,\mathbf{R})d\epsilon \tag{2.6}$$

where the explicit dependence on z is now included and we have replaced $\epsilon \rightarrow eV$ to highlight the dependence on bias voltage. From Equation 2.6 it is readily apparent that topographical information $(\mathbf{R}, z)$ and electronic information $\rho_s(eV,\mathbf{R})$ are convolved with one another.

2.2.2 Imaging

The most common imaging mode in STM is "constant current mode," in which a feedback loop adjusts the tip-sample separation z in order to maintain a constant tunneling current. The tip is then rastered in-plane (x, y) to yield a map of the surface z as a function of x and y. However, note that the image in this case is not completely topographical. Since the tunneling current is dependent on both z and the sample LDOS, the measured z variations acquired in this mode will also encode an electronic contrast.

This electronic contrast can be explored by recording STM images as a function of the bias voltage. As seen in Equation 2.6, the current is proportional to the integrated LDOS of the sample. By changing the bias voltage one changes the range of integration. This is especially important near the band edges of semiconductors, where the density of states varies rapidly and hence the resulting images can be quite sensitive to the bias voltage. But the most dramatic effects are often observed by changing the polarity of the bias voltage: here a negative sample bias corresponds to tunneling from filled states in the sample valence band to the tip, while positive sample bias corresponds to tunneling from filled states in the tip to empty states in the sample conduction band. This is shown schematically in Figure 2.4. On certain surfaces this principle can be used for atom selective imaging. Feenstra et. al. showed that on the (110) surfaces of III-V semiconductors such as GaAs, which is a plane containing both Ga and As atoms, the empty states are attributed to group-III atoms while the filled states are attributed to group-V atoms [35]. By simply changing the bias polarity they could selectively image Ga or As atoms. In Chapter 3 we exploit this electronic contrast to distinguish semimetallic ErSb nanoparticles from a semiconducting matrix.

2.2.3 Scanning tunneling spectroscopy

In addition to imaging the integrated sample LDOS, one can directly measure the LDOS at specified points on the sample surface. Differentiating the tunneling current in Equation 2.6 with respect to voltage, we find

$$\frac{dI}{dV} \propto \rho_t(0)\rho_s(eV, \mathbf{R}) \tag{2.7}$$

and hence the differential conductance dI/dV is a direct measure of the spatially resolved sample LDOS.

In practice, STS is performed by disengaging the feedback loop and sweeping the bias voltage while measuring the tunneling current. The bias sweep typically occurs over a few seconds so a very stable tip is required. In principle, dI/dV can be calculated numerically from the measured current, but in practice this can introduce a great deal of noise. Thus the derivative is often acquired by applying a sinusoidal voltage dV on top of the bias voltage and measuring the response dI using a lock-in amplifier. The frequency and magnitude of this sinusoidal voltage need to be chosen carefully so that they do not interfere with the rest of the STM electronics. Typically a frequency on the order of kHz and dV on the order of several mV are chosen. STS can be performed at individual points on a sample surface, or can be performed over a mesh of points on the surface to yield a real space map of the LDOS. A more recent development is that the Fourier transform of this LDOS map (FT-STS) yields a **k**-space map of the scattering, or quasiparticle interference (QPI) [36, 37]. With suitable models this QPI pattern can be directly compared to the bandstructure $E(\mathbf{k})$ measured by ARPES [38].

For STS measurements on semiconductors, one challenge is that within the bandgap the tunneling current goes to zero, thus requiring currents to measured over many orders of magnitude. To increase the dynamic range, Feenstra showed that spectroscopy can be performed in a variable gap mode where the tip is brought closer to the sample for low bias voltages, where the tunneling current is low, and pulled away for higher voltages where the tunneling current is high [39]. This makes use of the exponential dependence of the tunneling current on tip-sample separation, and a common tip-sample separation profile is $z(V) = z_0 + \alpha|V|$. To remove the distance dependence, the differential conductance dI/dV can normalized by the total conductance I/V. This normalization works nicely for metals and small bandgap semiconductors; however for large bandgap semiconductors the quantity $(dI/dV)/(I/V)$ diverges near the band edges because the current approaches zero faster than the differential conductance. Therefore the I/V is broadened by convolution with a Gaussian or an exponential function. Choosing the latter,

$$\overline{I/V} = \int_{-\infty}^{+\infty} \frac{I(V')}{V'} exp\left\{\frac{-|V'-V|}{\Delta V}\right\} dV' \tag{2.8}$$

where the broadening ΔV is typically chosen to be of similar magnitude as the bandgap [39]. Hence the normalized quantity $(dI/dV)/\overline{(I/V)}$ is proportional to the sample LDOS. An example of this normalization process is shown in Figure 2.6. In chapter 4 we use STS to measure the LDOS of ErAs and ErSb nanoparticles as a function of size, and in chapter 6 we measure STS spectra for various surface reconstructions of CoTiSb(001) and NiTiSn(001).

2.2.4 Tip shape and tip-induced band bending

Note that so far the treatment leading up to Equation 2.6 has been highly idealized. For one, the real tip shape and its wavefunction may not be spherically symmetric. Indeed, the symmetry of the wavefunction at the tip is expected to affect the tunneling process and the resulting STM images [29], and to that end some groups have explored functionalizing tips, e.g. with a single CO molecule at the end, to image sample orbitals of a certain symmetry. During scanning the tip can also change shape and affect the resulting images. To recover a good tip, some methods include briefly pulsing the tip to remove loosely adsorbed molecules, or intentionally dipping and extruding the tip from a noble metal surface with the intention terminating with a single atom with the desired

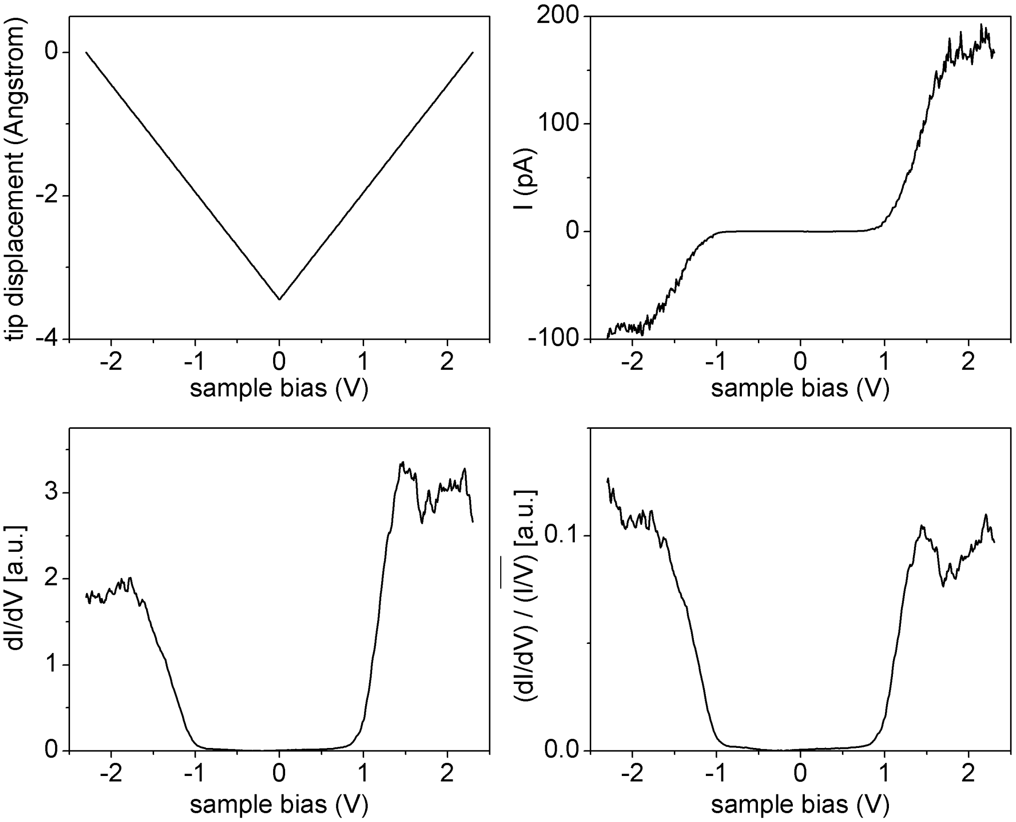

Figure 2.5. Plots of the tip displacement, tunneling current, differential conductance dI/dV, and normalized $(dI/dV)/\overline{(I/V)}$ for a GaAs(110) sample.

orbital symmetry.

Another simplification is that the voltage drop is not always entirely across the vacuum gap. When the metal tip is brought in close proximity to a semiconducting sample it will form a metal-insulator-semiconductor junction, where the mere existence of the tip is expected to bend the bands of the semiconductor. When a positive sample bias is applied, part of that bias will be dropped across the vacuum gap and part will be dropped across the sample itself, resulting in depletion. Similarly, for a negative sample bias, part of the bias is dropped across the vacuum gap and part across the sample, resulting in accumulation (Figure 2.4). This phenomenon is often called tip-induced band bending, and for this reason the measured bandgap by STM/STS is often slightly larger than the true bandgap of the sample.

2.2.5 Plan-view and cross-sectional STM

Due to the high surface sensitivity, STM measurements require atomically clean surfaces. In this dissertation two approaches have been used to produce clean surfaces: plan view STM of freshly grown samples, and cross-sectional STM of samples cleaved in vacuum.

Plan view STM of as-grown samples was performed by growing the samples in one of the connected MBE chambers and transferring the sample through ultrahigh vacuum to the STM chamber. In this way, the sample stays clean by avoiding exposure to air. For semiconductor surfaces such as GaAs and GaSb(001), since the surface reconstructions are very sensitive to the surface stoichiometry and annealing conditions, special care must

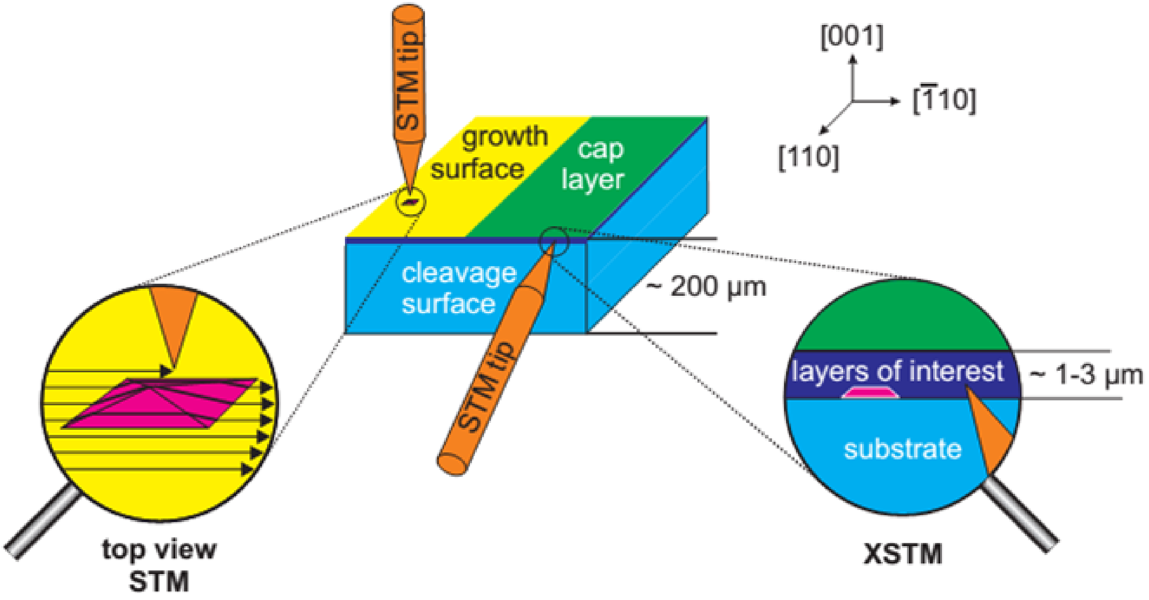

Figure 2.6. Comparison of plan-view and cross-sectional STM. From Ref. [26].

be taken during the final anneal in the MBE chamber just before transfer to the STM. For example, during cooldown from the growth temperature, a (2×4) GaAs surface reconstruction may transition to a $c(4 \times 4)$ due to excess arsenic in the system. In order to produce (2×4) surfaces for imaging, one method is to anneal the sample at the growth temperature $(540 - 610°\mathrm{C})$ with As_4 flux to stabilize the reconstruction, then shutter the arsenic while quenching the temperature rapidly to 200°C. In this way the residual arsenic in the chamber has time to be pumped out during cooldown rather than adsorbing on the GaAs surface and causing a transition to the As-rich $c(4 \times 4)$. Further adjustments to this procedure can be made by adding an additional lower temperature anneal step while slowly reducing the As_4 flux before the final As shutter and quench. Once the desired reconstruction is obtained after cooldown, the sample is then transferred out of the MBE sample while still warm $(\approx 200°\mathrm{C})$ so as to minimize adsorbates during transfer to the STM. Similar anneal and quench procedures were used in this dissertation to produce

GaSb(001)-$c(2 \times 6)$ surface reconstructions, as well as variety of CoTiSb(001) surface reconstructions.

Cross-sectional samples were also explored in this dissertation. This method allows samples that have been removed from vacuum to be imaged in STM, and is especially useful for imaging the internal structure of buried nanostructures. Here a small notch is scribed on the sample and the sample is mounted vertically on a special cross sectional XSTM block. Once reloaded into vacuum, the sample is cleaved by gently pressing with a wobble stick to produce a clean cleavage surface that can be imaged by STM. To aid in producing atomically flat cleaves, the sample is typically polished to both thin the sample and remove indium from the back side (if indium was used for MBE sample mounting). To aid in locating the regions of interest, marker layers such as an AlAs/GaAs superlattice are often grown at a defined depth above or below the region of interest. Once this superlattice is found, the tip can then be moved the known distance to the region of interest.

2.3 Photoemission spectroscopy

Angle-resolved photoemission spectroscopy (ARPES) is a natural complement to scanning tunneling microscopy and spectroscopy. While STM/STS visualizes the atomic positions and electronic states in real space $\mathbf{R}$, ARPES measures the electronic band-structure in momentum space ($\mathbf{k}$). In the experiment, a monochromatic beam of light is shined on the sample [Figure 2.7(a)]. Through the photoelectric effect, the light excites

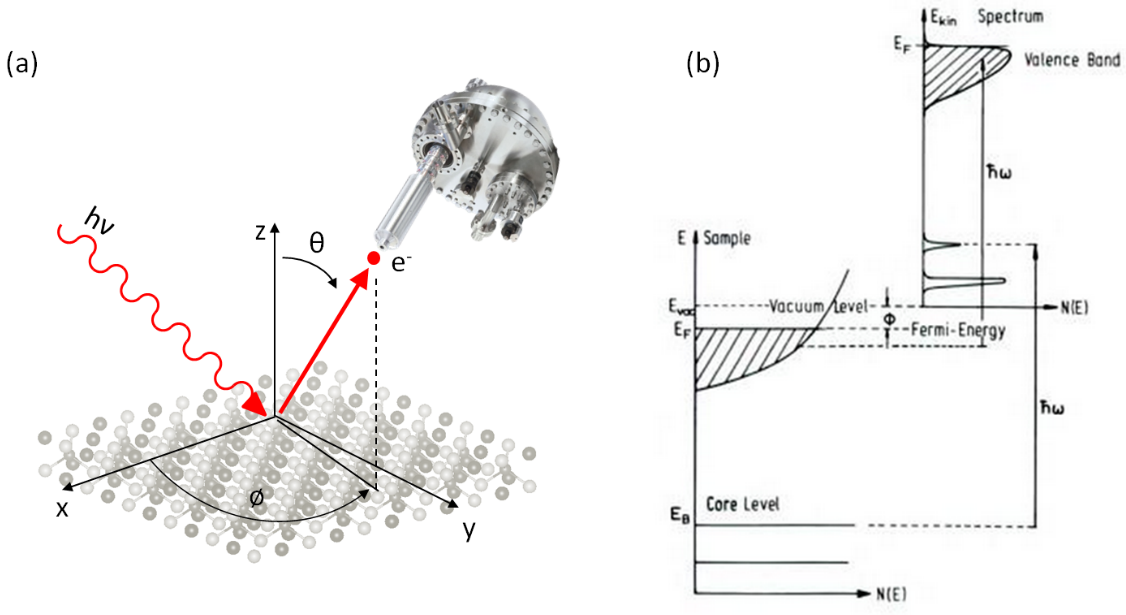

Figure 2.7. (a) Cartoon of the ARPES measurement. (b) Schematic of the energies involved in photoemission spectroscopy, from [40].

electrons from the sample and these electrons are detected by an electron analyzer. Here the energy is conserved, such that

$$E_{kin} = h\nu - E_B - \phi \tag{2.9}$$

where E_{kin} is the kinetic energy of the photoelectrons, $h\nu$ is the incident photon energy, E_B is the binding energy of the electron in the solid (also termed the initial state energy E_i), and ϕ is the workfunction [Figure 2.7(b)]. The measured quantity is the photoemission intensity I as a function of the electron kinetic energy E_{kin}, the emission angles θ and ϕ, and the incident photon energy $h\nu$. One can then convert this to the energy E_B versus wavevector $\mathbf{k}$ of the electrons in the solid, i.e. the electronic bandstructure.

A few comments are worthy of note. Unlike STM, in which the probe is an (atomically) sharp tip and the spacial resolution is on the order of Angstrom or less, the spot size of the light used for ARPES measurements is typically on the order of a few hundred microns. Hence ARPES is in general a spatially averaged probe, but recent efforts have explored the use of nanometer focused beams, e.g. the ANTARES beamline at SOLEIL [41], for spatially resolved ARPES. Another note is that photoemission only probes occupied states up to the Fermi level. To study the unoccupied states other techniques must be used, for example inverse photoemission or two photon photoemission. Finally, due to the very small inelastic mean free paths for photoelectrons excited by UV and soft x-rays (on the order of several Angstroms), photoemission experiments are generally extremely surface sensitive and care must be taken to preserve the cleanliness of sample surfaces.

This section outlines the theory and experimental considerations for ARPES and for core level photoemission, especially as applied to the measurement of samples with three dimensional band dispersions grown by MBE. In our case the MBE is not attached to the ARPES chamber, and hence special care is taken to protect sample surfaces such that they can be transferred through air. The 3D nature of the band dispersions necessitates the use of a light source that is tunable in energy and hence we use a synchrotron. More detailed reviews of ARPES and photoemission in general can be found in Refs. [40, 42, 43, 44, 45].

2.3.1 The three step model

Figure 2.7(b) shows a schematic of the energetics of the photoemission process. The initial state consists of a system with N electrons. Upon excitation by a photon of energy $h\nu$, an electron is photoemitted and leaves behind a photohole. The resulting final excited state consists of N-1 electrons plus the photoelectron. The challenge in photoemission is to relate this measured final state to the initial state. In the simplest picture, the measured intensity spectrum [Figure 2.7(b), right] reflects the density of occupied states in the sample, shifted by the photon energy minus the workfunction (Equation 2.9). At large binding energies one measures excitations from core levels, and these measurements are typically performed using soft x-rays ($h\nu$ on the order of hundreds to a few thousand eV). Smaller binding energies correspond to excitations from the valence band, and these measurements are typically performed using UV light due to the high photoinization cross sections and high energy resolution achieved using UV.

A very intuitive description for this process is the three step model of Berglund and Spicer [46]. In this model the photoemission is broken into three distinct and independent processes:

1. Optical excitation of the electron from an initial state $(E_i, \mathbf{k_i})$ to a final state $(E_f, \mathbf{k_f})$ inside the solid.
2. Transport of the photoelectron to the surface.
3. Escape of the photoelectron into vacuum $(E_{kin}, \mathbf{k}_{out})$.

These steps are shown schematically in Figure 2.8(a). Rigorously speaking this three step

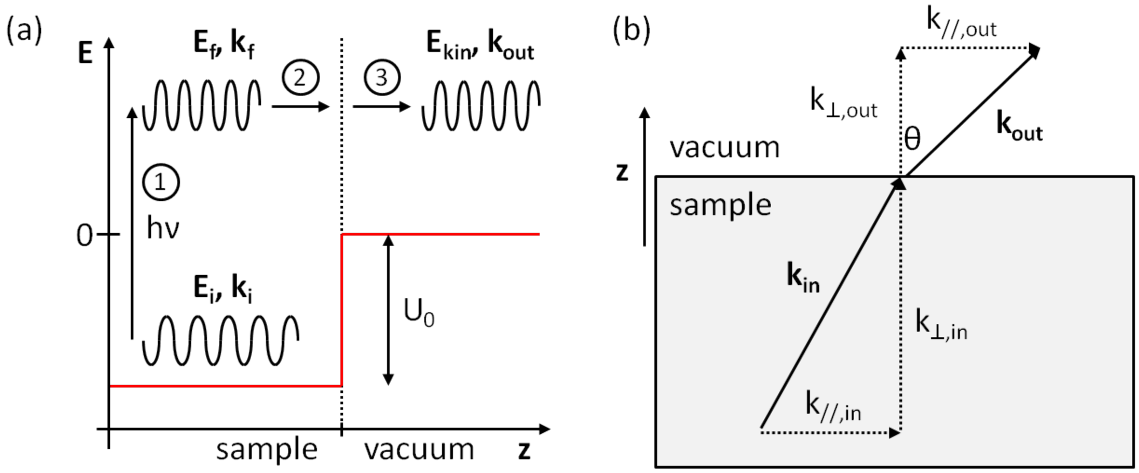

Figure 2.8. (a) Schematic of the three step model of photoemission and the relevant energies and momenta for each step. Upon escaping into the vacuum, the photoelectron must overcome a potential barrier U_0, often called the inner potential. (b) Schematic of the momentum changes upon crossing the sample/vacuum interface. The parallel component of momentum $k_{\|}$ is conserved; however due to the barrier U_0 the perpendicular component $k_{\perp}$ is not conserved.

process is not correct, as photoemission should be described by a single entirely quantum mechanical process. Nonetheless this description works remarkably well in general and gives quantitative agreement to photoemission measurements [40]. In this three step model, only the optical excitation in step 1 is treated quantum mechanically, and steps 2 and 3 are considered as attenuation and kinematic factors respectively.

The optical transition of step 1 can be described using time dependent perturbation theory. Using Fermi's Golden Rule the measured photocurrent can be expressed as a transition probability per unit time

$$\frac{d\omega_{fi}}{dt} = \frac{2\pi}{\hbar} \left|\langle f \left| H' \right| i\rangle\right|^2 \delta\left(E_f - E_i - h\nu\right) \tag{2.10}$$

where the perturbation is given by

$$H' = -\frac{e}{2mc}(\mathbf{A}\cdot\mathbf{p} + \mathbf{p}\cdot\mathbf{A}) \approx -\frac{e}{mc}\mathbf{A}\cdot\mathbf{p} \tag{2.11}$$

where we consider only the linear term, use the commutator relation $[\mathbf{p}, \mathbf{A}] = -i\hbar\nabla\cdot\mathbf{A}$, and use the dipole approximation to set $\nabla\cdot\mathbf{A} = 0$ [40]. When expressed in this form it becomes clear that the photoemission experiment does not directly measure the initial state i of interest, but rather measures a transition that is given by the matrix element $|\langle f\,|\mathbf{A}\cdot\mathbf{p}|\,i\rangle|^2$. Hence in an experiment the measured intensity can modulate or appear or disappear depending on the polarization or the energy of the incident light, and these are termed matrix effects. In chapter 4 we observe matrix effects that cause the ellipsoidal electron pockets at the $\overline{M}$ of ErAs(001) films to modulate in intensity as a function of photon energy, and in chapter 7 we observe matrix similar matrix effects for the Fermi surfaces of CoTiSb(001) films.

Although a full analysis of the matrix element requires knowledge of the initial state (which is what we are trying to measure in the first place), we can derive simple selection rules to determine whether a transition is allowed or not allowed based on symmetry arguments. For the matrix element to be nonzero, the total integrand must be even. Thus we can write

$$\langle f\,|\mathbf{A}\cdot\mathbf{p}|\,i\rangle \begin{cases} \phi_i^{\mathbf{k}} \text{ even} \quad \langle +\,|+|\,+\rangle \to \mathbf{A} \text{ even} \\ \phi_i^{\mathbf{k}} \text{ odd} \quad \langle +\,|-|\,-\rangle \to \mathbf{A} \text{ odd.} \end{cases} \tag{2.12}$$

2.3.2 Core level energy shifts

We mentioned previously that photoemission can be used both for the measurement of core levels, which do not have **k** dispersion, and valence bands, which do have **k** dispersion. In the case of core levels, one of the most useful aspects of photoemission is that the binding energies are sensitive to the local bonding environment. One can understand these core level shifts in terms of screening. For example, in the simple picture of a metal bonded to oxygen, the metal donates some of its valence electrons to the more electronegative oxygen. Due to the reduced screening, the core electrons on the metal feel a stronger Coulomb potential as a result of this electron transfer. Therefore the core level binding energies of the oxidized metal will be larger than that of the elemental metal. In chapter 6 we use core level shifts to measure changes in the bonding at CoTiSb(001) surfaces, and we also use core level intensities to determine relative compositions at the surface. More details on calculating compositions from core level intensities are found in the Appendix.

2.3.3 Band mapping

We now consider conservation of momentum through through each step of the three step model and show how photoemission is used to map the **k** dispersion of valence bands. Optical transitions correspond to vertical transitions ($\Delta\mathbf{k}$) from an initial state to a final state in the crystal that differ in energy by $h\nu$. Photons in the energy range of interest (UV) carry nearly zero momentum compared to electrons, and hence for a free electron this vertical transition is not possible since a change in energy would also require a change in momentum. However for a crystal, whose bands can be represented in a reduced zone scheme, the momentum change can be accommodated by a shift by a reciprocal lattice vector $\mathbf{G}$. Thus the momentum conservation relationship is

$$\mathbf{k_f} = \mathbf{k_i} + \mathbf{G} \tag{2.13}$$

where $\mathbf{k_i}$ and $\mathbf{k_f}$ are the initial and final state momenta inside the crystal. One then needs to connect the final state momentum of the electron in the crystal to the momentum of the photoemitted electron outside the crystal. Unfortunately, the surface breaks the periodicity of the crystal perpendicular to the surface, and as a result the electron passes through a potential barrier U_0 as it enters the vacuum [Figure 2.8(a)]. Hence $\mathbf{k_{out}} \neq \mathbf{k_f}$ [Figure 2.8(b)]. But by breaking the momentum into two components $\mathbf{k_{out}} = \mathbf{k_{out,\parallel}} + \mathbf{k_{out,\perp}}$ we can derive relationships for the parallel and perpendicular components separately.

Since the translational symmetry of the crystal parallel to the surface is not broken, the parallel component of momentum *is* conserved and we can write $\mathbf{k_{out,\parallel}} = \mathbf{k_{f,\parallel}} + \mathbf{g}$, where $\mathbf{g}$ is a surface reciprocal lattice vector. The presence of $\mathbf{g}$ suggests surface Umklapp scattering, and as we will see in chapter 7, Umklapp scattering on the (001) surface of fcc crystals can create replicas of states at the bulk Γ point that appear at bulk X, and vice versa. But for now, if we neglect Umklapp processes the relationship becomes $k_{i,\parallel} = k_{f,\parallel} = k_{out,\parallel}$ [Figure 2.8(b)]. Now, the electrons that have escaped into the vacuum must travel on the order of 1 m before reaching the detector, hence they can be treated as free electrons with kinetic energy $E_{kin} = \frac{\hbar^2}{2m} k_{out}^2$. Thus the parallel component of

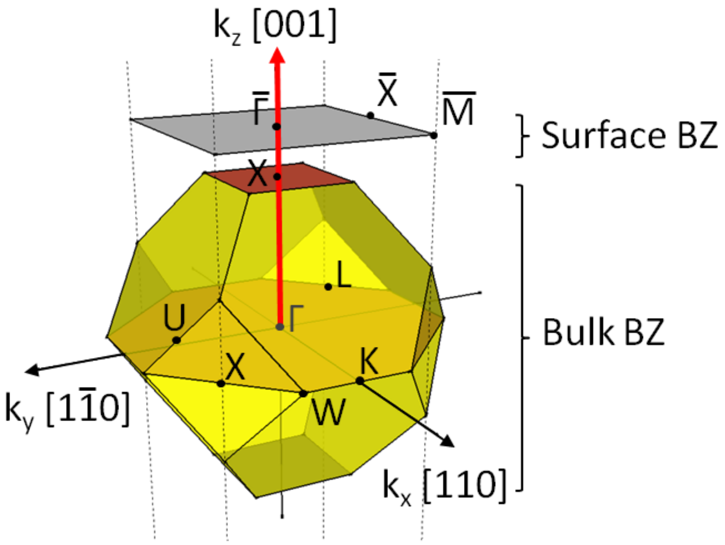

Figure 2.9. Bulk Brillouin zone for an fcc crystal along with the (001) surface Brillouin zone. Surface high symmetry points are denoted with overbars. Fixing the analyzer at normal emission ($\overline{\Gamma}$, $k_x, k_y = 0$) and varying the photon energy corresponds to traversing a reciprocal lattice rod along bulk $\Gamma - X$.

momentum is

$$k_{i,\|} = k_{f,\|} = k_{out,\|} = k_{out} sin\theta = \sqrt{\frac{2m}{\hbar^2}} \left(E_{kin}\right)^{1/2} sin\theta \tag{2.14}$$

or in a numerically useful form

$$k_{i,\|}[\mathring{A}^{-1}] = 0.512(E_{kin}[eV])^{1/2} sin\theta. \tag{2.15}$$

Thus for two dimensional states, one simply measures the in-plane dispersion $E_B(k_\|)$ by varying the emission angle θ. The binding energy is then given by Equation 2.9 and the parallel component of momentum by Equation 2.14.

On the other hand, the perpendicular component of momentum is not conserved and there is no simple relationship between the measured perpendicular momentum outside the crystal and the final state momentum inside the crystal. One simple approximation is to assume that the final state is free-electron like, with energy $E_f = \frac{\hbar^2}{2m^*}k_f^2 + |E_0|$ where E_0 is the energy measured from the bottom of the valence band to the Fermi level. Then the perpendicular component of momentum becomes

$$k_\perp = \sqrt{\frac{2m^*}{\hbar^2}} \left(E_{kin} cos^2\theta + U_0\right)^{1/2} \tag{2.16}$$

where $U_0 = E_0 + \phi$ is the "inner potential." Clearly this approximation is more valid for measurements at high photon energy, where the final state energy is also high and hence is more free-electron like [40].

Experimentally, one often simplifies the measurement and analysis of $k_\perp$ dispersions by fixing the analyzer at normal emission ($k_x = k_y = 0$) such that $cos^2\theta = 1$. One then varies the incident photon energy, which in turn varies the kinetic energy as $E_{kin} = h\nu - E_B - \phi$. For the (001) surface of an fcc crystal this corresponds to traversing a reciprocal lattice rod from the bulk Γ to bulk X high symmetry points (Figure 2.9). Now there are two parameters to be determined, m^* and U_0. One often assumes a free electron mass $m^* = m$ and uses U_0 as an adjustable parameter to match the periodicity of the measured bands [47]. Other more exact (but experimentally and theoretically more expensive) methods for determining $k_\perp$ include using calculated semi-empirical final state bands or triangulating the same final state via emission from two different crystal faces (triangulation method) [40, 47].

Finally we make a few comments about surface states versus bulk states. Surface states result from the abrupt change in potential in going from the sample to the vacuum, and are confined to the surface region where the wavefunction decays exponentially on either side. In the case of semiconductors, these surface states can often be related to dangling bonds or to dimers at the surface. In the ARPES measurement both 2D and 3D states will be measured simultaneously, so it is important to be able to distinguish the two. The following criteria must be met for a state to be a surface state:

1. For a fixed $k_{\|}$, the initial state energy of a peak must not vary with $h\nu$. If it varies with $h\nu$ it has $k_{\perp}$ dependence and must be a bulk state. However, the converse is not necessarily true. A state that does not vary with $k_{\perp}$ is not necessarily a surface state. It may in fact be simply a shallowly dispersing bulk state, for example, a bulk state from f orbitals.

2. A surface state must lie a gap in the projected bulk bandstructure.

3. Surface state lineshapes are generally narrower than bulk state lineshapes. This is because the inelastic mean free path is short, so photoelectrons stem from a short range of distances below the surface δz. Hence $k_{\perp}$ is broadened by an amount $\delta k_{\perp} = 2\pi/\delta z$, and all states within this δk window are emitted around the specific value of $k_{\perp}$. For bulk states that disperse with $k_{\perp}$, the k-broadening also implies an energy broadening [48]. But for surface states, which are independent of $k_{\perp}$, this source of broadening is irrelevant. We will later see these effects for ErAs and CoTiSb (001) thin films in chapters 4 and 7.

4. Most surface states are sensitive to impurities and can readily destroyed. Hence one test is to controllably dose the surface with an impurity such as atomic hydro-

gen or sulfur. This is the idea behind surface passivation of semiconductors. An exception to this trend is topological insulators, whose surface states are robust against nonmagnetic impurities.

2.3.4 Experiments and sample preparation

ARPES measurements were performed at beamline I4 of the MAX-Lab Synchrotron in Lund, Sweden, and complementary high resolution core level photoemission spectroscopy measurements were performed at beamline I311, also at MAX-Lab. In addition to the high photon flux ($10^{12} - 10^{13}$ photons per second at I4) one of the greatest advantages of using synchrotron light is that it is continuously tunable in energy. In the case of ARPES, this enables measurement of bulk $k_\perp$ dispersions. At I4 the energy range is $h\nu = 14 - 200$ eV, which spans nearly two full Brillouin zones for crystals with lattice constant on the order of 5 Å and inner potential on the order of 10 eV. In the case of core level photoemission, varying $h\nu$ can be used as a means for varying the photoelectron mean free path, and hence probing the sample as a function of depth.

However, one of the greatest challenges of using a synchrotron is preparing the samples for measurements. Typical ARPES measurements are performed with light in the UV ($15 < h\nu < 100eV$), which happens to sit at the minimum ($\lambda \approx 3$Å) of the "universal curve" of photoelectron mean free path (Figure 2.10). The mean free path for core level photoemission using soft X-rays is not much larger, approaching 1-2 nm. Thus the escape depth for photoelectrons is very small, on the order a few unit cells, and both ARPES and soft x-ray photoemission measurements are extremely surface sensitive. Ideally one

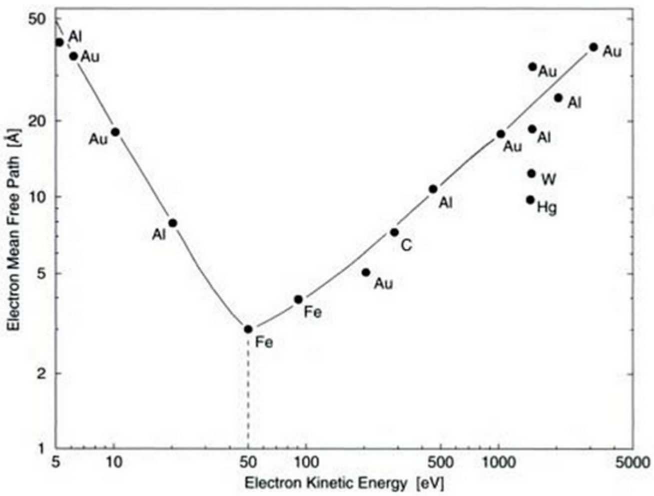

Figure 2.10. The "universal curve" of the photoelectron mean free path versus the kinetic energy. Taken from Ref. [40]. For UV and soft X-rays, with energies in the range of tens to 1000 eV, the photoemission measurements are extremely surface sensitive.

would like to have the growth chamber attached to the photoemission chamber such that one can grow and measure the sample without exposing it to atmosphere. But since growth chambers are highly specialized (for example, one cannot simply grow a Heusler alloy in a III-V or oxide MBE system), it is not always practical to have an MBE attached to the synchrotron beamline. For this reason other methods of protecting sample surfaces are needed.

In this dissertation we make use of volatile caps that are specifically chosen such that they do not react with the underlying film of interest. For III-V semiconductors such as GaAs and GaSb this technique is very well established. After growth, the sample is cooled below the growth temperature and capped with several hundred nanometers of As or Sb respectively. For GaAs, the capping is performed as cold as possible (< 0°C, achieved by cooling overnight facing the liquid nitrogen cryopanel) using a flux of As_4 atoms. At this temperature the arsenic sticks to the surface and forms a hazy capping layer. The advantage of the hazy As_4 cap is that it is very easy to see by eye if the cap has come off: the sample will appear shiny. On the other hand caps from an As_2 precursor are shiny and are not as easily distinguished from uncapped surfaces by eye. For GaSb, the capping is performed at 200°C using an Sb_2 flux. The higher capping temperature is argued to produce a more continuous film with no pinholes [49]. After capping, the samples can then be removed from vacuum as the cap protects the underlying film from oxidation. The shelf life of As and Sb caps when stored in a dry nitrogen box is typically a few months.

Once loaded back into vacuum the cap can be removed just before measurements by annealing at $325-350$°C for As-capped GaAs and $350-375$°C for Sb-capped GaSb. The removal of the cap corresponds to a spike and then decay of the chamber pressure, as well as a change from hazy to shiny surface for As-capped GaAs or a slight change in color for Sb-capped GaSb. The complete removal of the cap can be confirmed by measurements of photoemission core levels, and also by LEED or RHEED. Note that while As caps are typically amorphous, Sb caps on GaSb are psuedomorphic and hence the mere appearance of a LEED pattern does not guarantee that an Sb cap is fully removed. One needs to look for a particular LEED pattern, e.g. a $c(2\times 6)$ reconstruction or rely on the core levels.

For ErAs, ErSb, and CoTiSb samples we rely on similar As, Sb, and Sb caps respectively. Annealing temperatures for cap removal were similar to that of As-capped GaAs and Sb-capped GaSb respectively. In chapters 6 and 7, we show that upon annealing the Sb capped CoTiSb, we can recover the original (2×1) LEED pattern and core level measurements confirm complete Sb cap removal with no residual or reacted Sb. Cap removal can also be monitored by eye as the silver color of the Sb cap gives way to a slightly reddish color of the CoTiSb film. Unfortunately, we were unable to find a suitable capping materials for the other Half Heusler NiTiSn.

Once suitable samples were prepared, ARPES measurements were performed in the I4 analysis chamber using a SPECS Phoibos analyzer. The Phoibos is a two dimensional analyzer, which simultaneously collects the photoelectron intensity versus E_{kin} and emission angle θ. This can be readily converted to E_B versus one of the in-plane momenta $k_{\parallel}$ using Equation 2.14. To map the binding energy versus *both* in-plane momenta k_x and k_y we simply compile individual slices of the E_B versus the $k_{\parallel}$'s for a fixed $h\nu$. Here the direction of the analyzer emission angles is fixed such that it is oriented along the y axis to yield the k_y dispersion [Figure 2.7(a)]. An E_B versus θ_y spectrum is measured, and then the sample is rotated by by a small increment $\Delta\theta_x$ around the y axis and another E_B versus θ_y is measured. The compilation of a number of slices with incremented $\Delta\theta_x$ yields a full map of E_B versus k_x and k_y. The results can be viewed as a band dispersion of E_B versus any arbitrary $k_{\parallel}$, or as a (k_x, k_y) slice at constant energy. Such a slice taken at $E_B = E_F$ is a Fermi surface.

Chapter 3

Growth Mechanisms and Structure of RE-V/III-V nanocomposites

3.1 Introduction to rare earth monopnictides

Controlling the size, shape, and electronic properties of low dimensional metal - semiconductor hybrid structures is critical to the design of many nanoscale optical, electronic, and magnetic metamaterials and devices.[1] For example, the size, shape, and distribution of metallic nanoparticles embedded in a semiconducting matrix determine the wavelength of surface plasmon resonances for plasmonic devices, as well as the phonon scattering wavelength for applications in thermoelectrics [54]. In other geometries, arrays of embedded 1D metallic nanowires can be used as interconnects or polarization filters [55], while transparent 2D metallic planes can be used as embedded contacts in multijunction

---

[1] Some of the work presented in this chapter has previously appeared in the following publications: [50, 51, 52, 53].

photodetectors and solar cells.

The rare earth monopnictide (RE-V) / III-V semiconductor system is an ideal metal-semiconductor system for many of these applications. Although these compounds adopt two different crystal structures, with the semimetal RE-V (e.g. ErAs, ErSb) typically adopting a rocksalt structure and the III-V (e.g. GaAs, GaSb) typically adopting a zincblende structure, they share a common fcc sublattice of group V atoms [Figure 3.1(a,b)] and can be found in pairings with a small lattice mismatch (less than 0.2% for ErSb/GaSb and less than 1.6% for ErAs/GaAs). Additionally many of the RE-Vs and III-Vs are tie line compounds with one another and are hence thermodynamically stable in contact with one another, an example of which is shown for ErSb/GaSb in the Er-Ga-Sb phase diagram [Figure 3.1(c)] [56]. Thus the simultaneous growth by MBE of Er with GaSb (or Er with GaAs) just above the solubility limit yields ErSb (ErAs) nanoparticles phase segregated from a semiconducting GaSb (GaAs) matrix. The resulting nanocomposites have coherent and atomically abrupt ErSb/GaSb (ErAs/GaAs) interfaces [57, 58], allowing the metallic particles be placed in the semiconductor matrix without sacrificing the quality of the semiconductor. Similar phase behavior exists for (Sc,Er)As with GaAs [59], YbAs with GaAs [56], ErAs with In(Ga,Al)As [60], TbAs with In(Ga,Al)As [61], CeAs with In(Ga,Al)As (unpublished, P.G. Burke, H. Lu, and A. C. Gossard 2013), and many others. These nanocomposite systems have been studied extensively for applications in enhanced figure of merit thermoelectrics [62, 63], plasmonics [64], THz photomixers [65], enhanced tunneling for multijunction solar cells [66], and Schottky diodes [67]. Additionally, the thermodynamic stability of RE-Vs on III-Vs

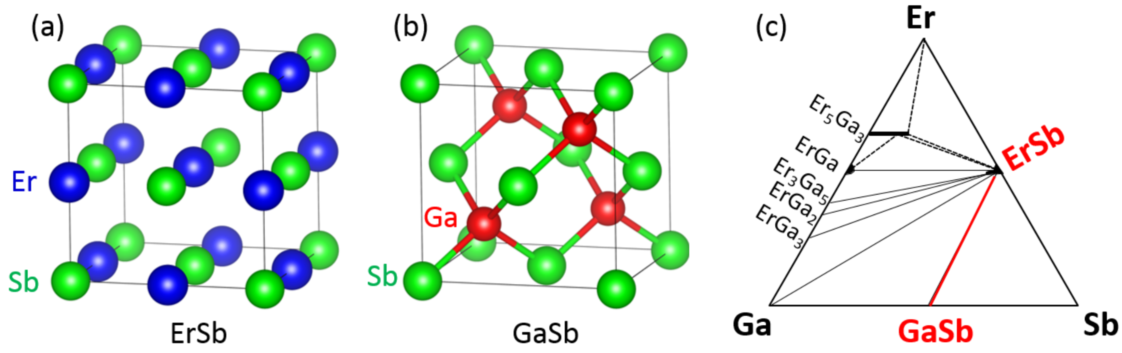

Figure 3.1. (a,b) Crystal structures for ErSb and GaSb respectively. (c) Ternary phase diagram for Er-Ga-Sb at 800 °C, adapted from Ref. [56].

enables them to serve as highly effective diffusion barriers to prevent interfacial reactions between transition metals and III-Vs [68].

However, the usage of these nanocomposites in optical, electronic, and magnetic devices requires understanding both of how to control the resulting morphologies, as well as how the reduced dimensionality affects electronic properties. While bulk ErAs and ErSb are both semimetals with overlapping valence and conduction bands at Γ and X respectively, simple quantum confinement models predicted that a band gap should open for ErAs thin films with thicknesses below 1.7 nm [69, 70]. Despite these predictions, magnetotransport and ARPES measurements saw no evidence for a bandgap [69, 71]. For even stronger cases of confinement, bandgaps were predicted for nanoparticles of ErAs [72] and also the related ErSb and ErP, and scanning tunneling spectroscopy measurements seemed to indicate the presence of a gap for some of these compounds in nanoparticle form [73, 74]. But in these specific tunneling spectroscopy measurements the samples were exposed to air and likely were oxidized. Hence, whether the RE-V nanostructures become semiconducting due to quantum confinement remains an open question. The effects of the RE-V/III-V interfaces will also need to be considered, as changes in bonding and symmetry across the interface may create additional electronic states.

This chapter explores the growth mechanisms and methods for controlling the size, shape, and distribution of the embedded ErSb and ErAs nanostructures with reduced dimensionality. Starting with a study of the nucleation of ErSb nanoparticles on GaSb (001), we then show that simultaneous growth of ErSb with GaSb produces a wide range of new self-assembled nanostructures, including arrays of vertically aligned nanorods, horizontally aligned nanorods, branched nanotrees, and lamellar nanosheets. These structures are reminiscent of the structures formed by spinodal decomposition and eutectic/eutectoid solidification [75]. Using *in-situ* STM we image the growth surface one atomic layer at a time and show that the nanostructures form via a surface-mediated self-assembly mechanism that is controlled entirely at the growth front and is not a product of bulk diffusion or bulk segregation. The possibility of tuning the size, shape, and distribution of these metallic nanostructures embedded coherently in a semiconducting matrix opens a wide range of new applications, in particular those which make use of the anisotropy. We also use cross sectional STM to measure ErAs nanoparticles and image regions of electronic contrast at the ErAs/GaAs interfaces.

The effect of reduced dimensionality on electronic structure will be the subject of Chapter 4.

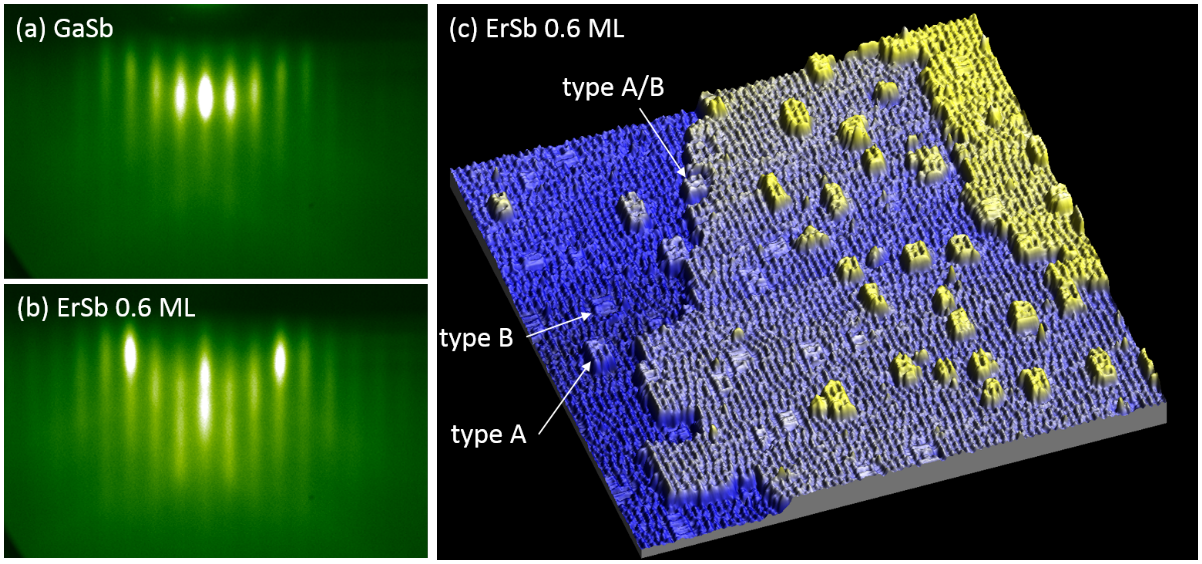

Figure 3.2. RHEED patterns along the [-110] azimuth for (a) the GaSb(001)-$c(2 \times 6)$ surface and (b) 0.6 ML ErSb nucleated on GaSb(001). (c) 100 × 100 nm STM image of 0.6 ML ErSb nucleated on the GaSb(001)-$c(2 \times 6)$ surface.

3.2 Nucleation of ErSb on GaSb

ErSb nucleates on the GaSb(001) surface via an embedded growth mode in which the impinging Er atoms displace Ga from the zincblende GaSb surface and bond with the remaining Sb to form rocksalt ErSb nanoparticles [76, 77]. The nanoparticles extend three to four atomic layers into the surface, and their depth is limited by the low diffusivity of Er through ErSb. The displaced Ga atoms are free to move on the surface and bond with the impinging Sb_2 flux to re-grow GaSb. After approximately 3 monolayers of deposition the ErSb islands coalesce into a continuous two dimensional film. Based on this growth mechanism, changes in the growth temperature should impact the surface mobilities of the Er and Ga adatoms. Thus we begin by studying the effects of temperature as a means of tuning the resulting nanoparticle size and shape during the first few monolayers of growth.

Samples were grown on GaAs(001) epi-ready substrates by molecular beam epitaxy in a modified VG V80H system with a base pressure $< 5 \times 10^{-11}$ mbar. After thermal desorption of the surface oxide using an As_4 overpressure, a 200 nm GaAs buffer layer was grown at 540 °C, followed by a 200 nm GaSb layer at 500 °C. Both layers were doped with 1×10^{18} Si atoms/cm^3. The sample temperature was then ramped to the desired growth temperature for ErSb (between 400 - 540 °C) and annealed with an Sb_2 overpressure sufficient to maintain a strong $c(2 \times 6)$ reconstruction as observed by reflection high-energy electron diffraction [RHEED, Figure 3.2(a)]. For growth temperatures below 430°C the Sb overpressure was reduced to prevent a transition to the $c(2 \times 10)$ reconstruction, and for growth temperatures above 530°C the Sb overpressure was increased to prevent decomposition of the surface. ErSb was then grown using a high temperature effusion cell for Er and a valved cracker for Sb_2 to produce a 0.6 monolayer (ML) equivalent coverage of ErSb, where 1 ML is defined to contain 5.4×10^{14} Er atoms/cm^2 and 5.4×10^{14} Sb atoms/cm^2. Upon deposition of 0.6 ML ErSb the RHEED pattern showed an increased intensity of the 1× streaks overlaid on the GaSb $c(2 \times 6)$ [Figure 3.2(b)]. Growth rates were calibrated from Rutherford backscattering spectrometry measurements (RBS) and from RHEED intensity oscillations obtained from ErAs growth on GaAs(001) surfaces. Following the growth of 0.6 ML ErSb, both the Er and Sb sources were shuttered and the sample was rapidly quenched to room temperature to retain the $c(2 \times 6)$ reconstruction. Sample temperatures were measured using a pyrometer and a thermocouple in contact with the sample block. After growth, samples were transferred in-situ through ultrahigh vacuum ($< 1 \times 10^{-10}$ mbar) to an Omicron variable temperature scanning tunneling microscope (VT-STM) to avoid sample contamination and oxidation. STM measurements were performed at room temperature.

Figure 3.3 shows a series of STM images for 0.6 ML ErSb on GaSb(001) grown at temperatures ranging from 400 to 540 °C. The ordered rows of Sb dimers oriented along [-110] correspond to the $c(2 \times 6)$ surface reconstruction of GaSb(001). Figures 3.3(c) (3D representation) and 3.2(c) (2D representation) show ErSb nanoparticles nucleated at 500°C. Two different types of ErSb nanoparticles are identified as previously reported [77]. Type A nanoparticles have their top most surface rising one atomic layer (3 Å) above the GaSb surface and type B particles have their top most surface in plane with the GaSb surface. The latter type B particles result from step-flow re-growth of GaSb around type A particles (see Figure 3.3(c), type A/B, for a type A particle that resides at a GaSb step edge, on the verge of GaSb step-flow regrowth). This GaSb regrowth arises from the Er-Ga displacement reaction.

The ErSb nanoparticles in Figure 3.3(c) are clearly distinguishable from the GaSb matrix as they do not exhibit the $c(2 \times 6)$ reconstruction of the GaSb. Instead, the ErSb particles are terminated with a mixture of rectangular domains oriented along the [110] and [-110] directions as shown in the Figure 3.3(c) inset. The lateral spacings are consistent with the $(1\times4)/(4\times1)$ pattern observed previously for ErSb films by low energy electron diffraction (LEED) and RHEED [77, 78]. This mixed phase reconstruction has been attributed to a sub-monolayer coverage of GaSb that rides on the surface of the ErSb as a result of the Er-Ga displacement mechanism [77]. The $(1 \times 4)/(4 \times 1)$ ErSb regions account for 15% of the sample surface, consistent with the surface coverage expected for the deposition of 0.6 ML ErSb nanoparticles with an average thickness of 4

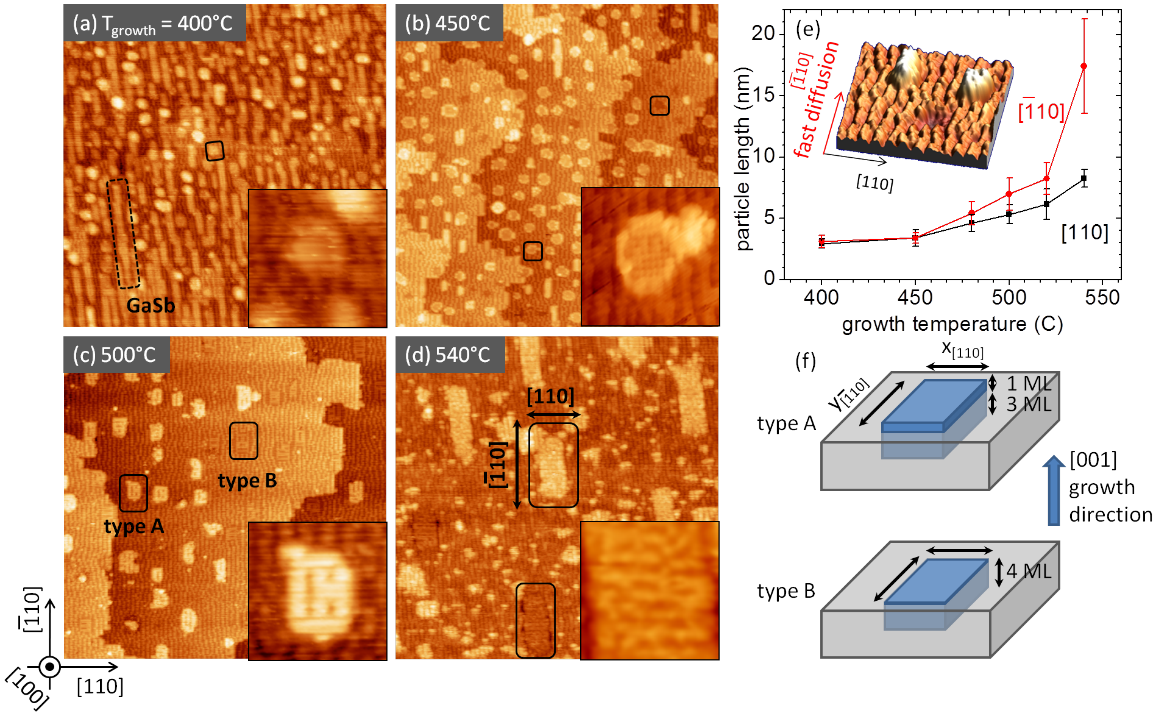

Figure 3.3. (a-d) 100 × 100 nm STM images of 0.6 ML ErSb nucleated on the GaSb(001) surface at various growth temperatures. Insets: 8.5 nm × 8.5 nm images showing the ErSb nanoparticle surface reconstructions. (e) Average ErSb nanoparticle dimensions along [-110] and [110] as a function of growth temperature. (f) Schematic of type A and B ErSb nanoparticles. Reprinted with permission from [51]. Copyright 2013 American Physical Society.

atomic layers.

For growth at 540 °C [Figure 3.3(d)], both type A and B particles are again identified and the surfaces show a mixed domain reconstruction, however the reconstruction is more disordered than for growth at 500 °C. Additionally there are small clusters on the surface, which could be small ErSb particles or clusters of GaSb. The disorder in the large ErSb nanoparticles and smaller clusters may result from an increase in the desorption rate of Sb at elevated growth temperatures, which becomes comparable to the incoming Sb flux at 540°C and eventually leads to the decomposition of the GaSb surface at higher temperatures.

At a growth temperature of 450 °C [Figure 3.3(b)], both type A and B ErSb particles are present, however, these nanoparticles are terminated with a clear (1×1) surface periodicity, as expected for an unreconstructed rocksalt ErSb surface. The (1×1) surface periodicity has also been observed by LEED and STM for ErAs(001) thin films grown at 350 °C [76, 79]. A 1.2 nm border region surrounds the edge of each ErSb nanoparticle that does not share the (1×1) surface periodicity and has similar contrast to the adjacent GaSb step edges. This border is not observed at the higher growth temperatures and is consistent with re-grown GaSb from the displaced Ga atoms. The difference suggests that an activation barrier prevents continued GaSb step-flow re-growth around the ErSb nanoparticles beyond the thin border region. The presence of type B nanoparticles indicates Ga is still able to diffuse across the GaSb surface and re-grow at the step edges as seen for higher temperatures.

When ErSb is grown at 400 °C [Figure 3.3(a)] the GaSb surface begins to roughen and in-plane (type B) ErSb nanoparticles are no longer observed. The type A islands still form as square 3×3 nm nanoparticles. These square sites account for 15% of the surface, consistent with the coverage expected for 0.6 ML ErSb. The surface roughness made it difficult to achieve adequate resolution in the STM to image the atomic periodicity on the type A surfaces. In addition to type A ErSb islands, another type of surface island is found consisting of elongated strips along the [-110] that rise 3 Å above the surface. These elongated islands are terminated with Sb dimer rows along the [-110] and are likely re-grown GaSb islands resulting from displaced Ga. The height corresponds to one atomic bilayer (3 Å) of GaSb and the lateral dimension along the [110] is 2.5

nm or the width of two adjacent Sb dimer rows in the $c(2 \times 6)$ reconstruction. These elongated islands account for 50-60% of the sample surface, consistent with the amount of Ga that would be displaced by 0.6 ML ErSb. The displaced Ga atoms do not have sufficient mobility at 400 °C to diffuse to the GaSb step edges, and instead they begin to nucleate GaSb islands near the sites where they were initially displaced. There is clearly some surface diffusion as seen by the preferential elongation of the GaSb islands along the [-110].

The switch from step-flow growth to layer-by-layer growth produces the apparent roughening of the GaSb and explains why no type B (in-plane) ErSb islands are observed as they result from GaSb step-flow re-growth around type A islands [76]. For ErSb nucleation at temperatures of 500 and 540 °C, the displaced Ga atoms have sufficient mobility to diffuse to step edges and particle edges and thus no GaSb islands are nucleated under stable growth conditions. The step-flow re-growth for temperatures 500 °C is consistent with the step-flow regime observed for GaSb homoepitaxy on vicinal surfaces [80]. Growth at 450 °C is an intermediate regime where some displaced Ga re-grows elongated GaSb islands on the surface [Figure 3.3(b)] and some re-grows GaSb around the type A ErSb nanoparticles and at GaSb step edges.

Higher growth temperatures also increase the ErSb nanoparticle sizes. As the growth temperature is raised from 400 to 540 °C, the size of the ErSb nanoparticles increase from squares with averaged in-plane dimensions of 3 nm × 3 nm to elongated rectangles with average dimensions of 8 nm × 17 nm [Figure 3.3(e)]. This elongation occurs preferentially along the [-110] direction due to increasing anisotropic surface diffusion of both Er and

Ga adatoms along the Sb dimer rows at higher growth temperatures. This direction is also consistent with the preferential diffusion of Ga adatoms on GaAs(001) $(2\times4)/c(2\times8)$ surfaces [76]. In the low temperature regime, the nanoparticle dimensions asymptote to an averaged minimum length of 3 nm along both $\langle110\rangle$ directions. The 3 nm length corresponds to slightly greater than the width of 2 Sb dimer rows for the GaSb $c(2 \times 6)$ reconstruction (one unit cell length along the [110] direction). This distance appears to be the minimum in-plane nucleation size for ErSb nanoparticles on the GaSb(001) $c(2 \times 6)$ surface. Despite the increase in the planar dimensions of the ErSb nanoparticles with temperature, the surface coverage of the nanoparticles in Figures 3.3(a-d) remains constant at roughly 15% indicating the ErSb nanoparticles maintain a thickness of 4 ML (1.2 nm) for each of the growth temperatures [Figure 3.3(f)].

Figure 3.4 shows STM tip height profiles along [110] for a single type B particle grown at 500 °C at various sample bias voltages, along with the corresponding images. The apparent height of the ErSb particle relative to the GaSb matrix varies as a function of the bias voltage, ranging from 0.2 Å above the GaSb surface at -2.0 V sample bias to 0.2 Å below the surface at +2.0 V sample bias. The strongest contrast is for large positive bias. This bias dependence reveals the apparent height differences results from electronic rather than topographical contrast. This electronic contrast, in addition to the difference in surface reconstructions, can be used to further distinguish the ErSb nanoparticles from the GaSb matrix. The direction of change in tip height suggests that relative to the GaSb matrix, the ErSb particles have a larger valence band density of states (filled states, resulting from tunneling of electrons from the sample to the tip at

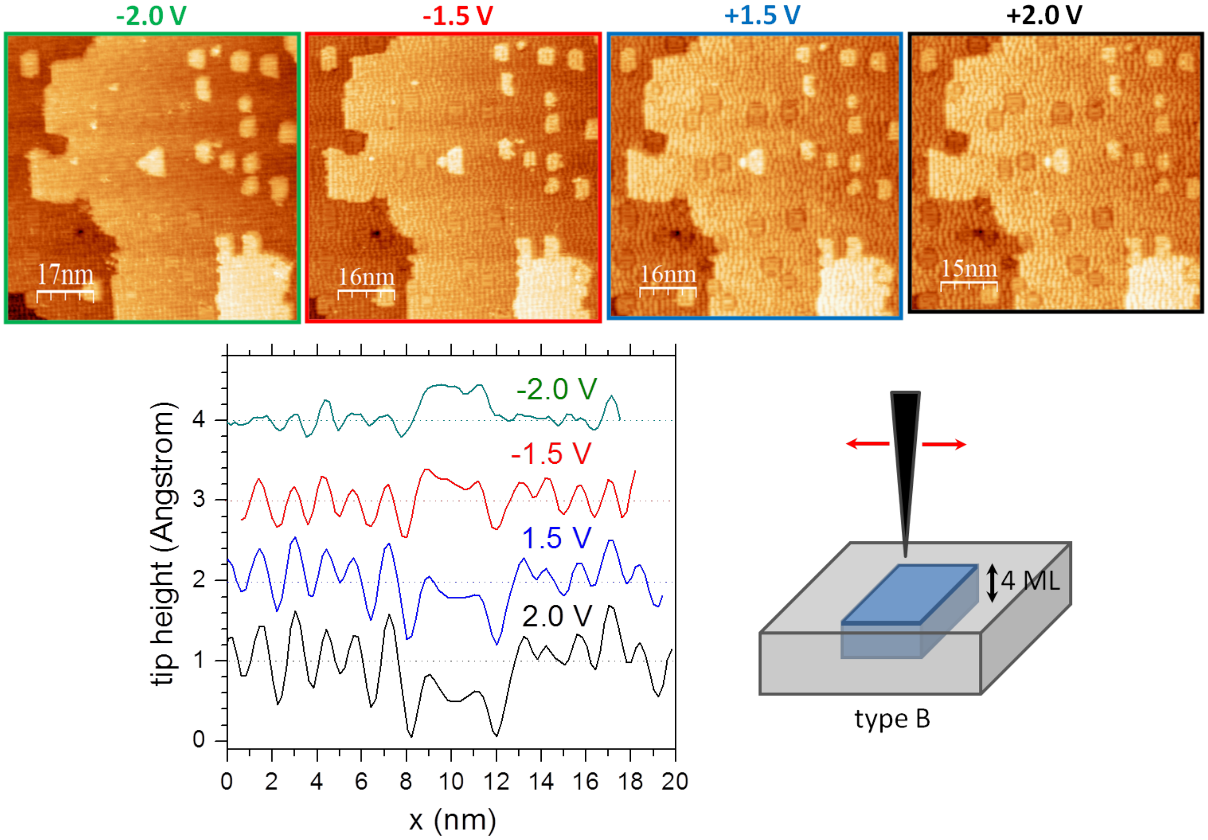

Figure 3.4. STM images and corresponding tip height profiles along [110] for a type B ErSb nanoparticle (top surface resides in-plane with the GaSb) at various sample bias voltages, demonstrating that the ErSb is electronically distinguishable from the GaSb matrix. The particles were nucleated at 500 °C.

negative sample bias) and a smaller conduction band density of states (empty states, resulting from electrons tunneling from tip to sample at positive sample bias).

3.3 Codeposition of $\mathrm{Ga}_{1-x}\mathrm{Er}_x\mathrm{Sb}$: nanoparticles, rods, trees, and lamellae

We next consider the mechanisms at play during the *simultaneous* growth of ErSb with GaSb. This process is more complicated than the simple nucleation of ErSb on GaSb, as here there are three impinging species (Er, Ga, and Sb) and the nanostructures form via a precipitation of ErSb from GaSb. A number of studies have investigated the simultaneous growth of low compositions of RE-V (less than 5 %) with III-V, which yield nearly spherical RE-V nanoparticles embedded in a III-V matrix. Here we show that by pushing the ErSb composition during simultaneous growth with GaSb a wide range of new embedded nanostructures form, including vertically aligned ErSb nanorods, horizontal nanorods, lamellar nanosheets, and branched nanotrees embedded in a semiconducting GaSb matrix. Using the combination of *in-situ* plan view STM and *ex-situ* TEM, we show that the nanostructures form simultaneously with the matrix and have epitaxial, coherent interfaces. The driving force for phase separation is analogous to that observed for eutectic (eutectoid) solidification, but instead of occurring at a liquid-solid (solid-solid) interface, here the growth occurs from the vapor at a solid surface. Additionally the mechanism is constrained by the growth surface, with a defined crystal orientation and epitaxial strain.

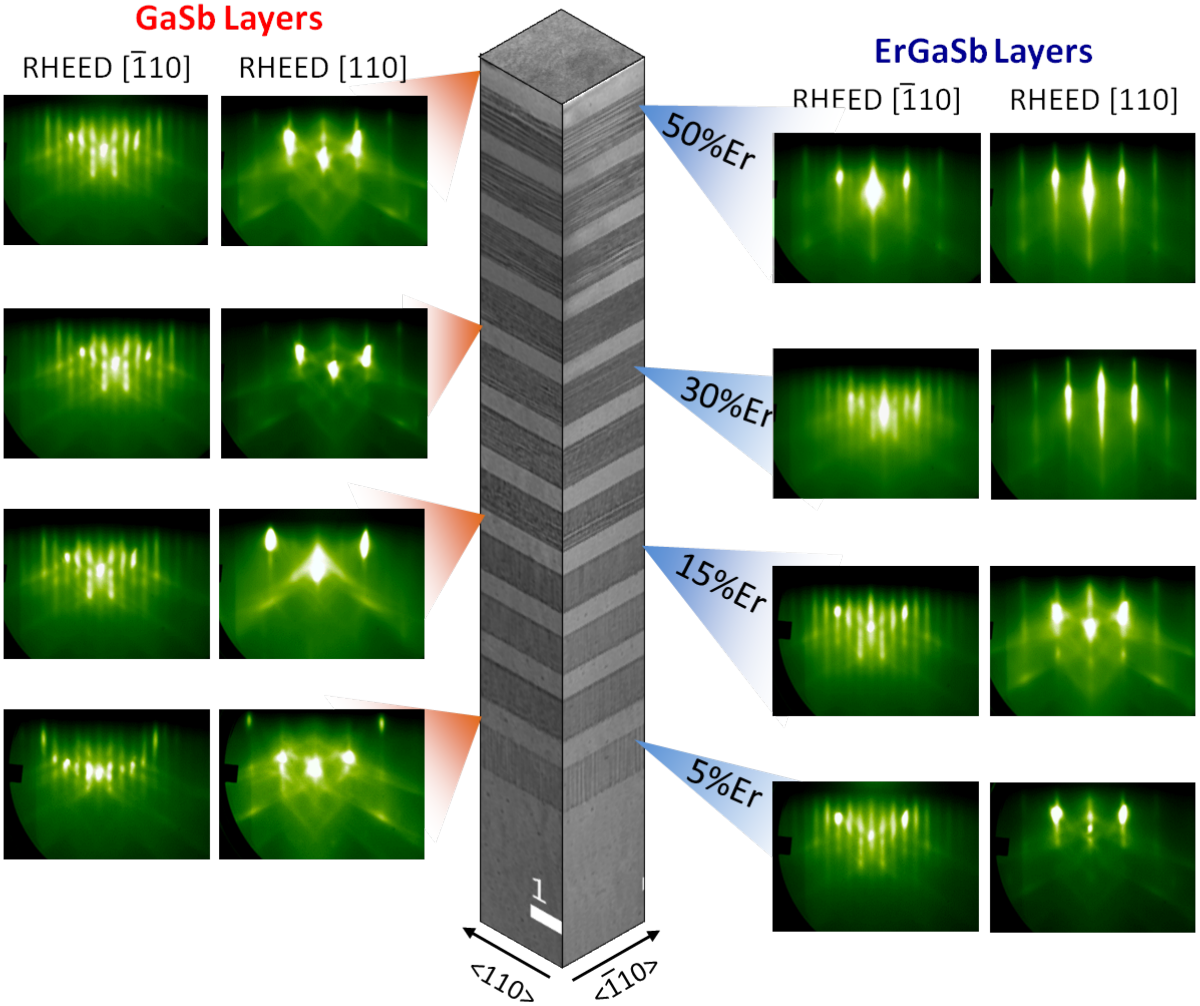

Figure 3.5. RHEED patterns (left and right) and cross sectional TEM images (center) for a multilayer sample consisting of 250 nm $Ga_{1-x}Er_xSb$ layers (dark layers in the cross sectional TEM image) followed by GaSb spacers (light layers in the TEM image).

Samples were grown by MBE in a VG V80H system using solid sources for Er, Ga, and Sb. Starting with the same GaSb/GaAs(001) buffer layer structure as in the previous section, codeposition of $Ga_{1-x}Er_xSb$ films was performed at specified temperatures by simultaneously opening individual shutters for Er and Ga under an Sb_2 flux (Sb_2 beam equivalent pressure of 10^{-6} mbar). A growth rate of approximately 200 nm/hr was used for codeposition of $Ga_{1-x}Er_xSb$ while a rate of 65 nm/hr was used for pure ErSb. All GaSb and $Ga_{1-x}Er_xSb$ layers were doped with 1×10^{18} Si atoms/cm^3 to yield conductive layers for scanning tunneling microscopy measurements.

Figure 3.5 shows overview bright field TEM images and RHEED patterns along [110] and [-110] for a multilayer sample grown at 500 °C. The sample consists of 250 nm $Ga_{1-x}Er_xSb$ layers followed by 100 nm GaSb spacers. The Er composition was varied from $x = 0.05$ to 0.50 in steps of $\Delta x = 0.05$. Note that two layers of $x = 0.10$ were grown. Surprisingly, the RHEED patterns remain very sharp and streaky throughout the sample growth. In the $Ga_{1-x}Er_xSb$ layers, for increasing Er composition the intensity of the $1\times$ streaks increases while the intensities of the reconstructed streaks fade, however even at $x = 0.50$ (50%) a GaSb-like $c(2 \times 6)$ is still faintly visible. Additionally, in each of the GaSb spacer layers a sharp $c(2 \times 6)$ pattern is observed. These findings suggest that the $Ga_{1-x}Er_xSb$ layers remain epitaxial for very large Er compositions of up to 50% without significant roughening of the surface and that GaSb readily overgrows on these layers.

Figure 3.6 shows bright field TEM images of several individual layers in the multilayer sample (middle column), along with high resolution z-contrast STEM images (right column, courtesy of H. Lu and T. E. Buehl). The formation of ErSb nanorods at 500

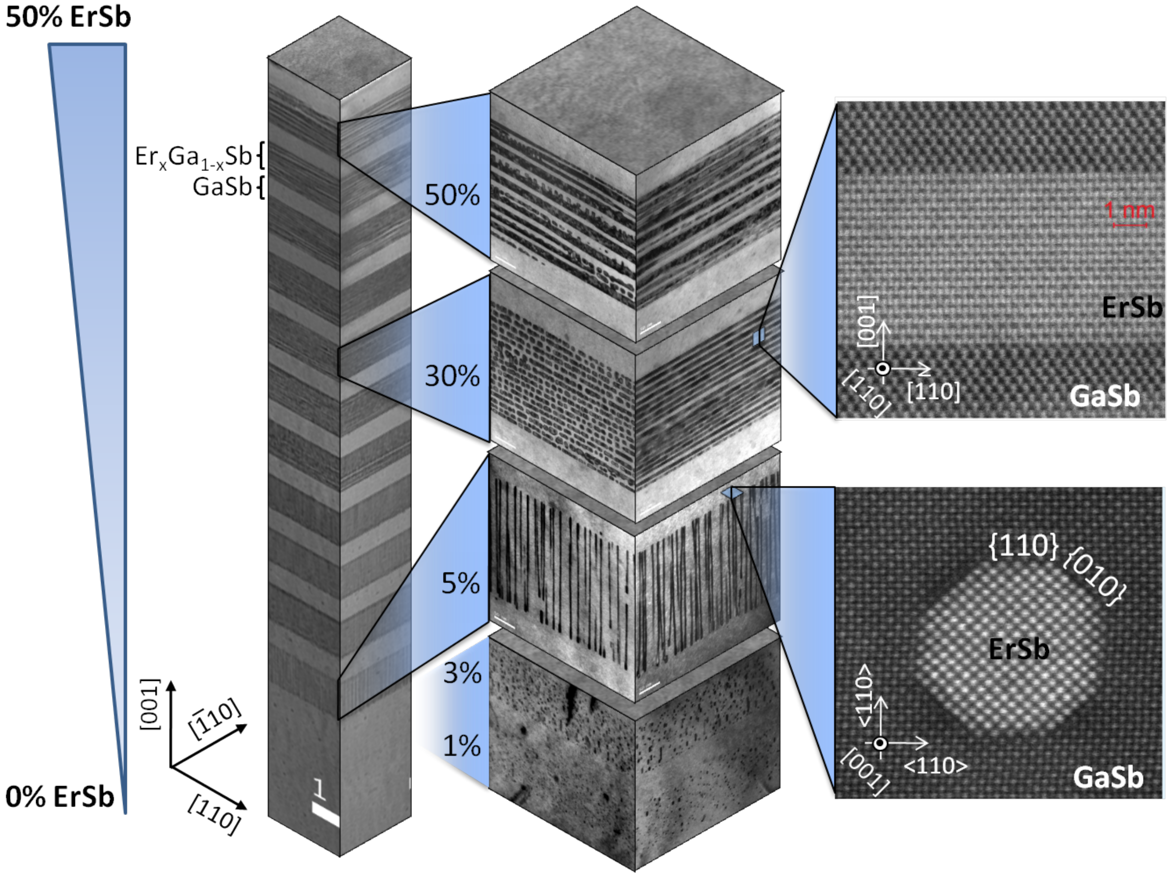

Figure 3.6. TEM images of individual layers within then multilayer Ga$_{1-x}$Er$_x$Sb. The left and middle columns show bright field images (scale bar for the middle column is 50 nm), while the right column shows STEM images. Bright field TEM courtesy of TEM Analysis, STEM courtesy of H. Lu and T. E. Buehl.

°C begins when the Er concentration is increased to around 5% Er (or x = 0.05), with lower Er concentrations ($x = 0.001 - 0.05$) producing ErSb nanoparticles. At 5% Er, the growth produces vertically aligned ErSb nanorods (dark regions in the bright field images) that are nearly continuous throughout the layer and aligned along the [001] growth direction. Post-growth annealing at 500 °C for up to 24 hours does not produce changes in the morphology, suggesting that these structures result from phase separation and diffusion at the growth surface rather than bulk diffusion.

As the Er concentration is further increased, rather than simply increasing the vertical nanorod density/diameter or forming vertically oriented lamellae, at 30% Er the nanorods flip orientation and align horizontally along the [-110] direction, perpendicular to the global [001] film growth direction. Increasing the composition to 50% Er results in horizontally oriented lamellar nanosheets, in contrast with conventional eutectic lamella, which would be expected to align vertically along the global growth direction. Surprisingly, in all cases the films remain epitaxial and single crystalline as observed by RHEED, selected area electron diffraction, and X-ray diffraction (XRD), despite the large amounts of ErSb incorporated.

We begin by exploring the mechanisms for vertical nanorod formation, and later extend these mechanisms to explain the growth of horizontal nanorods and nanosheets. The TEM images show that the vertical nanorods begin to form at the onset of codeposition of Er with GaSb. In order to gain a clearer picture of the nucleation process, the onset of codeposition was experimentally simulated by sequentially growing thin individual layers of ErSb and GaSb at 500 °C and examining the surface structure after each layer.

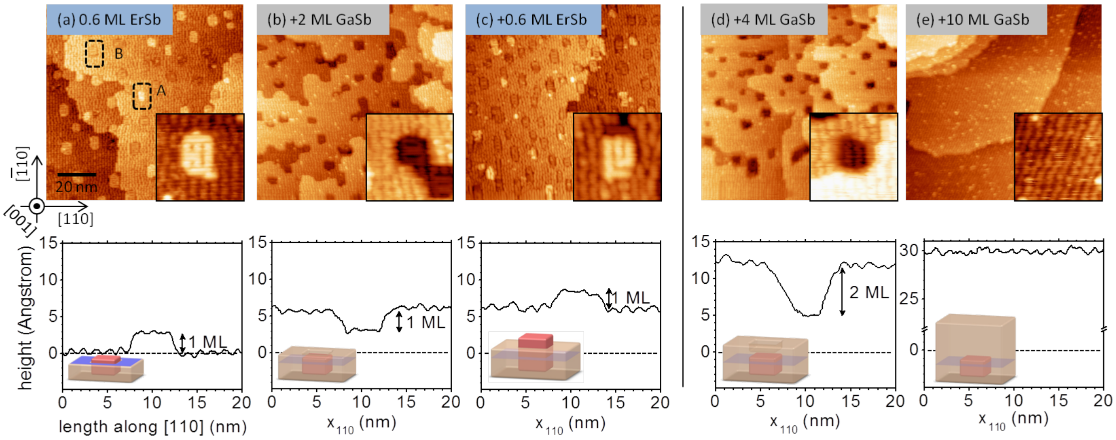

Figure 3.7. Filled states STM images (100 nm × 100 nm) following sequential depositions at 500 °C of (a) 0.6 ML ErSb on a GaSb (001) surface followed by (b) 2 ML of GaSb, which produces pits in the surface, followed by (c) an additional 0.6 ML ErSb, which grows in the pitted regions. (d & e) STM images acquired after depositing additional GaSb on the surface shown in (a), totaling (d) 4 ML of GaSb, and (e) 10 ML of GaSb. Higher resolution STM inserts (10 nm x 10 nm) show the surface reconstruction of the ErSb sites, with (a-c) showing exposed ErSb and (d,e) showing GaSb covering the ErSb sites. The corresponding height profiles and schematics of the ErSb regions are provided below each image. Reprinted with permission from [50]. Copyright 2013 American Chemical Society.

Figure 3.7(a) shows an in-situ filled states STM image acquired after the deposition of 0.6 monolayers (ML) of ErSb directly on a GaSb (001) surface. The ErSb nucleates via the thermodynamically favored embedding mechanism discussed in the previous section. Here, the impinging Er atoms exchange with Ga from the substrate surface. The displaced Ga diffuses on the surface to a GaSb step edge and bonds with incoming Sb to form additional GaSb [76, 77]. The step flow regrowth of the GaSb keeps the surface smooth, with only a few atomic steps visible in the 100×100 nm scans. The deposition of 0.6 ML of ErSb produces rectangular 5×7 nm islands embedded in the surface that are 4 atomic layers (1.2 nm) in thickness and encompass only 15% of the total surface area.

When a 2 ML thin layer of GaSb is subsequently deposited on the surface in Figure

3.7(a), it does not immediately wet the exposed ErSb island surfaces [Figure 3.7(b)]. The overgrown surface is characterized by 1-2 ML deep pits that have the same areal density as the starting 0.6 ML ErSb surface and terminated in the same $(1 \times 4)/(4 \times 1)$ reconstruction. The 2 ML of additional GaSb grows around the ErSb sites, but does not wet the surface of the ErSb islands. Instead, the surface mobility of Ga allows it to move to the nearest step edges of the GaSb and maintain a step flow growth process.

The addition of another 0.6 ML of ErSb onto the pitted surface in Figure 3.7(b) finds that the additional ErSb prefers to bond to the existing ErSb and fill in the pitted regions. As a result no pits are observed in the STM image in Figure 3.7(c) following such a deposition; instead, the surface shows a mixture of ErSb Type A and B islands similar to those found in Figure 3.7(a). The total surface coverage in Figure 3.7(c) is larger than the 15% coverage for the initially nucleated particles [Figure 3.7(a)] because the 0.6 ML additional ErSb is in excess of what is required to fill the pits, hence the excess Er nucleates ErSb islands at new sites. This preferential growth of ErSb at the nucleated sites, along with the preference of Ga to bond at GaSb step edges and to refrain from wetting the ErSb (001) surface, enables ErSb nanorods to form in the GaSb one atomic layer at a time.

The distribution of the ErSb nanorods is consequently determined by how the initial islands of ErSb first nucleate. The nucleation sites become the template for further ErSb growth. The mechanism relies upon maintaining a relatively smooth surface to ensure the newly deposited Ga and Er can migrate to their preferred bonding locations. The step flow growth regime for GaSb under these conditions enables significantly more continuous and well defined RE-V nanostructures to be formed in GaSb than in GaAs.

In contrast, for ErAs and GaAs under standard growth conditions ($540-620$°C), the GaAs grows in a layer-by-layer mode, and displaced Ga regrows GaAs as islands near the point of displacement rather than at a nearby GaAs terrace step edge [76]. The result is a significant roughening of the surface over time, which leads to a decrease in the mobility of Er and Ga adatoms on the surface, making it more difficult for Er to migrate to previously nucleated ErAs sites. However, for simultaneous growth of ErAs and GaAs at elevated temperatures (> 650°C, high enough to induce step-flow growth of GaAs) we speculate that the surface may be sufficiently smooth to produce nanorod growth.

The TEM images in Figure 3.6 reveal that upon termination of the codeposited $\mathrm{Ga}_1-x\mathrm{Er}_x\mathrm{Sb}$ layers, the protective GaSb capping layer completely overgrows the nanocomposite. This phenomenon seems surprising given that GaSb initially refrains from wetting exposed ErSb regions; however, this aversion is found to disappear as more GaSb is deposited. Figure 3.7(d) shows an STM image acquired after depositing 4 ML of GaSb over a surface embedded with 0.6 ML of ErSb nanoparticles. Surface pitting is again observed; however, the depths of the pits measure only 2 ML despite the deposition of 4 ML worth of GaSb. Additionally, the surface structure of the pits is the same as the Sb-dimer rows of the GaSb $c(2\times 6)$ reconstruction rather than the $(1\times 4)/(4\times 1)$ reconstruction of ErSb, indicating that a thin GaSb layer covers the ErSb nanoparticles.

Increasing the total additional amount of GaSb to 6 ML, the pitted areas remain 2 ML deep, while their lateral dimensions decrease from approximately 5 nm to 3 nm along

[110]. When the total surface coverage of GaSb reaches 10 ML [Figure 3.7(e)], no pitted regions remain visible and an atomically flat GaSb $c(2\times6)$ surface is obtained. Although GaSb initially leaves the ErSb surfaces exposed, as the surface concentration of GaSb increases, it begins to quickly cover over the ErSb.

During codeposition, a balance must be maintained between GaSb attempting to fill in the ErSb surface template and additional surface Er seeking out these ErSb regions for growth. By manipulating the growth conditions this surface balance can be altered, thereby changing the structure of the nanocomposite. Figure 3.8(a,b) shows cross-sectional TEM images of a 500 nm $\mathrm{Ga_{0.9}Er_{0.1}Sb}$ film grown at 540 °C. Instead of straight vertical nanorods that formed for the same Er composition grown at 500 °C [Figure 3.6(c,d)], the higher growth temperature produces branched nanorods (nanotrees).

The branched structures extend outward along the [-110] direction, but do not branch out along the [110]. The plan-view image [Figure 3.8(c)] also indicates a preferential ordering of the nanorods along the [-110] direction. In both cases, this preferred direction is attributed to faster diffusion along the [-110] oriented GaSb Sb-dimer rows. The average diameter of the branched nanorods doubles from roughly 5 nm for 500 °C growth to 11 nm for 540 °C growth.

The branching events occur at nearly regular 100 nm intervals during growth, as denoted by arrows in Figure 3.8(a). At each interval, a number of nanorods terminate just prior to the splitting of the remaining nanorods into two nanorods. The periodicity suggests that branching is triggered by reproducible instabilities at the growth surface where the balance between filling a pit with ErSb or with GaSb continues to switch. If

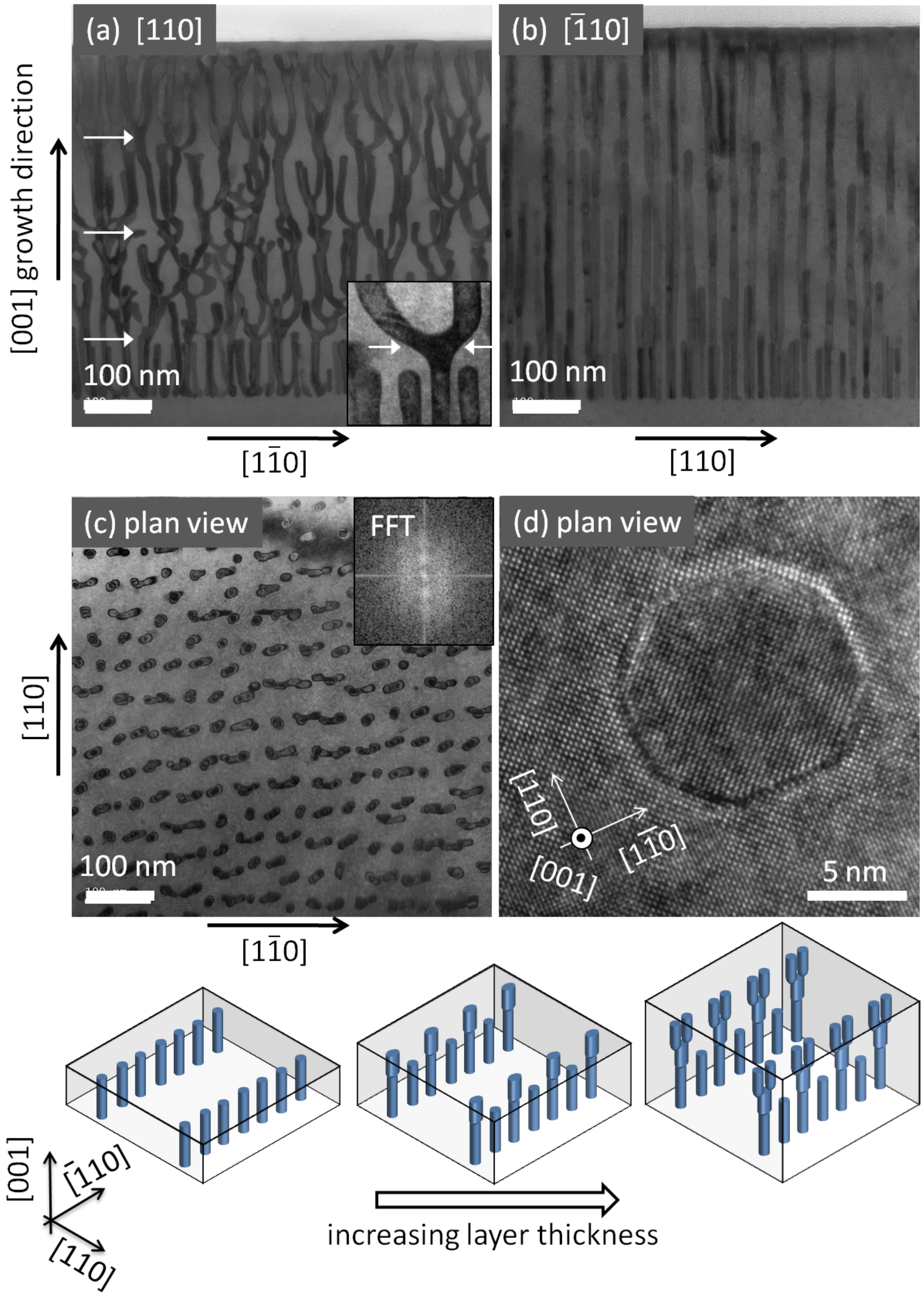

Figure 3.8. Bright field TEM images of a 250 nm thick Ga$_{0.9}$Er$_{0.1}$Sb (001) layer grown at 540 °C, along the (a) cross-sectional [110] zone axis, (b) cross sectional [1-10] zone axis, and (c) plan-view [001] zone axis. (d) High resolution plan-view TEM image of a single ErSb nanorod, showing a mixture of {010} and {110} facets. Bottom: schematic depicting nanorod branching. Reprinted with permission from [50]. Copyright 2013 American Chemical Society.

the surface becomes too GaSb rich many of the nanorods would simultaneously become overgrown by GaSb. The remaining rods in turn have to incorporate a higher concentration of ErSb, causing them to elongate in-plane along [-110] due to faster surface diffusion along that direction. However, as will be shown in the next few paragraphs, it is thermodynamically stable for the rod to split into two rods with octagonal cross sections than remain elongated in-plane. This is analogous to the growth front instabilities that produce branching during eutectic solidification [75, 81]. The nanorods expand in cross-section reaching 20 nm along the [-110] before bifurcating into two new branches, which immediately begin to separate from each other as they grow. With the surface balance of ErSb and GaSb restored, additional growth proceeds as in the case of the vertical nanorod templates until the balance tips again.

Throughout the nanocomposite, the ErSb/GaSb interfaces remain atomically sharp and completely epitaxial. The ErSb nanorods assume an octagonal cross-section with a mixture of {110} and {010} facets as seen in the high resolution plan-view TEM image [Figure 3.8(d)] and the STEM image (Figure 3.6). This faceting is observed for both branched and unbranched nanorods. The octagonal shape of the rods contrasts sharply with the more rectangular edges observed during the formation of the initial ErSb islands [Figures 3.7(a) and 3.3]. The differences in faceting and elongation are believed to result from differences in the thermodynamics of the two cases. For the nucleation of ErSb islands on GaSb (001), the islands are a flattened platelet only 1.2 nm (4 ML) in thickness. The (001) growth surface is much larger than the sidewall facet areas, and thus the surface energies of the sidewalls have a minimal contribution to the total surface energy of the island. But once the ErSb begins to form vertical nanorods, the surface area of its sidewalls become much larger than the area of the (001) growth faces and quickly become the dominant contribution to the total surface energy.

The relative thermodynamic stability of the two observed geometries can be estimated by assuming the rectangular geometry has only the observed {110} facets, the octagonal geometry has an equal mix of {110} and {010} facets, and both nanorod geometries have identical cross-sectional (001) areas and [001] lengths. Since ErSb readily wets the GaSb (001) surface and GaSb overgrows the ErSb (001) sites within only a few monolayers, the {010} surface energies for ErSb and GaSb are assumed to be roughly equal, i.e. $\gamma_{ErSb,010} = \gamma_{GaSb,010} = \gamma^{'}$. The relative difference in surface energies for the GaSb {010} and {110} planes is approximately $\gamma_{GaSb,110} \approx (2/3)\gamma_{GaSb,010} = (2/3)\gamma^{'}$ [82], while the relative difference in surface energies for ErSb is approximately $\gamma_{ErSb,110} \approx 3\gamma_{ErSb,010} = 3\gamma^{'}$ [83]. Because the ErSb-GaSb interfacial bonds are expected to be weak [84], the interfacial energy is approximated as the sum of the ErSb and GaSb surface energies. Using a Wulff construction to calculate the energies of the sidewalls and ignoring the top and bottom {001} planes, the relative free energies are found to be $G_{octagon} \approx 0.70 G_{square}$. Hence for a nanorod aligned along [001] the octagonal faceting is thermodynamically more favorable than either a rectangular or in-plane elongated nanorod. These surface energy arguments also explain why nanorods grown at higher temperatures tend to bifurcate into trees. Fast diffusion along [-110] at elevated temperatures causes the vertical nanorods to begin to elongate along [-110]. However, this in-plane elongation along [-110] is thermodynamically not favorable, hence the rods split/branch into two rods with octagonal cross section.

Thermodynamics plays an important role in determining which surface sites are energetically more favorable for newly deposited Er or Ga atoms to bond. The underlying structure does not change once the ErSb bonds are formed, but it does appear to influence where newly deposited Er atoms prefer to bond. Prior to bifurcation, the nanorods begin to expand in length along the [-110]. Continued growth increases the area of the {110} sidewalls, which is energetically less favorable than splitting into two rods with mixtures of {010} and {110} facets. Because the splitting occurs through the growth of one atomic surface layer at a time, the bonding preferences of the surface sites to Ga and Er must be influenced by the underlying structure.

Figure 3.9 shows a series of sequential STM images taken at different stages during the formation of a $Ga_{0.9}Er_{0.1}Sb$ nanocomposite layer grown at 540 °C depicting the transition from nucleated rectangular platelets to octagonal nanorods. After 3 nm of growth, the codeposited nanorods appear as 1 ML deep pits [Figure 3.9(e)] consistent with the pits observed during the initial nucleation of ErSb nanoparticles [Figure 3.7(b)]. The pitted regions are terminated in the $c(2 \times 6)$ reconstruction, indicating GaSb coverage. Because the STM is performed at room temperature, it is not certain as to whether this GaSb overlayer exists during growth or forms during cool down of the sample; however the areal density of the pits is consistent with the concentration of Er deposited.

The ErSb nanorods after 3 nm of growth are elongated along the [-110], but less rectangular in shape than the 0.6 ML islands. After 30 nm of growth, the nanorod regions appear more symmetrical and more consistent with the plan-view TEM. After 500 nm

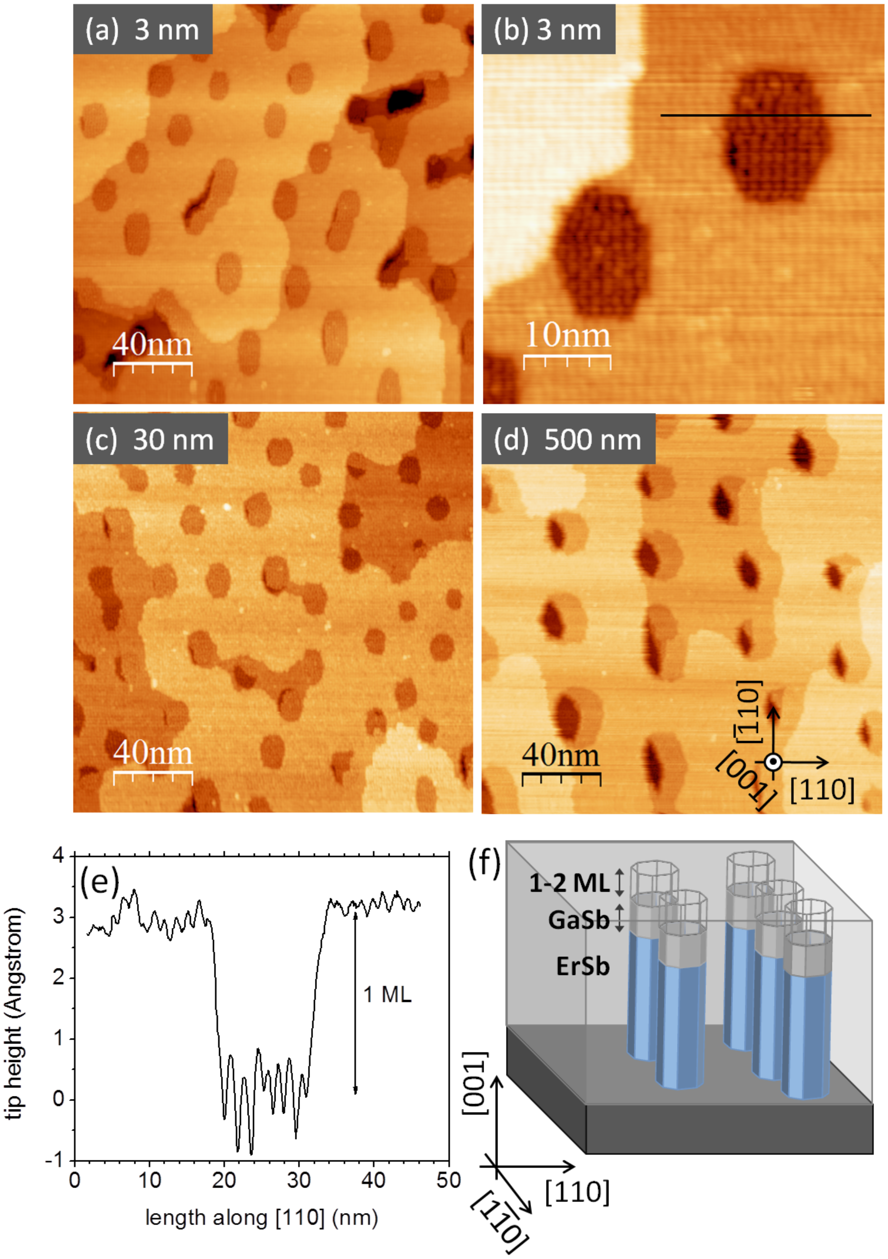

Figure 3.9. Sequential plan-view STM images of a $Ga_{0.9}Er_{0.1}Sb$ (001) nanocomposite surface grown by codeposition at 540 °C. (a) After 3 nm of growth, (b) a higher resolution image after 3 nm of growth, (c) after 30 nm of growth, and (d) after 500 nm of growth. (e) Height profile of the ErSb growth regions after 3 nm. (f) Schematic showing the basic surface structure leading to the propagation of the ErSb nanorods in GaSb. Reprinted with permission from [50]. Copyright 2013 American Chemical Society.

of growth [Figure 3.9(d)], the nanorods become aligned along the [-110] indicating this ordering develops over a series of branching events. The driving force for this ordering is not presently understood, although it is assumed to be strain related due to the slight lattice mismatch between ErSb and GaSb. Note that in the related ErAs/GaAs nanocomposite system, the measured lattice mismatch is actually larger than that predicted by Vegard's law due to an expansion in the lattice parameter at the ErAs/GaAs interfaces [85]. Hence interfacial strain is expected even for the ErSb/GaSb system, in which the bulk ErSb and GaSb lattice parameters are nearly matched.

A schematic of ErSb nanorod propagation is shown in Figure 3.9(f) showing a 1-2 ML deep pit in the surface above each nanorod and a thin GaSb overlayer covering the rods. Although the STM cannot measure the depth of the GaSb overlayer, following the GaSb overgrowth study in Figure 3.7(d,e), the GaSb overlayer is likely less than 10 ML in thickness, otherwise the pitted surface would be completely filled and a smooth GaSb surface would be recovered.

This surface mediated growth mechanism also explains the formation of the higher Er concentration horizontal nanorods and nanosheets (Figure 3.6). For the horizontal nanorods, as the Er concentration is increased beyond 10%, additional Er results in the nucleation of more [-110] elongated islands on the surface. The increase in surface area on the top and bottom {001} faces more than compensates for the increased area of {110} sidewalls. As enough Er is supplied, the elongated islands coalesce and further reduce the surface area of {110} sidewalls by forming a series of wires running horizontally along the [-110]. This process is enhanced by an increase in the surface roughness, which results in decreased terrace width and increases the probability of Er adatom step edge attachment over island nucleation on terraces. Atomic diffusion along the atomic step edge results in GaSb and ErSb phase separation and the growth of horizontal ErSb nanowires by a step-flow mode.

As growth continues, newly deposited Er forms ErSb on top of the underlying template layers. The growth causes the area of the {110} sidewalls to increase and the structures become less and less energetically content. The horizontal nanorods cannot split as in the case of the branched structures, and eventually reach a thickness where it becomes energetically unfavorable for them to support additional ErSb on the surface. The surface/interface energies, in addition to the step flow growth process, cause the structures become overgrown by GaSb, thus terminating as horizontal nanowires rather than growing into vertically oriented lamella. The Er that would have bonded to these nanorods instead bonds to other nanorods until they too reach a critical height and the process continues throughout the growth. Based on the TEM images (Figure 3.6), the critical height of the horizontal nanorods under these growth conditions is approximately 10 nm.

Further increases in the Er concentration cause a greater density of horizontal nanorods to nucleate adjacent to each other. Thus at 50% Er the ErSb nanosheets (Figure 3.6) result from the coalescence of horizontal nanorods, and the surface energy is minimized since the structure contains only {001} faces. A filled states STM image of the $Ga_{0.5}Er_{0.5}Sb$ (001) surface (grown at 500 °C) is shown in Figure 3.10. The surface is characterized by elongated islands that are 3-4 nm along [110] and extend up to tens of

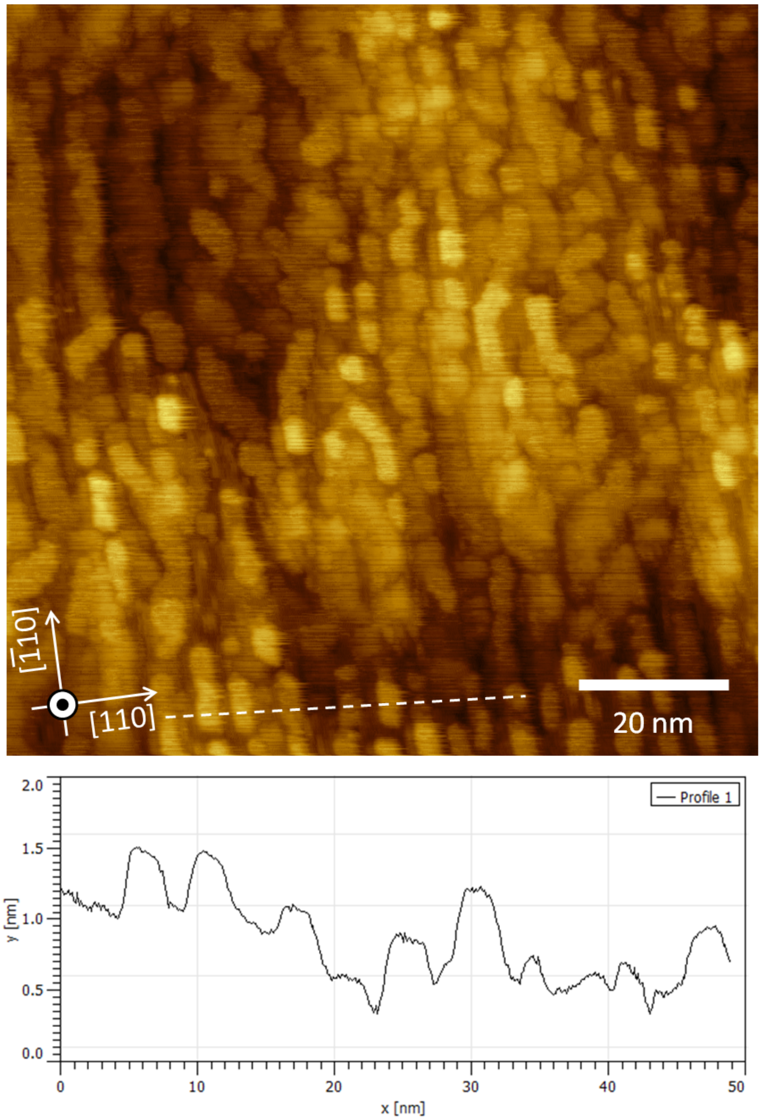

Figure 3.10. Filled states STM image and tip height profile of a 50% ErSb sample ($Ga_{0.5}Er_{0.5}Sb$) grown at 500 °C.

nanometers along [-110], consistent with the direction expected for fast surface diffusion along [-110]. These islands have step heights of approximately 3 Å, or 1 monolayer. The RHEED pattern showed an overall $c(2 \times 6)$ pattern (Figure 3.5); however due to the surface roughness it was not possible to resolve the surface reconstructions by STM. Therefore it is difficult to determine which of the regions are ErSb or GaSb-terminated.

To further explore the effects of composition another multilayer (250 nm $Ga_{1-x}Er_xSb$ / 100 nm GaSb) sample was grown at 500 °C for Er compositions from $x = 0.50$ to 1.00 in steps of $\Delta x = 0.05$. Bright field TEM images of this sample are shown in Figure 3.11, with the ErSb appearing as dark regions and the GaSb as light regions. For $0.50 < x < 0.70$ the $Ga_{1-x}Er_xSb$ layers show a lamellar morphogy and the corresponding RHEED patterns showed a very faint $c(2 \times 6)$ reconsruction. However for $x > 0.70$ the lamellae coalesce into more continuous bands of ErSb-like contrast and the surface roughens dramatically with a rapid decrease in the intensity of the RHEED pattern. For these very high Er compositions it is suspected that the $Ga_{1-x}Er_xSb$ may contain GaSb particles phase segregated from an ErSb matrix; however initial TEM images were not sufficient to resolve different phases within these high Er composition layers.

3.4 Cross sectional STM of ErAs nanoparticles

The preceding sections used *in-situ* plan view STM to image the growth surfaces and determine the mechanisms for ErSb nucleation on GaSb and phase segregation during simultaneous growth of ErSb with GaSb. But often at the growth surface the ErSb

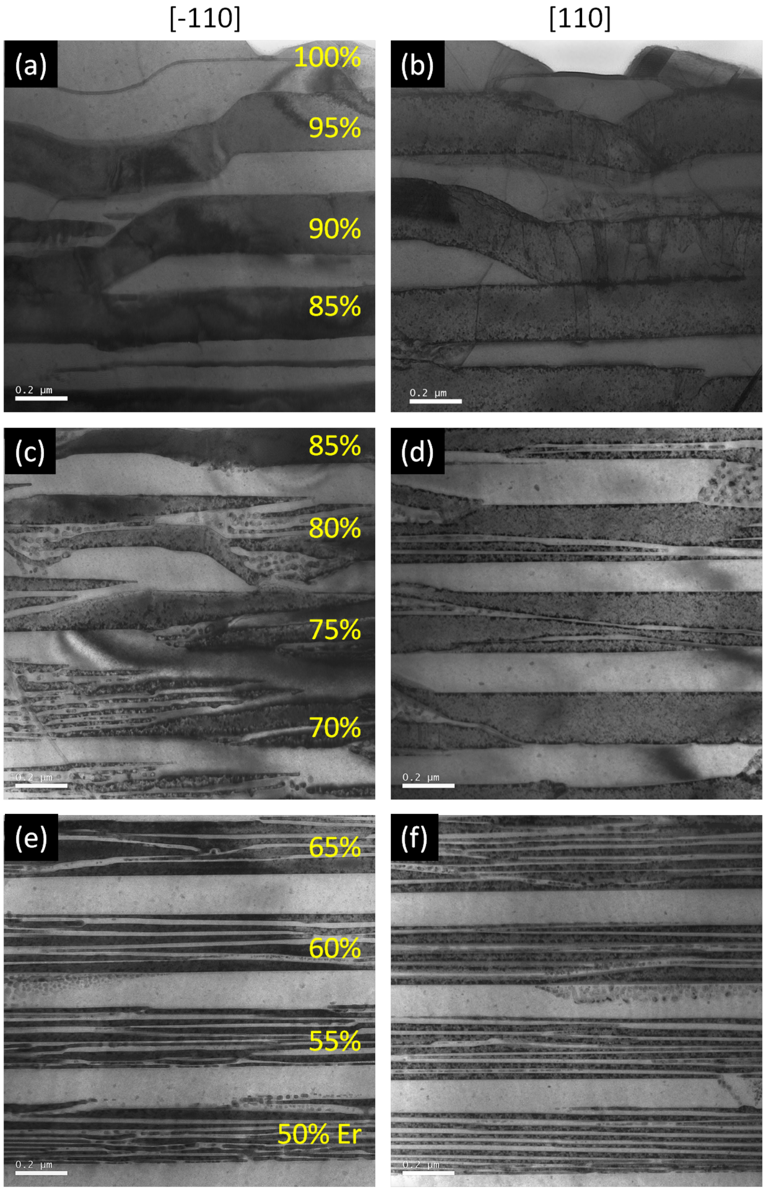

Figure 3.11. Bright field TEM images for $Ga_{1-x}Er_xSb$ sample for $x = 0.55$ to 1.00.

nanostructures of interest were buried under a thin layer of GaSb (Figure 3.9). In this section we use cross sectional STM as a method for measuring the *internal* structure of the related ErAs nanoparticles and nanorods embedded in a GaAs matrix.

The ErAs nanoparticle samples were grown on n-type GaAs (001) substrates in a VG V80H system. The epitaxial layer sequence consisted of GaAs (001) substrate / 170 nm GaAs / 50 × (20 ML AlAs/20 ML GaAs superlattice) / 500 nm GaAs / 4 (N ML ErAs/125 nm GaAs) / 500 nm GaAs, where N = 0.125, 0.25, 0.5, 1.0 (Figure 3.12). Layers were grown at rates of 0.5 ML/s for GaAs and AlAs and 0.025 ML/s for ErAs as calibrated by RHEED oscillations. All layers were grown with an As_4 overpressure, a constant substrate temperature of 540 °C and constant Si doping of 5×10^{18} cm^{-3}.

The nanorod samples were grown on n-type gallium-polar (114)A GaAs substrates in a Varian Gen II system (growth by T. E. Buehl). The epitaxial layer sequence consisted of a similar GaAs buffer layer and AlAs/GaAs superlattice, followed by a 500 nm $Ga_{0.94}Er_{0.06}As$ layer grown at 580 °C by codeposition of Er, Ga, and As. All layers had a Si doping concentration of roughly 10^{18} cm^{-3}. Further growth details of the ErAs nanowires in GaAs(114)A are provided elsewhere [86, 87].

After growth, the samples were cleaved in ultrahigh vacuum to expose a clean {110} surface and analyzed at room temperature in an Omicron variable temperature scanning tunneling microscope. Figure 3.12 presents an overview of the STM images for ErAs nanoparticles embedded in GaAs (001). All scans are made on the {110} surface at negative sample bias (filled states). The AlAs/GaAs superlattice serves as a marker to determine the position of the subsequent ErAs layers. The 1-2 ML thin clusters observed

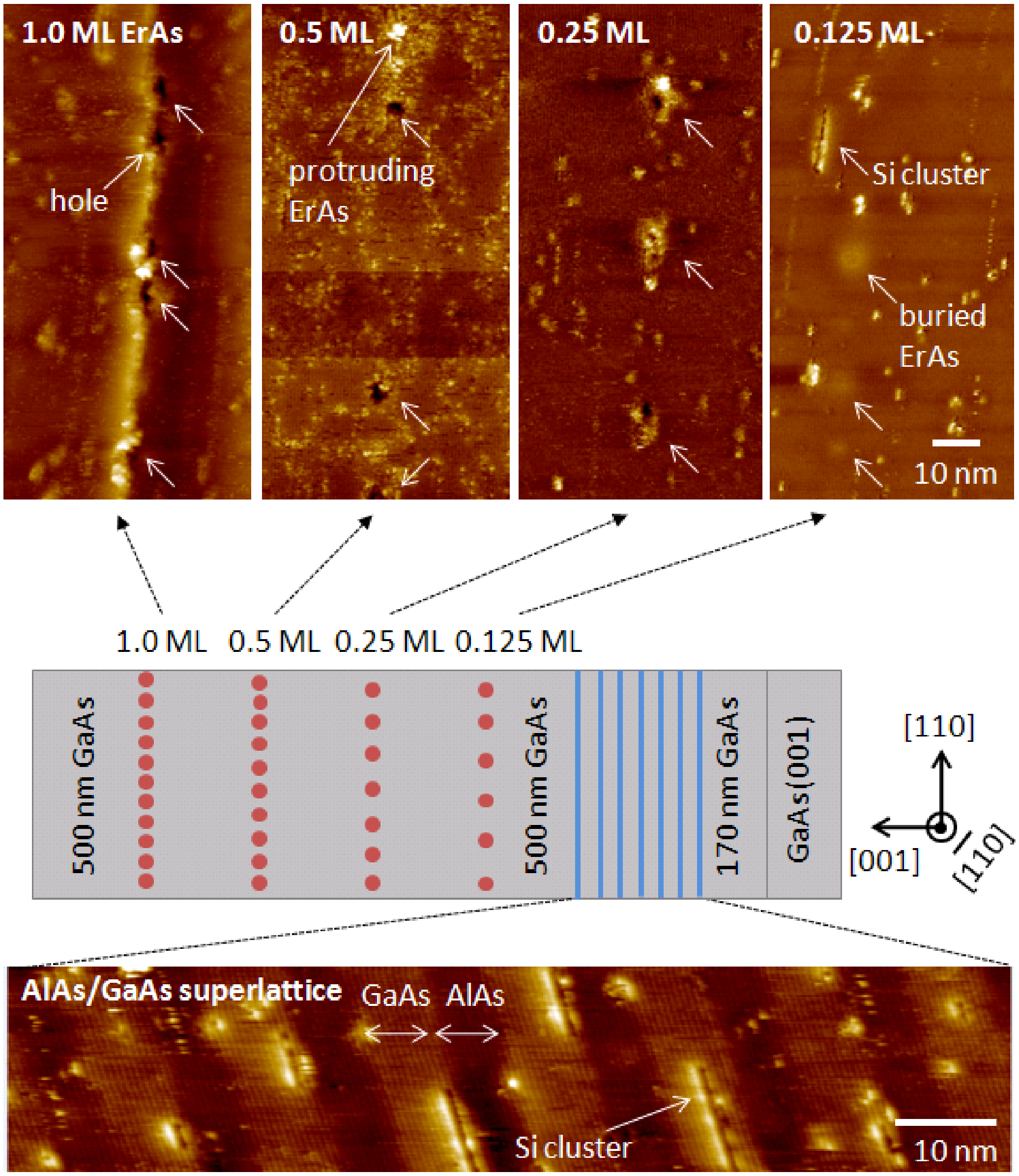

Figure 3.12. Schematic sample structure and filled states STM images of the {110} cleavage plane. The sample consists of varying coverages of ErAs separated by 125 nm of GaAs on a GaAs (001) substrate. Depending on their location relative to the cleavage plane, the ErAs can appear as protruding particles, buried particles, or holes. The unlabeled arrows denote ErAs sites. Reprinted with permission from [53]. Copyright 2011 American Institute of Physics.

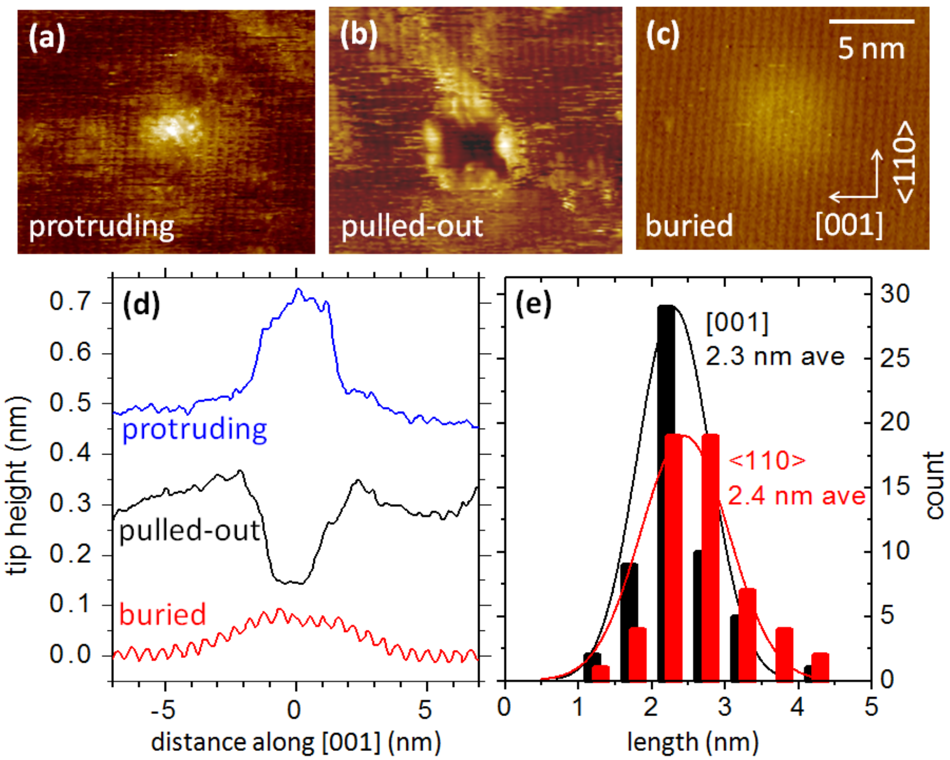

Figure 3.13. Filled states XSTM images of (a) protruding, (b) pulled-out, and (c) buried ErAs nanoparticles grown on (001) GaAs. (d) Height profiles of the three particle sites. (e) Histogram of the protruding and pulled-out particle lengths along [001] and ⟨110⟩. Reprinted with permission from [52]. Copyright 2011 American Physical Society.

in the GaAs spacers and AlAs/GaAs superlattice are Si precipitates due to heavy doping and are identical to those observed previously by cross sectional STM [88].

Figures 3.13(a-c) show higher magnification filled states XSTM images of the ErAs nanoparticles in the low coverage limit of less than 0.5 ML. The vertical lines are As atomic rows on the GaAs {110} surface. Since the {110} is not the rocksalt ErAs cleavage plane, the particles tend not to cleave [89]. Instead, the particles remain stuck in one of the cleavage surfaces and are pulled out of the other. This results in protruding particles [Figure 3.13(a)] or holes due to missing particles [Figure 3.13(b)] in the cross-sectional STM images. The corresponding height profiles are shown in Figure 3.13(d).

A histogram of particle lengths for the protruding and pulled-out particles is shown in Figure 3.13(e). The particles appear nearly spherical, with average lengths of roughly 2.4 and 2.3 nm along the [110] and [001] directions, respectively. The 2.4 nm length along [110] is consistent with Kadow et al. [90], who measure a 2 nm diameter in the (001) plane for particles grown at a similar temperature. Thus the particles are clearly within the sub-3nm regime where hard-walled potential models predict a band gap [91].

A buried ErAs nanoparticle is shown in Figure 3.13(c), with the corresponding height profile in Figure 3.13(d). Here we see a smooth profile 0.07 nm in height overlaid on the atomic corrugation. This profile is Gaussian in shape with a standard deviation of $\sigma =$ 4.1 nm and full width at half maximum of 4.8 nm. The apparent height further reduces from 0.07 nm to 0.05 nm when the sample bias is changed from -1.8 to -2.0 V. The small apparent height (less than one atomic step) and strong bias dependence suggest that this profile results from an electronic rather than a topographical feature. It is interpreted to be a buried ErAs particle whose electronic states induce electronic changes in the surrounding GaAs matrix, such as band bending or introduction of localized states into the GaAs band gap. If we consider the effective diameter of the electronic contrast to be roughly $2\sigma = 8.2$ nm, we find that this buried contrast is larger than the 2-3 nm diameter of the particles themselves.

Large area scans of the four ErAs layers of varying coverage are shown in the top panels of Figure 3.12. We find that with increasing ErAs coverage from 0.125 to 1.0 ML, the density of ErAs particles within the GaAs matrix increases. In the 1.0 ML region a step 1 ML in height is produced upon cleavage, and this step is likely due to the increased

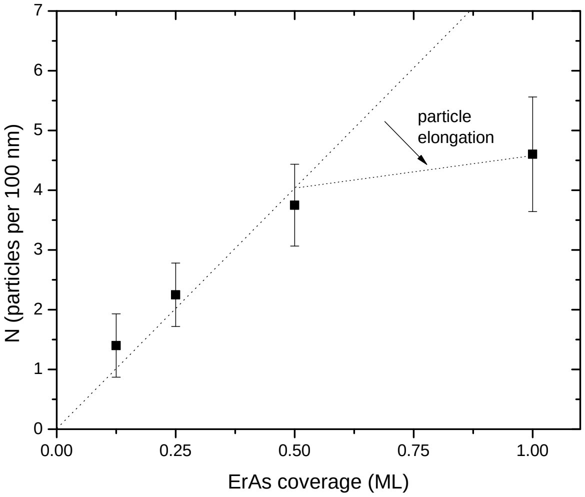

Figure 3.14. Plot of the particle density (number of particles per 100 nm) as a function of ErAs coverage. At low coverages (0.125 to 0.5 ML), the number of particles increases while the particle size remains roughly constant. The departure from linearity for coverages greater than 0.5 ML corresponds with the particles growing/elongating in the (001) plane. Reprinted with permission from [53]. Copyright 2011 American Institute of Physics.

particle density. It also appears that for low ErAs coverages in the range 0.125 to 0.5 ML the particles are nearly spherical (or cubic), with equal height and width in the [001] and [110] directions, and at a larger coverage of 1.0 ML the particles begin to elongate in the (001) plane. These results are consistent with TEM results by Driscoll et al [92] and plan view STM by Schultz et al [76], who found that ErAs particles first embed themselves 3-4 monolayers in depth before extending laterally in the (001) plane.

Figure 3.14 shows a plot of the particle density (number of particles per length along the layer) versus ErAs coverage. This plot was compiled by examining successive scan frames from each ErAs layer (100 nm frame height) and counting the number of particles in each frame. The number of particles N was then averaged over 5 successive frames (500 nm total length) for the 0.125 ML layer, and 10 successive frames (1 um total length)

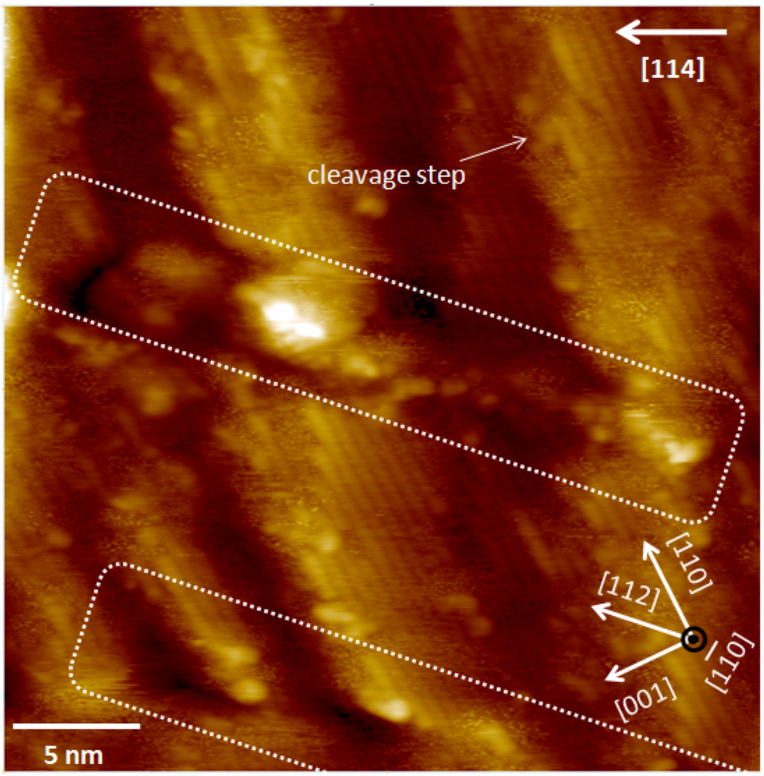

Figure 3.15. Filled states STM images of ErAs nanocomposites grown on (114)A GaAs surfaces under conditions that produce oriented embedded nanorods. The rectangular boxes in the figure show the location of the ErAs nanorods. The nanorods align along [112] and are roughly 2 nm in diameter. The diagonal lines are As atomic rows aligned along [110]. Due to difficulties in cleaving high index plane substrates, several cleavage steps are produced. Reprinted with permission from [53]. Copyright 2011 American Institute of Physics.

for the 0.25, 0.5, and 1.0 ML layers. The error bars represent the standard deviation in N per frame. In the range 0.125 to 0.5 ML the plot is linear, in agreement with the observation that in the low coverage regime, the number of particles increases while the particle size stays roughly constant. For coverages larger than 0.5 ML the plot begins to break from linearity and curve downward. By conservation, here the excess ErAs must be contributing to increase the particle size, and this is consistent with observations that at larger coverages, the particles begin to extend laterally in the (001) plane. Alternatively, the increase in apparent size could be due to coalescence of individual particles.

Cross-sectional STM studies were also performed on embedded ErAs nanorods grown on (114)A GaAs (Figure 3.15). Like the nanoparticle samples, the nanorod samples are also scanned on a cleaved {110} surface. Here due to the difficulty in cleaving high index plane substrates, several cleavage steps are produced; however both the [110] GaAs atomic rows and ErAs nanocomposites are still resolved. Due to the rough cleave it is difficult to determine whether these nanocomposites are continuous nanorods or rows of oriented nanoparticles, but previous cross sectional TEM work has suggesed that they are in fact continuous nanorods [86]. Based on a measured angle of $52 \pm 5°$ between the nanorods and the [110] atomic rows, the nanorods are found to be oriented along [112] (54.7° expected angle, in the {110} cleavage plane), in good agreement with previous TEM studies [86]. The nanorods have an average diameter on the order of 2-3 nm, also in agreement with Ref [86]. Further studies are required to develop methods for cleaving and obtaining higher resolution STM images of the ErAs nanorod/GaAs interface.

3.5 Conclusions

In summary, ErSb nucleates on GaSb(001) surfaces via an embedded growth mode, which is strongly dependent on growth temperature. At high growth temperatures, the high surface mobility of both Er and Ga adatoms leads to elongated nanoparticles with a Ga-induced $(1 \times 4)/(4 \times 1)$ surface reconstruction, and the surrounding GaSb matrix remains smooth due to the step-flow re-growth of the displaced Ga. At low temperatures, the reduced surface mobility of Er and Ga adatoms leads to smaller square ErSb nanoparticles with a (1×1) surface periodicity, and the surrounding GaSb matrix roughens due to predominantly layer-by-layer re-growth of GaSb islands.

During codeposition of ErSb with GaSb, we showed that a wide range of new nanostructures form including embedded ErSb nanowires with both vertical and horizontal orientations, bifurcated nanotrees, and nanosheets. These ErSb nanostructures form simultaneously with the GaSb matrix and have epitaxial, coherent interfaces with no evidence of stacking faults or dislocations as observed by high resolution TEM. The nanostructures form through a surface mediated growth mechanism and are not the result of a bulk phase separation mechanism. Growth is initiated with the formation of ErSb nanoparticles that phase separate from the GaSb and form a template for nanorod growth. A complex balance occurs at the surface of each nanorod as the ErSb and GaSb compete to wet the surface and minimize the overall surface energy of the nanostructures. Changes in the growth conditions can alter this balance and produce significant changes in the structure of the nanocomposite. The ease by which GaSb can wet the structures allows the nanocomposite layers to be incorporated easily into heteroepitaxial device structures allowing its conductive and photonic properties to be fully exploited, in particular devices that exploit the large shape anisotropy.

In the last section we explored the use of cross sectional STM for imaging the internal structure of ErAs nanoparticles and nanorods embedded in a GaAs matrix. Although the preferred cleavage planes for rocksalt ErAs and zincblende GaAs are not matched, {110}-type cleavage produced particles that protruded from the cleaved surface and could readily be imaged by STM. This enabled clear identification of the ErAs nanoparticles, which have been more difficult to distinguish in plan-view STM due to a roughening of the growth surface [76]. Moreover, cleaving produces nanoparticles with an exposed surface that are not covered with a wetting layer of GaAs, enabling direct characterization of the ErAs nanoparticle. This method would be especially useful for studies of the embedded ErSb nanorods in GaSb, which are covered with a thin wetting layer of GaSb on the growth surface but could be exposed by cleaving a cross section. Cleaves of ErSb:GaSb nanostructures have not yet been attempted but this could be an interesting area of further exploration.

Finally, bias dependent STM measurements over shallow buried nanoparticles showed that the spatial extent of electronic contrast was larger than the nanoparticles themselves, suggesting band bending or perhaps interface-induced electronic states extend into the GaAs matrix. Thus beyond imaging, the methods developed here enable local measurements of electronic structure by scanning tunneling spectroscopy (STS), to be discussed in the next chapter.

Chapter 4

Electronic Properties of low dimensional RE-V/III-V nanocomposites

4.1 Introduction: quantum confinement and interface effects

We now examine the effects of reduced dimensionality on electronic structure. Bulk ErAs is a semimetal with a valence band maximum at Γ, conduction band minimum at X, and $\Gamma - X$ band overlap of $\Delta = 700$ meV.[1] The hole pockets at Γ are spherical and have As 4p character while the electron pocket at X is ellipsoidal and has Er 5d character

---

[1] Some of the work presented in this chapter has previously appeared in the following publications: [51, 52].

[91, 93, 94]. The calculated bandstructure, along with cross sections of the hole and electron pockets are shown in Figure 4.1 (DFT-LDA bandstructure from Refs. [93, 94]). Other RE-V materials such as ErSb, ScAs, $Sc_{1-x}Er_xAs$, GdAs, ErP, and GdP show similar calculated bandstructures with $\Gamma - X$ overlap [95, 96, 97]. Detailed Shubnikov-de Haas measurements of $Sc_{1-x}Er_xAs$ films are consistent with the hole sphere / electron ellipsoid description of the Fermi surface [59].

Quantum confinement is expected to alter the bandstructure of the RE-Vs. Consider the example of a 2D quantum well, which in the simplest case can be modeled by a square well with infinitely high barriers. Here the subband energies are given by $E_n = \frac{\hbar^2\pi^2}{2m^*L^2}n^2$ where L is the width of the well (film thickness) and $n = 1, 2, 3$ indexes the levels. Indeed, Shubnikov-de Haas measurements of $Sc_{1-x}Er_xAs(001)$ thin films showed that the carrier density decreased with decreasing film thickness, and this was attributed to the creation subbands [59]. Angle resolved photoemission spectroscopy (ARPES) measurements of ErAs(001) films also saw evidence for confinement in that the perpendicular component of the electron effective mass changed with film thickness [71]. Under this simple infinite well model, the confinement-induced bandgap can be expressed as $E_g(L) = E_{1,e}(L) + E_{1,h}(L) - \Delta$, where $E_{1,e/h}(L)$ are the ground state energies ($n = 1$) for electrons and holes respectively [70] and Δ is the bulk band overlap. For ErAs this model predicts that a bandgap should open for films of thickness 1.73 nm (6 monolayers, ML) or less [69]. However, magnetotransport [69] and angle resolved photoemission spectroscopy measurements [71] have shown that such films remain semimetallic for thicknesses as low as 0.86 nm (3 ML). Clearly the model is an oversimplification as real barriers are not infinite or perfectly square.

For ErAs nanorods and nanoparticles the confinement effects are expected to be even stronger, resulting from the reduced dimensionality of the nearly 1D nanorods and 0D nanoparticles. ErAs nanoparticles embedded within GaAs exhibit optical absorption peaks in the near infrared region [64], and one interpretation is that the absorption results from transitions across a confinement-induced band gap [91]. Based on this interpretation, Scarpulla et al. proposed a hard-walled finite-potential model that predicted a gap opening for embedded ErAs nanoparticles with diameters of approximately 3 nm [91]. However, given the failures of infinite potential model for ErAs thin films, this hard-walled finite potential model has remained controversial. An alternative explanation is that the nanoparticles remain semimetallic, with the absorption resulting from excitation of surface plasmon resonances [64]. Similar semimetal to semiconductor transitions have been suggested for TbAs nanoparticles based on pump-probe measurements [98] and for ErSb and ErP particles based on scanning tunneling spectroscopy (STS) measurements [74, 99]. However, in the latter STS measurements the ErSb and ErP samples were exposed to air and were likely oxidized. Thus it remains on open question whether many of the RE-V nanoparticles become semiconducting due to confinement. A direct measurement of local electronic structure on clean samples is needed.

In this chapter we use angle resolved photoemission spectroscopy (ARPES) and *in-situ* plan-view and cross-sectional scanning tunneling spectroscopy (STS) to measure the electronic structure of ErAs and ErSb subject to varying degrees of reduced dimensionality. ARPES is used to study the momentum-resolved bandstructure of ErAs and ErSb

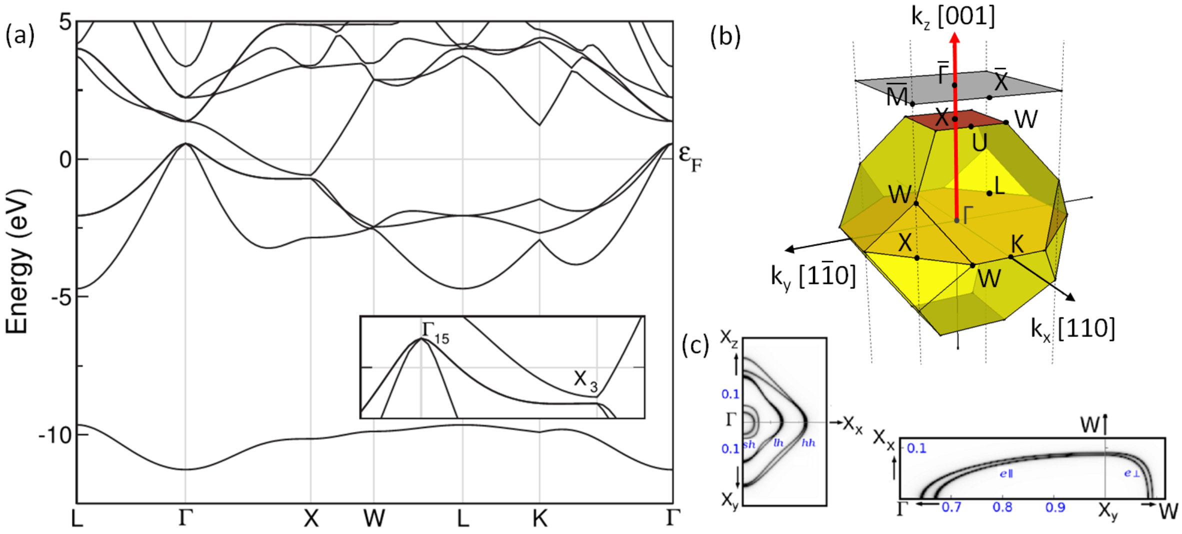

Figure 4.1. (a) DFT-LDA bandstructure of ErAs. Adapted from Refs [93, 94]. (b) Schematic of the bulk Brillouin zone (yellow) and surface Brillouin zone (grey). High symmetry points on the surface Brillouin zone are denoted with overbars. The red sections denote the $\Gamma - K - X$ and $X - W - U$ planes through the bulk Brillouin zone. (c) Cross sections of the spherical hole pockets at Γ and ellipsoidal electron pocket at X in the bulk Brillouin zone.

thin films, from which we observe both three dimensional and two dimensional states that cross through the Fermi level, keeping all films semimetallic. Then using plan-view and cross-sectional STS, we directly measure the local electronic structure of ErSb and ErAs nanowires and nanoparticles, showing that they too remain semimetallic. Using STS we measure changes in the local density of states across the ErAs nanoparticle / GaAs interface and propose that electronic states at that interface may prevent a bandgap from opening.

4.2 ARPES of ErAs and ErSb films

Here we measure the in-plane (k_x, k_y) and out-of-plane (k_z) band dispersions for ErAs(001) films as a function of film thickness. Samples were grown by MBE on n-type

GaAs(001) substrates and consist of a 500 nm GaAs buffer layer (Si doped with 10^{18} cm^{-3}) followed by the ErAs layer. The GaAs layers were grown at 580 °C and showed a sharp (2×4) reconstruction by RHEED and the ErAs layers were grown at 350 °C and had a (1×1) RHEED pattern. Growth rates were calibrated by RHEED intensity oscillations. After growth the samples were capped with approximately 200 nm amorphous arsenic (from an As_4 flux) to protect the surfaces from oxidation during subsequent transfer through air. ARPES measurements were performed at beamline I4 of the MAX-Lab synchrotron facility in Lund, Sweden. Upon reloading samples into ultrahigh vacuum the arsenic cap was removed by annealing at 350 °C until a bright (1×1) LEED pattern appeared. Removal of the cap was also confirmed by measurements of shallow core levels. ARPES measurements were performed using synchrotron light at incident photon energies from $h\nu$ =15 to 160 eV in an analysis chamber with a base pressure of less than 5×10^{-11} mbar. Unless otherwise noted all measurements were performed at room temperature.

Figure 4.2 shows normal emission ($k_x = k_y = 0$) energy dispersion curves for ErAs(001) films with thickness 10, 6, and 3 monolayers (3.35, 1.71, and 0.86 nm). In this orientation, varying the incident photon energy corresponds to traversing k_z along the $\Gamma - X$ direction in the bulk Brillouin zone [Figure 4.1(b)]. In the 10 ML film we observe clearly dispersing bulk bands that disperse with k_z. A binding energy minimum is reached near a photon energy of $h\nu = 105$ eV, which we attribute to the bulk X point, and binding energy maxima occur near $h\nu = 65$ eV and 150 eV, which we attribute to bulk Γ points. At these Γ points the bands cross through the Fermi level (binding energy of 0), hence

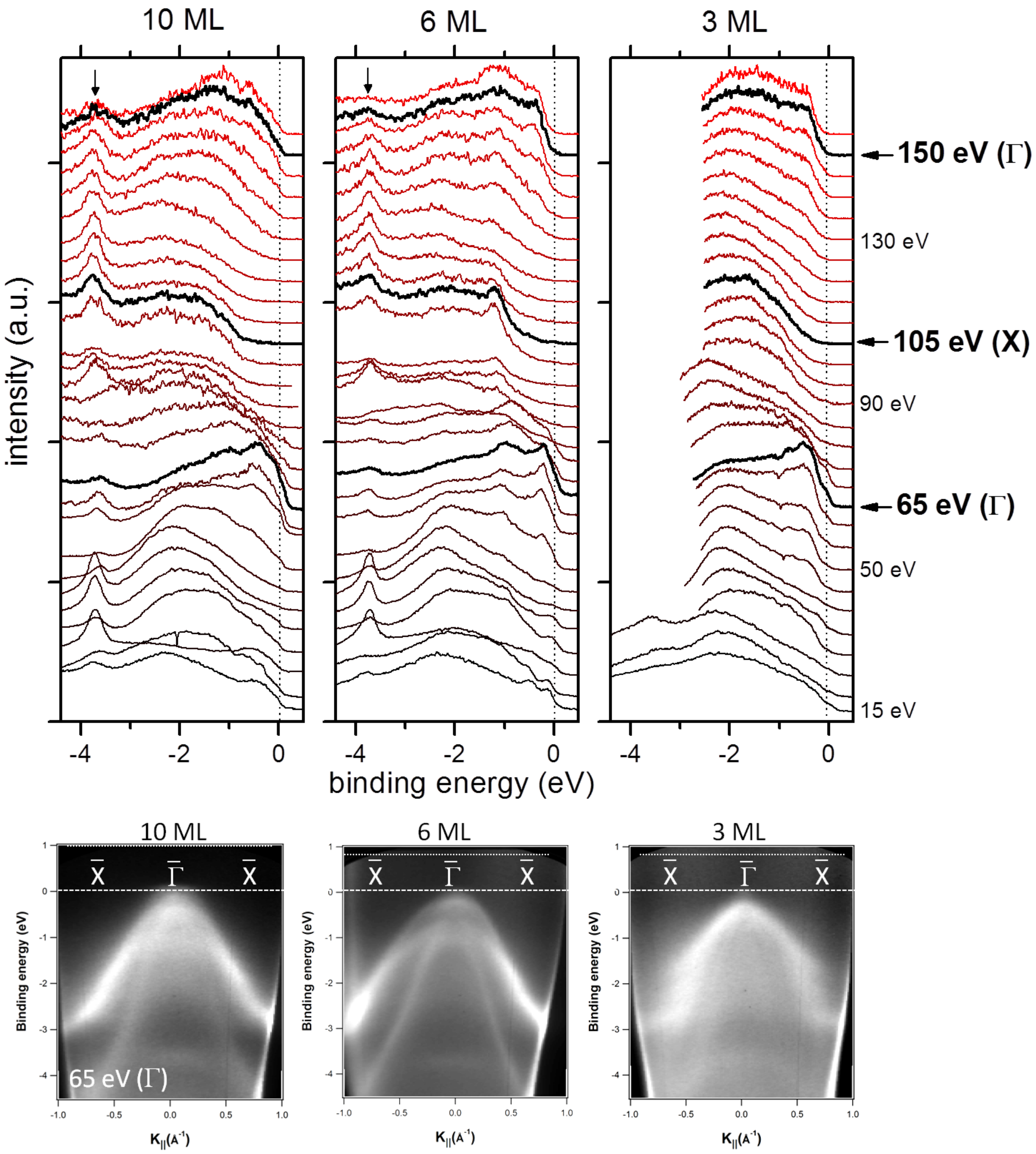

Figure 4.2. Top: energy dispersion curves at normal emission photon energies from 15 to 155 eV in steps of $\Delta h\nu = 5$ eV, corresponding to the bulk $\Gamma - X$ dispersion. The Γ high symmetry points are reached near photon energies of $h\nu = 65$ and 150 eV, while the X high symmetry point is reached near $h\nu = 105$ eV. Bottom: in-plane dispersions for the 10, 6, and 3 ML samples measured using a photon energy of $h\nu = 65$ eV, which corresponds approximately to the bulk Γ at normal emission.

the 10 ML film shows (semi-) metallic behavior. At high photon energies ($h\nu > 50$ eV) the bulk dispersions are well fit with a free electron-like model of final states [47], i.e.

$$k_z = \sqrt{\frac{2m}{\hbar^2}} \left(E_{kin} cos^2\theta + U_0\right)^{1/2} \tag{4.1}$$

where $E_{kin} = h\nu - |E_B| - \phi$, the emission angle $\theta = 0$ for normal emission, and we use an inner potential of $U_0 = 19$ eV. However, at lower photon energies the model identifies a photon energy of 27 eV as the X point whereas the measured bulk X appears to lie closer to $h\nu = 40$ eV and the low energy Γ appears near a photon energy of 25 eV. The failure of free-electron-like final states at low photon energy is likely due to the fact that at low photon energies E_{kin} is of similar magnitude as U_0 [40].

The bulk dispersion is in general agreement with the calculated dispersion of valence bands along bulk $\Gamma - X$; however, note that due to significant k_z broadening it is difficult to determine the exact binding energy positions of the bulk bands, much less resolve the two bands that are expected to disperse to approximately 0.75 and 3 eV below the Fermi level at X (Figure 4.1). The measured dispersion is also in good agreement with Komesu et al [79], who measured ErAs(001) in normal emission over a smaller range of photon energies ($h\nu = 50 - 85$ eV). Considering the calculated bandstructure, for a bulk-like sample we would also expect to see conduction band states that cross the Fermi level at bulk X. However, we do not observe this Fermi level crossing at X ($h\nu \approx 105$ eV). The absence of this crossing may result from confinement along k_z for the 10 ML film, which would be expected to push the the conduction band minimum upwards. We also observe a state at a binding energy of 3.7 eV that does not disperse in k_z (marked with an arrow). This does not correspond to any of the expected bulk states and may be a surface state.

The lower left plot in Figure 4.2 shows the in-plane $\overline{\Gamma} - \overline{X}$ dispersion for the 10 ML film measured at a photon energy of 65 eV. At normal emission ($k_{\parallel} = 0$, or $\overline{\Gamma}$) this corresponds to the bulk Γ point, and from a projection onto the $\Gamma - K - W - X$ plane, the surface $\overline{\Gamma} - \overline{X}$ direction corresponds approximately to the bulk $\Gamma - K$ direction [Figure 4.1(b)]. At normal emission the Fermi level crossing is clearly observed, and the bands disperse downward to a binding energy of 2.5 eV at $\overline{X}$. The measured dispersion is in good agreement with the calculated $\Gamma - K$ from Figure 4.1. An inner band with steeper dispersion is also observed, which may reflect the small-hole band that disperses to nearly 4 eV below the Fermi level between Γ and K.

Surprisingly, measurements of the 6 and 3 ML films also yield bulk dispersing $\Gamma - X$ bands that cross through the Fermi level at bulk Γ ($h\nu = 65$ eV, lower middle and lower right of Figure 4.2, photon energy dispersions in upper middle and upper right). Previously, Ilver et al found that two dimensional states cross the Fermi level at $\overline{M}$ for all film thicknesses [71], but here we find that there are also three dimensional states at Γ that cross the Fermi level and cause the thinnest films to remain semimetallic. The 3 ML sample has the shallowest bulk $\Gamma - X$ dispersion and the smallest Γ overlap at the Fermi level, nonetheless it too has a Fermi level crossing. These results suggest that despite the predictions of the simplest quantum confinement models, the ErAs films remain (semi-) metallic. Note that at large photon energies, the spectral intensity near the Fermi level at Γ ($h\nu = 150$ eV) for the 6 and 3 ML samples is not as large as for the 10 ML sample. This likely results from a contribution from the GaAs buffer layer in the thinner samples since at these high photon energies the photoelectron inelastic mean free path (approximately 1 nm) is of similar magnitude as the thickness of the ErAs films (1.71 and 0.86 nm for the 6 and 3 ML films).

Figure 4.3(a-c) shows the in-plane dispersions along the $\overline{\Gamma} - \overline{M}$ direction for the 10, 6, and 3 ML samples (measured at $h\nu = 30$, 30, and 35 eV respectively). For all samples, in addition to the Fermi level crossing at $\overline{\Gamma}$, a state centered at $\overline{M}$ crosses the Fermi level and disperses to a minimum of approximately 0.21 eV below the Fermi level. This state has also been observed by Ilver et al, who observed a weak dependence of the depth of dispersion on film thickness and attributed it to a quantum well state from confinement along k_z [71]. However, from our data the dependence on film thickness is unclear. The $\overline{M}$ surface point corresponds to excitations along the $W - X - W$ line of the bulk Brillouin zone, and hence these states may be derived from the electron pocket at X (Figure 4.1).

For a clearer understanding of the $\overline{M}$ state we study its dependence on photon energy. Figure 4.3(d) shows energy dispersion curves at varying photon energy for the 6 ML sample. Here the emission angle was adjusted to hold the in-plane momentum constant at $\overline{M}$. The $\overline{M}$ state at a binding energy of 0.21 eV does not vary with photon energy, and the corresponding in-plane dispersions at several photon energies are shown in Figures 4.3(e-g), showing that the in-plane dispersions do not vary with photon energy. These observations indicate that the state is two-dimensional, in agreement with the observations by Ilver [71].

We further examine the Fermi level crossings at $\overline{M}$ and $\overline{\Gamma}$ by measuring their in-

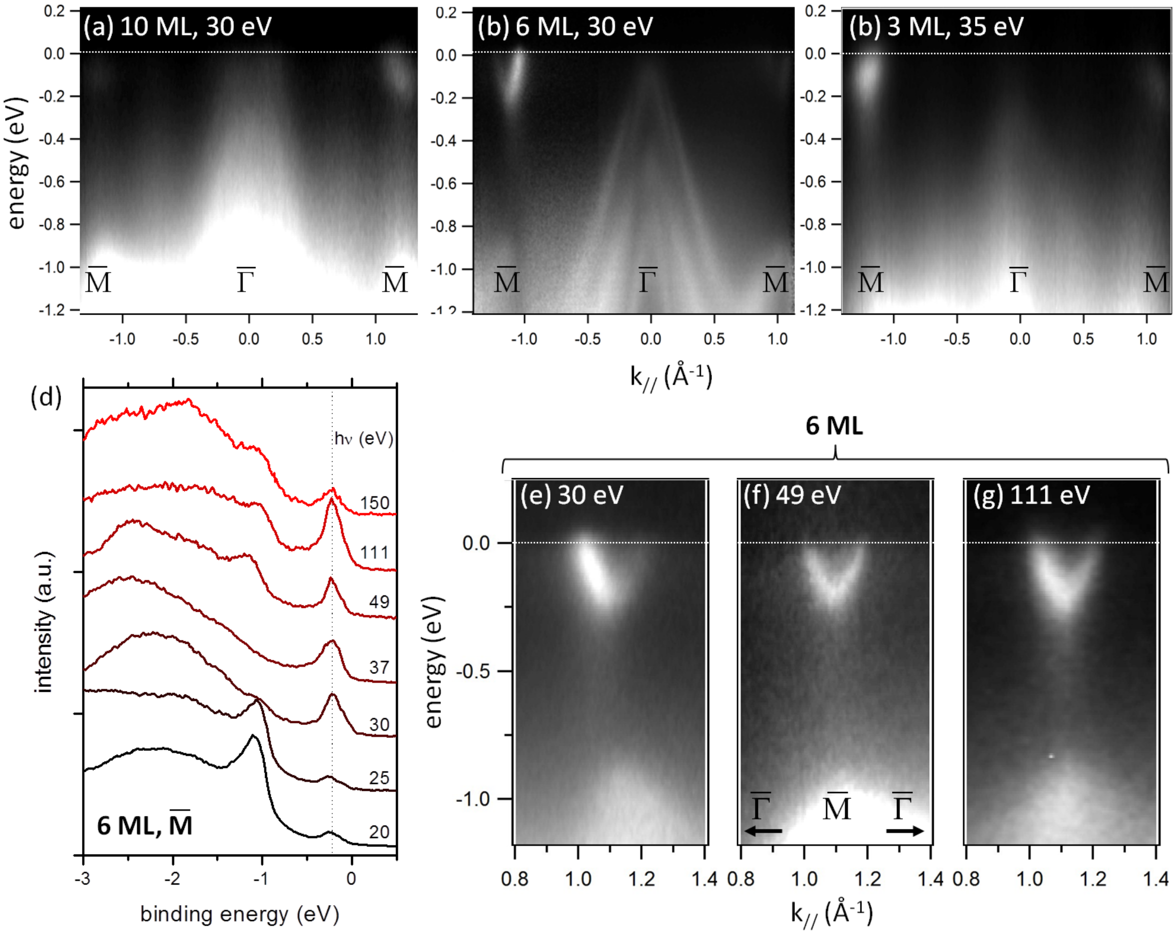

Figure 4.3. (a-c) In-plane dispersions along the $\overline{M} - \overline{\Gamma} - \overline{M}$ direction for films of thickness 10, 6, and 3 monolayers. (d-g) Bandstructure around the $\overline{M}$ symmetry point for the 6 ML ErAs(001) film. (d) Energy dispersion curves as a function of incident energy. The polar emission angle was adjusted such that the in-plane momentum was held constant ($k_{\|} = \overline{M}$). (e), (f), and (g) show the in-plane dispersions of the $\overline{M}$ state along the $\overline{\Gamma} - \overline{M} - \overline{\Gamma}$ direction at photon energies of 30, 49, and 111 eV.

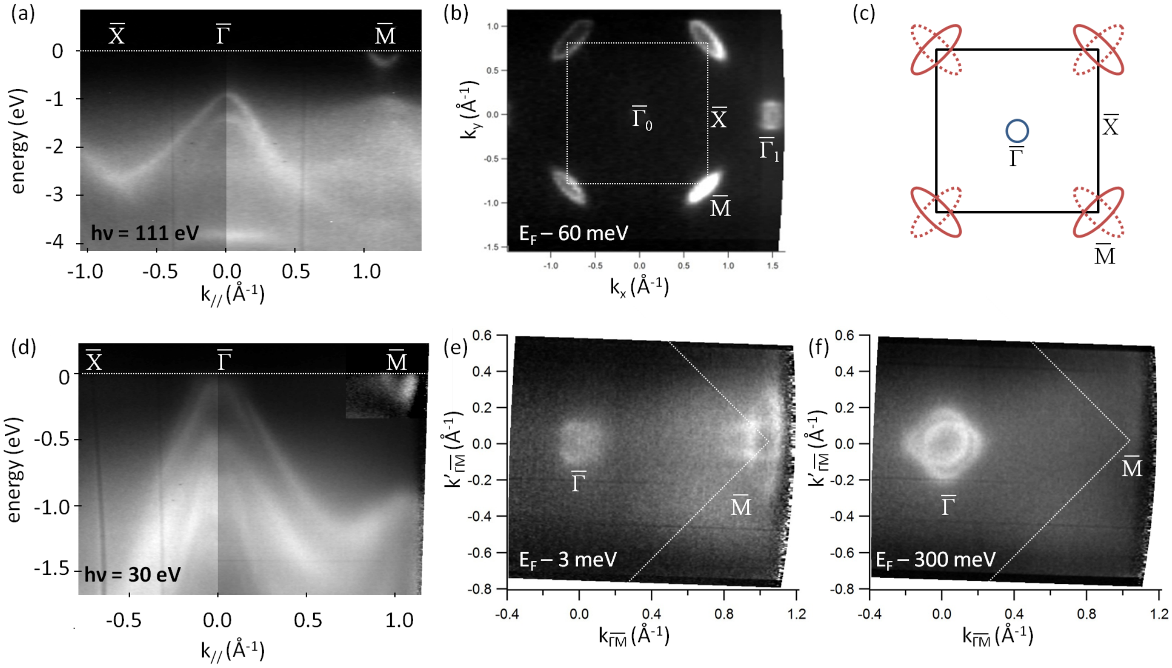

Figure 4.4. In-plane dispersions energy dispersions $E(k_{//})$ and constant energy surfaces (k_x, k_y) for the 6 ML sample. (a) In-plane dispersions measured using a photon energy of 111 eV. (b) Constant energy map of (k_x, k_y) just below the Fermi level, measured using a photon energy of 111 eV. (c) Schematic of a constant energy surface at the Fermi level, showing the 2D elliptical electron pockets at $\overline{M}$ and the 3D spherical hole pockets at $\overline{\Gamma}$. At a photon energy of 111 eV the second set of electron pockets at $\overline{M}$ is not observed (dotted), and is attributed to a matrix effect. (d) In-plane dispersions measured using a photon energy of 30 eV. (e) Constant energy map of (k_x, k_y) just below the Fermi level, measured using a photon energy of 30 eV. (f) Constant energy map of $k_x, k_y)$ at 300 meV below the Fermi level, measured using a photon energy of 30 eV.

plane symmetry along k_x and k_y for a fixed photon energy. Figure 4.4 shows dispersions along the high symmetry $\overline{\Gamma} - \overline{X}$ and $\overline{\Gamma} - \overline{M}$ in-plane directions and the corresponding constant energy surfaces for the 6 ML sample. The top panels (a-b) are measured at $h\nu = 111$ eV, which corresponds approximately to a plane that cuts through the bulk X point ($X - U - W$ plane in Figure 4.1). The bottom panels (d-f) were measured at $h\nu = 30$ eV, which corresponds approximately to a plane cutting through the bulk Γ point ($\Gamma - K - W - X$ plane in Figure 4.1).

We begin with a discussion of the state at $\overline{M}$. In the constant energy map just below the Fermi level using $h\nu = 111$ eV photons [Figure 4.4(b)], these states appear as ellipses that are oriented away from $\overline{\Gamma_0}$ of the central Brillouin zone and pointed towards the zone center of the adjacent Brillouin zone $\overline{\Gamma_1}$. These states are similar in shape to the ellipsoidal electron pockets expected at the bulk X point (Figure 4.1). However, given the (1×1) periodicity of the surface, one would expect that an additional set of ellipses oriented towards the central $\overline{\Gamma_0}$ should also be observed [Figure 4.4(c)] (otherwise the surface periodicity would be $c(2 \times 2)$ in reciprocal space). Indeed, when measured using $h\nu = 30$ eV photons [Figure 4.4(e)] this second set of "missing" ellipses is observed. The absence of the second set of electron ellipses at $h\nu = 111$ eV is likely a matrix effect. In general, we observe both sets of ellipses at photon energies corresponding to near the bulk Γ point ($h\nu = 30$, 78, 150 eV) and only one set of ellipses for energies near the bulk X point ($h\nu = 111$ eV).

These states are similar in shape to the ellipsoidal electron pockets expected at the bulk X point (Figure 4.1), and by fitting their energy dispersions to parabolas we ex-

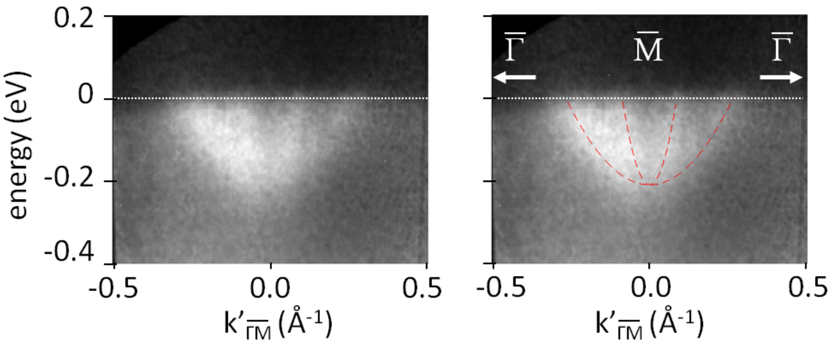

Figure 4.5. Extraction of the effective masses. The direction $k'_{\overline{\Gamma M}}$ corresponds to a vertical slice through the $\overline{M}$ pocket in Figure 4.4(e).

tract in-plane longitudinal and transverse effective masses of $m^*_{long}/m_0 = 1.28 \pm 0.3$ and $m^*_{trans}/m_0 = 0.14 \pm 0.03$ (Figure 4.5). These values are in good agreement with the X point electron effective masses of $m^*_{long}/m_0 = 1.289$ and $m^*_{trans}/m_0 = 0.176$ calculated by G_0W_0 [72], and also in good agreement with the 1.42 and 0.17 logitudinal and transverse effective masses for $\mathrm{Sc}_{1-x}\mathrm{Er}_x\mathrm{As}(001)$ films extracted from Shubnikov-de Haas measurements [59]. Note that in the bulk, only one spheroidal electron pocket exists at X and it points towards the bulk Γ, while in this surface measurement we observe two electron pockets at each $\overline{M}$, one pointed toward and one pointed away from $\overline{\Gamma}$. This likely results from the stacking of bulk Brillouin zones and the projection of these bulk X ellipsoids onto the surface: in such a (001) stacking of bulk Brillouin zones the ellipsoids alternate direction with each layer. Hence in our ARPES measurements we observe two sets of ellipses, one towards and one away from the zone center, and these states are two-dimensional due to the confinement in the k_z direction. Our electron effective masses are also in good agreement with the $m^*_{trans}/m_0 = 0.2$ and $m^*_{long}/m_0 = 1.1$ extracted from ARPES measurements by Ilver et al [71].

We next discuss the bulk bands at $\overline{\Gamma}$. In Figure 4.4(a), the photon energy of 111 eV corresponds to a k_z value in the $X-U-W$ plane of the bulk Brillouin zone. Here the $\overline{\Gamma}-\overline{M}$ direction maps onto the bulk $X-W$, and the measured sharp dispersion from a binding energy of about 1 eV at $\overline{\Gamma}$ to 3 eV part way towards $\overline{M}$ is in good agreement with the sharp dispersion calculated along bulk $X-W$ (Figure 4.1).

Figure 4.4(d) plots the high symmetry in-plane dispersions measured using 30 eV photons. When measured at a photon energy of 30 eV, this corresponds approximately to a k_z value near the bulk Γ, and hence the $k_{//}$ values lie approximately in the $\Gamma-K-W-X$ plane. However, note that from the normal emission scans at varying photon energy in Figure 4.2 it is difficult to determine the exact position of the low photon energy Γ point. Along the $\overline{\Gamma}-\overline{M}$ direction, which projects onto the bulk $\Gamma-X$, we observe a band that disperses downwards to about 1.2 eV binding energy before turning up and reaching a local maximum at $\overline{M}$. In contrast, in the calculated bulk bandstructure along $\Gamma-X$ there are two bands, one that disperses to a shallow minimum of roughly 0.7 eV at X, and the other that disperses to a deeper local minimum of approximately 3 eV before turning up to a local maximum at X. The qualitative shape of the measured band is closer to the latter; however the depth of dispersion is much smaller than 3 eV. This discrepancy may be caused by confinement along k_z, which would push bands up. Alternatively, the discrepancy could arise from the fact that the k_z value corresponding to $h\nu = 30$ eV is slightly off from bulk Γ.

We also observe a number of additional states at $\overline{\Gamma}$ that are not expected from the bulk bandstructure calculation. These states likely result from a folding in of the bands

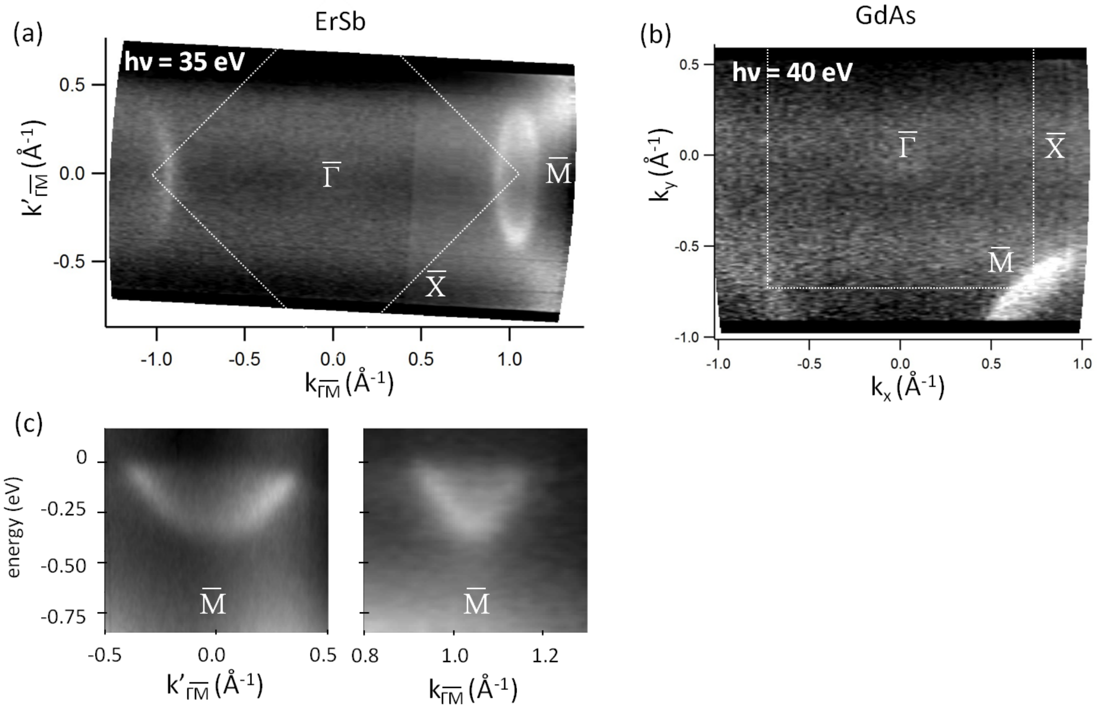

Figure 4.6. ARPES measurements for ErSb(001) and GdAs(001). (a and b) Constant energy surfaces through the Fermi level for ErSb and GdAs respectively. (c) In-plane dispersions for the elliptical $\overline{M}$ state for ErSb.

along $\Gamma - X$ due to the finite thickness of the 6 ML film.

Figure 4.4(e) and (f) show constant energy contours just below the Fermi level and at 300 meV below the Fermi level respectively. The bands at $\overline{\Gamma}$ just cross the Fermi level, and in the slice 300 meV below the Fermi level we resolve the shape of the hole pockets near the bulk Γ point. Here the hole pocket has 4-fold rotational symmetry and is in good agreement with the calculated hole pockets from Figure 4.1.

Preliminary ARPES measurements for 10 ML ErSb films grown on GaSb(001) and GdAs films grown on GaAs(001) show similar behavior as the ErAs films. ErSb films exhibit two dimensional elliptical electron pockets at $\overline{M}$ that do not disperse with photon energy [Figure 4.6(a,c)], and we extract effective masses of $m^*_{long}/m_0 = 1.50 \pm 0.3$ and

$m^*_{trans}/m_0 = 0.15 \pm 0.03$, comparable to that of the ErAs films. Measurements at normal emission for varying photon energy also show bands with bulk $\Gamma - X$ dispersion that cross the Fermi level at Γ. Similarly, for GdAs films we also observe the elliptical states centered at $\overline{M}$ [Figure 4.6(b)] and states with bulk $\Gamma - X$ dispersion that cross the Fermi level at Γ. Hence at 10 ML, ErSb and GdAs also remain semimetallic.

In summary, despite the predictions of confinement models, ErAs films down to a thickness of 3 ML remained semimetallic. In each of the samples two types of states were observed: bulk dispersing bands at $\overline{\Gamma}$ and two-dimensional states at $\overline{M}$. The former result from bulk dispersions along the bulk $\Gamma - X$ direction, and the latter result from a projection of the states at X. The RE-Vs ErSb and GdAs show a similar bandstructure as ErAs, and they too are semimetallic for thickness 10 ML.

4.3 Scanning tunneling spectroscopy of ErSb and ErAs nanoparticles and nanorods

In the previous section we showed that no bandgap and the thinnest ErAs and ErSb films remain semimetallic. But perhaps confinement to 1D or 0D may be sufficient to open a gap. Here we use scanning tunneling spectroscopy to measure the local electronic structure of ErAs nanowires grown on GaAs(114)A, ErAs nanoparticles grown on ErAs(001), and ErSb nanoparticles of various sizes grown on GaSb(001).

We first examine the cleaved ErAs nanowires on GaAs(114)A and ErAs nanoparticles on GaAs(001) from Figures 3.13 and 3.15. Scanning tunneling Spectroscopy (STS) measurements were performed in an Omicron VT-STM by interrupting the feedback and simultaneously measuring the tunneling current (I) and the differential conductance (dI/dV) as a function of voltage (V) at specified points on the {110} surface. The conductance was measured using a lock-in amplifier with a 30 mV, 1.3 kHz modulation on the tip-sample bias. In order to amplify the conductance signal and gain a greater dynamic range, spectroscopy measurements were performed in variable gap mode [100]. To remove the tip-sample distance dependence, dI/dV was normalized by the absolute conductance I/V, which we have broadened by convolution with an exponential function in order to avoid divergence at the band gap [100]. After normalization, the quantity $(dI/dV)/((\overline{I/V}))$ is proportional to the local density of states (LDOS), where the sample voltage corresponds to energy, in eV, referenced to the Fermi level [100].

Figure 4.7(a) shows normalized dI/dV spectra for the GaAs matrix (black) and protruding ErAs nanoparticles (red). Both spectra were measured on the ErAs/GaAs(001) nanoparticle sample from Figure 3.13, for which the nanoparticles had averaged diameters of 2.3-2.4 nm, below the 3 nm diameter where the hard walled potential model predicted a band gap [91]. A dI/dV spectrum for a cleaved ErAs nanorod grown by codepostion on (114)A GaAs is also shown (blue, see Figure 3.15 for image). The ErAs nanoparticle and GaAs matrix curves are averaged over at least 20 individual spectra, and the ErAs nanrod averaged over 10 spectra. In the GaAs spectra a clear band gap extending from -1 to 0.8 V is observed. Because of tip-induced band bending the measured band gap of 1.8 eV is larger than the true band gap of 1.4 eV, consistent with previous STS studies [101]. Additionally, despite the heavy n-type doping (5×10^{18} cm^{-3} Si) the GaAs Fermi

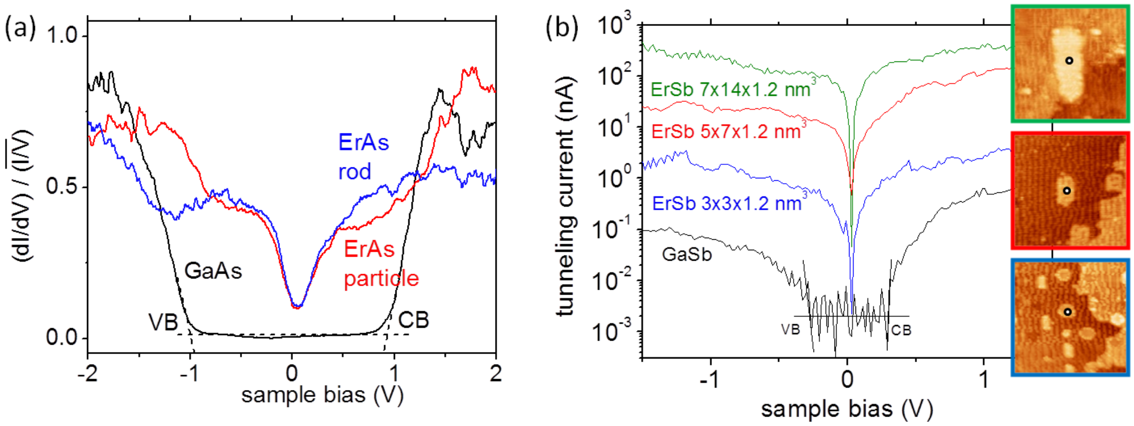

Figure 4.7. (a) Averaged differential conductance for protruding ErAs nanoparticles (red), nanorods (blue), and the GaAs matrix (black). The GaAs matrix spectrum was taken from the nanoparticle sample. (b) Tunneling I(V) point spectra for the GaSb matrix and for ErSb nanoparticles with in-plane dimensions of 3.3 nm × 3.3 nm, 5.3 nm × 7.0 nm, and 8.0 nm × 17 nm and a constant thickness of 4 atomic layers (1.2 nm) These dimensions correspond to growth temperatures of 450, 500, and 540 °C respectively. Reprinted with permission from [52]. Copyright 2011 American Physical Society.

level is pinned near midgap, which is often observed for metal-GaAs interfaces [67, 102] and for cleaved surfaces due to atomic steps [103].

The ErAs nanorod and nanoparticle dI/dV shows no evidence of a band gap. Instead, the dI/dV (LDOS) for both samples exhibit a sharp but finite minimum at the Fermi level, indicating that both the nanorods and nanoparticles are semimetallic. This curve is qualitatively similar to density functional theory (DFT) calculations for the bulk ErAs density of states [93]. Additionally, spectra measured directly over buried particles [Figure 3.13(c)] are nearly identical to spectra measured over protruding particles [Figure 3.13(a)]. Thus the observed semimetallic behavior is not induced by cleavage defects or the vacuum interface, but is instead a feature of the particles themselves. These measurements suggest that the previously observed near-IR optical absorption [64] is probably not due to optically driven electron-hole excitations, but instead results from the excitation of surface plasmons. This lies in direct contrast with the simple hard-walled finite potential model, which predicts that 2.3 nm spherical particles should have a band gap on the order of 0.5 eV [91].

ErSb nanoparticles nucleated on GaSb(001) show similar behavior, even as a function of decreased nanoparticle size. Figure 4.7(b) shows tunneling current point spectra I(V) for ErSb nanoparticles grown at 540, 500, and 450 °C and for the surrounding GaSb matrix. These temperatures correspond to ErSb nanoparticles with average in-plane dimensions of 8.0 nm × 17 nm, 5.3 nm × 7.0 nm, and 3.3 nm × 3.3 nm, with a constant out-of-plane depth of 4 atomic layers (1.2 nm). Each spectrum was averaged over 15-20 individual nanoparticles or locations within the GaSb matrix. The STS spectra from the surrounding GaSb (bottom curve), contains a region extending from approximately -0.3 V to +0.3 V with zero tunneling current consistent with the expected band gap of GaSb. The Fermi level (V=0) is found to be mid-gap, in contrast with the p-type character expected for Si-doped GaSb [104]. The mid-gap position is likely a result of surface Fermi level pinning.

For the largest ErSb particles grown at 540 °C there is a clear overlap between valence and conduction bands with no discernible band gap, which is consistent with semimetallic ErSb in the bulk limit. For the smaller particles, both those grown at 500 °C and those at 450 °C, simple quantum confinement models predict a gap should start to open [91]. Despite these predictions, STS measurements show there are still overlapping valence and conduction bands and no sign of a band gap opening. The ErSb nanoparticles remain semimetallic down to the smallest particles (3.3 nm × 3.3 nm) that could be nucleated on GaSb.

One caveat to the analysis is that in addition to the lateral dimensions of the ErSb nanoparticles, the surface termination may be expected to affect the nanoparticle LDOS. As noted in the previous chapter, for growth at 500°C and higher the $(1 \times 4)/(4 \times 1)$ surface termination of the ErSb nanoparticles has been attributed to a sub-monolayer coverage of Ga that rides on top of the ErSb nanoparticles [Figure 3.3(c) inset], whereas a (1×1) surface periodicity is observed for Ga-free ErSb surfaces [Figure 3.3(b) inset]. The bonding of the residual Ga (or GaSb) on the ErSb surface is not known, and from the STS spectra the effect of residual Ga on the nanoparticle LDOS remains unclear. However, the fact that the even the smallest ErSb nanoparticles grown at low temperature, which show a (1×1) surface periodicity and are Ga-free, have semimetallic LDOS suggests that the ErSb nanoparticles themselves remain semimetallic. Hence the semimetallic behavior is likely not Ga-induced.

4.3.1 Effect of ErAs/GaAs interfaces

The local electronic features across the interface between the RE-V nanoparticles and III-V matrix may influence the nanoparticle electronic structure. Recall that the buried ErAs nanoparticle from Figure 3.13(c,d) showed a region of electronic contrast whose spatial extent was larger than the nanoparticle itself. Thus electronic states from the ErAs or interface states may extend into the GaAs matrix.

Figure 4.8(a) shows a series of individual normalized dI/dV spectra starting at a point directly on top of a nanoparticle and moving in steps of 1.3 nm along the [110]

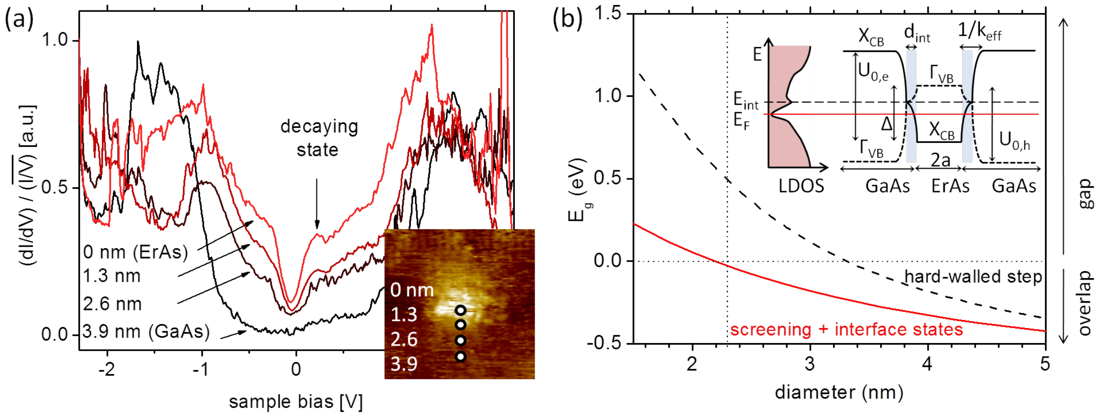

Figure 4.8. (a) Individual differential conductance spectra at varying points directly on top of a particle (0 nm) and moving in steps of 1.3 nm into the GaAs matrix (3.9 nm). (b) Calculated energy gap vs ErAs particle diameter. Inset shows schematic of the modified confinement model. Reprinted with permission from [52]. Copyright 2011 American Physical Society.

direction into the GaAs matrix. Directly on top of the ErAs particle (0 nm) and near the particle edge (1.3 nm) the spectra retain the finite minimum at the Fermi level, consistent with semimetallic behavior. In both curves there is clear evidence of an extra state, not derived from bulk GaAs or ErAs, at 0.2 eV, indicated by an arrow. Moving across the ErAs/GaAs interface to a distance of 2.6 nm, which is roughly 1.4 nm into the GaAs matrix, the state at 0.2 eV begins to decay and the minimum at the Fermi level broadens; however there are still states within the GaAs band gap close to the particle. These states continue to decay and the bulk GaAs DOS is recovered near a distance of 3.9 nm from the particle center. This 3.9 nm decay radius is in good agreement with the $\sigma = 4.1$ nm radius of electronic contrast for the buried particle observed by XSTM [Figure 4.8(c)].

These states within the band gap, and, in particular, the state at 0.2 eV that decays with distance into the GaAs matrix, may result from interface states. Note that the state at 0.2 eV does not appear in DFT calculations for bulk ErAs [93] or in photoemission spectra of continuous ErAs films [79]. But for ErAs/GaAs interfaces, DFT calculations predict the existence of interface states for both (001) [67, 105] and (110) planar interfaces [105] at positions within the GaAs band gap. These states arise from differences in bonding and coordination across the ErAs (rocksalt) / GaAs (zincblende) interface, and they peak at the interface and decay into the GaAs matrix, just as observed in our XSTS measurements. Here the decay occurs primarily into the GaAs side because in the case of a semimetal/semiconductor interface, the interface states correspond to extended states from the semimetal ErAs side [105].

These interface states may be responsible for preventing the opening of a band gap. For ErAs thin film superlattices on (001) GaAs, DFT calculations by Said et al. show that ErAs/GaAs interface states persist even with reduced ErAs film thickness, and their positions at and near the Fermi level prevent a gap from opening [106]. Additionally, tight binding calculations for GdAs/GaAs superlattices by Xia et al. [96] identify a heavy hole interface band along the $\Gamma - X$ dispersion that curves up and turns into a conduction band. This partially filled interface band prevents GdAs/GaAs superlattices from turning into a semiconductor, and Xia et al. argue that the same may be true for ErAs/GaAs planar superlattices.

Similar mechanisms may prevent ErAs nanoparticles from opening a band gap; however for the case of embedded nanoparticles, the interfaces are more complicated than the simple (001) and (110) planar interfaces.

A potential effect of the observed interface states is to effectively reduce the size of the confining potential over some length scale into the GaAs matrix. Following Scarpulla et al. [91], we begin modeling the confinement using a spherically symmetric step potential whose height is given by the energy differences in the band extrema for GaAs and ErAs [Figure 4.8(b) inset]. The potential height for holes is $U_{0,h} = \Gamma_{VB,ErAs} - \Gamma_{VB,GaAs} = 1.03$ eV and for electrons is $U_{0,e} = X_{CB,GaAs} - X_{CB,ErAs} = 1.47$ eV. Note we used the room temperature band gap for GaAs, whereas Scarpulla et al. used the 0 K band gap. Our effective masses were $m_h^*/m_0 = 0.5$ (0.235) and $m_{e,X}^*/m_0 = 0.32$ (0.25) for GaAs (ErAs) [91].

We next apply two modifications to the finite-step potential model to include (1) the effects of interface states and (2) many-body effects [Figure 4.8(b) insert]. In the first modification we model an interface state as an intermediate step in the confinement potential with energy E_{int} and spatial extent d_{int}. From XSTS measurements this state is located at approximately $E_{int} = 0.2$ eV above the Fermi level, and from DFT [105] and XSTS we find that the state is highly localized at the interface with width on the order of $d_{int} = a_{GaAs}$ (lattice constant of GaAs, 5.65 Å). The resulting interface step potential has the form $U_{step}(r) = 0$ for $r < a$, $U_{step}(r) = U_{0,int}$ for $a < r < a + d_{int}$, and $U_{step}(r) = U_{0,e/h}$ for $r > a + d_{int}$, where a is the radius of the spherical ErAs nanoparticle.

To model many-body effects at the interface we note that the semimetallic nature of bulk ErAs, and the potential presence of surface plasmons at the ErAs/GaAs interface, motivate a Thomas-Fermi-like screening of the confining potential of the form $U_{screen}(r) = 1$ for $r < a$ and $U_{screen}(r) = -exp[-k_{eff}(r - a)] + 1$ for $r > a$, where k_{eff} is the effective screening wave number. For an electron density of 5×10^{18} cm^{-3} the Thomas-

Fermi wave number is 3.57 nm^{-1}, and we use this to guide the order of magnitude of the screening wave vector: $k_{eff} = 1$ nm^{-1}. The total confinement potential is given by $U_{total,e/h}(r) = U_{step,e/h}(r) U_{screen}(r)$, where we have adjusted $U_{0,int}$ such that after multiplying by the screening, $U_{total,e/h}(a + d_{int}) = E_{int}$ [Figure 4.8(b) insert].

We next solve the Schrodinger equation in spherical coordinates to find the band shifts of occupied electron and hole states subject to this confining potential. The confinement-induced ErAs band gap is given by $E_g(a) = E_e(a) + E_h(a) - \Delta$. The results for the modified model with interface states and screening are shown in Figure 4.8(b).

We find that compared to the simple hard-walled step-potential model, the presence of features associated to interface states and metallic screening provides a strong modification to the predicted confinement-induced gap opening. With these effects, at 2.3 nm diameter the particles are predicted to remain semimetallic, consistent with our XSTS measurements. Furthermore, when solved for a 2D thin film, the interface and screening model predicts that ErAs films should remain semimetallic down to a critical thickness of 0.15 nm. This 0.15 nm thickness is much less than the 1 ML (0.287 nm) physical limit, indicating that ErAs thin films will in fact never become semiconducting, consistent with previous experimental [69, 71] and DFT [96, 106] work on ErAs and GdAs thin films.

Our analysis clearly demonstrates that the choice of the form of the confining potential has a strong effect on the predictions of simple one-electron confinement models. Our results also highlight the importance of including physically motivated features of the interface electronic structure in modeling the subtle effects of quantum confinement, especially in systems where differences in bonding and crystal structure across the interface lead to highly localized interface states. However, we caution that the results of such simple models are strongly dependent on the choice of parameters. For example, a choice of $k_{eff} = 0.5$ nm^{-1} instead of 1 nm^{-1} with the same values of E_{int} and d_{int} yields a band gap opening at 1.5 nm diameter instead of roughly 2.2 nm. Thus while these modifications may capture more of the complex interfacial physics, they also motivate future theoretical work of fully atomistic and parameter-free calculations to provide a truly quantitative understanding of the effects of quantum confinement in ErAs/GaAs.

4.4 Conclusions

In summary, we have shown that ErAs and ErSb nanostructures embedded within a semiconductor matrix remain semimetallic down to their smallest dimensions. In the case of ErAs(001) films, ARPES measurements showed that films with thickness 10, 6, and 3 monolayers all have bulk $\Gamma - X$ dispersion. While these dispersions are shallower for the thinner films, in all cases there is a Fermi level crossing at Γ, keeping the films semimetallic. Additionally, we observe two dimensional states at the $\overline{M}$ points of the surface Brillouin that cross through the Fermi level. These states are ellipsoidal and disperse to a minimum of approximately 0.21 eV below the Fermi level, roughly independent of film thickness. The $\overline{M}$ states are likely derived from the ellipsoidal electron pockets at the X point of the bulk Brillouin zone, and the electron masses along the transverse and longitudinal directions agree well with DFT calculated effective masses at bulk X, as well as the masses extracted from Shubnikov-de Haas measurements of Sc$_x$Er$_{1-x}$As films. Initial measurements for ErSb(001) and GdAs(001) films show similar behavior, with bands crossing the Fermi level at bulk Γ and ellipsoidal electron pockets at $\overline{M}$.

For ErSb and ErAs nanowires and nanoparticles, scanning tunneling spectroscopy was used as a spatially resolved probe of the density of states. Using cross sectional STS, we find that both ErAs nanowires grown on GaAs(114) and ErAs nanoparticles grown on GaAs(001) have a semimetallic density of states, with a finite minimum at the Fermi level and no evidence of a gap. Note that these ErAs nanoparticles were of dimensions below where simple quantum confinement models predicted the opening of a gap. Similarly, ErSb nanoparticles measured by plan view STS also showed semimetallic behavior, even down to the smallest $3.3 \times 3.3 \times 1.2$ nm^3 particles that could be nucleated.

The data strongly suggest that previously observed optical absorption in ErAs:GaAs and ErSb:GaSb nanocomposites is due to surface plasmon resonances and that the simple hard-walled potential model does not provide an accurate description of quantum confinement for embedded ErAs/ErSb nanoparticles. For the ErAs particles, tunneling spectroscopy shows a state at 0.2 eV above the Fermi level that decays with distance across the ErAs/GaAs interface, and we attribute this to an interface state. We have shown that small changes to the model potential, motivated by the presence of interface states and metallic screening, strongly modify the predictions of the model and provide agreement with measurements, demonstrating the importance of considering the atomistic and electronic structure of the interface itself.

The electronic structure characterization methods developed in this chapter could be extended to the study of many of the other rare earth monopnictides. Sparked by interest in thermoelectrics and plasmonics applications, the field of embedded rare earth monopnictides continues to expand and now includes CeAs [107], TbAs [61], LuAs [108], LaAs [109], and others. In the case of TbAs embedded in GaAs, pump probe measurements suggest that these particles become semiconducting for diameters of several nanometers [98]. Scanning tunneling spectroscopy would be a nice complement to the pump probe measurements and provide a direct measure of the LDOS.

More broadly the preserved metallicity of the embedded nanostructures, in addition to control of the size and shape demonstrated in the previous chapter, enables the design of highly tunable plasmonic, metamaterial, spintronic, and other “active metal” devices. One study has already made use of the semimetallic and anisotropic nature of embedded ErSb nanorods for use in polarization filtering [55]. The suite of applications could be expanded to look at embedded semimetallic wires as interconnects, or use the anisotropy as a parameter for tuning the thermoelectric figure of merit.

Chapter 5

Growth of Semiconducting Half Heuslers

5.1 Introduction to Heuslers

The Heusler compounds are a large class of ternary intermetallics with several hundred members. They have composition X_2YZ (Full Heusler) or XYZ (Half Heusler), where X and Y are transition or rare earth metals and Z is a p-block metal, and they crystallize in the $L2_1$(Full) and $C1_b$ (Half) crystal structures respectively (Figure 5.1).[1] These crystal structures consist of four interpenetrating fcc sublattices with element Z at Wyckoff 4a $(0, 0, 0)$, Y at 4b $(1/2, 0, 0)$, and X at 4c $(1/4, 1/4, 1/4)$. In the Full Heusler a second X' sublattice resides at 4d $(3/4, 1/4, 1/4)$, while in the Half Heusler structure this sublattice is unoccupied. The Half Heusler structure can also be described as a "stuffed zincblende"

---

[1] Some of the work presented in this chapter has previously appeared in the following publications: [110, 111].

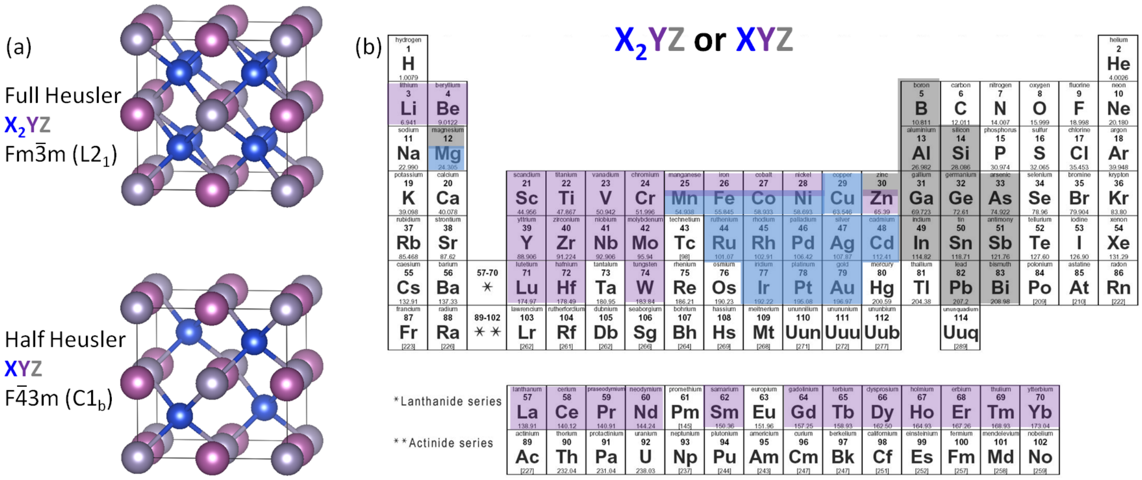

Figure 5.1. (a) Crystal structures for the Full and Half Heusler compounds. (b) Periodic table depicting the wide range of compositions. The occupancies for elements X, Y, and Z in the Full and Half Heusler structures are color coded.

[112, 113] or "stuffed rocksalt" [114] structure, as the XZ and XY sublattices form a zincblende structure while the YZ sublattice forms a rocksalt structure.

These compounds offer a wide range of tunable electronic and magnetic properties not often found within a single materials family. Historically the Full and Half Heuslers have been most studied for their properties associated with metallic behavior [115, 116], including ferro- and antiferromagnetism [113, 115], shape memory effect [10, 117], and magnetocaloric effect [118]. Superconductivity [119, 120] and heavy fermion behavior [9] have also been reported in some of the Half Heuslers. But more recently it has been realized that some of the Half Heuslers can exhibit properties associated with bandgaps. This includes semiconducting behavior [6, 112, 114, 121], for which a bandgap exists at the Fermi level for both spin up and spin down electrons, half-metallic ferromagnetism [7], for which a gap exists for one spin while the other spin bands are partially occupied, and predicted topological insulators [11, 12], for which a gap exists for both spins in the bulk but the surface has metallic states due to band inversion.

Regarding semiconductors, many of the Half Heuslers with 8 or 18 valence electrons per formula unit show semiconducting-like transport properties [121] despite being composed entirely of metals. Density functional theory calculated bandgaps range from a few hundred meV to just over 1 eV, and some of the prototypical examples include NiTiSn and CoTiSb. In the simplest picture, this 8 (or 18) valence electron condition corresponds to completely filled bands $[(d^{10})s^2p^6]$, implying insulating behavior [6, 122]. The states at the conduction and valence band edges have strong d character [114, 123], and hence many of the semiconducting Half Heuslers have large Seebeck coefficients [124, 125]. Furthermore, the Half Heuslers can be readily alloyed into quaternary, quinternary, or higher order compounds (e.g. $\mathrm{Ni(Ti_{0.5}Zr_{0.25}Hf_{0.25})(Sn_{0.998}Sb_{0.002})}$ [126]) or alternatively have secondary phases precipitated to enhance phonon scattering. These two factors, large Seebeck and the enhanced photon scattering, have made semiconducting Half Heuslers a promising material for high figure of merit thermoelectric applications [124, 125, 127]. But most studies have focused on alloying for thermoelectrics, and very little experimental work has investigated fundamental electronic bandstructure of the parent ternary compounds.

Other Full and Half Heuslers, in particular the Half Heuslers with 22 valence electrons per formula unit, are predicted to be half metals in which the bandstructure resembles a metal for one spin and an insulator for the other spin. In principle, such compounds have 100% spin polarization at the Fermi level and hence show great promise for spintronics applications. Examples of predicted half metals include the Half Heusler NiMnSb and the Full Heusler $\mathrm{Co_2MnSi}$. However, experimentally many of these predicted half metals have spin polarization less than 100%, presumably due to defect states within the minority spin gap [128]. Furthermore, although the bulk materials may be predicted to be half metallic, the spin polarization at surfaces and interfaces is highly sensitive to the surface/interface composition and is generally less than 100% [13, 129, 130, 131, 132]. Therefore, understanding and controlling the surfaces and interfaces is of vital importance.

Finally, topological insulators are a subset of the 8 or 18 valence electron semiconducting Half Heuslers in which there exists a bandgap in the bulk, but due to strong spin-orbit coupling there exist metallic surfaces states that are "protected" by time reversal symmetry [11, 12]. These metallic surface states are robust against backscattering and are promising for applications in dissipationless transport, spintronics, and fault-tolerant quantum computing [38]. However, the existence of topological states in a Half Heusler has not yet been verified experimentally [133]. Additionally, as with the trivial (non topological) 18 valence electron Half Heuslers, many of these samples do not show clear evidence of a bulk bandgap.

5.1.1 Why semiconducting Half Heuslers?

In each of these cases a fundamental understanding of the electronic bandstructure, in particular the origin of the bandgap, is key to understanding the properties and implementing these Half Heuslers in devices. Hence it is important to first understand the simplest case: the semiconducting Half Heuslers.

A number of theory papers have investigated the electronic bandstructure of semiconducting Half Heuslers; however, controveries exist regarding the origins of the bandgap. In one description the bandgap arises from the covalent character of the XZ zincblende sublattice [112, 122, 123]. Here it is argued that the most electropositive element Y transfers its electrons to the more electronegative X and Z to form a covalently bonded zincblende sublattice $[XZ]^{n-}$ that is "stuffed" with positive ions Y^{n+}. For CoTiSb this would correspond to $[CoSb]^{4-}$ stuffed with Ti^{4+}. Here the $[CoSb]^{4-}$ sublattice is isoelectronic and isostructural with zincblende GaSb, and the resulting CoTiSb is semiconducting. This simplified picture implies formal electron occupancies of d^0 for Y, d^{10} for X, and s^2p^6 for Z.

An alternate description highlights the stability of the YZ rocksalt sublattice and the symmetry breaking of element X. Calculations by Ogut and Rabe, using pseudopotentials and the local density approximation (LDA), for NiZrSn (X = Ni, Y = Zr, Z = Sn) show that the valence band maximum at Γ had strong Zr d character, and along the $\Gamma - X$ direction these Zr d states hybridize strongly with Sn p states [114]. They propose that the bandgap arises from a combination of the high stability of the ZrSn rocksalt sublattice and symmetry breaking imposed by the Ni sublattice [114]. This description is in general agreement with subsequent LDA and GGA calculations by Larson et. al. [134, 135].

In practice, experimental verification of the bandstructure of Half Heuslers and the origins of the bandgap has been limited by the quality of the samples. Most samples to date have been in bulk polycrystalline form, and hence are not suitable for direct measurements of the momentum ($\mathbf{k}$) resolved bandstructure. Furthermore, despite modest calculated bandgaps of up to 1 eV for some of the semiconducting Half Heuslers, experimentally most samples have behaved more like poor metals in transport with weak temperature dependence on resistivity, high carrier density (typically $n > 10^{20}$ cm^{-3}), and low carrier mobility (< 100 cm^2/Vs) [136, 137, 138, 139, 140, 141]. This has largely been attributed to defects and deviations from stoichiometry [14, 114, 142]. But growths of bulk single crystalline NiTiSn by the flux method show marked improvements in transport properties [16]. Recently there also have been reports of NiTiSn film growth by sputtering [143], opening the way to direct application in epitaxial devices. However the sputtered samples showed lower mobility and higher background carrier densities than the best bulk grown counterparts, likely due to sputter induced damage and challenges in controlling the composition. Hence a method of growing high quality single crystalline films epitaxially is needed.

Our approach is to use molecular beam epitaxy to grow semiconducting Half Heusler thin films. MBE is a method for growing high quality single crystal films with atomic level control of surfaces and interfaces. Furthermore it is a low energy deposition technique and hence produces films with fewer defects than sputtering. MBE has shown success in growing high quality films of the magnetic Full Heuslers, e.g. Co_2MnSi, Ni_2MnIn, Ni_2MnGa, and the Half Heusler NiMnSb, demonstrating the importance of controlling the ordering, interface stoichiometry, and thickness and their effect on magnetic properties [13, 144, 145]. However, no work has yet explored semiconducting Half Heuslers by MBE.

In this chapter we demonstrate the first epitaxial growth of single crystalline CoTiSb and NiTiSn films by MBE. CoTiSb and NiTiSn are two prototypical semiconducting Half Heuslers with 18 valence electrons per formula unit and indirect $\Gamma - X$ bandgaps of 1 and

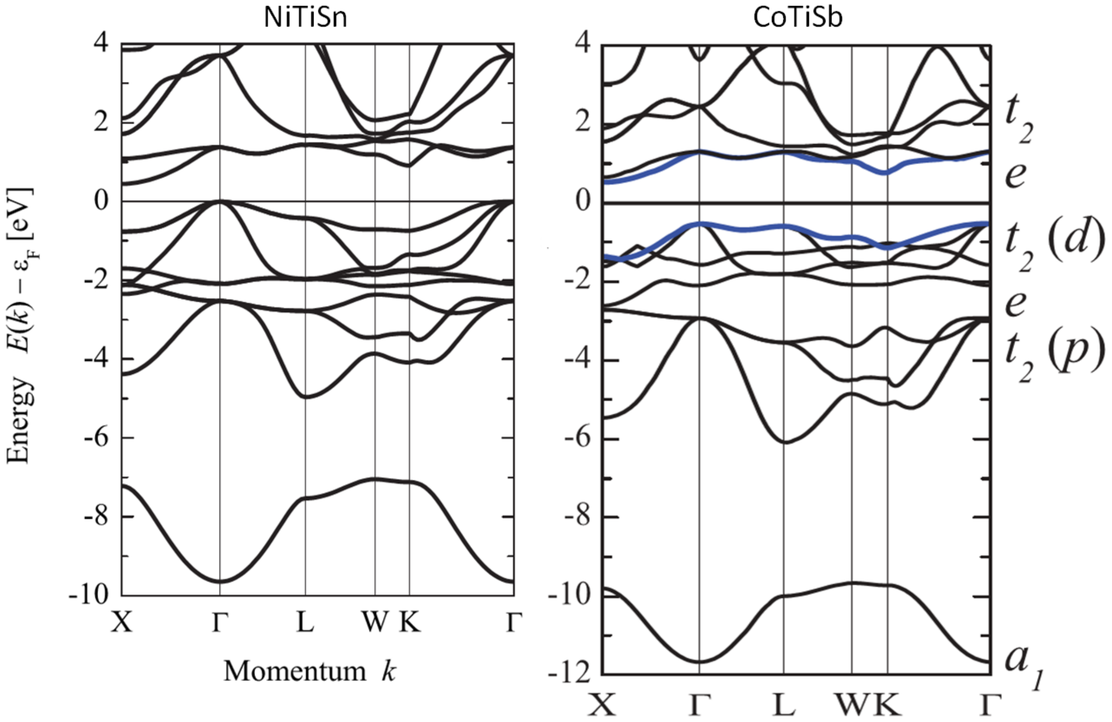

Figure 5.2. DFT-GGA bandstructure calculations for NiTiSn and CoTiSb, adapted from Refs. [14] and [146] respectively. The irreducible representation of the states at Γ for CoTiSb are labelled to the right.

0.5 eV respectively (from DFT-GGA [14, 146], Figure 5.2). These compounds are also the parent compounds some of the highest figure of merit Half Heusler thermoelectric materials, e.g. $Ni(Ti_{0.5}Zr_{0.25}Hf_{0.25})(Sn_{0.998}Sb_{0.002})$ [126]. Additionally, they can be used as a platform for growing all Heusler heterostructures and combining Full and Half Heusler layers with different functionality. Both NiTiSn and CoTiSb films show transport that is consistent with semiconducting behavior, and the CoTiSb films show the highest carrier mobility and lowest background carrier density of any Half Heusler with finite band gap to date [111].

Then in the next two chapters we develop methods for the direct measurement of both surface and bulk electronic bandstructure of these semiconducting Half Heusler films. In Chapter 6 we present surface structure measurements of CoTiSb(001) and NiTiSn(001), showing that both exhibit a variety of surface reconstructions that are analogous to the reconstructions observed in the III-V semiconductors. We present models of the reconstructions, which are a prerequisite for calculations of the surface electronic bandstructure, and also demonstrate methods for capping the samples such that *ex-situ* synchrotron based ARPES measurements can be performed. In Chapter 7 we present ARPES measurements of the surface and the bulk electronic bandstructures and compare them with theory.

Finally, in Chapter 8 we explore Full Heusler / Half Heusler nanocomposites of Ni_2TiSn/NiTiSn for applications in thermoelectrics.

5.2 MBE growth of NiTiSn and CoTiSb

5.2.1 Choice of substrate

Since no native substrates are available for Half Heusler on Half Heusler homoepitaxy, one must first choose a suitable substrate for heteroepitaxial growth of Half Heuslers. The ideal substrates would be both chemically and structurally compatible with the film.

In many ways the compound semiconductors are an ideal substrate. For one, the zincblende compound semiconductors are a close symmetry match to the Half Heuslers, as the XZ and XY sublattices in the Half Heusler structure are also zincblende [Figure 5.3(a)]. Additionally the III-V compound semiconductors have lattice parameters that are very close to that of the Half Heuslers [Figure 5.3(b)] and by tuning the composition of an MBE grown III-V ternary alloy, e.g. $\mathrm{In}_x\mathrm{Ga}_{1-x}\mathrm{As}$ or $\mathrm{In}_x\mathrm{Ga}_{1-x}\mathrm{Sb}$, one can span lattice parameters from that of GaAs (5.65 Å) to that of InSb (6.48 Å) and produce a very flat, lattice matched buffer layer. Therefore in the (001) orientation a cube-on-cube epitaxial relationship is expected, and like the case of ErAs on GaAs, it may be possible to grow Half Heuslers on III-Vs with a continuous fcc (or zincblende) sublattice across the interface. Several groups have previously demonstrated the MBE growth of magnetic Full and Half Heuslers on III-Vs [147, 148], but the growth of semiconducting Half Heuslers by MBE has not been explored before this dissertation. In the present studies grow semiconducting CoTiSb ($a = 5.884$ Å) [149] and NiTiSn ($a = 5.919$ Å) [14] by MBE on InP substrates ($a = 5.869$ Å) with a lattice matched $\mathrm{In}_x\mathrm{Al}_{1-x}\mathrm{As}$ buffer layer.

However, one of the challenges of using III-V substrates is controlling reactions at the Heusler/III-V interface. For example some transition metals, e.g. Ni, are highly reactive with III-Vs even at room temperature [150]. To mitigate these reactions two approaches are employed in this dissertation. The first is to grow a low temperature seed layer of Half Heusler on the III-V followed by annealing and then growth at higher temperatures. Since bulk diffusion is much slower than surface diffusion during growth, interfacial reactions should be substantially reduced using this low temperature initiation layer. This approach will be demonstrated for CoTiSb on InAlAs/InP. A second approach is to use thermodynamically stable diffusion barriers. Previous studies have shown that the rocksalt rare earth monopnictides (RE-V), e.g. ErAs, can be used as a diffusion barrier to prevent reactions between transition metals and III-Vs [68]. This approach will be demonstrated for CoTiSb and NiTiSn on ErAs/In(Ga,Al)As/InP. However, since rocksalt ErAs has four-fold rotational symmetry, the growth of two-fold Half Heusler on ErAs produces two domains of Half Heusler rotated 90 degrees from one another. Additionally, since ErAs is semimetallic, such buffer layer structures are not suitable for in-plane transport measurements as the ErAs serves as a parallel conduction path.

Another substrate choice is MgO. MgO has rocksalt structure with a fairly small lattice parameter of $a_{MgO} = 4.21$ Å, but this matches fairly well with NiTiSn and CoTiSn with a 45 degree rotation around the z axis ($a_{MgO} = 5.95$ Å) [Figure 5.8(e)]. MgO also has the benefit of being very stable due to the strength of the Mg-O bond, hence growth of Half Heuslers on MgO at high temperatures is possible with minimal or no interfacial reactions. This substrate is especially useful for NiTiSn growth, since elemental Ni is extremely reactive with III-Vs. However, as with growth on rocksalt ErAs, growth on

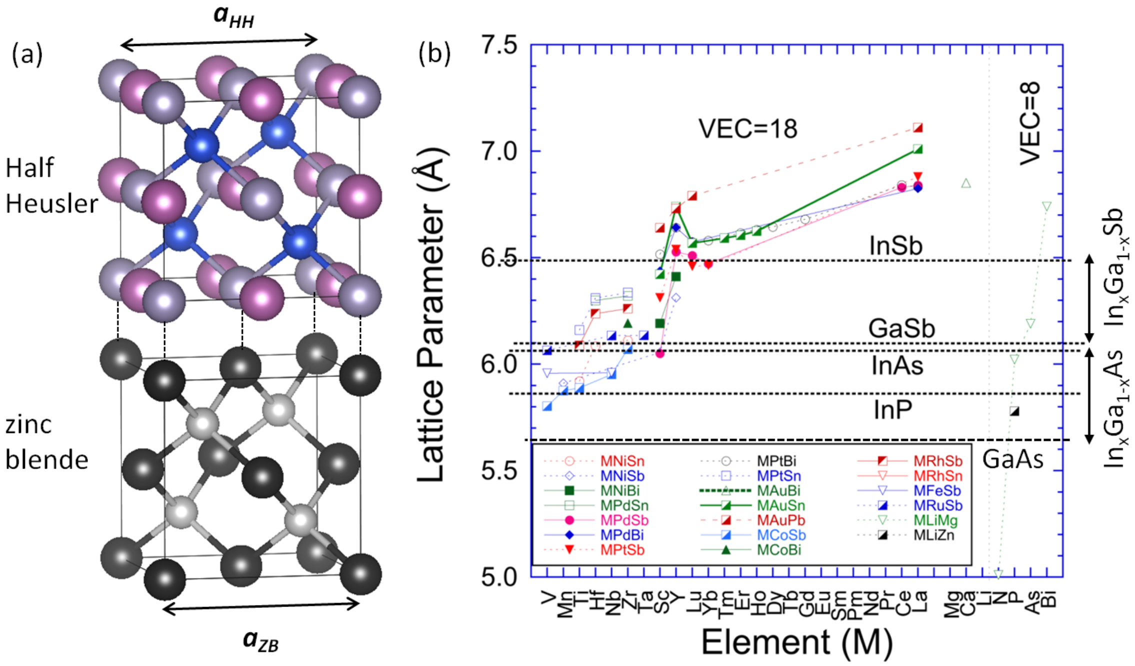

Figure 5.3. (a) Cube-on-cube epitaxial alignment of Half Heusler films on zincblende substrates. (b) Lattice parameter versus composition for a number of the 8 and 18 valence electron Half Heusler compounds.

rocksalt MgO produces two rotational domains of Half Heusler. In addition it is more difficult to grow smooth MgO buffer layers (by electron gun deposition) than to grow smooth III-V buffer layers (by MBE).

5.2.2 Controlling the composition

Controlling the stoichiometry is one of the most challenging aspects of Heusler growth by MBE, especially for semiconducting films in which deviations from stoichiometry may be expected to produce electrically active defects. As an upper bound estimate, if each stoichiometry related defect produced one carrier, a deviation from stoichiometry on the order of 1% would produce a background carrier density on the order of 10^{20} to 10^{21} cm^{-3}. In contrast, conventional semiconductors such as GaAs ($E_g = 1.42$ eV) and InAs

($E_g = 0.35$ eV) have similar bandgaps as the semiconducting Half Heuslers ($E_g = 1.42$ and 0.35 eV respectively) but have lower intrinsic carrier densities(10^6 and 10^{15} cm^{-3} respectively at room temperature). Thus for good semiconducting Half Heusler films it is desirable to control the stoichiometry to the percent level or better.

In conventional III-V MBE the stoichiometry is controlled by growing in a group-V adsorption limited regime. Due to the high volatility of the group-V species (e.g. As or Sb), stoichiometric films of III-V are easily grown while supplying an excess of group-V to the surface [17, 18]. This self-limited regime occurs over a finite range of growth temperatures and group-V overpressures and is often called the "growth window." Similar adsorption limited regimes have also been demonstrated for MBE growth of some of the complex oxides using elemental precursors [151, 152, 153] and using metallorganic precursors [154].

However for growth of many intermetallic Heuslers by MBE the existence of a growth window using elemental precursors is unlikely. Most transition metals are fairly non-volatile and have near unity sticking coefficients, hence controlling the stoichiometry of the films using elemental precursors requires very precise control of the incident fluxes. For some of the group-V containing Half Heuslers, e.g. CoTiSb and NiMnSb, it may be possible to grow in a group-V adsorption-limited regime similar to that demonstrated for the III-Vs. In such a scenario the ratios of Sb:(Co+Ti) or Sb:(Ni+Mn) may be self-limited and only the Co:Ti or Ni:Mn ratios would need to be precisely controlled. Such a growth window for any of the Full or Half Heuslers has yet to be established.

In this dissertation we use elemental precursors and control the incident fluxes via a combination of *ex-situ* Rutherford Backscattering Spectrometry (RBS) as an absolute measure of fluxes, and *in-situ* beam flux measurements using an ionization gauge. We use standard effusion cells for Sb and Sn, and high temperature cells for Co and Ni. For Ti we use a special high temperature effusion cell and crucible that are capable of handling molten Ti (DCA instruments), which enables higher and more stable fluxes. To calibrated the fluxes, calibration samples were grown on silicon substrates and their absolute compositions were measured by RBS. An example of measured and simulated RBS spectra for one calibration sample are shown in Figure 5.4(a). Several samples are grown at different effusion cell temperatures, and when plotted versus cell temperature the absolute flux measured by RBS follows an Arrhenius relationship as expected [Figure 5.4(b) example for Sn effusion cell] and is reasonably stable over time. However, note that since the RBS spectrometer is not attached to the MBE system (samples were sent to the Univerity of Minnesota and Arizona State University for RBS), it is not practical to grow an RBS calibration sample before each real sample growth.

Therefore in order to account for day to day fluctuations, *in-situ* flux measurements were performed before each growth using a home-built beam flux ionization gauge. To minimize the effect of reactions from residual species adsorbed on the ion gauge, we first coat the ion gauge head with the flux to be measured, then shutter the effusion cell and measure a background pressure ϕ_0. We then open the effusion cell shutter and record the flux gauge pressure after 2 minutes of exposure ϕ_{2min}, which we have found is sufficient time to eliminate flux transients and asymptote to a stable effective pressure. We then define the the beam equivalent pressure (BEP) as $BEP = \phi_{2min} - \phi_0$, and as a function of effusion cell temperature the BEP also follows an Arrhenius relationship [Figure 5.4(b) example for Sn effusion cell]. Finally, we correlate the *in-situ* measured BEP to the real flux measured by RBS, and the results are shown in Figures 5.4(c,d) for the Co, Ni, Ti, Sn, and Sb cells. In this way, the calibration of real RBS flux versus temperature is used as a rough temperature set point for each effusion cell, and immediately before each growth *in-situ* measurements of the BEP are used to fine tune the effusion cell temperatures to yield the desired flux. For NiTiSn and CoTiSb films we find that using this method we are able to control the compositions to atomic compositions 1.00 ± 0.03 Ni : 1.00 ± 0.03 Ti : 1.00 ± 0.03 Sn, and 1.00 ± 0.03 Co : 1.00 ± 0.03 Ti : 1.00 ± 0.03 Sb using 1:1:1 stoichiometric fluxes. However finer control of the compositions requires identifying an adsorption-limited regime, which will briefly be discussed in the next two subsections.

5.2.3 Growth of CoTiSb on InAlAs/InP(001)

Here we demonstrate the epitaxial growth of single crystalline CoTiSb on $In_{0.52}Al_{0.48}As$ / InP(001) heterostructures. Samples were grown by MBE on semi-insulating InP:Fe (001) substrates. After thermal desorption of the native oxide under an As_4 flux, a lattice-matched unintentionally doped 400 nm $In_{0.52}Al_{0.48}As$ layer (abbreviated to InAlAs) was grown on the InP at 500 °C in a modified VG V80H system that is dedicated for III-V growth. This buffer layer and substrate were chosen due to the close lattice match between CoTiSb (a = 5.884 Å) and InP (a = 5.869 Å) [146]. On some samples a 3 nm strained ErAs layer was grown on top of the InAlAs in order to minimize interfacial

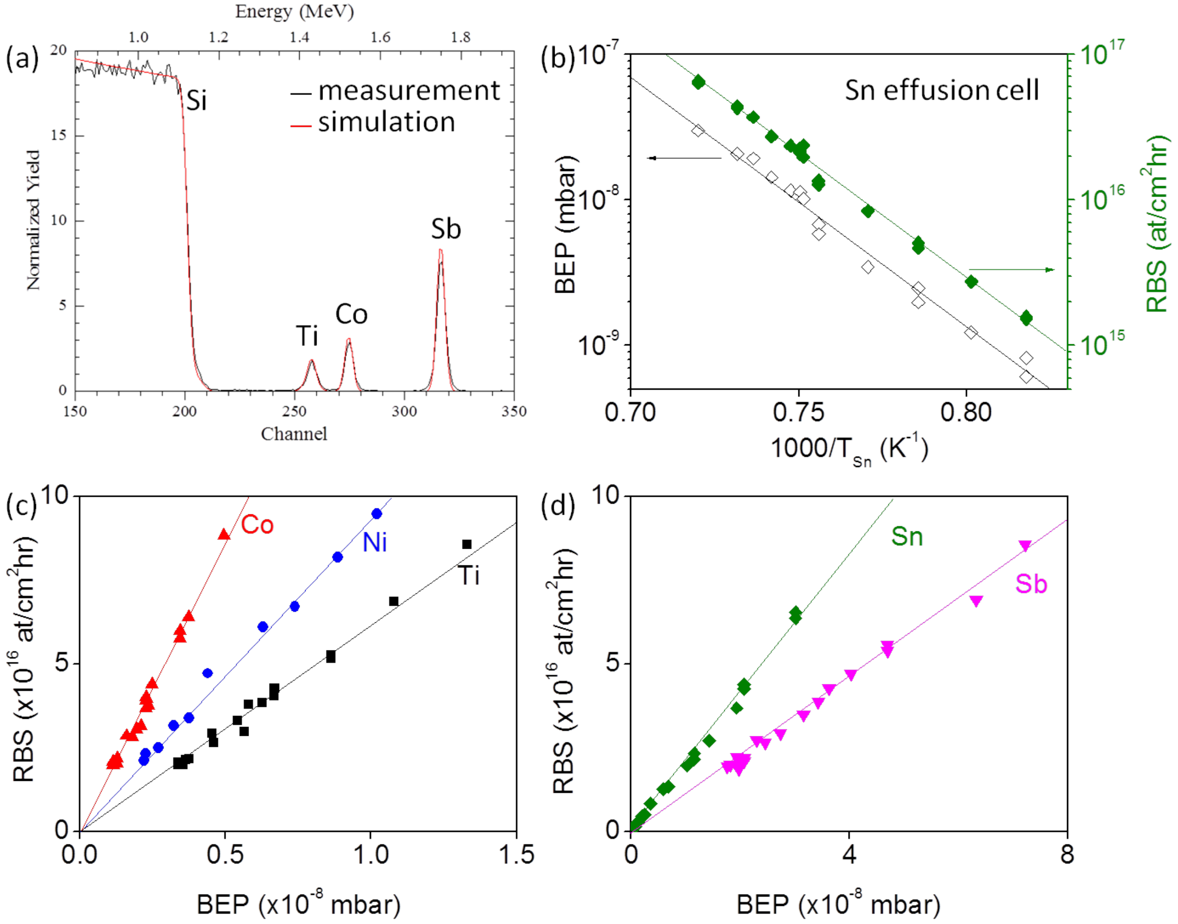

Figure 5.4. (a) RBS spectrum of a calibration sample grown on silicon. (b) Arrhenius plots of the real flux measured by RBS and the *in-situ* beam equivalent pressure (BEP) measured using a beam flux ionization gauge for the Sn effusion cell. (c and d) Plots of the RBS flux versus the BEP.

reactions that are expected to occur at the interface between the CoTiSb and the InAlAs.

To minimize substrate preparation variations the 2 inch samples were capped with 200 nm amorphous As (using an As_4 flux) before removal from the III-V MBE system, cleaved into smaller samples, and then loaded into a dedicated metals MBE system (VG V80) for CoTiSb growth. This allowed the same prepared substrate to be used for multiple CoTiSb growth sequences. After thermal desorption of the As_4 cap at 350 °C to produce an InAlAs (2×4) surface reconstruction (substrate temperature calibrated to the As desorption temperature of As capped GaAs), CoTiSb was grown by simultaneous deposition from elemental Co, Ti, and Sb effusion cell sources. Growth was performed using 1:1:1 stoichiometric fluxes at a rate of 2.0×10^{16} atoms/cm^{2}hr per effusion cell. Initial investigations of growth with an Sb overpressure have also been performed, i.e. Co:Ti:Sb flux ratios of $1 : 1 : (1 + \delta)$, in order to identify an adsorption-limited growth window.

During the nucleation of CoTiSb on the InAlAs (2×4) surface at 260 °C the RHEED pattern becomes slightly diffuse and spotty, but after 3-4 bilayers of growth (one bilayer is defined as 5.95×10^{14} atoms/cm^2 each of Co, Ti, and Sb) the pattern becomes streaky indicating relatively smooth epitaxial growth. Figures 5.5(a-c) show RHEED patterns after 5 nm growth at 260 °C. The patterns show a clear (2×1) surface reconstruction demonstrating a well ordered surface with a $2\times$ periodicity when viewed along the [110] azimuth [Figure 5.5(a)], and $\times 1$ periodicity when viewed along [1-10] [Figure 5.5(b)]. This reconstruction likely results from surface Sb-dimerization analogous to III-V (001) surfaces and will be discussed in further detail in chapter 6.

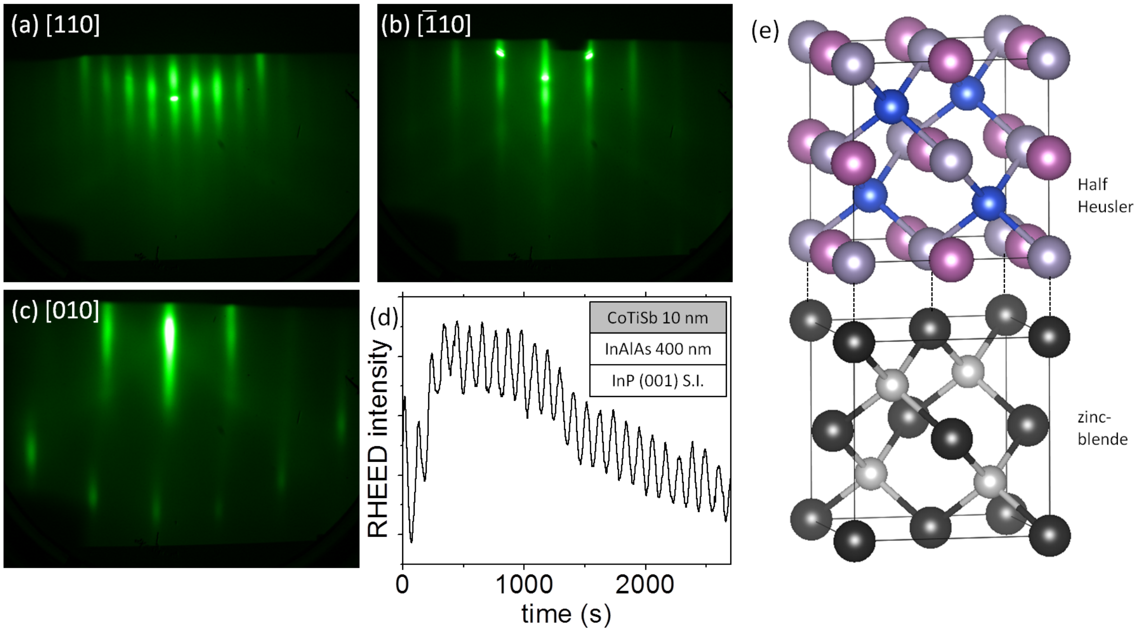

Figure 5.5. (a-c) RHEED patterns of a 5 nm CoTiSb on InAlAs/InP(001) film grown at 260 °C, along the [110], [1-10], and [010] azimuths. (d) RHEED intensity oscillations of the [010] specular spot demonstrating layer-by-layer growth. Reprinted with permission from [111]. Copyright 2014 American Institute of Physics.

Figure 5.5(d) shows RHEED intensity oscillations of the [010] specular spot, indicating a layer-by-layer growth mode. Each oscillation corresponds to one atomic bilayer of growth and the period of 107 seconds corresponds to a growth rate of 9.9 nm/hr in good agreement with the rate of 10.2 nm/hr expected from RBS. The oscillations persist for up to 50 periods, suggesting that the films remain relatively smooth throughout growth.

Growth of CoTiSb directly on InAlAs/InP has been performed at temperatures up to 360 °C; however it was found that for nucleation above 360 °C the RHEED pattern begins to lose intensity, presumably due to reactions at the CoTiSb/InAlAs interface. To minimize this interfacial reaction two approaches have been employed. The first approach was to grow a lower temperature seed layer of CoTiSb at 260 °C for 3 nm, then anneal and continue CoTiSb growth at a higher temperature. Using this seed layer approach, CoTiSb has been grown at temperatures up to 460 °C without a significant reduction of the RHEED intensity. For all growths using stoichiometric fluxes and substrate temperatures within the range 260 460 °C, the (2×1) surface reconstruction is observed.

Additionally, for growth above 425 °C (well above the Sb desorption temperature) growth can also be performed using an Sb overpressure of 20% (i.e. Co:Ti:Sb flux ratios of 1:1:1.2) while maintaining a streaky RHEED pattern. These initial findings suggest that an adsorption limited growth window may exist for CoTiSb; however, a full systematic study of the film compositions as a function of Sb overpressure and temperature has not yet been performed.

The second approach was to grow a thin ErAs diffusion barrier between CoTiSb and the InAlAs layers. With the ErAs diffusion barrier, growth on ErAs/InAlAs/InP has been performed at temperatures in excess of 510 °C without a substantial reduction in intensity of the RHEED pattern.

Figure 5.6(a) shows an overview XRD $\theta - 2\theta$ scan of 10 nm CoTiSb on InAlAs/InP(001) grown at 260 °C. The sharp peaks at $2\theta = 30.48^\circ$ and 63.39° correspond to the InP (002) and (004) substrate reflections, respectively, and the CoTiSb and InAlAs (002) and (004) peaks are nearly overlaid on the InP peaks indicating the close lattice match. Finite thickness fringes centered around the (002) and (004) reflections are present, indicating high quality interfaces, and the period of $\Delta(2\theta) = 0.89^\circ$ corresponds to a thickness of 9.9 nm, in good agreement with the CoTiSb film thickness expected from the RBS and RHEED oscillation rates (10.2 and 9.9 nm respectively). Other than the (00L) peaks and fringes, no additional peaks in the XRD scans are observed. These x-ray diffraction

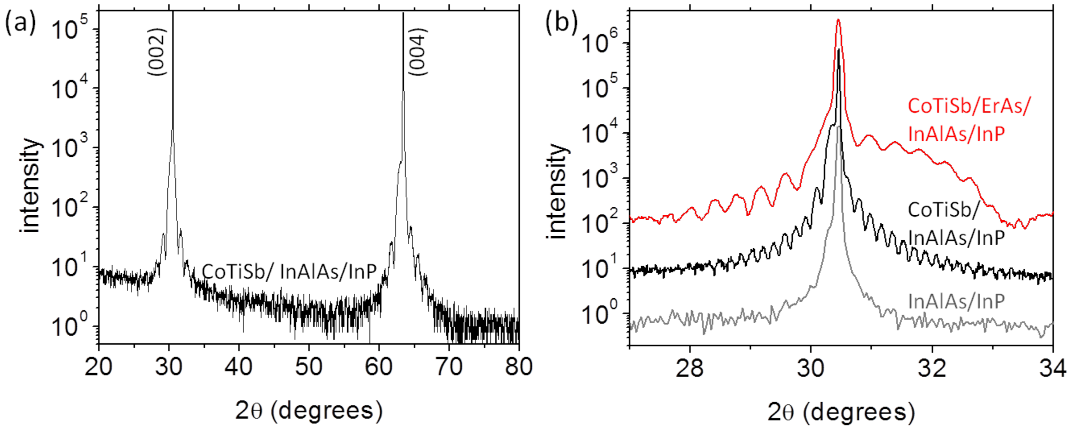

Figure 5.6. (a) XRD $\theta - 2\theta$ scan for 10 nm CoTiSb on InAlAs/InP(001) grown at 260 °C. The insert shows the Half Heusler and zincblende crystal structures, highlighting the similarity between the two crystal structures and the expected epitaxial cube-on-cube alignment. For the Half Heusler CoTiSb, Co occupies the (1/4, 1/4, 1/4) sites (red), Ti occupies the (1/2, 0, 0) (blue) and Sb occupies the (0, 0, 0) (green). Vacancies are found at the (3/4, 1/4, 1/4) sites. (b) XRD $\theta - 2\theta$ scans of the (002) reflection for three samples. The bottom (grey) shows the 400 nm InAlAs buffer layer on InP before CoTiSb growth, and the middle (black) shows 50 nm CoTiSb on InAlAs/InP (260 °C seed, 360 °C growth), and the top (red) shows 20 nm CoTiSb on (3 nm ErAs)/InAlAs/InP (460 °C seed and growth). Adapted with permission from [111]. Copyright 2014 American Institute of Physics.

patterns combined with the RHEED patterns indicate an epitaxial cube-on-cube growth with no detectable secondary phases or orientations.

Figure 5.6(b) shows scans around the (002) reflection for the InAlAs/InP buffer structure and for two different CoTiSb samples. The bottom (gray) curve shows the 400 nm InAlAs/InP buffer capped with amorphous As_4 (before subsequent CoTiSb growth). Here only a small shoulder to the left of the InP (002) peak is observed, indicating the very close lattice match between the InAlAs buffer layer and the InP. The middle (black) curve shows a 50 nm CoTiSb film grown on the InAlAs/InP buffer, which was performed by seeding 3 nm of CoTiSb at 260 °C and then continuing growth at 360 °C. The peak centered at 30.36° (just to the left of the substrate peak) corresponds to the CoTiSb (002)

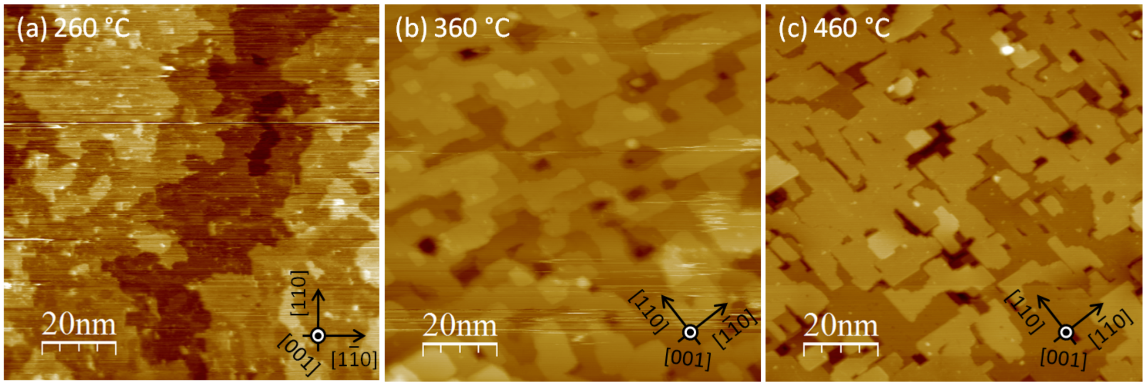

Figure 5.7. Plan view filled states STM images of CoTiSb grown on ErAs/InAlAs:Si/InP:S (001) at temperatures of (a) 260, (b) 360, and (c) 460 °C.

reflection and a lattice parameter of 5.88 Å, in good agreement with the bulk CoTiSb lattice parameter of 5.884 Å [146]. Additionally, fringes with spacing $\Delta(2\theta) = 0.177°$ are observed, corresponding to a CoTiSb film thickness of 49.9 nm. The clear fringes demonstrate that the usage of the lower temperature seed layer approach enables further growth at higher temperatures while retaining high quality interfaces. The top (red) curve shows a 20 nm CoTiSb film grown directly on (3 nm ErAs)/InAlAs/InP at 460 °C. The broad peak centered at $2\theta = 31.28°$ corresponds to the ErAs (002), and the fringes with period $\Delta(2\theta) = 0.452°$ correspond to the CoTiSb layer with thickness 19.5 nm. The presence of fringes also confirm that the ErAs diffusion barrier enables growth of CoTiSb at high temperatures while retaining high quality interfaces.

Further investigations of the growth temperature were performed using *in-situ* scanning tunneling microscopy. Figure 5.7 shows filled states STM images of 10 nm CoTiSb films grown directly on ErAs/InAlAs:Si/InP:S (001) at temperatures of 260, 360, and 460 °C. For growth at 260 °C a number of step edges are observed; however these step edges are randomly oriented. For growth at 360 °C the step edges become faceted along the ⟨110⟩ directions and the surface is characterized by 10-20 nm platelets. With further increases in growth temperature to 460 °C these platelets increase in lateral dimensions, resulting in smoother films. Hence a minimal growth temperature of around 360°C is required to achieve well defined step edges.

5.2.4 Growth of NiTiSn on MgO (001)

NiTiSn films were grown by MBE on MgO (001) substrates in a VG V80 MBE system by simultaneous deposition from elemental Ni, Ti, and Sn effusion cell sources. After annealing the substrates in the MBE chamber at 400 °C, an approximately 5 nm thick MgO buffer layer was grown at 400 °C by electron beam evaporation of MgO. Samples were then ramped to the desired temperature for NiTiSn growth. NiTiSn films were grown using a 1:1:1 stoichiometric ratio of fluxes for Ni, Ti, and Sn at rates of $1.0 - 5.0 \times 10^{16}$ atoms/(cm^2*hr) per effusion cell. Unlike the case of CoTiSb, where the Sb is much more volatile than Co or Ti, for NiTiSn the Sn is not much more volatile than Ni or Ti. Hence within the range of achievable growth temperatures in our MBE ($<$ 650°C), instead of self-limiting, growth with an overpressure of Sn simply lead to incorporation of the excess Sn since Sn is not very volatile at these growth temperatures.

Figure 5.8(c,d) shows RHEED patterns along the [010] and [110] azimuths following electron beam deposition of the MgO buffer layer. Note these directions are referenced to the MgO (001) substrate. The streaky patterns indicate a smooth starting surface. Upon the deposition of the first few atomic layers of NiTiSn the RHEED pattern becomes spotty, indicating three dimensional diffraction. Here the surface likely roughens

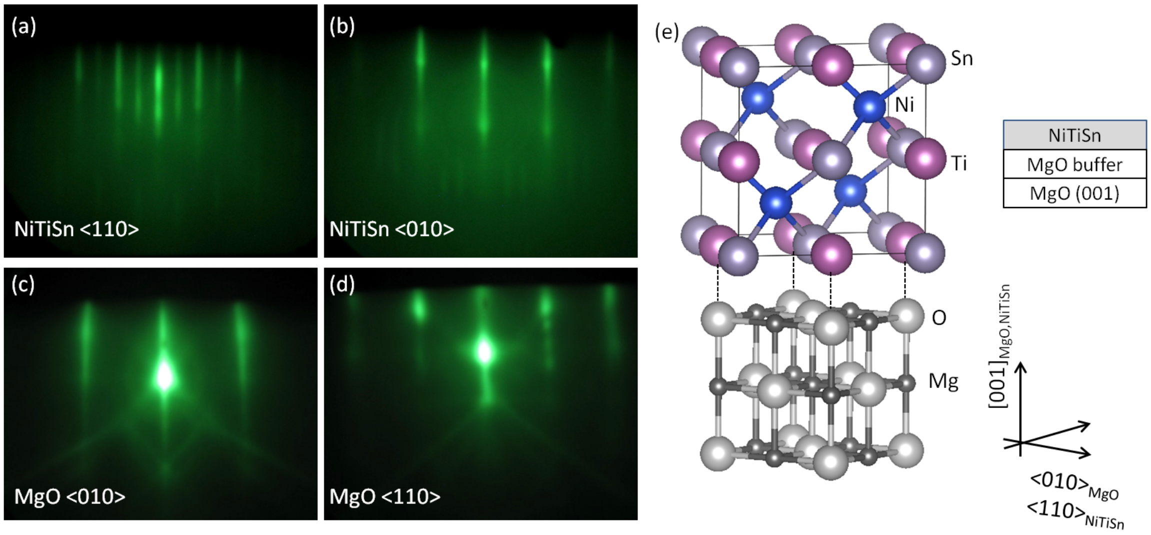

Figure 5.8. (a,b) RHEED patterns for a 50 nm epitaxial NiTiSn film grown at 450 °C on MgO (001) showing a mixed domain $(2 \times 1)/(1 \times 2)$ surface reconstruction. The directions are referenced to the NiTiSn. (c,d) RHEED patterns for the MgO buffer layer, referenced to the MgO (001) crystal directions. (e) Model of NiTiSn on MgO (001) showing a 45° rotated cube-on-cube epitaxial relationship. Reprinted with permission from [110]. Copyright 2013 American Institute of Physics.

into islands due to poor wetting and the 0.65% lattice mismatch between MgO and NiTiSn. The RHEED pattern becomes streaky again after approximately 5 nm of continued growth, suggesting island coalescence and reduction in the surface roughness. Figure 5.8(a,b) shows the streaky RHEED patterns following 50 nm growth of NiTiSn. Here the directions are referenced to the NiTiSn film. The in-plane epitaxial alignments of NiTiSn $\langle 110 \rangle$ // MgO $\langle 010 \rangle$ and NiTiSn $\langle 010 \rangle$ // MgO $\langle 110 \rangle$ confirm a 45° rotated cube-on-cube epitaxial relationship, i.e. NiTiSn (001) $\langle 110 \rangle$ // MgO (001) $\langle 010 \rangle$. The epitaxial relationship is shown schematically in Figure 5.8(e). Due to the much larger heats of formation for Ti oxides than Ni or Sn oxides [155, 156, 157], the interface stacking sequence is assumed to be Ni/TiSn/MgO rather than TiSn/Ni/MgO, such that Ti-O bonds are formed at the interface.

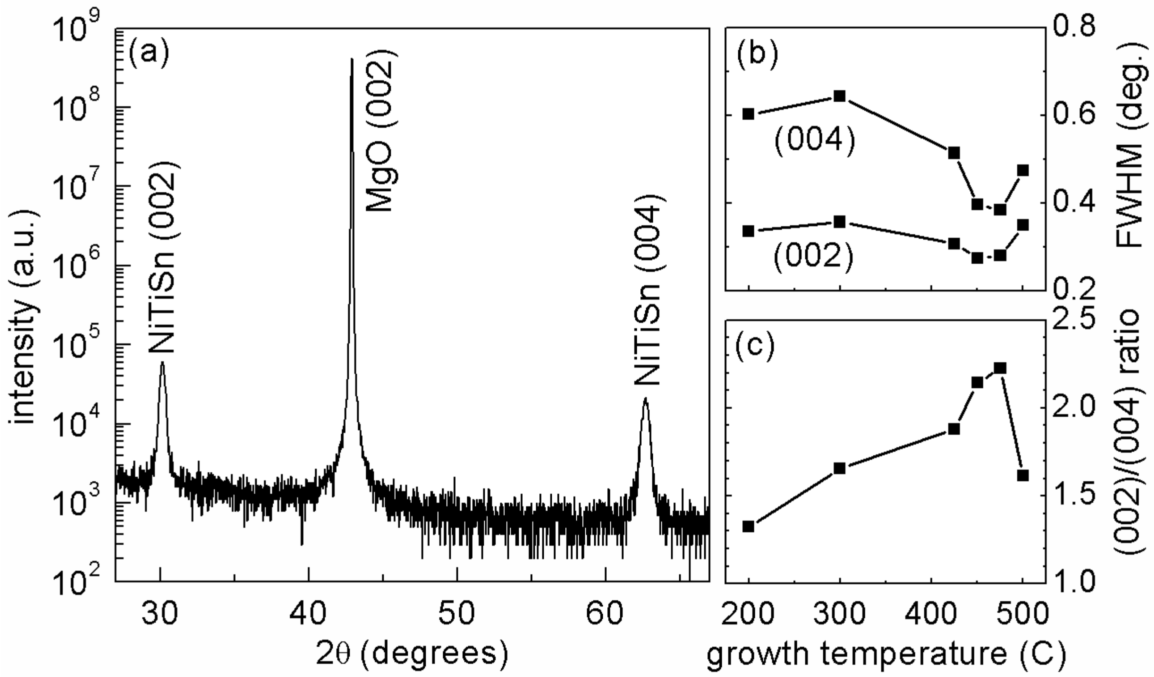

Figure 5.9. XRD $\theta - 2\theta$ scan of a NiTiSn / MgO (001) film grown at 450 °C. (b) Full width at half maximum for the (002) and (004) NiTiSn peaks for samples grown at various temperatures. (c) Integrated area ratio of the (002) and (004) peaks as a function of growth temperature. Reprinted with permission from [110]. Copyright 2013 American Institute of Physics.

For the NiTiSn film a 2× periodicity is observed in the RHEED pattern along both [110] and [1-10] NiTiSn directions [Figure 1(a)] and 1× periodicity along both [100] and [010] [Figure 5.8(b)]. This periodicity suggests a mixed reconstruction of (2×1) and (1×2) domains rotated 90 degrees from one another, resulting from the growth of 2-fold rotationally symmetric Half Heusler NiTiSn (001) on the 4-fold symmetric rocksalt MgO (001) surface. A (2×2) reconstruction is ruled out because a (2×2) would have a 2× periodicity along the $\langle 010 \rangle$ directions. Recall that a (2×1) reconstruction has also been observed for CoTiSb(001) (Figure 5.5).

Figure 5.9(a) shows an XRD $\theta - 2\theta$ scan of a 50 nm NiTiSn film grown at 450 °C. The peak at $2\theta = 42.91°$ corresponds to the MgO (002) substrate reflection. Two additional peaks are observed at 30.17° and 62.73° corresponding to the NiTiSn (002) and (004) reflections with a lattice constant of 5.92 Å. This matches the experimental lattice constant of 5.919 Å for bulk NiTiSn [14]. Only the (00L) peaks are observed, where L is even, consistent with the allowed peaks for a (001) oriented single crystal Half Heusler film. No discernible secondary phases or orientations are detected by XRD.

To investigate the ordering in the NiTiSn films, 50 nm samples were grown at temperatures from 200 to 500 °C. Within this range of growth temperatures only the (00L) peaks were observed by XRD and streaky RHEED patterns were also observed, indicating that films remain epitaxial. The full width at half maximum (FWHM) of the (002) and (004) NiTiSn reflections are plotted in Figure 5.9(b). The FWHM for both reflections reach minima of 0.275° and 0.385°, respectively, for growth temperatures of 450-475 °C suggesting that this temperature window produces the most ordered films. However the FWHMs are broadened: from the Scherrer equation ($\tau = (K\lambda)/(\beta cos\theta)$ where τ is the film thickness, $K = 1$ is the shape factor, and β is the FWHM) if the films were perfectly ordered out of plane, the FWHMs would be expected to be 0.18° for the (002) and 0.33° for the (004). This broadening suggests there is a mosaic in the out of plane component due to relaxation by misfit dislocations with Burgers vectors with an out of plane component.

For NiTiSn crystallizing in a Half Heusler structure, there are three possible lattice arrangements depending on whether Ni, Ti, or Sn occupies the double tetrahedral site (Wyckoff 4c). Only the phase with Ni at the double tetrahedral is expected to be a gapped semiconductor [114]. To distinguish between the three lattice arrangements, structure factors were calculated using the CaRine Crystallography package and assuming perfect ordering of each phase with a lattice constant of 5.92 Å to match the experimentally observed lattice constant. The calculated (002)/(004) intensity ratios are 2.00, 3.63, and 0.005 for Ni, Ti, or Sn at the double tetrahedral (4c) site, respectively. Figure 5.9(c) plots the measured integrated (002)/(004) intensity ratios. For growth temperatures of 425-475 °C the ratio varies from 1.88 to 2.23, consistent with Ni at the double tetrahedral site, the desired phase for a semiconducting NiTiSn. This range of temperatures also coincides with the narrowest FWHM for the (002) and (004) reflections.

Deviations from the calculated (002)/(004) ratio may result from an increased number of point defects. For example Ouardi et. al. suggest a large density of Ti-Vc (titanium-vacancy) antisite swaps for bulk polycrystalline NiTiSn [14]. Assuming stoichiometry is retained, a 5% Ti-Vc swap (modeled by site occupancies of 0.95 Ti at the 4b site, 0.05 Ti at the 4d, 1.00 Sn at the 4a, and 1.00 Ni at the 4c) would yield a (002)/(004) ratio of 1.81, within the range of ratios measured. These Ti-Vc swaps have been proposed to create electronic states within the NiTiSn band gap [14]. Alternatively, Miyamoto et. al. [158] suggest the presence of electrically active Ni-Vc swaps, which would not change the (002)/(004) ratio but still could be present. Sn-Vc antisites would decrease the ratio to 1.56 for a 5% swap, which is significantly smaller than the ratios measured for $T_{growth} = 425 - 475$ °C and is thus less likely than Ni-Vc or Ti-Vc. Ni-Ti substitutions could also be present, which would increase the (002)/(004) ratio to 2.07 for a 5% substitution. However, given that the atomic radii for Ni and Ti are quite different (Ni 1.24 Å, Ti 1.47 Å, Sn 1.58 Å), it has been suggested that this substitution is unlikely [158].

Deviations from the calculated (002)/(004) ratio may also result from deviations in stoichiometry. For example, a 3% deficiency in Ni composition (modeled by a site occupancy of 0.97 Ni at 4c) yields a calculated (002)/(004) ratio of 2.11, and a 3% excess in Ni (1.00 Ni occupancy at 4c and 0.03 Ni occupancy at 4d) yields a ratio of 1.89. A 3% excess of Ti or Sn at the vacancy site gives similar values of 1.92 or 1.89 respectively, while 3% Ti or Sn deficiencies yield values of 1.964 or 1.920 respectively. All of these calculated ratios are within the range of ratios measured for growth temperatures of 425-475 °C. Due to challenges in controlling the effusion cell fluxes by better than 3%, it is assumed that these deviations from stoichiometry are the primary factor responsible for the deviations in (002)/(004) ratio.

Growth of NiTiSn was also attempted on InGaAs/InP(001) and InAlAs/InP(001) buffers. However it was found that single phase NiTiSn could not be grown directly on InAlAs (InGaAs) without significant reactions (as observed by a substantial dimming of the RHEED pattern), even at room temperature. This is presumably due to the high reactivity of Ni with III-Vs. But by using an ErAs diffusion barrier, NiTiSn films were successfully grown on ErAs/InAlAs/InP and ErAs/InGaAs/InP at temperatures of up to 500 °C without a dimming of the RHEED pattern. For growths on the ErAs diffusion barrier the NiTiSn films showed a $(2 \times 1)/(1 \times 2)$ RHEED pattern (see chapter 6).

5.3 Transport

5.3.1 CoTiSb

For ex-situ magnetotransport measurements, prior to removal from ultrahigh vacuum the CoTiSb samples were capped with 5-10 nm AlO_x (grown in-situ by electron beam evaporation of Al_2O_3) to protect the films from oxidation. Contacts were made in a Van der Pauw geometry using annealed indium, and the magnetotransport measurements were performed in a Quantum Design PPMS using a custom breakout box and lock-in amplifier.

Figure 5.10 shows temperature dependent transport measurements for a 30 nm CoTiSb film on InAlAs/InP(001) grown using the seed layer approach (260 °C seed, 410 °C continued growth). As the measurement temperature increases from 2 to 300 K the zero field resistivity decreases [Figure 5.10(a)], consistent with semiconducting-like transport and thermally activated behavior.

Figure 5.11 shows the transverse Hall resistance (R_{xy}, dashed curves) and longitudinal magnetoresistance ($\Delta R_{xx}(B)/R_{xx}(0) = [R_{xx}(B) - R_{xx}(0)]/R_{xx}(0)$, solid curves) versus magnetic field at various fixed temperatures. In both sets of measurements the magnetic field was oriented perpendicular to the sample surface. We first discuss the Hall resistance and the extracted carrier density and mobility, then return to discuss the magnetoresistance. Within the range of temperatures from 300 to 2 K, the Hall resistance was linear and had negative slope with magnetic field out to 3 T, suggesting that the conduction is dominated by an n-type carrier. Using a single carrier model, the n-type carrier density

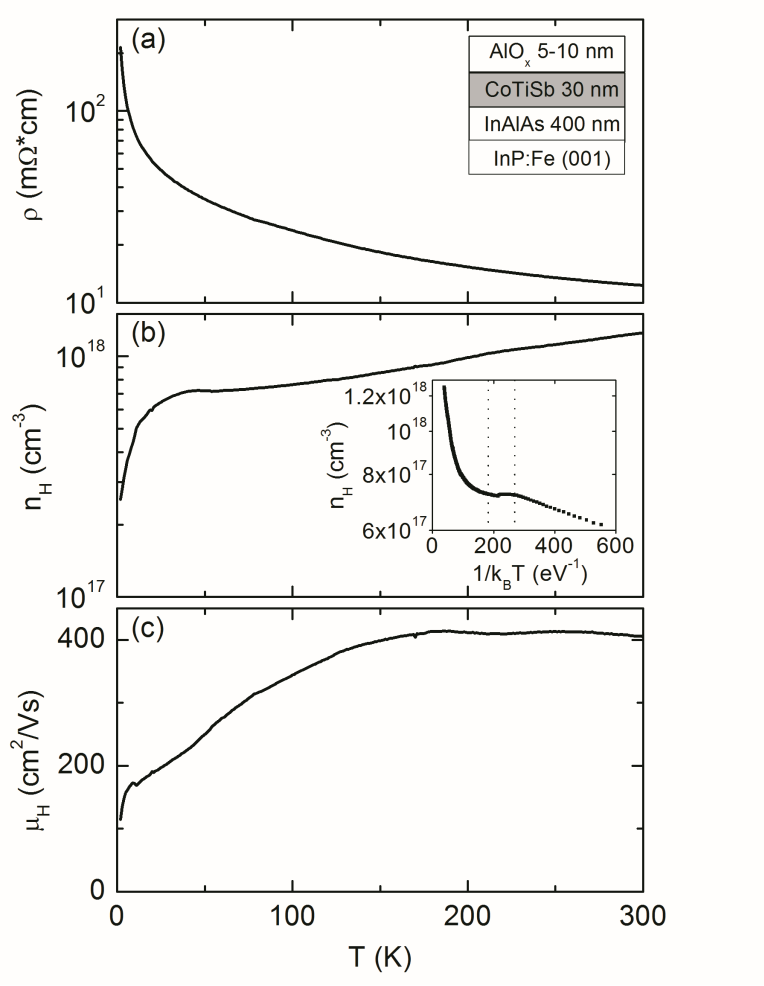

Figure 5.10. Temperature dependent transport measurements for a 30 nm CoTiSb film on InAlAs/InP. (a) Zero field resistivity. (b) and (c) plot the single carrier Hall density (n-type) and mobility extracted from R_{xy} at $B = \pm 1$ T. The insert of (b) shows the density replotted in logarithmic scale versus $1/k_BT$. Reprinted with permission from [111]. Copyright 2014 American Institute of Physics.

(n_H, extracted from the slope of R_{xy} vs. B at ±1T), decreases smoothly from 1.3×10^{18} cm^{-3} at 300 K to 7.2×10^{17} cm^{-3} at 43 K, before rapidly falling to 2.5×10^{17} cm^{-3} at 2 K [Figure 5.10(b)]. Note these carrier densities are among the lowest yet reported for Half Heusler compounds, suggesting the films have a comparably low density of defect states.

In Arrhenius form [Figure 5.10(b) insert, logarithm of n_H versus $1/k_BT$] the temperature dependent Hall carrier density shows three distinct regions upon cooling – a decrease in density from room temperature to 64 K ($1/k_BT < 180$ eV^{-1}), a plateau from 64 to 43 K (180 to 270 eV^{-1}), and a decrease below 43 K (> 290 eV^{-1}) – that are reminiscent of the intrinsic, saturation, and freeze-out (or localization) expected for heavily doped semiconductors. In the high temperature region (< 180 eV^{-1}), although 300 K is not quite high enough to approach the expected $n \propto exp(-E_g/2k_BT)$ dependency for intrinsic behavior and activation across the bandgap, from a fit in the range 240-300 K we estimate a lower bound for the bandgap of $E_g > 0.13$ eV. This is considerably smaller than the DFT bandgap of 1 eV [146], and further measurements at higher temperatures are required to determine the transport bandgap.

The Hall electron mobility (μ_H) is shown in Figure 5.10(c). For this sample the mobility was 406 cm^2/Vs at 300 K and was roughly constant from 300 to 150 K. Upon cooling below 150 K the mobility decreases and follows a $\propto T^{0.4}$ dependence in the region 46-150 K and $T^{0.2}$ below 46 K. These power laws are shallower than the $T^{1.5}$ expected for ionized impurity scattering but close to the $T^{0.5}$ expected for disorder scattering, suggesting that at low temperatures the CoTiSb film is a disordered electronic system

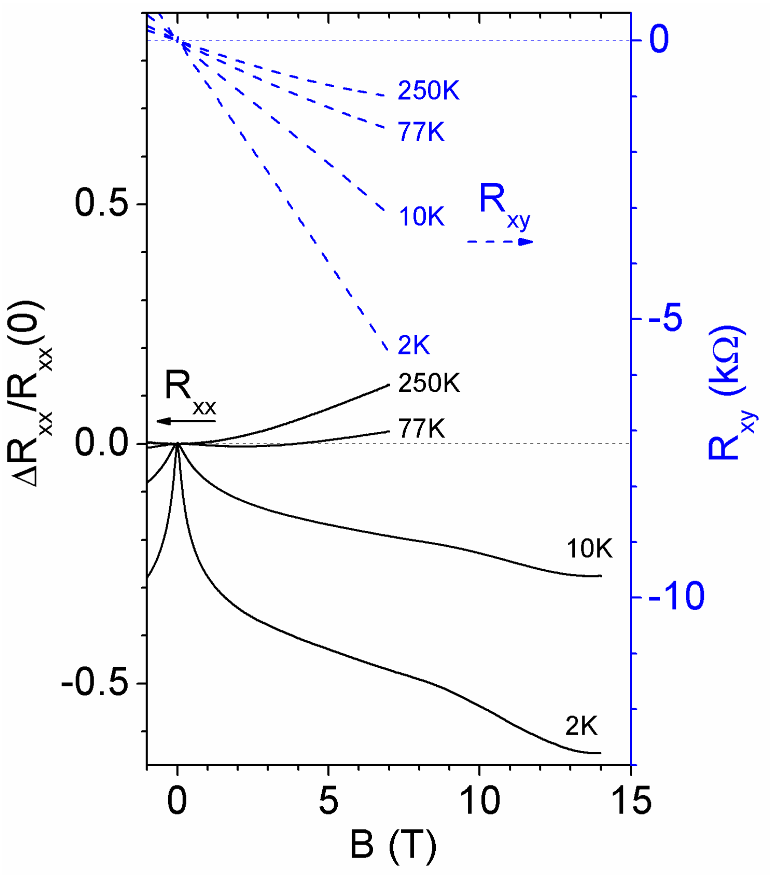

Figure 5.11. Transverse Hall resistance (R_{xy}, blue upper) and longitudinal magnetoresistance ($\Delta R_{xx}(B)/R_{xx}(0) = [R_{xx}(B) - R_{xx}(0)]/R_{xx}(0)$, black lower) as a function of magnetic field B at various temperatures. Reprinted with permission from [111]. Copyright 2014 American Institute of Physics.

[159]. A similar low temperature $T^{0.5}$ dependence has been observed for epitaxial films of the Full Heuslers Ni_2MnX [160].

Further information about the low temperature scattering mechanisms is obtained by examination of the magnetoresistance (Figure 5.11, solid curves). At 250 K the magnetoresistance shows a nearly quadratic dependence on magnetic field as expected for a diamagnetic semiconductor. However at 77 K the low field (< 2 T) magnetoresistance is negative and shows a peak at zero field before reverting to the quadratic dependence at higher fields (> 2 T). With decreasing temperature the magnitude of this zero field peak increases and its width broadens such that at 2 K the magnetoresistance at 14 T is -65%. This zero field peak is consistent with localization [161], suggesting that at low temperatures the transport is governed by hopping rather than activation across the bandgap.

The large magnetoresistance at 2 K suggests that localization may result from magnetic polarons. While the 18 valence electron CoTiSb is expected to be a diamagnetic semiconductor, it sits between Half Heuslers with 17 or 19 valence electrons, which are typically ferromagnetic metals, e.g. the 17 valence electron CoTiSn [6]. Defects or slight deviations from stoichiometry may change the effective electron count and produce local magnetic domains at low temperature, potentially producing bound magnetic polarons [162]. However, initial SQUID magnetometry measurements were unable to detect a magnetic signal beyond the diamagnetic background of the InP substrate. Further magnetometry measurements on thicker films are required, and higher magnetic field temperature dependent magnetotransport measurements would give additional insight in the origins for the magnetoresistance peak.

Despite the anomalous low temperature behavior, the room temperature transport properties of the MBE grown CoTiSb films compare favorably with 18 valence electron Half Heuslers in the literature. Figure 5.12 shows the room temperature (300 K) Hall mobility versus carrier density for a number of MBE grown CoTiSb films (filled red squares). For comparison literature values for a number of semiconducting Half Heusler compounds and for bulk Si are also included (open black squares) [110, 136, 137, 138, 139, 140, 141, 143]. Unless otherwise noted, the literature data points are for bulk

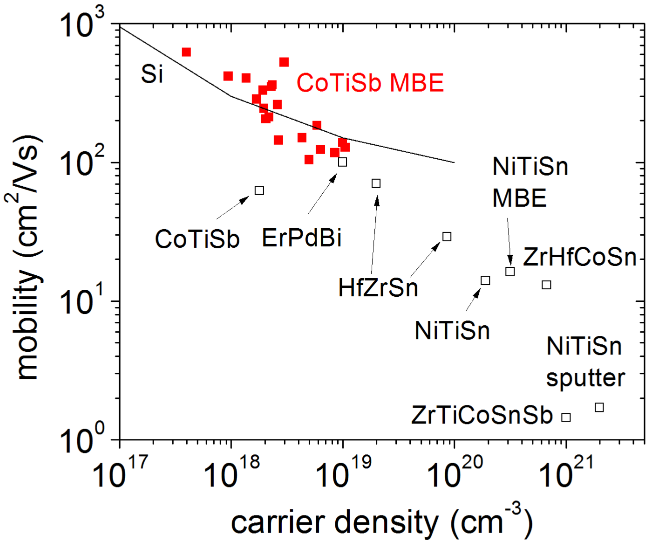

Figure 5.12. Room temperature (300 K) mobility and carrier density of CoTiSb on InAlAs/InP(001) (filled red squares) compared to Half Heuslers in the literature with predicted bandgap > 100 meV (open squares, CoTiSb [136], ErPdBi [137], ZrNiSn [138, 139], NiTiSn [139], ZrHfCoSn [140], ZrTiCoSnSb [140], NiTiSn sputter [143], and NiTiSn MBE [110]) and silicon [141]. Unless otherwise noted, the samples in the literature are bulk. Reprinted with permission from [111]. Copyright 2014 American Institute of Physics.

samples. The mobilities and carrier densities for the MBE-grown CoTiSb films are the highest ($\mu_H = 530$ cm^2/Vs) and lowest ($n_H = 9.0 \times 10^{17}$ cm^{-3}), respectively, reported for Half Heuslers with a predicted finite bandgap (> 50 meV). Surprisingly, the mobility is comparable to that of Si for the same carrier density (solid line), indicating the high quality of the MBE-grown films on InP(001) substrates.

5.3.2 NiTiSn

Figure 5.13 shows temperature dependent transport measurements for a 25 nm NiTiSn film grown on MgO at 450 °C. This sample was capped with 5 nm MgO by electron beam deposition in order to protect the NiTiSn surface from oxidation. Hall effect measurements were performed in a van der Pauw gemoetry using annealed indium contacts.

The room temperature (300 K) resistivity of 1.22 mΩcm is comparable to the 0.5-3.0 mΩcm resistivities observed for bulk single crystalline and sputtered thin film NiTiSn [16, 138, 143]. In the range of 10 to 220 K the resistivity decreases with increasing temperature, suggesting semiconducting-like transport. Alternatively this temperature dependent could result from localization of a disordered metal [163]. The magnitude of change is very small, but is comparable to measurements of sputtered NiTiSn films [143]. At higher temperatures ($>$ 220 K) the resistivity increases with temperature, suggesting metallic or semimetallic conduction.

For all temperatures measured the Hall Voltage was linear and had negative slope with magnetic field out to 0.6 T, suggesting a single n-type carrier dominated transport. Assuming this single carrier, at 300K the carrier density is $n = 3.2 \times 10^{20}$ cm^{-3} and the mobility is $\mu = 16$ cm^2/Vs, which is an improvement over sputtered NiTiSn films with density and mobility of $n = 2.0 \times 10^{21}$ cm^{-3} and $\mu = 1.7$ cm^2/Vs [143]. However, while the mobility is comparable to the 20-70 cm^2/Vs mobilities observed for the best bulk samples, the carrier density is still about an order of magnitude higher than for the bulk samples [16, 138]. With varying temperature, the carrier density increases weakly from thermal activation and the mobility decreases with acoustic phonon scattering.

5.4 Conclusions

In summary we have demonstrated the first MBE growth of the semiconducting Half Heusler compounds CoTiSb and NiTiSn. These films were grown on InAlAs/InP(001)

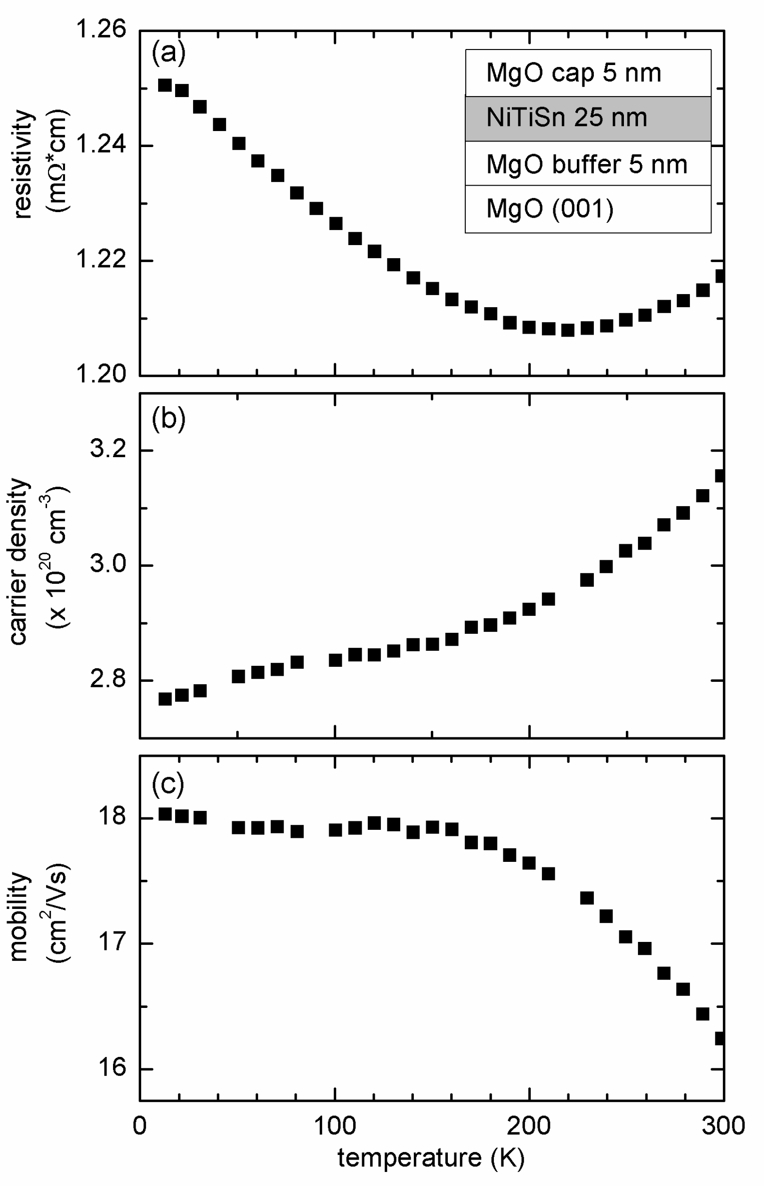

Figure 5.13. Temperature dependent resistivity, carrier density, and electron mobility for a 25 nm NiTiSn on MgO(001) sample with a 5 nm MgO cap. Reprinted with permission from [110]. Copyright 2013 American Institute of Physics.

and MgO(001) respectively. The films are epitaxial and single crystalline as observed by RHEED and XRD, and grow in a layer-by-layer mode with a well ordered (2×1) surface reconstruction. Temperature dependent magnetotransport measurements indicate that both CoTiSb and NiTiSn films are n-type and have semiconducting-like temperature dependence on resistivity. For the CoTiSb films, the electron mobility and background carrier density are the highest and lowest yet reported for any Half Heusler with finite bandgap, and have similar mobility as n-type Si with similar density. At low temperature the CoTiSb films show a large negative magnetoresistance with a peak at zero field that may be due to localization or magnetic polarons. Further magnetometry and magnetotransport measurements at higher fields are aimed at understanding the low temperature behavior.

The NiTiSn films also show semiconducting-like transport, but have higher background carrier densities and lower mobility than the CoTiSb films. This may be due in part to the higher quality of the InAlAs/InP buffer layers used for CoTiSb, which were grown by MBE, than the MgO buffer layers used for NiTiSn, which were grown by electron beam evaporation. These MBE-grown NiTiSn films show higher mobility and lower density than their counterparts grown by sputtering, but lower mobility and higher density than the best bulk NiTiSn grown by the flux method.

Initial studies suggest that it is possible to grow CoTiSb in an Sb adsorption limited regime, but more systematic studies of the composition versus growth temperature and Sb overpressure are required. Unfortunately due to the low volatility of Sn, a similar adsorption limited regime for NiTiSn growth could not be identified. Additionally, while we were able to grow CoTiSb directly on InAlAs buffer layers using a colder initiation layer, it was not possible to grow NiTiSn directly on InAlAs or InGaAs without substantial interfacial reactions. This is presumably due to the high reactivity of Ni with III-Vs. For this reason, all NiTiSn growths used an ErAs diffusion barrier between the NiTiSn and InAlAs, or were performed on MgO substrates.

Growth of these compounds with well ordered surfaces opens the door to detailed surface studies of Half Heuslers as well as measurements of the **k**-resolved electronic structure. These topics of will be the subject of the next two chapters.

Chapter 6

Half Heusler Surfaces

6.1 Why surfaces

Surfaces play a critical role for growth, properties, and device applications.[1] In general the breaking of bonds at the surface will cause surfaces to relax in the case of metals, or reconstruct in the case of semiconductors. Hence the atomic structure at surfaces can be very different than in the bulk, and so too can the resulting electronic structure [164, 165].

As with surface electronic states on conventional semiconductors, for Heuslers sometimes these surface states are highly undesirable. For example, while the Half Heusler NiMnSb and Full Heusler Co_2MnSi are expected to be a half metallic ferromagnets in the bulk with 100% spin polarization, in real samples there is a significant reduction of

---

[1] Some of the work presented in this chapter has previously appeared in the following publications: [110].

the spin polarization at the surfaces and interfaces due to surface/interface states in the minority spin gap [166, 167, 168]. In other cases surface states are desirable. For example, theory predicts that some Half Heuslers are topological insulators in which there exists a bandgap for the bulk but topologically protected metallic states at the surfaces [11, 12]. These metallic surface states have the unique property that they are immune to backscattering and have a number proposed applications, e.g. in fault tolerant quantum computing [38]. But just as for the conventional surface states, the dispersions of topological states can be sensitive to the particular surface termination [169, 170] and can even hybridize with conventional dangling bond-like surface states [171]. Therefore in order to realize and use the properties of Heuslers in devices, it is critical to both understand and control their surface atomic and electric structures.

Due to their unusual bonding character, the Half Heuslers also provide a unique system in which to explore surface reconstructions and their effect on surface electronic structure. Within the Half Heusler crystal structure, the XZ zincblende sublattice has strong covalent character [112], and due to the strong directionality of covalent bonds, covalently bonded solids are often expected to reconstruct at their surfaces. Examples of reconstructed covalent surfaces are the (001) surfaces of III-V compound semiconductor, which typically form zincblende or wurtzite lattices. The driving force for reconstruction in the III-Vs is the minimization of dangling bonds (and hence dimerization), and these surface have been well described by surface electron counting models [165]. But one complication for Half Heuslers is that instead of the simple sp^3 bonding found in the wurtzite and zincblende compound semiconductors, the Half Heuslers also have d-d and p-d hybridization [114].

In addition to the covalent bonding, the Half Heusler structure contains ionic character in Y element that "stuffs" the crystal to form a rocksalt YZ sublattice [112]. Due to the long range, non-directional nature of the Coulomb interaction, ionically bonded solids typically do not reconstruct at their surfaces and instead only show a weak relaxation. Here the driving force is a minimization of Coulomb forces [172]. For Half Heuslers, in which there exists a mixture of strong covalent and ionic bonding, the mechanisms for surface reconstruction remain unclear.

In this chapter we experimentally and theoretically study the CoTiSb and NiTiSn (001) surfaces as model systems for understanding surface reconstructions and electronic bandstructure in the Half Heusler compounds. CoTiSb and NiTiSn are chosen because they are prototypical semiconducting Half Heuslers (already studied widely for their thermoelectric properties [173]) with fairly large calculated bandgaps of approximately 1 eV and 0.5 eV respectively (indirect, calculated by DFT-GGA [146]). Both are diamagnetic and topologically trivial, enabling a detailed study of "conventional" surface states before considering the spin splitting or more complicated topological states of half metals and topological insulators. Note that topological insulator Half Heuslers may be considered a subset of the semiconducting Half Heuslers in which there is sufficiently large spin orbit coupling to create band inversion [167, 168].

One challenge in surface science that once clean, well ordered surfaces are grown, they must be kept clean and well ordered for measurements. To this end, most of the experiments in this chapter were performed in an interconnected growth and surface analysis system such that samples can be transferred from the growth chamber to analysis chambers (LEED, STM, XPS) without being removed from ultrahigh vacuum. However, for higher resolution photoemission studies synchrotron light was required, and hence samples needed to be removed from vacuum and transported to a separate synchrotron facility in Lund, Sweden. Therefor, this chapter also explores capping and decapping schemes to protect CoTiSb(001) and NiTiSn(001) surfaces such that synchrotron photoemission measurements can be performed.

6.2 Bonding and crystal structure at (001) Half Heusler surfaces

Bulk CoTiSb adopts the Half Heusler $C1_b$ crystal structure (space group $F\bar{4}3m$, lattice constant $a = 5.88$ Å) in which Sb and Ti form a rocksalt sublattice [positions (0,0,0) and (1/2, 0, 0)] and Co fills half of the doubly tetrahedrally coordinated interstitials (1/4, 1/4, 1/4). A vacancy sublattice resides at the other tetrahedral interstitials (3/4, 1/4, 1/4). This structure may be alternatively described as a CoSb zincblende sublattice with Ti "stuffed" at the (1/2, 0, 0) sites. The (001) orientation of this crystal consists of alternating planes of 1 monolayer (ML) Co and 1 ML each Ti and Sb (Figure 6.1), where 1 ML is defined as $2/a^2 = 5.78 \times 10^{14}$ atoms/cm^2 and the spacing between layers is $a/4 = 1.47$ Å. Hence a (001) truncated crystal surface is expected to be either Co or Ti-Sb terminated.

CoTiSb grows on InAlAs/InP(001) (lattice constant 5.86 Å) with a cube-on-cube epitaxial relationship, and across the CoTiSb/InAlAs interface the face centered sublattice of group-V atoms (As, Sb) is expected to be continuous. Hence for a Ti-Sb terminated surface, the Sb back-bonds to Co are expected to project along [110] and the Sb dangling bonds at the surface along [-110]. Figure 6.1 shows a schematic of the CoTiSb surface with TiSb termination, in which all atomic positions have been fixed to their bulk positions. However, for a real surface the positions of the atoms in the top most layers are expected to relax or reconstruct.

NiTiSn in the (001) orientation can similarly be viewed as alternating planes of Ni and TiSn. Ni occupies the (1/4, 1/4, 1/4) positions, while Sn and Ti occupy (0,0,0) and (1/2, 0, 0) respectively. The lattice constant is $a = 5.92$ Å. When grown on MgO(001) or ErAs/InGaAs/InP(001), since both ErAs and MgO have 4-fold rotational symmetry while NiTiSn has 2-fold symmetry, mixed domains of NiTiSn appear that are rotated by 90 degrees with respect to one another.

6.3 CoTiSb(001) surfaces

Samples were grown by MBE on sulfur doped InP (001) substrates and consist of a 400 nm $In_{0.52}Al_{0.48}As$ lattice matched buffer layer followed by a 20-40 nm CoTiSb layer. The InAlAs layer was doped with approximately 5×10^{18} Si atoms/cm^3 to yield a conductive buffer for STM and photoemsission spectroscopy measurements. On some samples a 3 nm ErAs diffusion barrier was grown between the CoTiSb and InAlAs layer to prevent interfacial reactions between the CoTiSb and InAlAs and to enable higher

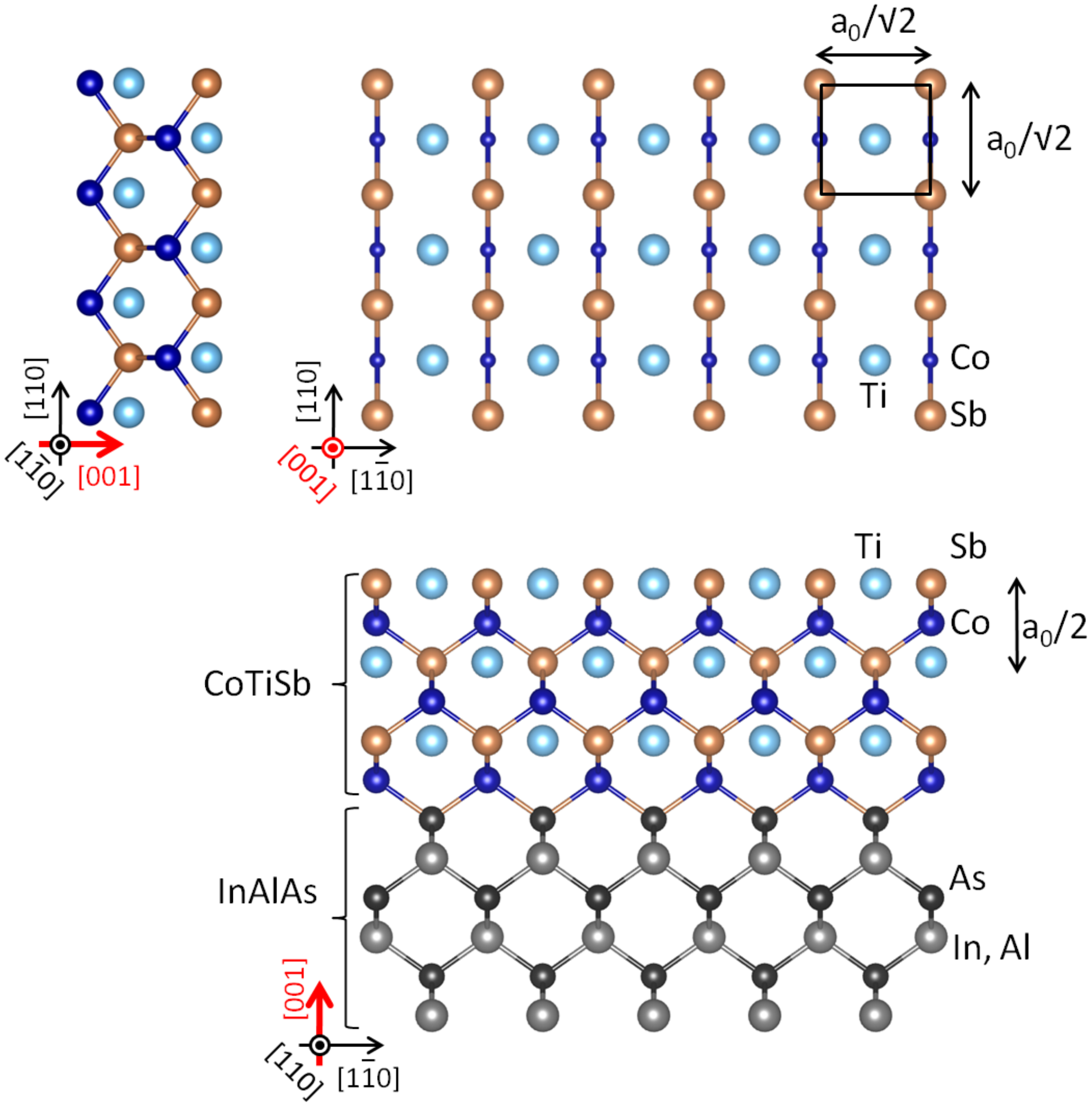

Figure 6.1. Crystal structure of bulk-terminated CoTiSb (001). The main panel shows a plan view image looking down on the (001) surface, with a (1 × 1) surface unit cell outlined. The bottom shows a cross section looking along a [110] zone axis and the left shows a cross section along a [1-10] zone axis. The (001) oriented CoTiSb consists of alternating planes of Co and TiSb.

annealing temperatures. Further growth details are provided in Chapter 5.

After growth the Co and Ti effusion cells were shuttered and the samples were annealed at various temperatures with and without an impinging Sb flux. Sb was chosen because among the constituent elements Co, Ti, and Sb, Sb is the most volatile and it is also possible to grow stoichiometric CoTiSb films using a slight excess of Sb in an adsorption-limited regime, similar to the way III-V semiconductors are grown by MBE. Following the anneal, the Sb cell was shuttered and the samples rapidly quenched to room temperature while observing the RHEED pattern in order to retain the desired surface reconstruction. Samples were then characterized in situ by low energy electron diffraction (LEED), X-ray photoelectron spectroscopy (XPS, Al $K\alpha$ source), and scanning tunneling microscopy/spectroscopy (STM/STS) in an interconnected MBE-surface analysis system such that growth and characterization were performed without removing samples from ultrahigh vacuum ($< 2 \times 10^{-10}$ mbar). Samples were also characterized by high resolution photoemission spectroscopy (beamline I311) at the MAX-Lab Synchrotron facility in Lund, Sweden, using an Sb capping scheme to protect the sample surfaces. All binding energies are referenced to the Fermi level as determined by measuring the Fermi level of a tantalum or gold foil that is in electrical contract with the sample.

6.3.1 RHEED and LEED: periodicity of the reconstructions

During growth the CoTiSb(001) surface exhibits a (2×1) surface reconstruction, which has also been observed for the Half Heuslers NiTiSn and NiMnSb [110, 148, 174].

But upon post-growth annealing as a function of temperature and Sb flux two additional surface reconstructions are observed (Figure 6.2). In order of decreasing Sb flux (or increasing anneal temperature), the reconstructions follow the progression $(1 \times 4) \rightarrow (2 \times 1) \rightarrow c(2 \times 4)$. The corresponding RHEED and LEED patterns are shown in Figures 6.2 (a-c), (d-f), and (e-g), respectively, along with a reconstruction phase diagram in (j). At very low temperatures an Sb cap begins to deposit on the surface as evidenced by a spotty (1×1) pattern.

Transitions between the Sb cap $\leftrightarrow (1 \times 4)$ are reversible, indicating that Sb capping may be a method for protecting sample surfaces for *ex situ* photoemission spectroscopy measurements (more on Sb capping in the next section). Additionally the $(1 \times 4) \leftrightarrow (2 \times 1)$ transition is reversible. However, the $(2 \times 1) \rightarrow c(2 \times 4)$ transition has only been observed in one direction (upon heating) suggesting that the (2×1) reconstruction may be metastable. Note we also observe a $(2 \times 1) \rightarrow c(2 \times 4)$ transition for high temperature anneals (> 500°C) of NiTiSn on MgO(001).

To investigate which species (e.g. Co or Ti-Sb) are terminating for each reconstruction, we start with a (2×1) surface and monitor changes in the RHEED pattern as we expose the surface to atomic fluxes of Co, Ti or Sb at a rate of 3.0×10^{16} atoms/(cm^2*hr). The results are shown in Figure 6.2(k), where we plot the intensity of the 1/2 order diffraction streak (which gives the 2× periodicity) normalized to the intensity of the 1st order diffraction streak when viewed along the [110] azimuth [see Figure 6.2(d) for indices]. This is performed at two different temperatures: the closed symbols are for depositions at 410 °C and the open symbols are for deposition at 460 °C. For exposure to Ti at both

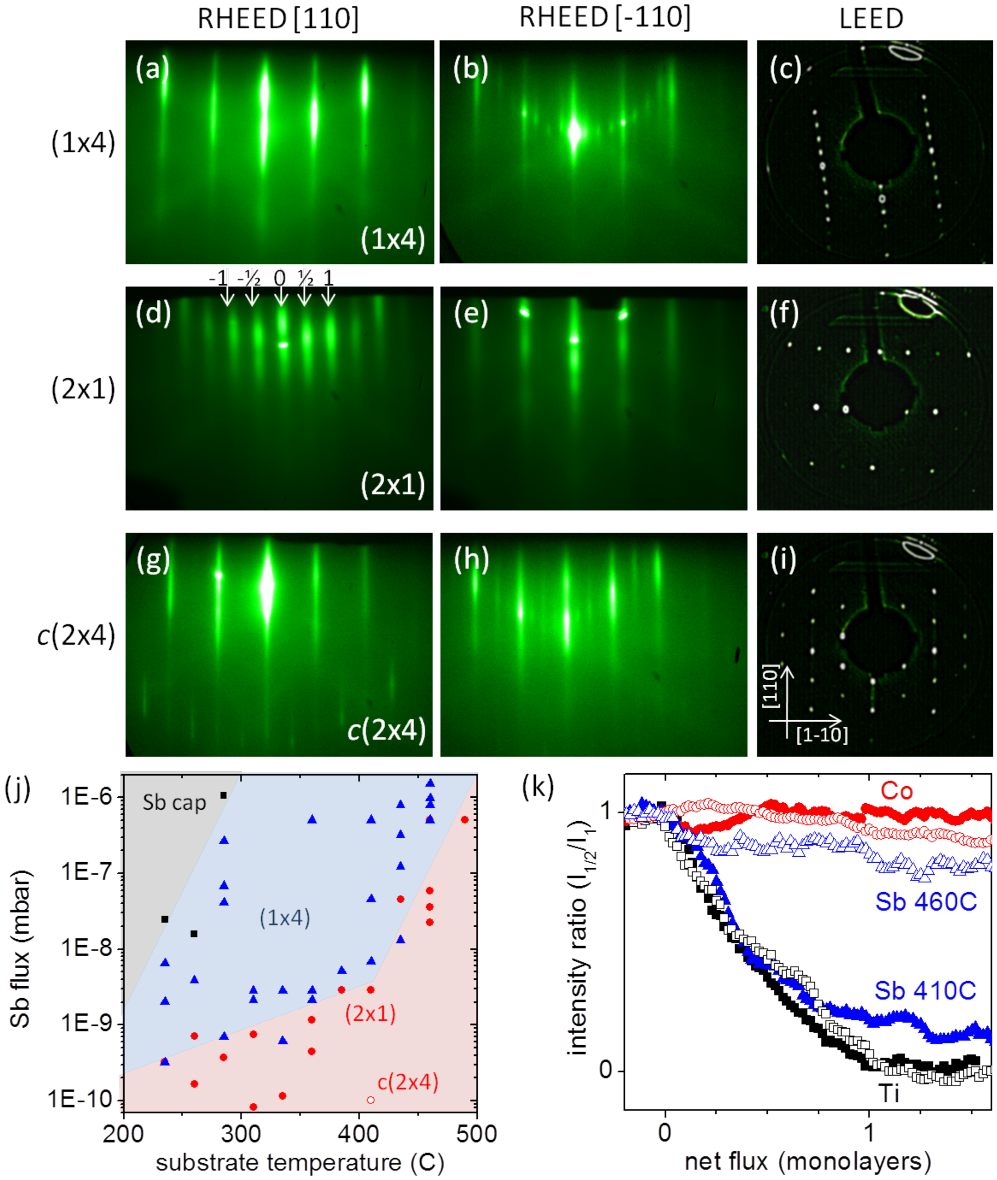

Figure 6.2. Reflection high energy electron diffraction (RHEED) and low energy electron diffraction (LEED) for three different surface reconstructions of CoTiSb on InAlAs/InP(001): (a-c) the Sb-rich (1×4), (d-e) the as-grown (2×1), and (g-i) the high temperature $c(2 \times 4)$. (j) Surface reconstruction phase diagram as a function of anneal temperature and Sb flux. (k) Normalized intensity ratio of the 1/2 order streak to the 1 order streak upon exposure of the (2×1) surface to fractional coverages of Co, Ti, or Sb at 410 °C (closed symbols) and at 460 °C (open symbols).

410 and 460 °C, the intensity of the 1/2 order diffraction streak fades away and a streaky (1×1) pattern is obtained after a net flux of 1 ML Ti. Hence the (2×1) is unstable for excess Ti. For deposition of Co at both 410 and 460 °C the (2×1) pattern is retained for up to 1 ML excess Co, but a (1×1) pattern of spots begins to form superimposed on the streaky (2×1) pattern, indicating the formation of Co islands. Hence the (2×1) is likely not Co terminated either. Finally for Sb deposition, exposure at 460 °C retains the (2×1) reconstruction even for continued flux well beyond tens of monolayers. This suggests the surface is Sb stabilized and that at 460 °C an equilibrium between Sb adsorption and desorption is reached and the (2×1) remains stable. For Sb deposition at 410 °C the RHEED pattern fully changes from a (2×1) to a streaky (1×4) after 1-2 ML net flux and retains a stable (1×4) pattern indefinitely.

Performing the same experiment for the binary combinations, we find that CoTi exposure produces a (1×1) pattern, CoSb produces a (2×1), and TiSb produces a (2×1). These findings suggest that the CoTiSb (2×1) surface is Ti-Sb terminated but may have a slight deficiency in Ti. This Ti-Sb or Sb termination is consistent with the Mn-Sb termination that has been suggested for NiMnSb [148, 168] and the Mn-Ga termination that has been observed for the Full Heusler Ni_2MnGa [175].

More generally, the strong dependence of CoTiSb (001) surface reconstruction on Sb flux and anneal temperature is similar to the dependence observed for conventional III-V compound semiconductor surfaces, e.g. GaAs and GaSb (001). Given the strong structural similarities between the III-V semiconductors, which typically adopt a zincblende lattice, and the Half Heusler, in which two of the constituents form a zincblende sublattice, these findings suggest that the mechanisms for surface reconstructions in Half Heuslers may also be similar to that of III-Vs. For example, the CoTiSb (1×4) produced during Sb-rich conditions may result from an ad-layer of Sb on the surface, analogous to the fractional monolayer of As that characterizes the GaAs(001)-$c(4 \times 4)$ surface [176]. The amount of excess Sb on the (1×4) is estimated to be on the order of 1 ML because at 410 °C the (2×1) surface changes to the (1×4) upon exposure to a net flux of 1-2 ML Sb [Figure 6.2(k)]. Other reconstructions such as the (2×1) and $c(2 \times 4)$ may result from Sb dimerization at the surface in order to minimize the number of dangling bonds and satisfy electron counting and charge neutrality, analogous to the As dimerization observed for the GaAs(001)-(2×4) [165].

6.3.2 XPS: bonding and stoichiometry

To investigate composition and bonding at the surface for the various reconstructions, core levels were measured by photoemission spectroscopy. Figures 6.3(a-c) show the Co 2p, Ti 2p, and Sb 3d core levels for the (1×4), (2×1), and $c(2 \times 4)$ surfaces measured *in-situ* using Al $K\alpha$ radiation ($h\nu = 1486.7$ eV). In order to minimize sample preparation variations and ensure that the composition of underlying "bulk-like" CoTiSb remained constant, the same sample was used for both (1×4) and (2×1) measurements, with the (2×1) produced by subsequent annealing of the (1×4). Similarly the same sample was used for both (2×1) and $c(2 \times 4)$ measurements, with the $c(2 \times 4)$ produced by subsequent annealing of the (2×1). All core level intensities are normalized to the Co 2p for each reconstruction.

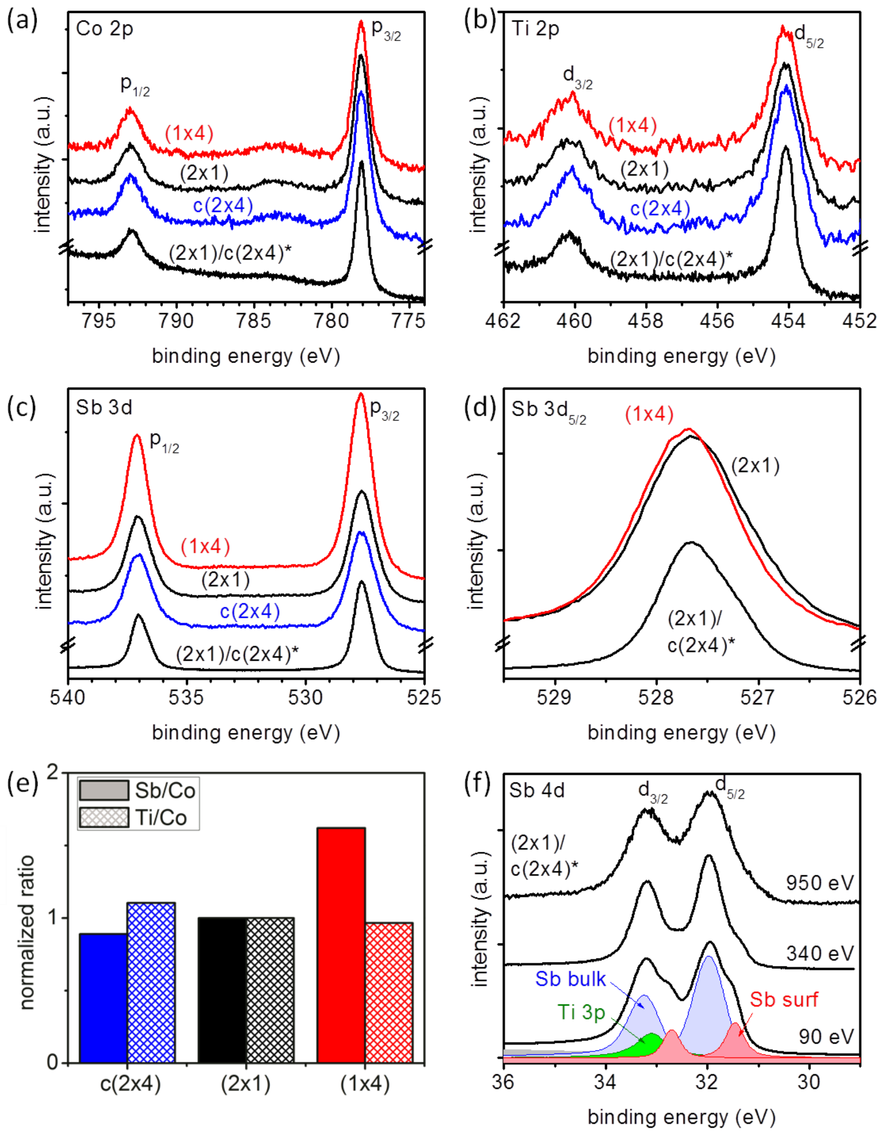

Figure 6.3. (a-c) XPS core levels for the various reconstructions of CoTiSb(001). All intensities are normalized to the Co 2p. The upper curves for the (1×4) (red), (2×1) (black), and $c(2\times4)$ (blue) were measured in situ using an Al $K\alpha$ source. The lower curves denoted with an asterisk (*) were measured on a mixed $(2\times1)/c(2\times4)$ surface using synchrotron light at energies 905, 575, and 650 eV for the Co 2p, Ti 2p, and Sb 3d respectively. (d) Magnified view of the Sb $3d_{5/2}$ component from (c), with the (1×4) and (2×1) rescaled to the same intensity to highlight changes in bonding components. (e) Sb/Co and Ti/Co core level intensity ratios for the three surface reconstructions, showing the changes in composition relative to the (2×1). The normalized intensity ratios are given by $\frac{I^X/I^{Co2p}_{(n\times m)}}{I^X/I^{Co2p}_{(2\times1)}}$. (f) Sb 4d core level of the $(2\times1)/c(2\times4)$ reconstruction measured using synchrotron light at various incident photon energies.

Stoichiometry of the (1×4) and (2×1)

We first compare the core levels for the (1×4) and (2×1) reconstructions. In Figure 6.3(a), the main peaks at binding energies of 778 and 792 eV are the spin-orbit split Co $2p_{3/2}$ and $2p_{1/2}$ components respectively. The broad peak shifted to 5 eV higher binding energy from the Co $2p_{3/2}$ is a commonly observed satellite that has been attributed to a 2 core hole final state [40, 177]. The shapes of the Co 2p core levels for the (1×4) and (2×1) surfaces are indistinguishable to the limits of our experimental resolution ($\approx$ 700 meV), indicating similar bonding components. Similarly, in Figure 3(b) the shapes of the Ti $2p_{3/2}$ and $2p_{1/2}$ core levels for the (1×4) and (2×1) are indistinguishable, indicating similar Ti bonding environments for the two surfaces. Additionally, the normalized Ti 2p intensities are also nearly equal, indicating a similar surface Ti to Co composition ratio for the (1×4) and (2×1) reconstructions.

However, the Sb 3d core level for the (1×4) reconstruction shows a roughly 60% larger intensity than the (2×1) [Figure 3(c)], indicating a higher concentration of surface Sb. Furthermore, the Sb 3d for the (1×4) shows a small component shifted by 0.1-0.2 eV to a higher binding energy [Figure 6.3(d)], consistent with an Sb ad-layer on the surface [176].

For quantitative analysis of the compositions, the integrated intensities of the core levels are plotted in Figure 6.3(e), where we show the Sb3d/Co2p and Ti2p/Co2p integrated intensity ratios for the (1×4), (2×1), and $c(2 \times 4)$ reconstructions. Here each intensity ratio has been normalized to the same intensity ratio for the (2×1) reconstruction, i.e. $\frac{I^X/I^{Co2p}_{(n\times m)}}{I^X/I^{Co2p}_{(2\times 1)}}$ for X = Co 2p, Ti 2p, or Sb 3d. This method of normalization removes the kinetic energy dependent instrument factors. Fitting the integrated core level intensities to an atomic layer attenuation model (see Appendix), these results suggest that the (1×4) surface is covered with an excess ad-layer of Sb on the order of 1.5 ML, comparable to the 1 ML suggested by RHEED from the $(1 \times 4) \rightarrow (2 \times 1)$ transition [Figure 6.2(k)].

Bonding in the (2×1) and $c(2 \times 4)$

Comparing the (2×1) and $c(2 \times 4)$ reconstructions in Figures 6.3(a-c), to the limits of our resolution the shapes of the Co 2p, Ti 2p, and Sb 3d core levels are not distinguishable for these two reconstructions, indicating similar surface bonding components. Additionally the relative intensities of the core levels do not change significantly [approximately 10% increased Ti/Co and 10% decreased Sb/Co for the $c(2 \times 4)$, Figure 6.3(e)], indicating that the surface compositions of these two reconstructions is similar. These findings suggest that the differences between the (2×1) and $c(2 \times 4)$ reconstructions are primarily configurational rather than due to differences in stoichiometry.

To gain further information about the bonding in the (2×1) and $c(2 \times 4)$ reconstructions, higher resolution core levels for a sample with mixed domains of (2×1) and $c(2 \times 4)$ were measured using synchrotron light. Upon reloading an Sb-capped CoTiSb sample into vacuum at beamline I311 of the MAX-Lab Synchrotron facility, this surface was prepared by annealing at 400 °C until the Sb cap desorbed and a $(2 \times 1)/c(2 \times 4)$ LEED pattern appeared. Figures 6.3(a-c) (lower black) show the Co 2p, Ti 2p, and Sb 3d core levels after removal of the Sb cap, using incident photon energies of 905, 575, and 650 eV respectively (corresponding to kinetic energies of 110-130 eV). The peak shapes are comparable to those measured in-situ in the lab source XPS (upper curves) and no oxide peaks or components are present, demonstrating that the Sb cap successfully protected the sample surface.

Depth dependent bonding components were determined by measuring core levels as a function of incident photon energy. Figure 6.3(f) shows the Sb 4d core level for the $(2\times1)/c(2\times4)$ surface measured at photon energies of 950 eV (bulk like, mean free path > 1 nm), 340 eV, and 90 eV (surface sensitive, mean free path ≈ 3 Å). At $h\nu = 950$ eV we observe two peaks at 31.9 and 33.2 eV, which are the spin-orbit split $d_{5/2}$ and $d_{3/2}$ components. As the incident photon energy is decreased, a secondary set of components at lower binding energy appears and gains intensity as the measurement becomes more sensitive to the surface. This lower binding energy component is consistent with Sb-Sb dimerization at the surface [178] and is also observed in the Sb 3d core level for the $(2\times1)/c(2\times4)$ measured using synchrotron light and for the Sb 3d of the (2×1) measured in situ using Al $K\alpha$ [Figure 6.3(e)]. Furthermore, no depth dependent bonding components were observed for the Co 2p (measured using $h\nu = 905$ to 1085 eV) or Ti 2p core levels ($h\nu = 575$ to 755 eV). These findings suggest Sb-Sb dimerization at the CoTiSb (2×1) and $c(2\times4)$ surfaces, similar to the As-As dimerization on the GaAs(001)-(2×4) surface.

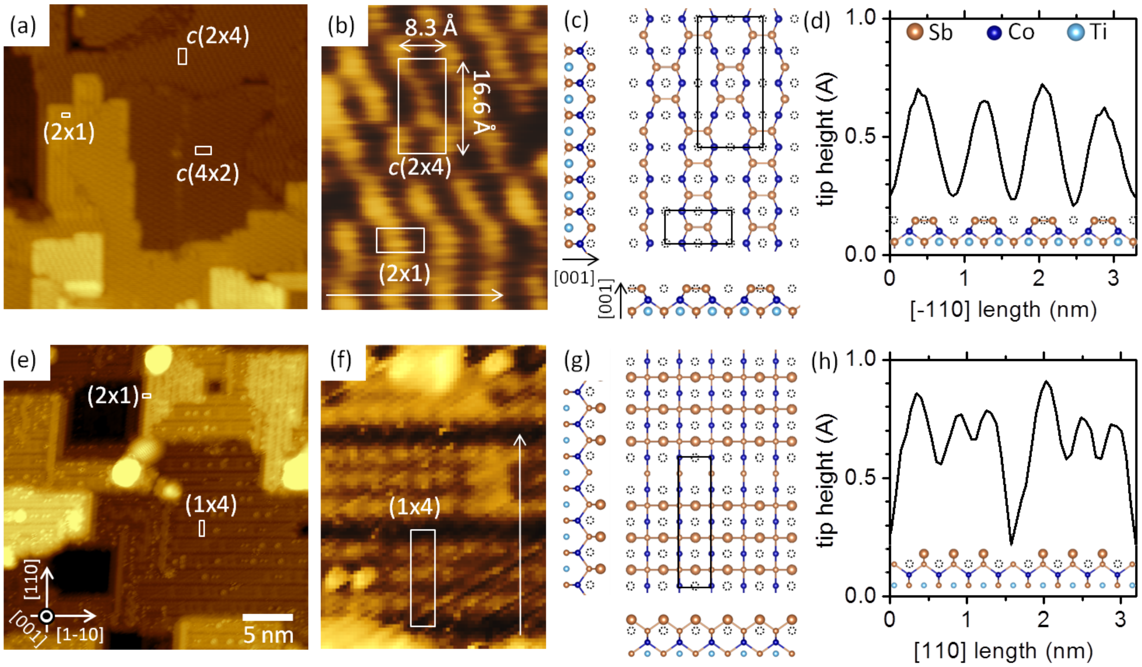

Figure 6.4. Filled states STM images, structure models, and tip height profiles for (a-d) the (2×1) and $c(2 \times 4)$ reconstructions and (e-h) the (1×4) reconstruction.

6.3.3 STM and surface reconstruction models

In order to visualize the surface reconstructions in real space, in-situ room temperature STM measurements were performed on each of the reconstructions. Figure 6.4(a) shows a 30×30 nm filled states STM image of a $(2 \times 1)/c(2 \times 4)$ terminated CoTiSb film grown on ErAs/InAlAs/InP. Since ErAs is 4-fold rotationally symmetric, mixed rotational domains of both $(2 \times 1)/(1 \times 2)$ and $c(2 \times 4)/c(4 \times 2)$ are observed where the (1×2) and $c(4 \times 2)$ are rotated from the (2×1) and $c(2 \times 4)$ respectively by 90 degrees. A number of steps are observed on this surface, each with a height of 2.9 Å $=$ $a/2$, which corresponds to the spacing between Ti-Sb/Ti-Sb planes (Figure 6.1). All step edges are $\langle 110 \rangle$ type and are predominantly (2×1) terminated, suggesting that (2×1) edge terminations are energetically more favorable than $c(2 \times 4)$ edge terminations.

Figure 6.4(b) shows a magnified filled states STM image in which both $c(2 \times 4)$ and (2×1) unit cells are resolved. No clear dependence on sample biases in the range -1.5 to +1.5 V was observed. Both reconstructions are characterized by clusters with a periodicity of 8.3 Å along [-110], or twice the bulk-spaced unit cell, which are the length and direction expected for surface Sb dimers (Figure 6.1). Additionally, there is no step height variation between the two domains.

We briefly summarize the experimental observations of the (2×1) and $c(2 \times 4)$ surfaces from the previous sections: these two reconstructions are the as-grown and high temperature annealed reconstructions of CoTiSb(001). From studies of explicit surface terminations monitored by RHEED [Figure 6.2(k)], they are nominally Ti-Sb terminated but may be deficient in surface Ti. Core level photoemission measurements suggest these two reconstructions have nominally the same surface stoichiometry and bonding components (Figure 6.3), and hence the differences between the two are primarily configurational. Higher resolution photoemission measurements suggest surface Sb-Sb dimerization.

Based upon these findings we propose models for the (2×1) and $c(2 \times 4)$ surface reconstructions in Figure 6.4(c). The models are consistent with all experimental data and are characterized by Sb dimers, where the Sb dimer bonds are oriented along [-110]. The (2×1) consists of rows of dimers oriented along the [110] direction, while the $c(2 \times 4)$ consists of a checkerboard pattern of dimers. The amount of Ti at the surface is not clear, but initial DFT calculations suggest Sb-dimerization is stable for a slightly Ti-deficient surface, while a stoichiometric TiSb surface would not dimerize and instead retain a

(1×1) surface unit cell (courtesy of A. Roy and A. Janotti). Since the exact surface Ti occupancy is unclear, surface Ti is denoted by dashed open circles. Figure 6.4(d) shows a measured tip height profile for the (2×1) reconstruction along [-110], showing good agreement with the model.

One can understand this Sb dimerization and subsequent Ti deficiency in terms of electron counting. In the simplest picture of Half Heusler bonding, Ti donates its electrons to Co and Sb to attain a d^0 configuration. Here, Sb has a fully occupied s^2p^6 configuration with sp^3-like bonding while the Co d is completely filled with d^{10} configuration [112, 122, 123]. Energetically, the surface would favor Sb-Sb dimerization in order to minimize the number of Sb dangling bonds. However the creation of Sb dimers would lead to excess electrons at the surface (2 electrons excess per sp^3-sp^3 dimer). This excess of electrons can be accommodated by simply removing some of the Ti from the surface layer.

Room temperature STM measurements were also performed on the (1×4) surface [Figure 6.4(e)]. This sample was grown directly on InAlAs/InP(001) and hence no 90 degree rotational domains are observed. In addition to the (1×4), small domains of the (2×1) reconstruction are also observed primarily at [110] step edges, suggesting that (2×1) termination at [110] edges may be energetically more favorable. Steps between two (1×4) regions have height of 2.9 Å $= a/2$, just as observed for steps on the $(2 \times 1)/c(2 \times 4)$ surface. However, the height difference between the (1×4) and (2×1) domains is 1.5 Å $= a/4$ (Figure 6.5), consistent with the height expected for an ad-layer of Sb. Figure 6.4(f) shows a magnified filled states image of a (1×4) region. The (1×4) unit cell is characterized by three atoms oriented along [110] followed by a trench.

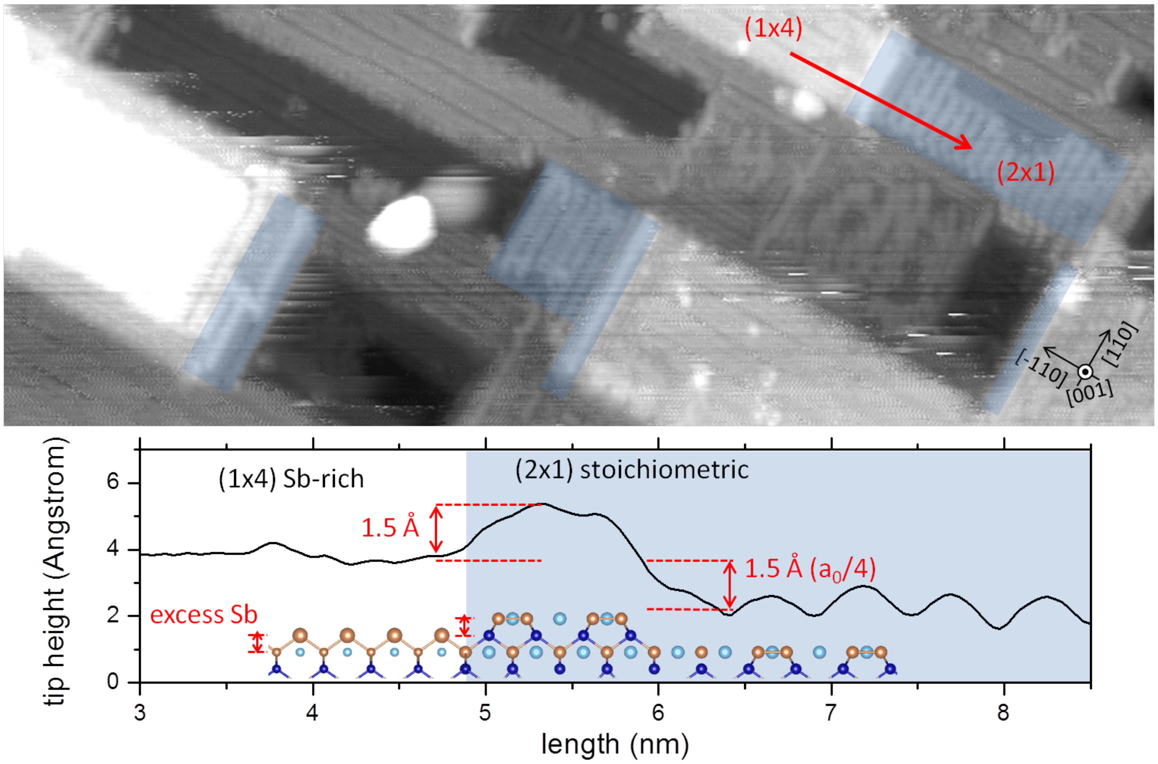

Figure 6.5. Filled states STM image (top) and line profile (bottom) showing the interfaces between domains with (2×1) surface reconstruction and Sb-rich (1×4) reconstruction. The step height between (2×1) and (1×4) domains is $a/4$.

We briefly summarize the experimental observations of the (1×4) surface. This surface is produced by annealing with a high Sb flux. Surface termination experiments in the MBE [Figure 6.2(k)] and core level photoemission measurements [Figure 6.3] suggest that compared to the (2×1) surface, the (1×4) has an excess ad-layer of Sb on the order of 1 ML. Analysis of the Sb 3d core level suggests that this surface has a metallic Sb bonding component.

Based on these measurements a model for the (1×4) reconstruction is proposed in Figure 6.4(g). The model is characterized by rows of 3 Sb atoms on top of the TiSb-terminated (or slightly Ti deficient) surface followed by a trench, corresponding to a 0.75 ML fractional Sb coverage for the (1×4) reconstruction. A measured tip height profile is shown in Figure 6.4(h), showing good agreement with the model. Note the asymmetry is caused by the STM tip raster direction.

This 0.75 ML model coverage is consistent with the 1ML estimated from the flux required for the $(2 \times 1) \rightarrow (1 \times 4)$ transition [Figure 6.2(k)] and consistent with the STM measured step height of $a/4$ between (1×4) and (2×1) regions. Note that if the amount of excess Sb on the surface were greater than 1 ML, then the step height between these two region would be expected to be larger than $a/4$ (assuming that the areal density of an Sb ad-layer cannot exceed 1 ML $= 5.78 \times 10^{14}$ atoms/cm^2). However, the model 0.75 ML coverage is less than the 1.5 ML estimated by XPS. This discrepancy may arise from the method of sample preparation. The (1×4) was prepared by annealing with a high Sb flux and then shuttering the Sb and rapidly quenching to room temperature while monitoring the RHEED pattern. During this quench, some residual Sb may have adsorbed on the surface. These small regions of Sb cap would be difficult to distinguish in the overall (1×4) pattern observed by RHEED during the quench. Hence the macroscopically averaged Sb composition measured by XPS may be larger than the local composition of the (1×4) regions measured by STM.

Electronic structure of the reconstructions

These reconstructions are also distinguishable by their electronic structures. Figure 6.6(a) shows an angle integrated photoemission spectrum of the valence band for the $(2\times1)/c(2\times4)$ surface measured using synchrotron light with an incident photon energy of 70 eV, corresponding to a photoelectron mean free path on the order of 5 Å (roughly 2 atomic bilayers). The measured spectrum is in general agreement with the calculated valence band density of states [28], with peaks at binding energies of 3.1 and 1.5 eV corresponding to Co 3d t_{2g} and e_g states. Additionally, an intense shoulder is observed extending from 1.2 to 0.8 eV, corresponding to Ti t_{2g} states, followed by a steep edge from 0.8 to 0.6 eV and a shallow shoulder of states from 0.6 eV to the Fermi level (0 eV). Similar features near the Fermi level have previously been observed by high energy XPS for bulk polycrystalline samples of both CoTiSb and NiTiSn, with the steep edge attributed to the valence band edge and the states at the Fermi level attributed to in-gap defect states [146, 158]. Defect states within the gap may be a possible explanation for the observed states at the Fermi level in our CoTiSb(001) films. But given the high surface sensitivity of the present measurement, the states near the Fermi level may also be surface related.

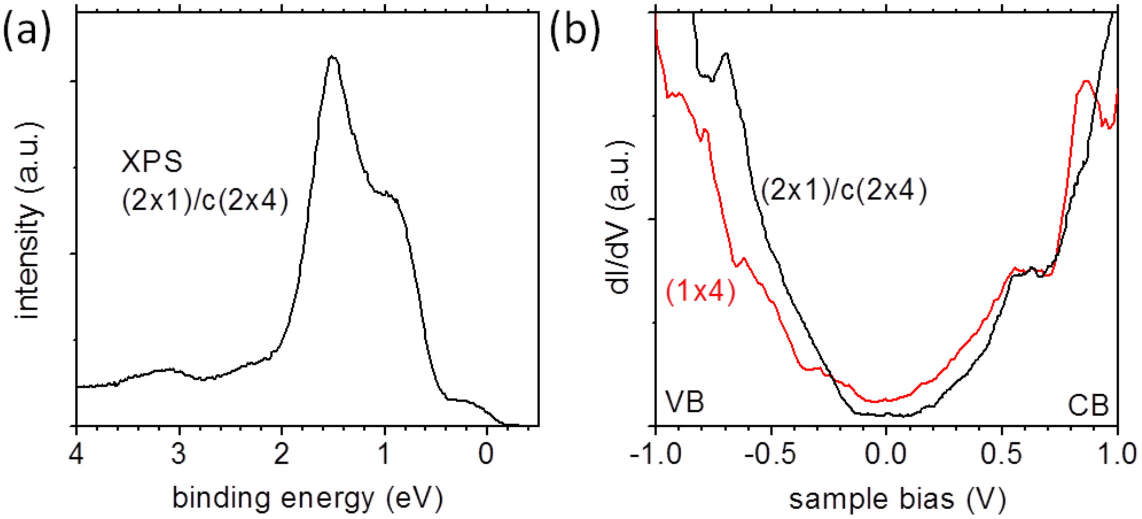

Figure 6.6. (a) XPS of the valence band at a photon energy of 70 eV. (b) STS differential conductance (dI/dV) curves for the nominally stoichiometric $(2 \times 1)/c(2 \times 4)$ surface and for the Sb-rich (1×4) surface.

Figure 6.6(b) shows STS differential conductance (dI/dV) curves measured for the (1×4) and $(2 \times 1)/c(2 \times 4)$ surfaces, which we use to distinguish the contributions from surface states. Each curve was averaged over more than 15 individual point spectra. The dI/dV curves are roughly proportional to the local density of states, where the sample bias in V corresponds to energy in eV and zero bias corresponds to the Fermi level [179]. Through a comparison of the two spectra and a tangent line construction we estimate positions for the bulk valence and conduction band edges [179].

Three distinct regions of the spectra are observed. For biases less than -0.7 V, both (1×4) and $(2 \times 1)/c(2 \times 4)$ spectra show a very steep negative slope. This -0.7 V bias corresponds roughly to the steep edge of states observed by photoemission [Figure 6.6(a)], presumably reflecting the bulk valence band edge. Above 0.5 V bias, the two spectra also show similar behavior with a shoulder of states from 0.5 to 0.7 V and a sharp rise of states above 0.7 eV.

However, in the region around the Fermi level from -0.7 V to 0.5 V, the two surfaces are distinguishable from one another. While the $(2 \times 1)/c(2 \times 4)$ is pseudo gapped at the Fermi level, the (1×4) shows no evidence of a gap, consistent with a metallic ad-layer of Sb on the (1×4) surface. Since the bulk band structure of CoTiSb should be unaffected by the particular surface reconstruction, these results suggest that bulk CoTiSb is semiconducting, with a valence band maximum near -0.7 V and conduction band minimum near 0.5 V. The corresponding bulk bandgap of 1.2 eV is slightly larger than the 1.0 to 1.1 eV bandgap expected from DFT [112]. This discrepancy may be caused by tip induced band bending, which would cause the measured STS gap to overestimate the real gap. However, we caution that due to the nonzero density of states over a fairly broad range, the determination of either band edge from a tangent construction is not so clear.

6.4 NiTiSn(001) surfaces

6.4.1 Surface structure by LEED and STM

NiTiSn surfaces show similar reconstruction behavior as CoTiSb. Figure 6.7(a) shows a LEED pattern of a (2×1) NiTiSn film grown on ErAs/InGaAs/InP(001). Due to the 4-fold rotational symmetry of the ErAs diffusion barrier, mixed domains of the (2×1) rotated 90 degrees from one another are observed. Contributions from these two rotational domains are denoted by the red and blue spots in the schematic LEED pattern at the bottom of Figure 6.7(a). Upon further annealing to 500°C with no excess Sn flux

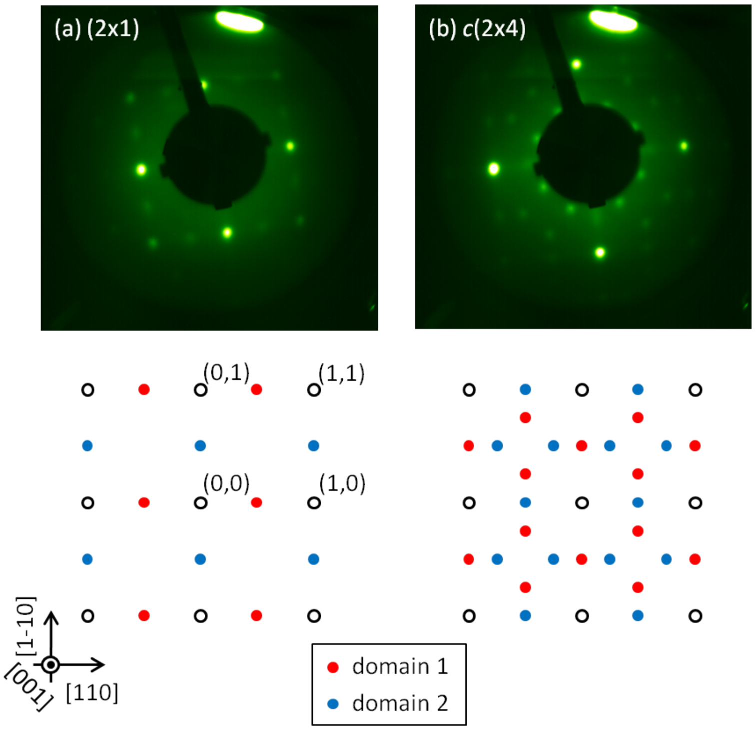

Figure 6.7. (a) LEED pattern measured at 42 eV for as-grown NiTiSn(001) surface (T_{growth} = 400°C) showing a (2×1) surface reconstruction with two rotational domains. (b) LEED pattern measured at 68 eV following an anneal at 500°C showing a $c(2\times4)$ reconstruction. Schematics of the LEED patterns showing the contributions from the two rotational domains are shown below.

the surface exhibits a $c(2\times4)$ [Figure 6.7(b)], just as observed for CoTiSb. We have not yet observed a third reconstruction for annealing under Sn-rich conditions, which could be analogous to the CoTiSb (1×4). Further experiments are needed to determine whether excess Sn induces a third reconstruction before simply capping the surface.

Figure 6.8(a) shows a filled states STM image of the (2×1) NiTiSn film grown on ErAs/InGaAs/InP(001). Although the NiTiSn is rougher than the CoTiSb films, for small scan areas the 2× periodicity of the (2×1) surface unit cell is resolved. However, from these images it is not clear whether the surface has Sn-Sn dimers, analogous to the Sb-Sb dimers proposed for the CoTiSb (2×1) and $c(2\times4)$. Additionally, unlike the

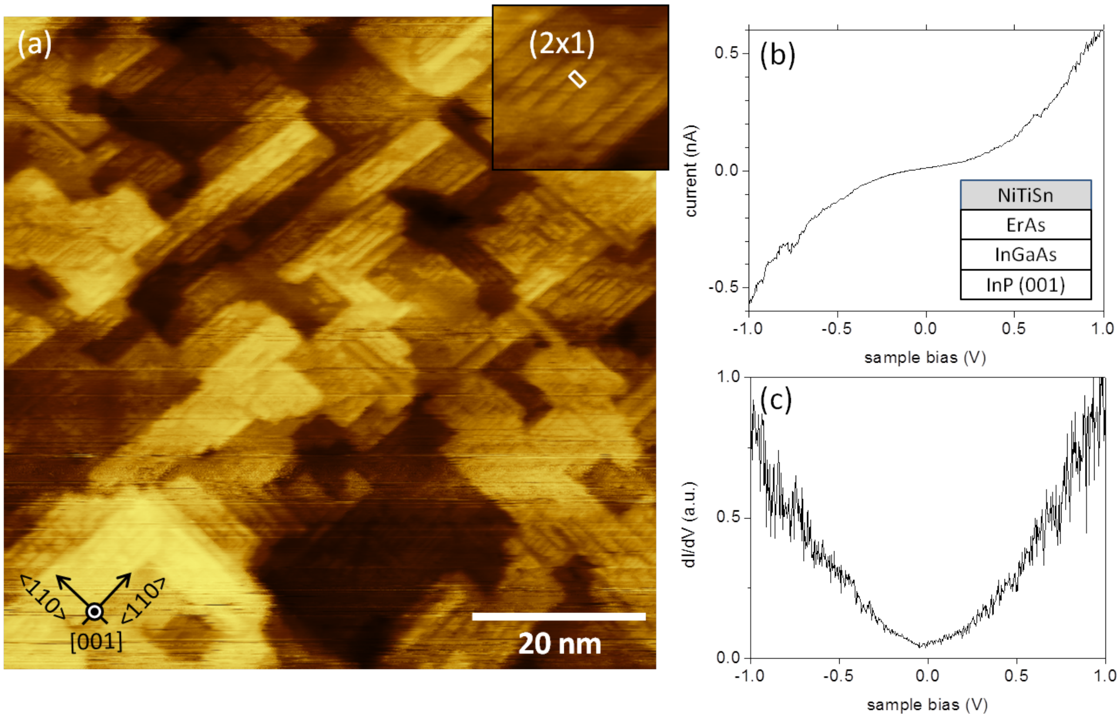

Figure 6.8. (a) Filled states STM image of the NiTiSn (2 × 1) surface. The (2 × 1) surface unit cell is marked in the insert. (b) STS I-V and (c) dI/dV curves for the (2 × 1) surface, indicating metallic behavior.

(2 × 1) CoTiSb surface, initial scanning tunneling spectroscopy measurements for the (2 × 1) NiTiSn surface show a finite density of states at the Fermi level, indicating a metallic surface [Figure 6.8(b,c)]. However we have only performed STS on one NiTiSn sample and further investigations are needed.

Figure 6.9 shows *in-situ* XPS measurements of the Ni 2p, Ti 2p, and Sn 3d core levels for a NiTiSn (2 × 1) sample measured using an Al $K\alpha$ X-ray source ($h\nu = 1486.7$ eV). Measurements of the the Ni 2p and Ti 2p [Figure 6.9(a,b)] show the expected spin-split $p_{3/2}$ and $p_{1/2}$ peaks. A broad satellite is also observed for the Ni 2p at a binding energy of 861 eV (labeled A), which is attributed to final state effects [180]. For the Sn 3d [Figure 6.9(c)] we observe the spin split $d_{5/2}$ and $d_{3/2}$ peaks. But due to the limited

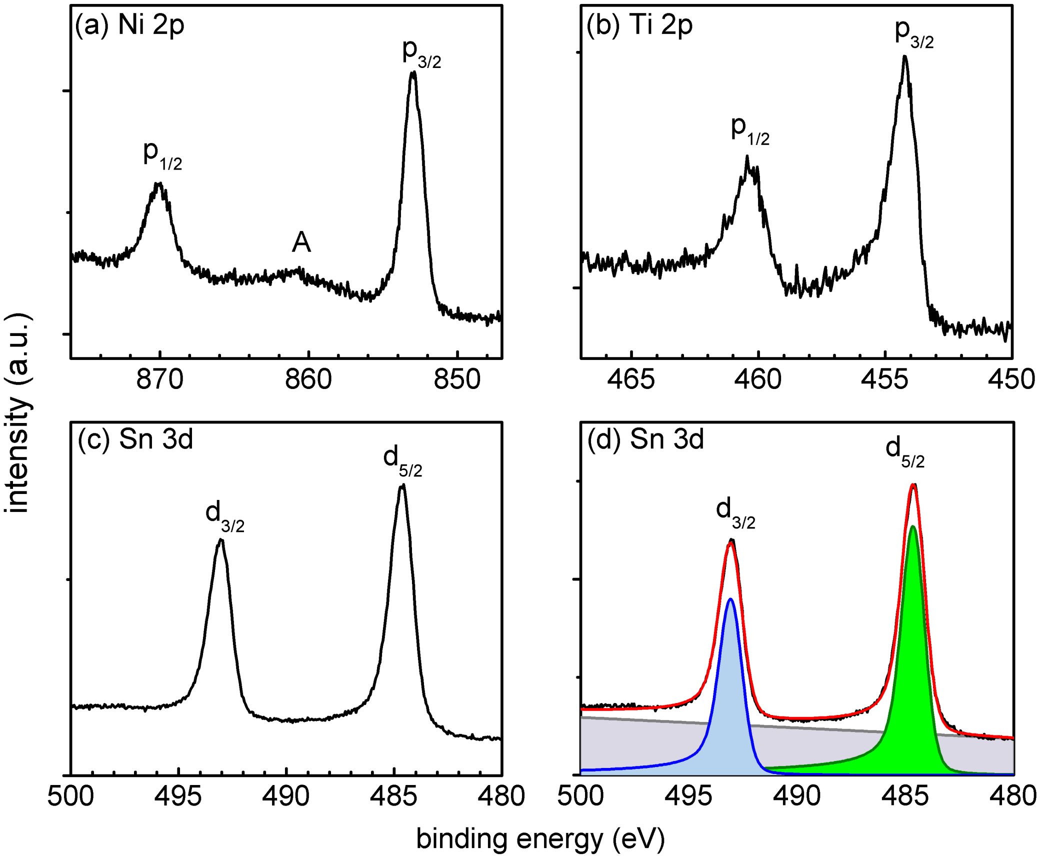

Figure 6.9. (a-c) Ni 2p, Ti 2p, and Sn 3d photoemission core levels respectively for a NiTiSn (001)-(2 × 1) sample measured using an Al $K\alpha$ x-ray source. (d) Gaussian-Lorentzian fit to the Sn 3d core level. The measured spectrum is shown in black, while the fitted $d_{3/2}$ and $d_{5/2}$ components are in blue and green respectively. The background is in gray, and the total fit is in red. No secondary components are resolved, and higher resolution spectra may be required to determine whether secondary bonding components exist.

experimental resolution using the Al $K\alpha$ source (about 700 meV) and the inability to vary the incident photon energy, from these measurements it is difficult to determine whether any secondary Sn bonding components exist. As shown in Figure 6.9(d), the measured Sn 3d spectra can be reasonably fit to single component Gaussian-Lorentzian functions.

Thus from these initial LEED, STM, and XPS measurements it is difficult to comment on the atomic structure of the NiTiSn(001) surface reconstructions. Like CoTiSb(001), NiTiSn(001) also exhibits a (2×1) and a $c(2 \times 4)$ reconstruction, with the $c(2 \times 4)$ occurring for high temperature anneals with no excess Sn. Based on these similarities we suspect that the NiTiSn reconstructions may be characterized by Sn-Sn dimers, similar to the Sb-Sb dimers proposed for the CoTiSb (2×1) and $c(2 \times 4)$. However, the spatial resolution of the STM images in Figure 6.8 and the energy resolution of the *in-situ* XPS core levels in Figure 6.9 do not give definitive proof.

6.4.2 Challenges of capping and decapping for high resolution photoemission spectroscopy

To gain more information on the NiTiSn surface reconstructions we have attempted higher resolution photoemission measurements using synchrotron light. In the case of CoTiSb, the synchrotron photoemission measurements made possible by the fact that we could cap the CoTiSb surface with Sb to protect it during transfer through air, and that we could remove the Sb cap and recover the original surface by simply annealing the sample.

Here we explore Sn capping as a means of protecting the NiTiSn surfaces for high resolution photoemission measurements. Sn was chosen as the capping material because it is one of the constituents of NiTiSn, and of the three constituents has the largest vapor pressure, hence it should be the one to thermally desorb most easily. Furthermore, in the Ni-Ti-Sn ternary phase diagram there is a tie-line between NiTiSn and Sn [181], meaning that NiTiSn and Sn are thermodynamically stable with one another and no additional phases are expected to form at their interface. However, note that since Sn is not as volatile as Sb, it is expected that higher temperatures may be required to remove Sn caps from NiTiSn than Sb caps from CoTiSb. Commonly used III-V semiconductor capping materials such as Sb and As were not used because As-NiTiSn reactions were found to occur at the interface as measured by in-situ XPS, and similar reactions are expected for Sb-NiTiSn.

NiTiSn films with thickness 25-50 nm were grown on MgO(001) substrates as described in Chapter 5. After following growth the samples were cooled to -30 °C and capped with 5-10 nm Sn. Samples were then removed from vacuum and transferred through air to the MAX-Lab synchrotron facility in Lund, Sweden. After reloading the samples in vacuum at beamline I311, we explored two methods for removing the Sn cap: annealing and argon sputtering.

We first examine annealing as a method for removing the Sn cap. After reloading into UHV the capped samples were annealed and characterized by microbeam low energy electron diffraction (μLEED) and spectroscopic photoemission and low energy electron micrsocopy (SPELEEM). Figure 6.10(a) shows a mirror-mode low energy electron micrograph (MEM), and Figure 4(b) shows an X-ray photoemission electron micrograph (XPEEM) tuned to the Sn 4d core level, for a sample after a 400 °C anneal in UHV. The surface is characterized by 300-500 nm diameter Sn-rich islands that are spaced 1-5 microns apart. In the regions between the Sn-rich islands, very faint Ni 3p and Ti 3p core levels are observed in addition to intense Sn 4d levels. The Ni 3p and Ti 3p have low intensities due to their small cross section at these energies relative to Sn 4d ($\sigma_{Ni3p} = 0.9$ Mbarn at $h\nu = 70$ eV, $\sigma_{Ti3p} = 0.8$ Mbarn at $h\nu = 150$ eV, and $\sigma_{Sn4d} = 24$ Mbarn at

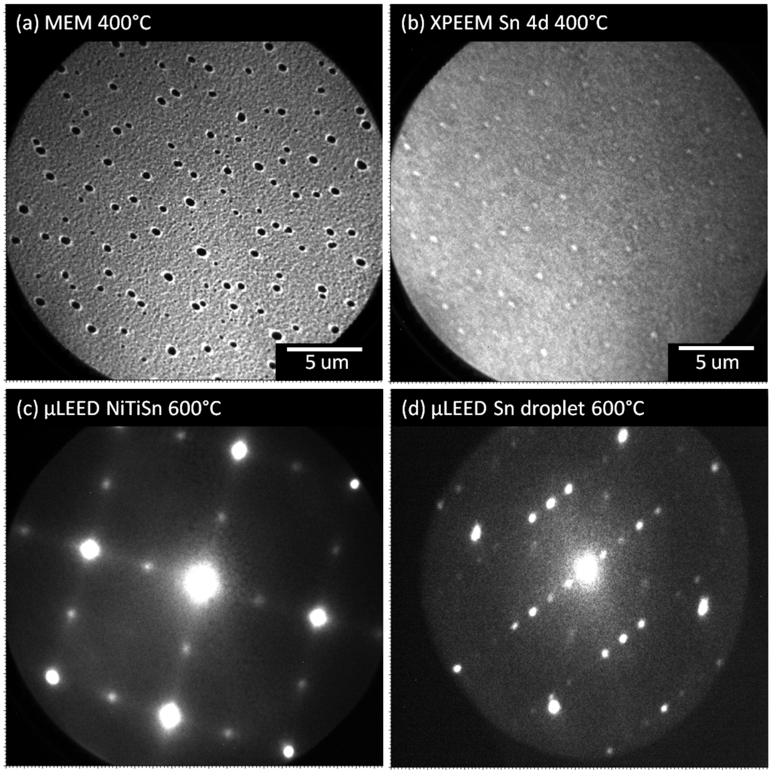

Figure 6.10. SPELEEM micrographs and μLEED patterns during the anneal removal of an Sn cap from the NiTiSn surface. (a) Mirror electron mode image following a 400 °C anneal, and (b) X-ray photoemission image at the Sn 4d binding energy following a 400 °C anneal. (c,d) μLEED patterns for an exposed NiTiSn region and a Sn droplet region. Reprinted with permission from [110]. Copyright 2013 American Institute of Physics.

$h\nu$ = 70 eV). This suggests that upon annealing to 400°C the Sn cap begins to dewet and ball up into islands. Upon further annealing to 600°C the Sn islands grow and are spaced roughly 20 microns apart.

Using μLEED with a 5 micron diameter spot, a mixed $(2\times1)/(1\times2)$ reconstruction is observed in the regions between Sn islands [Figure 6.10(c)], consistent with the RHEED and LEED patterns observed for NiTiSn samples before capping. The Sn-rich islands are clearly distinguishable from the matrix region by their μLEED pattern [Figure 6.10(d)], however their exact composition is not known. This suggests that some of the regions between the Sn islands may be clean NiTiSn, however other regions between the Sn islands appear to be dewetting or decomposing as Mg 2p core levels are measured in some of these regions. Further anneals above 650°C were not sufficient to completely remove the residual Sn islands without dewetting or decomposing the entire NiTiSn film. However, using a focused light source with sufficient flux it may be possible to perform nanoARPES or nanoXPS measurements on the clean NiTiSn regions between islands [182, 183]. Unfortunately, due to the present limits in spatial resolution at beamline I311, high resolution photoemission measurements between the islands were not obtained.

We next explore argon sputtering as a method to completely remove the Sn cap. Figure 6.11 shows the Sn 3d, Ni 2p, and Ti 2p core levels measured at various stages before and after the capping and cap removal process by argon sputtering at 1kV with no external heating. The before capping spectra were measured on a NiTiSn sample in-situ immediately following growth using a laboratory Al $K\alpha$ light source that is connected to the MBE growth chamber (bottom curves, same spectra as Figure 6.11). The spectra

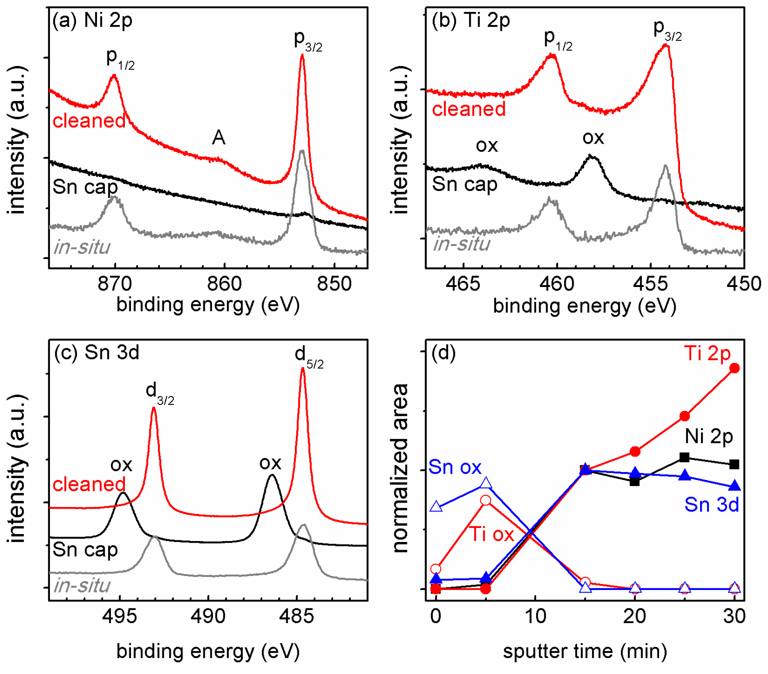

Figure 6.11. (a-c) XPS core levels for a NiTiSn sample before the Sn cap, after the Sn cap, and after sputter removal of the Sn cap. The before cap spectra were measured in-situ using an Al K source ($h\nu = 1486.6$ eV). The Sn cap and sputter cleaned spectra were measured using synchrotron light with incident photon energies of 610 eV for Sn 3d, 980 eV for Ni 2p, and 580 for Ti 2p such that the kinetic energy was held roughly constant at 120 eV. (d) Integrated core level intensities as a function of sputter time. Reprinted with permission from [110]. Copyright 2013 American Institute of Physics.

show no signs of oxidation and serve as a baseline for comparison with spectra after capping and sputter cleaning.

After reloading the samples into UHV, the Sn cap and sputter cleaned spectra were measured using synchrotron light with energies $h\nu = 980$ eV for Ni 2p, $h\nu = 580$ eV for Ti 2p, and $h\nu = 610$ eV for Sn 3d. These incident photon energies were chosen such that the kinetic energy of the photoelectrons was held roughly constant at approximately 120 eV for each of the core levels, corresponding to a mean free path on the order of 5 Å (approximately 2 atomic bilayers). For the spectra of the Sn capped sample before sputter cleaning, the Sn 3d is dominated by strong oxide peaks shifted towards higher binding energy, consistent with an oxidized Sn cap. Oxide peaks are also observed for the Ti 2p, suggesting Ti oxidation at the Sn/NiTiSn interface. No oxide peaks are observed for the Ni 2p, and only a very faint unoxidized Ni $2p_{3/2}$ component is observed. These observations suggest the NiTiSn surface is almost completely covered with Sn but there may be small pinholes or grain boundaries through which oxygen was able to diffuse and bond to Ti. Usage of a thicker Sn cap may help prevent Ti oxidation at the Sn/NiTiSn interface.

Upon sputtering, both Sn 3d-oxide and Ti 2p-oxide peaks decrease and are almost completely removed after 15 minutes [Figure 6.11(c)]. 15 minutes also coincides with the appearance of unoxidized Ti 2p, Ni 2p, and Sn 3d peaks, suggesting the removal of the oxidized Sn cap and appearance of a clean NiTiSn film [Figure 6.11(d)].

With continued sputter time beyond 15 minutes the intensities of the Ni 2p and Sn 3d peaks remain roughly constant, but the intensity of the Ti 2p increases. This suggests a preferential sputtering effect or a segregation of Ti to the surface. Due to this increase in Ti 2p intensity even after the Sn cap removal, the surface most likely resembles the stoichiometry of the original NiTiSn surface just after the initial removal of the Sn cap, i.e. around 15-20 minutes of sputtering. The red curves in Figure 6.11 show the sample after 20 minutes of sputter cleaning. No oxide peaks are observed and the peak shapes are similar to those measured in-situ before capping. Both Ni 2p and Sn 3d can be fit well to single peak Gaussian/Lorentzian functions. However, note that argon sputtering damages the sample surface, as no LEED pattern was observed for the films after sputter cleaning and subsequent annealing. Thus argon sputtering is not to be an acceptable means of removing the Sn cap from the NiTiSn surface. This is in contrast to annealing alone, which left residual Sn islands on the surface but did produce μLEED patterns between the islands.

6.5 Conclusions

In summary, we have measured the periodicity, bonding, and electronic structure of the Half Heusler CoTiSb(001) and NiTiSn(001) surfaces. For CoTiSb(001), we observe three surface reconstructions that vary with Sb flux and anneal temperature, similar to the reconstruction behavior for the (001) surfaces of zincblende compound semiconductors. Using *in-situ* and synchrotron based photoemission spectroscopy, we showed that the (1×4) reconstructions is characterized by an ad layer of Sb, while the (2×1) and $c(2 \times 4)$ are likely characterized by Sb dimers. Using STM/STS we imaged the surface reconstructions in real space and showed that they are electronically distinguishable, with the (2×1) and $c(2 \times 4)$ producing a pseudo-gapped density of states and the (1×4) producing a metallic density of states. Based upon these measurements we proposed atomic models for the CoTiSb(001) reconstructions and commented on their stability using electron counting.

Of special note is that the synchrotron photoemission measurements were enabled by the fact that we could cap the CoTiSb. We demonstrated that Sb caps protect the CoTiSb surfaces for transfer through air, and once reloaded into vacuum the Sb caps can be readily removed by annealing to produce clean (2×1) or $c(2 \times 4)$ surfaces for surface sensitive photoemission measurements. Note that it is more difficult to reproducibly anneal to the Sb-rich (1×4): doing so without the aid of an Sb source during decapping requires very careful control of decapping temperature such that the cap is removed without annealing too hot and producing a (2×1). In the next chapter we rely on this capping and decapping scheme to measure the electronic bandstructure of CoTiSb using angle-resolved photoemission spectroscopy (ARPES).

For the NiTiSn(001) surfaces we observe similar reconstruction behavior as for CoTiSb. NiTiSn(001) also exhibits (2×1) and $c(2 \times 4)$ reconstructions, with the $c(2 \times 4)$ appearing for higher temperature anneals. We suspect that these two reconstructions are characterized by surface Sn-Sn dimerization, similar to the Sb-Sb dimerization suggested for the corresponding CoTiSb reconstructions. However, measurements of the Sn core levels using a standard lab based Al $K\alpha$ source did not have sufficient resolution to determine whether a distinct surface Sn bonding component exists.

We explored Sn capping as a method for protecting the NiTiSn surfaces for synchrotron photoemission measurements. However, it was found that due to the low volatility of Sn, the caps could not be completely removed by annealing and instead formed droplets of Sn on the surface. Between the droplets we observed (2×1) regions by μLEED, suggesting that these regions may be clean NiTiSn that could in principle be measured in photoemission using a light source with a sufficiently focused beam. We also explored argon sputtering as a method to remove the cap. We found that argon could remove the Sn cap and reveal a surface that is oxide free; however the sputter induced damage was so great that the resulting film did not have a well resolved LEED pattern. Further anneals were not successful in recovering a LEED pattern.

Beyond the atomic structure and bonding at Half Heusler surfaces, this chapter establishes the prerequisites for understanding the electronic structure at Half Heusler surfaces. From the measurements we have proposed atomic models for the CoTiSb surface reconstructions, and in the next chapter we will use these models as starting points for calculations of the surface electronic structure of CoTiSb(001).

Chapter 7

Electronic structure of CoTiSb

7.1 Introduction

In this chapter we use angle-resolved photoemission spectroscopy (ARPES) to measure both the bulk (k_z) and surface (k_x, k_y) electronic structure of CoTiSb(001) films. Recall that DFT-GGA calculations suggest CoTiSb has a valence band maximum at Γ and conduction band minimum at X, leading to an indirect gap of approximately 1 eV (Figure 7.1).

Samples were grown by MBE as described in Chapter 5 and consisted of CoTiSb(10nm) / InAlAs / InP(001). After growth samples were capped with a few hundred nanometers of Sb at a substrate temperature of $150-200$°C. After transporting samples through air and reloading them into vacuum at beamline I4 of the MAX-Lab Synchrotron facility in Lund, Sweden, samples were decapped in vacuum by annealing at $350-400$°C until a (2×1) or $c(2\times4)$ pattern was observed by LEED. Cap removal was confirmed by

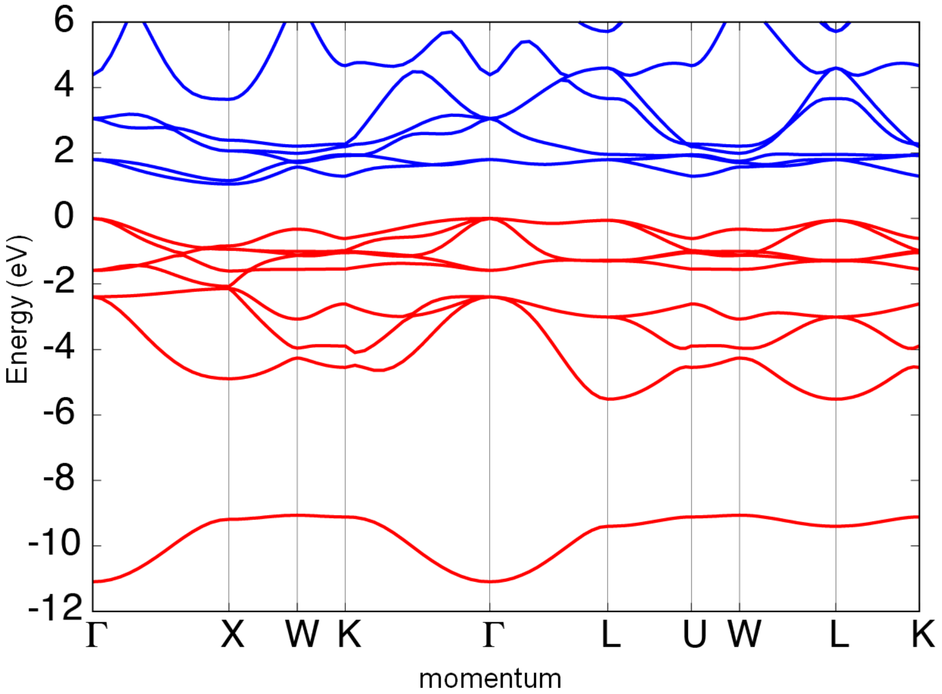

Figure 7.1. Calculated bandstructure for CoTiSb (DFT-GGA). The zero in energy is referenced to the top of the valence band. Courtesy of A. Janotti and A. Roy.

measurements of shallow core levels in photoemission.

7.2 Normal emission for (001): Bulk $\Gamma - X$

In Figure 7.2 we show normal emission measurements for a $c(2 \times 4)$ terminated CoTiSb (001) sample. The $c(2 \times 4)$ was chosen because it is the most repeatable surface that can be produced by annealing Sb-capped CoTiSb. At normal emission varying the incident photon energy corresponds to varying the prependicular component of momentum k_z along the $\Gamma - X$ direction of the bulk Brillouin zone [Figure 7.2(d)]. The data are plotted in two forms. In Figure 7.2(a) we show the energy dispersion curves measured using incident photon energies from 14 to 178 eV. In Figure 7.2(b) we re-plot the photoemission intensity as a function of binding energy and final state momentum. The final state momentum was calculated assuming free-electron-like final states, i.e. $k_z = \sqrt{2m/\hbar^2(E_{kin} + U_0)}$, with an inner potential of $U_0 = 12.0$ eV. Here the inner potential was used as an adjustable parameter to match the periodicity of measured bands [47].

In the data two types of states are observed. The first type disperses with photon energy and results from bulk states. The k_z values for reaching the bulk Γ point ($k_z = 6.41, 4.27, 2.14$ Å^{-1}) correspond to photon energies of 150, 62, and just below 14 eV. At these points the bulk valence band reaches a maximum of 0.8 eV below the Fermi level ($E_B = 0$), in reasonable agreement with the 0.7 eV valence band edge estimated by STS and angle-integrated XPS. The k_z values for bulk X ($k_z = 5.21, 5.34$ Å^{-1}) correspond to photon energies of 31 and 102 eV, where the bands disperse to 1.6 and 2.3 eV below the Fermi level. No bulk states are observed crossing the Fermi level, suggesting that the CoTiSb film has a bulk bandgap.

A second type of state is observed at binding energies of 0.4 and 0.6 eV (labeled s1 and s2 and denoted by arrows). These states do not disperse with incident photon energy (or k_z), but they do have in-plane (k_x, k_y) dispersions [Figure 7.2(e,f)]. Hence they are surface states that reside within the bulk bandgap, and they have increased intensity when they are in resonance with the bulk Γ points. We return to a discussion of the surface states in the next section.

Figure 7.2(c) shows the measured bulk $\Gamma - X$ dispersions plotted with the calculated bulk bandstructure. Reasonable agreement between the measurement and theory is ob-

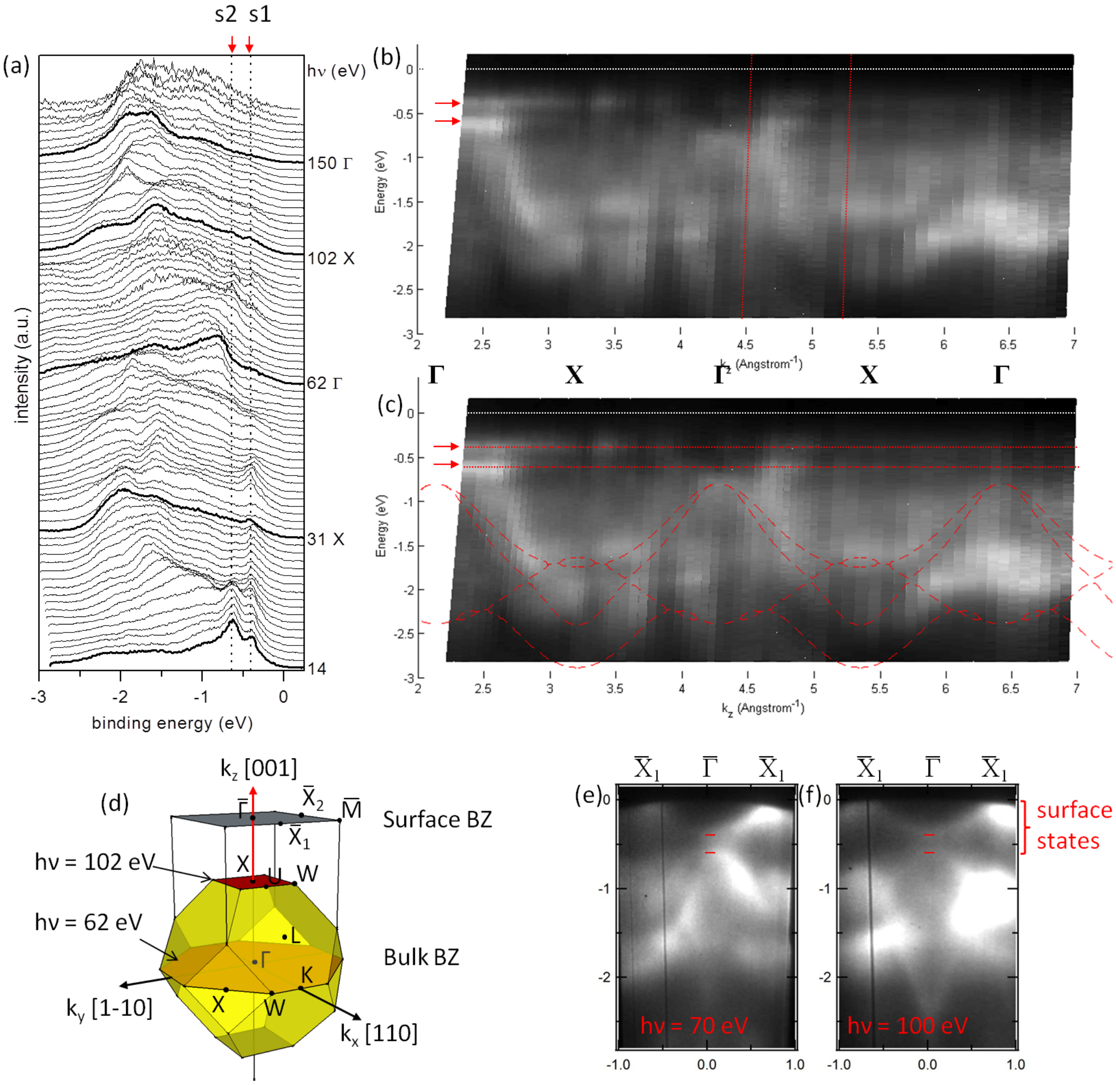

Figure 7.2. Normal emission measurements for CoTiSb (001). (a) Energy dispersion curves as a function of incident photon energy, which probes along the $\Gamma - X$ direction of the bulk Brillouin zone. (b) Photoemission intensity as a function of binding energy and final state momentum assuming free-electron-like final states. (c) Comparison with the DFT-GGA calculated bandstructure (dotted red lines). (d) Schematic of the bulk and surface Brillouin zones, showing sections through bulk Γ and X. (e) In-plane dispersion for $h\nu = 70$ eV, near the bulk Γ. (f) In-plane dispersion for $h\nu = 100$ eV, near the bulk X.

served at high photon energies; however, there are several departures are worthy of note. For the lowest photon energies ($h\nu < 20$ eV, $k_z < 2.7$ Å^{-1}) the measured bands appear to be shifted to higher k_z values than theory. This is likely because the assumption of free-electron-like final states is not valid when the kinetic energy of the photoelectons ($<$ 15 eV) is of similar magnitude as the inner potential (12 eV) [40]. At these low photon energies a more sophisticated model of the final states is required to find the correct values of k_z. Additionally, at the high photon energy Γ point ($h\nu = 150$ eV, $k_z = 6.$ Å^{-1}) we observe an increased spectral intensity at binding energies in the range 1.5 to 2.0 eV, which does not correspond to any expected bands at a Γ point. Here the measured intensity may arise from surface Umklapp scattering from an X point in a neighboring Brillouin zone. Surface Umpklapp is often observed in ARPES measurements of other fcc based crystals, e.g. Si [40]. Finally, the measured bandwidth is slightly shallower than theory.

The in-plane dispersion in Figure 7.2 (e) and (f) also roughly correspond to high symmetry bulk directions. In Figure 7.2(e), for a photon energy of 70 eV the in-plane (k_x, k_y) correspond approximately to a plane just above the $\Gamma - K - W - X$ plane in the bulk Brillouin zone just above the bulk Γ point [Figure 7.2(f)]. Here the in-plane $\bar{\Gamma} - \bar{X}_1$ direction corresponds approximately to the bulk $\Gamma - K$, and the downward dispersing band from 0.8 eV to about 1.3 eV is in good agreement with theory (Figure 7.1). Similarly, in Figure 7.2(f) the photon energy of 100 eV corresponds nearly to a plane that contains a bulk X point, and here the surface $\bar{\Gamma} - \bar{X}_1$ maps onto bulk $X - U$.

The Fermi level position measured by ARPES suggests surface band bending/pinning by surface states. In our ARPES measurements, in which the kinetic energies of the photoelectrons correspond to a mean free path on the order of a few monolayers, we measure a surface Fermi level position that is 0.8 eV above the valence band maximum. DFT-GGA predicts a bandgap of 1.1 eV, suggesting a mid-gap position of the Fermi level at the surface. However, Hall effect measurements for CoTiSb samples show n-type bulk carrier densities in the high 10^{17} cm^{-3} range, which would suggest a bulk Fermi level position much closer to the conduction band edge. Here the band bending could be caused by the surface states that we observe at 0.4 and 0.6 eV.

7.3 Surface states for the $c(2 \times 4)$ reconstruction

Further investigations of the CoTiSb(001) $- c(2 \times 4)$ surface states were explored by measuring the in-plane dispersions. Figures 7.3(a,c) show a Fermi surface and dispersions along the high symmetry surface directions measured using an incident photon energy of 100 eV. The high symmetry directions in the surface Brillouin zone are labeled in Figure 7.3(e). Below the valence band maximum at 0.8 eV the states are mostly bulk-like. In the bulk bandgap, starting from $\bar{\Gamma}$ the state at 0.4 eV at turns upward and crosses the Fermi level at $\bar{X}_1$, while the state at 0.6 eV disperses downward and terminates at bulk states before reaching $\bar{X}_1$. At a photon energy of 100 eV the surface state dispersion along $\bar{\Gamma} - \bar{X}_2$ is not as clear.

Figures 7.3(b) and (d) show a Fermi surface and in-plane dispersions respectively measured using an incident photon energy of 40 eV, which gives a higher sensitivity

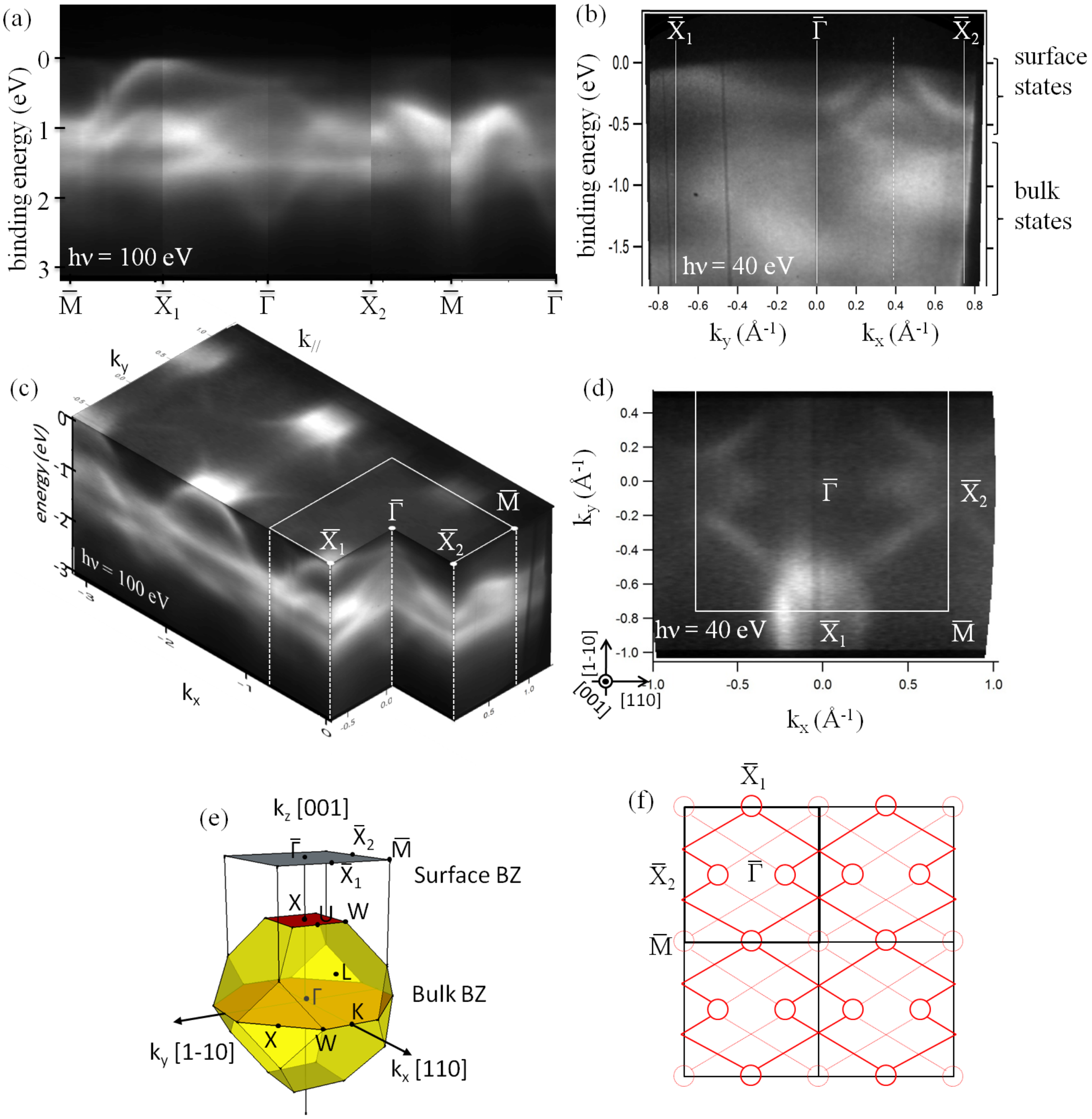

Figure 7.3. In-plane dispersions (E vs. k_x, k_y) and Fermi surfaces (slice of k_x, k_y at the Fermi energy) for the CoTiSb(001)-$c(2 \times 4)$ surface measured using incident photon energies of 100 eV (a and c), and 40 eV (b and e). Measurements at 40 eV show a higher sensitivity to surface states. (a) In-plane dispersions along all the high symmetry surface directions, measured at $h\nu = 100$ eV. (b) In-plane dispersions along $\bar{\Gamma}-\bar{X}_1$ and $\bar{\Gamma}-\bar{X}_2$ measured at $h\nu = 40$ eV, showing the crossings at $\bar{X}_1$ and half way between $\bar{\Gamma}$ and $\bar{X}_2$. (c) Three-dimensional representation of the Fermi surface and in-plane dispersions measured at $h\nu = 100$ eV. (d) Fermi surface measured at $h\nu = 40$ eV. Surface states cross the Fermi level at the $\bar{X}_1$ points as well as half way between $\bar{\Gamma}$ and $\bar{X}_2$. (d) Schematic of the bulk and surface Brillouin zones. (f) Schematic of the Fermi surface, highlighting the $c(2\times4)$ periodicity of the surface states. Note that from this periodicity we also expect states to cross the Fermi level at $\bar{M}$. However, in the measurement from panel (d), these states are not observed, likely due to a matrix effect.

to the surface. Here again the surface state with minimum of 0.4 eV disperses along upward to reach a maximum at $\bar{X}_1$, but it is found to disperse along $\bar{\Gamma} - \bar{X}_2$ with half the periodicity, i.e. the state at 0.4 eV at $\bar{\Gamma}$ turns upward and reaches a maximum half way between $\bar{\Gamma}$ and $\bar{X}_2$, then turns downward to reach a minimum at $\bar{X}_2$. Figure 7.3(f) shows a schematic of the Fermi surface, highlighting the $c(2 \times 4)$ periodicity of surface states. Note that for the Fermi surface at $h\nu = 40$ eV in Figure 7.3(d) the state at $\bar{M}$ is not visible but that it does appear faintly for the Fermi surface at $h\nu = 100$ eV in Figure 7.3(c). This is likely due to a matrix effect, and for emphasis the $\bar{M}$ states are denoted by dotted lines in Figure 7.3(f).

Ongoing work is aimed at comparing the measured surface state band dispersions with the dispersions expected from the Sb dimer reconstruction models in Chapter 6.

7.4 Normal emission for (111): bulk $\Gamma - L$

Bulk band dispersions were also measured for the CoTiSb (111) surface. Here, 10 nm CoTiSb films were grown on InAlAs/InP(111). For the (111) surface, varying photon energies at normal emission corresponds to traversing a reciprocal lattice rod along the $\Gamma - L$ direction of the bulk Brillouin zone. Figure 7.4 shows normal emission measurements for a CoTiSb sample grown on InAlAs/InP:S(111). Again the data are plotted in two forms. Figure 7.4(a) shows energy dispersion curves for incident photon energies from 14 to 180 eV. Figure 7.4(b) shows the photoemission intensity as a function of binding energy and final state momentum assuming free-electron-like final states and an inner

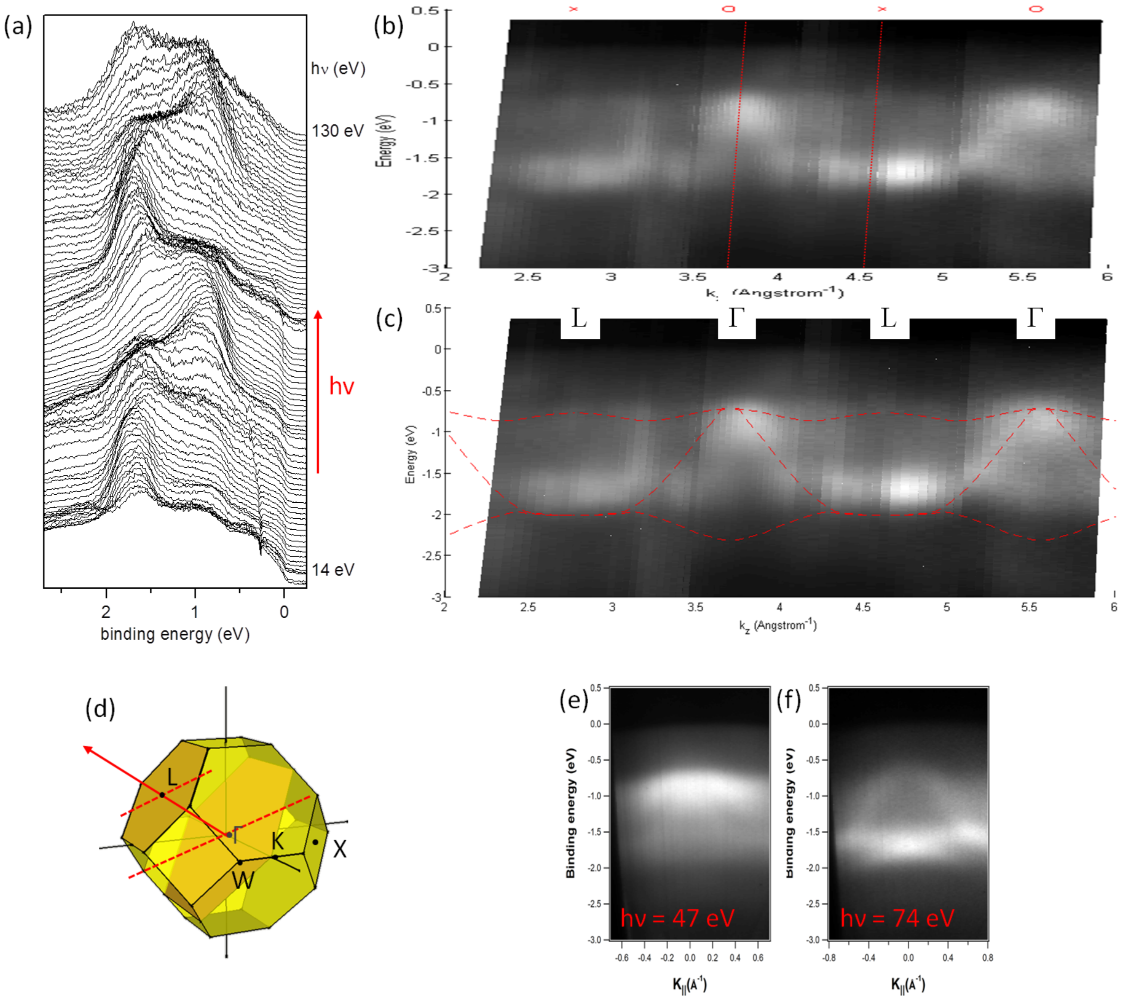

Figure 7.4. Normal emission measurements for CoTiSb (111). (a) Energy dispersion curves as a function of incident photon energy, which probes along the $\Gamma - L$ direction of the bulk Brillouin zone. (b) Photoemission intensity as a function of binding energy and final state momentum assuming free-electron-like final states. (c) Comparison with theory (dotted red lines). (d) Schematic of the bulk Brillouin zone showing sections through bulk Γ and L. (e) In-plane dispersion for $h\nu = 47$ eV, near the bulk Γ. (f) In-plane dispersion for $h\nu = 74$ eV, near the bulk L.

potential of 12.0 eV. The agreement with theory in Figure 7.4(c) is good, with maxima observed at Γ and broad minima observed at L. However, like the $\Gamma - X$ dispersion from figure 7.2, the measured $\Gamma - L$ dispersion in Figure 7.4 is shallower than theory. Figures 7.4(e) and (f) plot the in-plane dispersions for photon energies that correspond approximately to planes crossing through the bulk Γ and bulk L points respectively. These planes are illustrated in Figure 7.4(d).

7.5 Conclusions

In this chapter we demonstrated the first ARPES measurements for a semiconducting Half Heusler compound. Using an Sb capping and decapping scheme to protect the sample surfaces, we measured the bulk and surface bandstructures for CoTiSb (001) and (111) films. Normal emission scans along for the (001) films yield bulk $\Gamma - X$ dispersions that agree with density functional theory calculations, with a valence band maximum at Γ that lies roughly 0.8 eV below the Fermi level. From normal emission scans for (111) oriented films we also extract the $\Gamma - L$ bulk dispersions, which are also in good agreement with theory. These measurements confirm that CoTiSb is a bulk semiconductor.

The CoTiSb(001)-$c(2 \times 4)$ also has surface states within the bulk bandgap. These surface states cross the Fermi energy at $\bar{X}_1$ and half way between $\bar{\Gamma}$ and $\bar{X}_2$, and their periodicity matches the $c(2 \times 4)$ atomic periodicity measured by LEED. Ongoing work is aimed at comparing the measured surface state dispersions with theory based on the surface reconstruction model proposed in Chapter 6. These surface state calculations will serve as a test of the accuracy of our reconstruction models.

Chapter 8

Ni_2TiSn/NiTiSn nanocomposites for potential thermoelectric applications

8.1 Introduction to Half Heusler thermoelectrics

Thermoelectric materials, which enable solid-state conversion between thermal and electrical energy, show great promise for applications in power generation (e.g. from waste heat recovery) as well as both heating and refrigeration. These materials are characterized by a dimensionless figure of merit, $ZT = (S^2\sigma/\kappa)T$, where S is the Seebeck coefficient, σ is the electrical conductivity, and κ is the thermal conductivity. Here the electronic information is contained primarily in the numerator $S^2\sigma$ (often called the power factor), while the thermal information is carried in the denominator. The semiconducting Half Heusler compounds are good candidate thermoelectric materials because they have a large electronic term. The strong d character at their band edges gives rise to sharp peaks in the density of states, and when combined with small bandgaps (typically 1 eV or less), these materials exhibit both high Seebeck coefficients and high electrical conductivity. Additionally many of the Half Heuslers are stable at high temperatures and are composed of elements with high Earth abundance and low toxicity, making them scalable and able to perform in real environments.

In the previous chapters we showed that growth by MBE produces semiconducting Half Heusler films with high electron mobility and low background carrier density as compared to their bulk counterparts. This is especially important for thermoelectrics because for many materials ZT is maximized for carrier densities in the range $10^{19} - 10^{20}$ cm^{-3} [184]. While these densities are *lower* than the background carrier density for most bulk Half Heuslers, the densities are well within the range achievable for MBE grown Half Heusler films.

One challenge is that Half Heuslers, like most intermetallics, also have large thermal conductivities ($\kappa = \kappa_e + \kappa_{lat}$). While the electronic component of thermal conductivity κ_e is inherently tied to electrical conductivity σ via Wiedemann–Franz law, in some cases the lattice component κ_{lat} can be tuned somewhat independently of σ, e.g. by nanostructuring. Previous work in the RE-V/III-V systems (the subject of Chapters 3 and 4) has shown that the inclusion of metallic RE-V nanoparticles embedded coherently within a semiconducting III-V matrix can substantially reduce κ_{lat} without sacrificing σ, hence increasing ZT. Here the coherent nanoparticle/matrix interfaces scatter phonons but contribute minimally to electron scattering [185].

The Full Heusler / Half Heusler Ni_2TiSn/NiTiSn system shows similar promise for

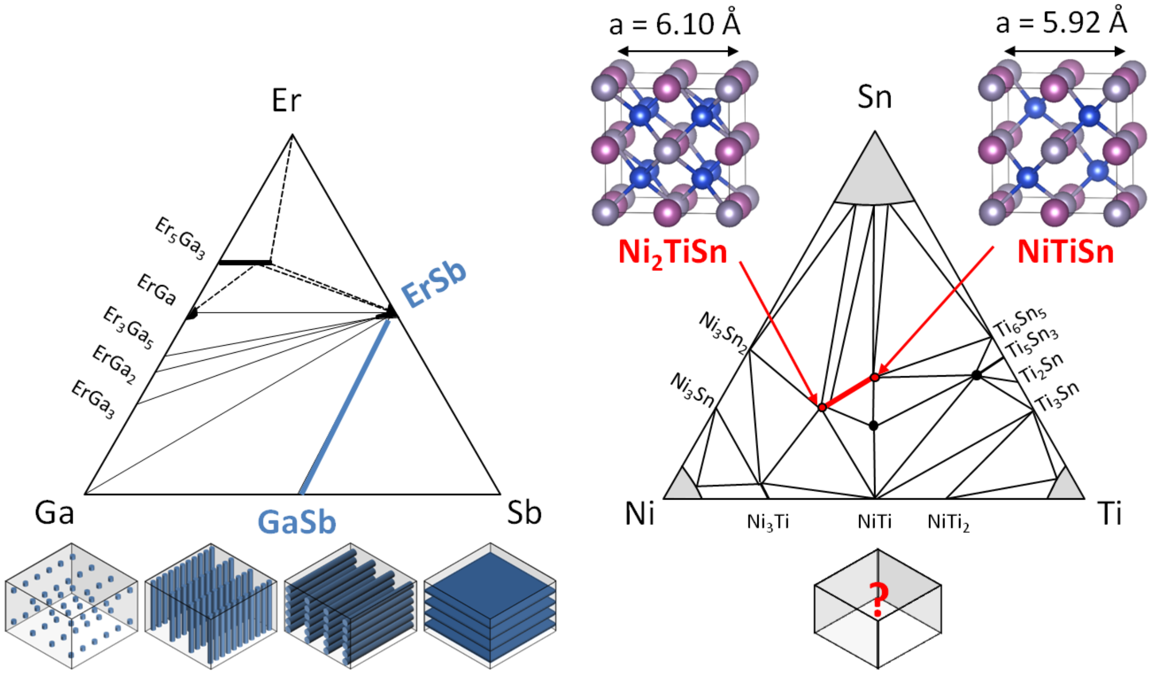

Figure 8.1. Isothermal ternary phase diagrams at 800°C for (a) Er-Ga-Sb and (b) Ni-Ti-Sn. After Refs.[56, 186]. Due to the close crystal symmetry it may be possible to phase segregate metallic Ni_2TiSn precipitates from a semiconducting NiTiSn matrix, similar to what we have previously demonstrated for ErSb/GaSb.

coherent nanostructuring. While Ni_2TiSn is metallic with Full Heusler structure and NiTiSn is semiconducting with Half Heusler structure, the two are related simply by removal of one of the Ni sublattices and have a reasonably small lattice mismatch of 3%. Furthermore like the RE-V/III-Vs, Ni_2TiSn and NiTiSn are tie line compounds as shown in the ternary phase diagram, suggesting that they are thermodynamically stable in contact with one another (Figure 8.1). Indeed, work on bulk samples has shown that it is possible to precipitate Ni_2TiSn from NiTiSn with coherent interfaces [187], and the resulting nanostructured material shows improved thermoelectric performance [188, 189]. However, in these bulk materials it has been difficult to control the size, shape, and distribution of the Full Heusler precipitates, which are important parameters for tuning ZT.

Here we explore MBE as a method for growing Full Heusler / Half Heusler nanocomposites consisting of metallic Ni_2TiSn precipitated from a semiconducting NiTiSn matrix. MBE offers the possibility of controlling the size, shape, and distribution of the precipitates similar to the control we previously demonstrated for ErSb/GaSb in Chapters 3 and 4.

8.2 MBE growth of $Ni_{1+\delta}TiSn$ nanocomposites

A series of $Ni_{1+\delta}TiSn$ samples were grown by molecular beam epitaxy on MgO(001) substrates where the excess Ni content was varied from $\delta = 0$ to 0.5. Here $\delta = 0$ corresponds to the Half Heusler and $\delta = 1$ corresponds to the Full Heusler. All $Ni_{1+\delta}TiSn$ films were grown at 460°C and the compositions were measured using a beam flux ionization gauge that is calibrated by Rutherford Backscattering Spectrometry, as described in Chapter 4. The films had a nominal thickness of 25 nm: here the total amount of Ti and Sn were fixed and only the Ni flux was varied. The full layer structures are shown in the lower left of Figure 8.2.

Figure 8.2 shows RHEED patterns for films with $\delta = 0$, 0.1, 0.2, 0.3, and 0.5 as measured along the $\langle 110 \rangle$ and $\langle 010 \rangle$ azimuths. Note these directions are referenced to the NiTiSn. Within this range of compositions all films are epitaxial with streaky RHEED patterns; however at higher Ni compositions some spots begin to form indicating three dimensional island growth, presumably due to the increased strain as the $Ni_{1+\delta}TiSn$ films approach the Full Heusler limit. Additionally, the reconstruction changes with varying

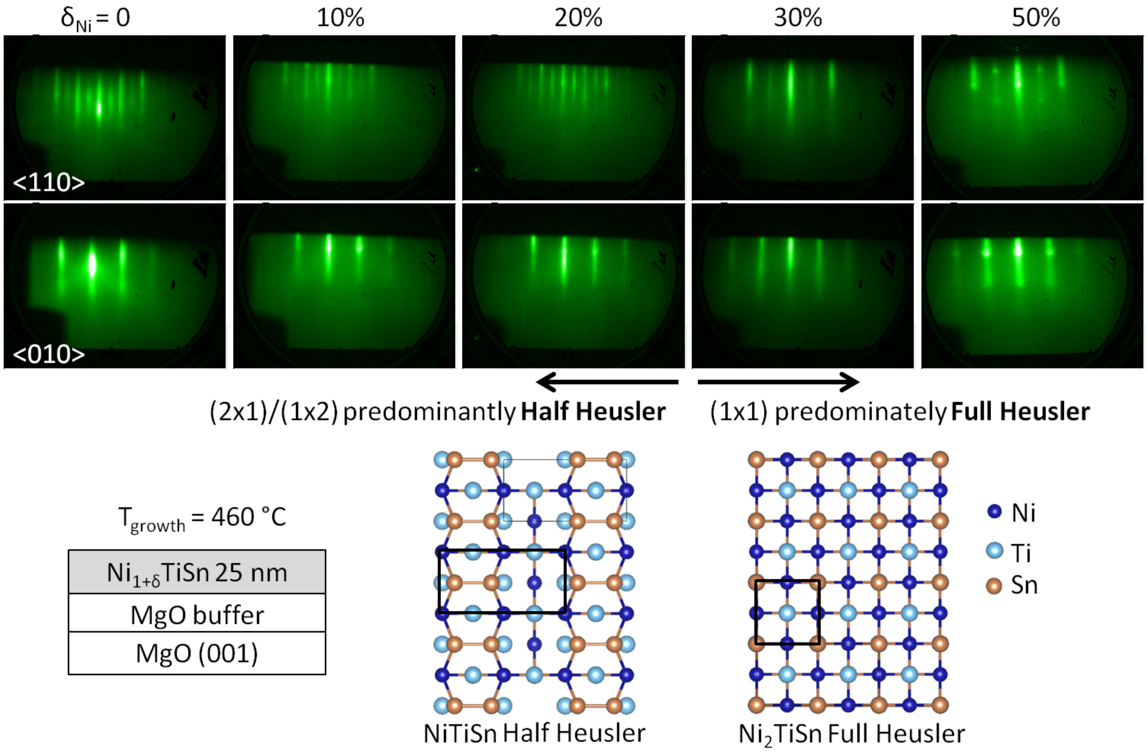

Figure 8.2. RHEED patterns along the ⟨110⟩ and ⟨010⟩ azimuths for $Ni_{1+\delta}TiSn$ samples grown on MgO(001). The bottom left shows a schematic sample structure. The bottom right shows models of the (001) surface for the (2×1) reconstructed Half Heusler surface and the (1×1) Full Heusler surface.

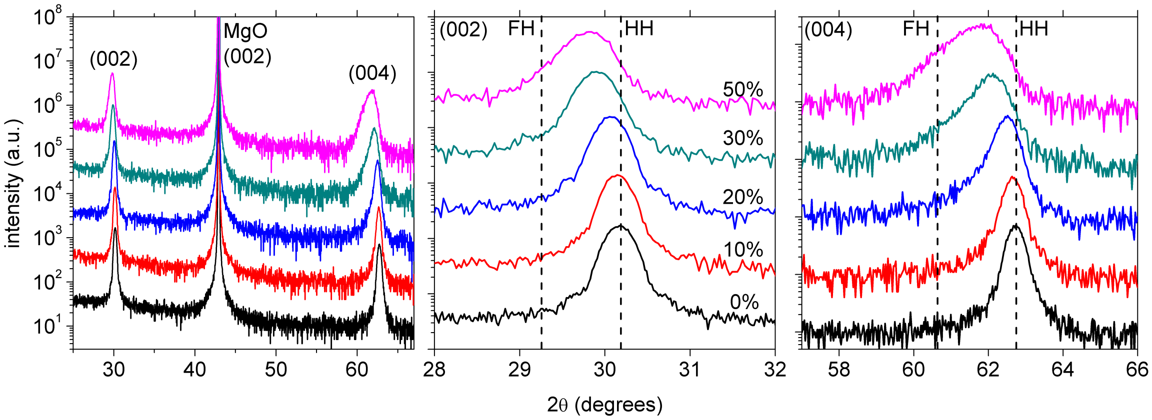

Figure 8.3. XRD 2θ scans for the $Ni_{1+\delta}TiSn$ samples measured using Cu $K\alpha$ radiation. (left) Overview scan, (middle) zoom in on the (002) $Ni_{1+\delta}TiSn$ reflection, (right) zoom in on the (004) $Ni_{1+\delta}TiSn$ reflection. The peak positions for the Full and Half Heusler bulk lattice parameter are indicated with dotted lines.

Ni content. For low excess Ni contents, ($\delta \leq 20\%$) the RHEED shows a $(2 \times 1)/(1 \times 2)$ reconstruction, the same reconstruction observed for stoichiometric Half Heusler NiTiSn. A model for the reconstruction, characterized by Sn-Sn dimers, is shown at the bottom of Figure 8.2. For higher compositions ($\delta \geq 30\%$) the RHEED transitions to a (1×1), the pattern expected for an unreconstructed Full Heusler surface. From the reconstructions in RHEED it is difficult to discern whether the excess Ni is being incorporated uniformly into the film as an alloy or whether it leads to precipitation of a secondary Full Heusler phase. Note that the growth temperature of 460°C is significantly lower than that shown in the ternary phase diagram from Figure 8.1(b). Furthermore, MBE is a nonequilibrium growth process. Thus while Ni_2TiSn and NiTiSn are both line compounds at 800°C, under MBE growth conditions it is feasible for a metastable Half Heusler phase to exist that accommodates some excess Ni.

A clearer identification of phases is determined from the X-ray diffraction 2θ scans shown in Figure 8.3 (Cu $K\alpha$ radiation). In the overview scan [Figure 8.3(left)], peaks centered near $2\theta = 30°$ and $62°$ are observed, corresponding to the $Ni_{1+\delta}$TiSn Full/Half Heusler (002) and (004) reflections respectively, along with an intense MgO (002) substrate reflection. To the limits of our resolution no other peaks are observed, suggesting that no additional phases have formed except the Half and possibly Full Heusler. Figure 8.3(right) show a magnified view of the (004) reflection. The $\delta = 0$ curve shows a relatively sharp peak at $2\theta = 60.72°$, corresponding to the nominally pure phase Half Heusler. For an excess Ni content of $\delta = 0.1$ the (004) reflection is similar in shape as the $\delta = 0$ but slightly shifted to smaller angle, or larger lattice parameter. As the Ni content increases to $\delta > 0.2$ a distinct secondary component appears at lower angle and gains in intensity while shifting to lower angles. This suggests the formation of a secondary phase phase with larger lattice parameter, presumably the Full Heusler. A secondary peak could also reflect twinning; however no chevron pattern is not observed by RHEED. Similar behavior is observed for the (002) reflection [Figure 8.3(middle)].

Since two phases are expected to occur, we approximate the system by fitting the (004) reflections to two Gaussians. The bulk lattice constants of the Full Heusler Ni_2TiSn and Half Heusler NiTiSn are $a = 6.10$ and 5.92 Å respectively, and their 2θ positions are marked in Figure 8.4 by dotted lines. The best fits occur if we allow the peak position of each Gaussian to move in angle 2θ rather than fixing them to the positions expected for the bulk Full Heusler and Half Heusler lattice parameters. This suggests that there are lattice distortions in the Full Heusler / Half Heusler nanocomposites, perhaps due to strain at the interfaces. Such distortions have been also observed for

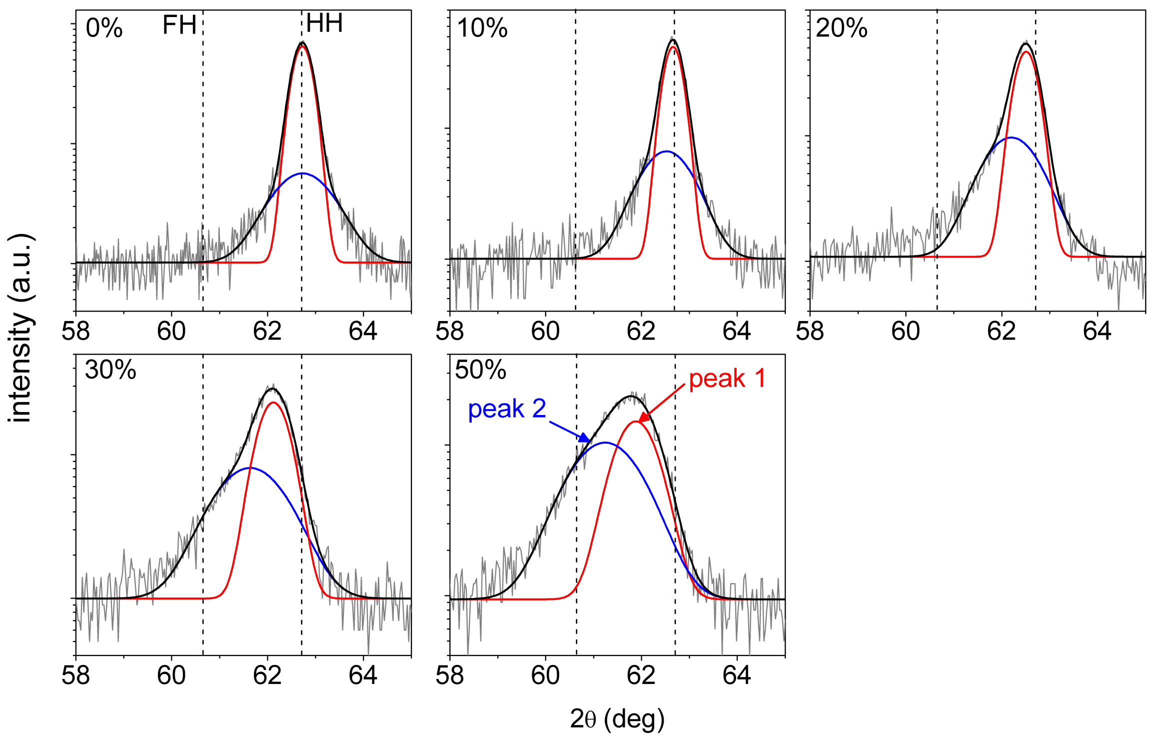

Figure 8.4. Fits of the (004) $Ni_{1+\delta}TiSn$ reflection using two Gaussians. With increasing Ni content, both Gaussians are shifted to the left towards larger lattice parameter, with the broad peak 2 moving faster. Peak 1 is expected to nominally correspond to a Half Heusler phase and peak 2 to a Full Heusler. However, note that the weight in peak 2 does not result entirely from a Full Heusler peak, as this peak 2 component exists for $\delta = 0$.

ErAs/GaAs nanocomposites [85]. Additionally the varying peak positions could reflect nonstoichiometric amounts of Ni being incorporated, e.g. an alloy of $Ni_{1.15}TiSn$, rather than phase pure regions of Ni_2TiSn and NiTiSn. In our fitting the full width at half maximum for each Gaussian was also allowed to vary to account for changes in domain size, strain, or defects. The fits are shown in Figure 8.4, along with the extracted lattice constants, full width at half maximum, and area fraction $A_2/(A_1 + A_2)$ in Figure 8.5, where A_1 is the area of the high angle peak and A_2 is the area of the broader low angle peak.

Upon initial inspection the broader peak 2 (blue) is assumed to correspond approximately to precipitates of a Full Heusler phase and the sharper peak 1 (red) to a Half Heusler matrix. The lattice constants for both peaks 1 and 2 are $a = 5.92$ Å for $\delta = 0$, corresponding to the Half Heusler, and with increasing Ni content both lattice parameters increase, with peak 2 increasing more rapidly and approaching the lattice parameter expected for the Full Heusler (6.10 Å) (Figure 8.5 top). This suggests that with increasing Ni content, the lattice parameter of the Full Heusler precipitates relaxes and approaches the bulk value, presumably due to an increasing domain size of the Full Heusler precipitates and a smaller fraction of the interfacial area. But surprisingly the lattice parameter extracted from peak 1 also increases with Ni content rather than remaining constant, perhaps due to the strain from a larger volume fraction of Full Heusler. This change in lattice parameter from peak 1 could also reflect an enlarged phase field for the Half Heusler. Although the Half Heusler is nominally a line compound, under MBE growth conditions the phase field might enlarge by allowing the excess to Ni to occupy some of the (3/4, 1/4, 1/4) vacancy sites. Similarly, the phase field of the Full Heusler could be enlarged by accomodating vacancies at at the (3/4, 1/4, 1/4) sites.

Assuming that the Full Heusler precipitate size increases with Ni content, the fwhm of peak 2 might be expected to decrease with Ni content via the Scherer equation. However, the fitted fwhm for both peaks actually increases slightly with Ni content, perhaps due to strain and defects (Figure 8.5 middle).

However, we caution that in this simple two Gaussian fit, the weighting of peak 2 does not result entirely from a secondary Full Heusler phase. Some of the weight of peak 2 likely result from strain or from a non-Gaussian lineshape of the real diffraction peaks. This is clearly seen by examining the fit for the $\delta = 0$ sample in Figure 8.4, which is nominally pure phase Half Heusler. Here the lineshape is well reproduced by a fit to two Gaussians, with the peak 2 Gaussian broader than peak 1. But both Gaussians are centered at the same angle 2θ and hence have the same lattice constant. One source of this secondary component may be a mosaic in the out-of-plane lattice constant due to misfit dislocations. The broadening may also result from a disordered NiTiSn region at the NiTiSn film / MgO substrate interface. Such disordered interfacial regions have been observed in other epitaxial Heusler alloys by TEM [190] and may result from strain at the interface. Finally, the broadening could stem from the fact that real X-ray diffraction lineshapes are better described as combined Gaussian/Lorentzians than single Gaussians. A more accurate fitting would need to include the proper Gaussian/Lorentzian lineshape; however it is difficult to proceed with such a fitting without knowing the potential contribution of interfacial strain or mosaic broadening and the proper Gaussian/Lorentzian

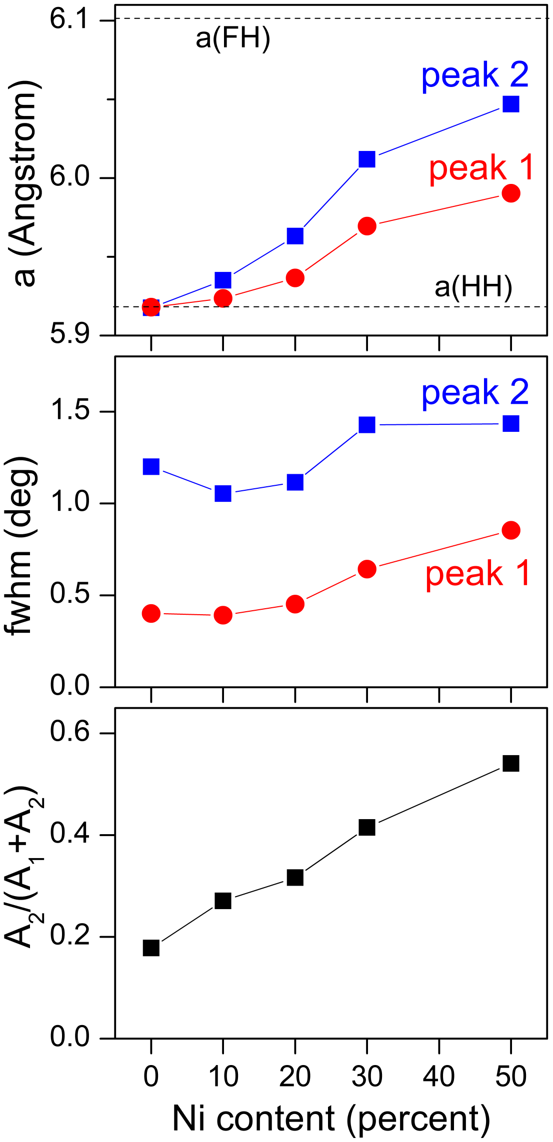

Figure 8.5. Lattice constants a_0, full width at half maximum, and area ratio for fitting the (004) reflections to two Gaussians.

weighting. A more accurate model may also need to include a third peak to account for the strained Half Heusler / Full Heusler interfaces. Nonetheless, the simple 2 Gaussian fit still captures the basic trends, namely that with increasing Ni content a secondary phase forms and that the lattice constants for both phases change with Ni content.

8.3 Transport of $Ni_{1+\delta}TiSn$ nanocomposites

Figure 8.6 shows room temperature transport measurements for the 25 nm $Ni_{1+\delta}TiSn$ films. Each sample was capped with 5-10 nm MgO to prevent the films from oxidation. Hall effect measurements were performed in a Van der Pauw geometry using annealed indium contacts, and Seebeck measurements (courtesy of Anthony Rice) were measured in a Seebeck bar geometry also using annealed indium. In general the films become more metallic with increasing Ni content, as the resistivity ρ and electron mobility μ decrease, the electron density n increases, and the absolute value of the Seebeck coefficient S decreases. However, ρ, μ and $|S|$ show a maximum and n shows a minimum near a Ni excess of 5%. Here the excess Ni may be acting to compensate defect induced charge carriers, since for bulk NiTiSn samples it has been suggested that Ni-vacancy antisites are common [158]. The resulting power factor $S^2\sigma$ is also maximized for 5% excess Ni. Also of note is that for an excess Ni content of 10% the transport properties are very similar to that of the nominally pure phase Half Heusler. These results suggest that modest amounts of excess Ni do not significantly hamper the electronic transport properties. Additional thermal conductivity measurements (e.g. by time-domain thermal reflectance or 3-omega measurements) are necessary to determine the effect of excess Ni on phonon scattering and calculate ZT.

8.4 Conclusions

In summary we have demonstrated the MBE growth of $Ni_{1+\delta}TiSn$ films for excess Ni contents of up to $\delta = 0.5$. Within this range of compositions all films were epitaxial as observed by RHEED. At low compositions the films show a Half Heusler-like (2×1) surface reconstruction, and for higher compositions the films show a Full Heusler-like (1×1) surface. Initial X-ray diffraction measurements show that there are two components to the out of plane lattice constant. With increasing Ni content both components shift towards higher lattice constant, with one of the components moving faster towards larger lattice constant than the other. These results suggest that a secondary phase, presumably Full Heusler, may be precipitating from the matrix. However, this second component does not align with the bulk Full Heusler lattice parameter, and both peak components move with excess Ni content. Hence they appear to be lattice distortions in both the precipitate and matrix phases. These distortions could be cause by interfacial strain or from nonstoichiometric amount of Ni being incorporated. Further TEM and selected are diffraction measurements may help to determine the crystal structure and stoichiometry of the precipitates.

Electrical transport measurements were also performed for films with varying Ni content. In general the films show more metallic transport properties for increasing Ni content, but the electron mobility and power factor are maximized (and carrier density

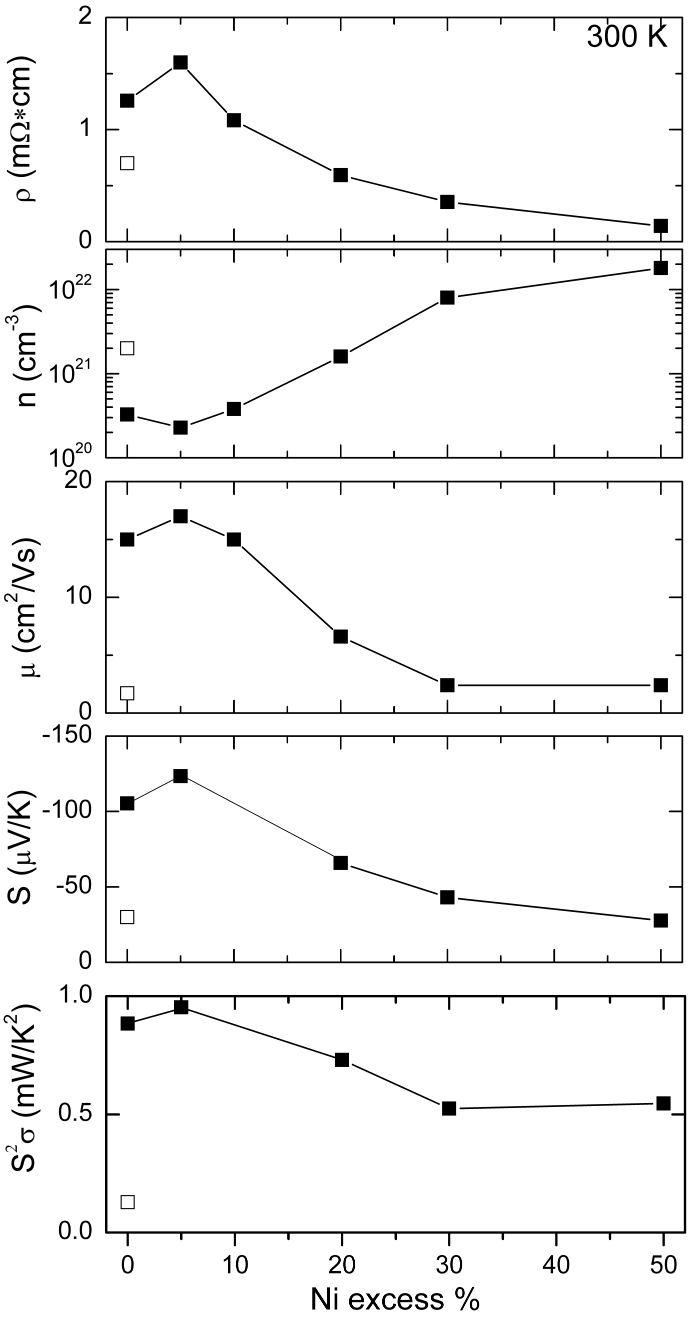

Figure 8.6. Room temperature resistivity (ρ), electron density (n), electron mobility (μ), Seebeck coefficient (S), and power factor ($S^2\sigma$) measurements for the 25 nm $Ni_{1+\delta}TiSn$ samples as a function of excess Ni content δ (closed squares). For comparison, the corresponding values for a stoichiometric NiTiSn sample grown by sputtering are also plotted (open squares, from Ref. [143].

minimized) for an excess Ni content of 5%. The results suggest that moderate amounts of excess Ni do not significantly hamper the electronic transport properties, and for 5% excess Ni transport properties are in fact enhanced. Additional thermal conductivity measurements (e.g. by time-domain thermal reflectance or 3-omega measurements) are necessary to determine the effect of excess Ni on phonon scattering and calculate ZT.

Chapter 9

Conclusions and Outlook

In this dissertation we have investigated the epitaxial growth, surface, and electronic properties of two materials systems: (1) rare earth monopnictide (RE-V) nanostructures embedded in III-V compound semiconductors and (2) semiconducting Half Heusler alloys.

9.1 Embedded RE-V / III-V nanocomposites

In the first part we demonstrated the controlled growth of a wide range of semimetallic ErSb nanostructures embedded within a semiconducting matrix. While previous work has focused primarily on the growth of embedded RE-V nanoparticles for application in thermoelectrics, here we showed that by increasing the Er composition (and temperature) during simultaneous growth with Ga and Sb, a wide range of new nanostructures form including vertically aligned nanorods, horizontally aligned nanorods, branched nanotrees, and lamellar nanosheets. These ErSb nanostructures form simultaneously with the GaSb matrix and have epitaxial, coherent interfaces. By combining MBE growth with *in-situ* STM, we imaged the growth surfaces one atomic layer at a time and showed that the nanostructured composites form via a surface-mediated self-assembly mechanism that is controlled entirely at the growth front and is not a product of bulk diffusion or bulk segregation.

Using ARPES and scanning tunneling spectroscopy we showed that despite the predicted effects from simple quantum confinement models, the ErSb and related ErAs nanostructures remain semimetallic down to their smallest dimensions. Measurements of the local density of states across the ErAs/GaAs interface reveal a state within the GaAs bandgap that decays into the GaAs matrix, and we proposed a model based on interface states and screening that may explain why the ErAs nanostructures remain semimetallic.

This retained metallicity and the ability to control the size and shape of the nanostructures makes the RE-V / III-V system attractive for application in many "active metal" devices. Here the shape anisotropy can be used as an adjustable parameter, and one promising application for the embedded nanorods is in all epitaxial polarization filters, which enables direct integration into optoelectronic devices [55]. One could also use these nanorods for embedded interconnects, plasmonic devices (e.g. enhanced light absorption in solar cells), or selectively etch the ErSb nanorods from the GaSb matrix to yield porous membranes.

However, more fundamental work is needed to understand the growth mechanism and control the morphologies at high Er composition, especially the crossover from vertically to horizontally aligned nanorods. While the vertical nanorods for moderate Er composition ($< 15\%$ Er) are continuous throughout the layer, the horizontally aligned nanorods at higher Er composition ($> 20\%$ Er) tend to be more segmented, with average lengths on the order of tens of nanometers. One possible method for growing more continuous wires may be to use vicinal substrates to induce a lateral step-flow growth mode, and also to increase the growth temperature to increase the anisotropic surface diffusion. Such longer more continuous wires may enable lower frequency or DC applications of the in-plane nanorods. One could also envision engineering more exotic nanostructures, such as tapered vertical nanorods, by modulating the Er composition, substrate temperature, or V/III flux ratio during growth.

Additionally, the details of the RE-V/III-V interfaces and their impact on electronic structure are still not well understood. While we have shown that the presence of ErAs/GaAs interface states and screening provide a strong modification to the simple effective mass model [72], the details of that interface and other RE-V/III-V interfaces (e.g. ErSb/GaSb, TbAs/GaAs), are not well understood. One could extend the ARPES and cross sectional STS used in this dissertation, in combination with STEM-EELS, for more detailed studies of the RE-V/III-V interfaces.

Many of these developments were enabled by the fact that the semimetallic RE-V and semiconducting III-V are thermodynamically stable in contact with one another and have similar crystal structures with a small lattice mismatch. In recent years the field of embedded RE-V nanostructures in III-Vs has continued to expand and now includes CeAs in In(Ga,Al)As [107], TbAs In(Ga,Al)As [61], LuAs in GaAs [108], and LaAs in GaAs [109]. Recent studies by Rachel Koltun in our group have also explored ScAs [191] and GdAs (unpublished) nanoparticles embedded in InGaAs. But beyond other RE-V/III-Vs, the studies presented here can be used to guide the search for other materials systems with similar metal/semiconductor coexistence. One of those systems is the Full Heusler/Half Heusler system.

9.2 Semiconducting Half Heusler compounds

In the second part we demonstrated the first growth of semiconducting Half Heusler compounds by MBE. The resulting CoTiSb and NiTiSn films, grown on InAlAs/GaAs(001) and MgO(001) respectively, are epitaxial and single crystalline as observed by RHEED and XRD. The films show semiconducting-like transport properties as a function of temperature, with higher electron mobilities and lower background carrier densities ($\mu > 500$ cm^2/Vs and $n < 10^{18}$ cm^{-3} for CoTiSb at room temperature) than their bulk counterparts.

These CoTiSb(001) and NiTiSn(001) films exhibit a number of different surface reconstructions, with phase behavior that is similar to that observed for III-V semiconductors. As a function of anneal temperature and Sb flux, CoTiSb(001) exhibits three different surface reconstructions. LEED, XPS, and STM measurements suggest that two of the reconstructions are characterized by surface Sb-Sb dimers and the third is characterized by an ad-layer of Sb on the surface. These reconstructions are also electronically distinguishable, emphasizing the importance of controlling the particular surface reconstruction. Based on these measurements we proposed atomic models of the surface reconstructions.

NiTiSn(001) shows similar phase behavior. To enable high resolution synchrotron photoemission spectroscopy measurements, we developed an Sb capping scheme to protect the CoTiSb surfaces. A suitable capping scheme for NiTiSn could not be found.

Using this capping scheme we demonstrated the first **k**-resolved bandstructure measurements for CoTiSb, or any semiconducting Half Heusler with finite bandgap. The measured bulk band dispersions along $\Gamma - X$ and $\Gamma - L$ are in general agreement with the DFT calculated bandstructure, confirming that CoTiSb is a semiconductor with a bandgap of at least 0.7 eV. The CoTiSb(001)-$c(2 \times 4)$ reconstruction also exhibits metallic surface states that lie within the bulk bandgap. Ongoing work is aimed at comparing these surface states to calculations based on the proposed reconstruction models.

Armed with a clearer understanding of the pure phase semiconducting Half Heuslers, and motivated by previous studies on RE-V/III-V nanocomposites, we explored the growth of Full Heusler / Half Heusler Ni_2TiSn/NiTiSn nanocomposites for thermoelectric applications. Initial X-ray diffraction measurements suggest the precipitation of a secondary phase, and room temperature transport measurements suggest that moderate amounts of excess Ni ($\delta = 5\%$) actually *improve* the electronic transport properties. Further TEM measurements are needed to identify the secondary phase, and thermal transport measurements are needed to determine the effect of the secondary phase on phonon scattering.

Moving forward, while the NiTiSn and CoTiSb films show good transport properties, the growth of these Half Heuslers by MBE is far from optimized and there is much room to improve. For example, initial growths with an Sb overpressure suggest that it may be possible to grow CoTiSb in an adsorption-limited growth window, similar to the As- or Sb- limited regime used for the MBE growth of III-As and III-Sb compounds. More systematic studies are needed in order determine the growth window. However, one challenge is that if the growth temperature is raised too high, reactions will occur at the CoTiSb film / InAlAs buffer layer interface. Additionally, while an adsorption limited growth window may exist for CoTiSb, such a window should be regarded as the exception rather than the rule for Heuslers. Many Full and Half Heuslers, e.g. NiTiSn, are composed of elements with very low vapor pressures and hence an adsorption-limited window is not guaranteed. But the replacement of elemental sources with more volatile metallorganic precursors may provide an avenue towards finding a growth window for Heuslers and other intermetallics.

Many additional measurements would also be helpful. For one, the ARPES measurements in this dissertation only probe occupied states, and from STS we only have a rough estimate of the bandgaps. Optical absorption would be a helpful for measuring the bandgap and probing unoccupied states. Initial measurements in the IR did not yield any significant absorption peaks beyond the background from the substrate, but more measurements in the IR and UV-visible are necessary. Additionally, since the carrier density for the CoTiSb films is reasonably low ($< 10^{18}$ cm^{-3} at room temperature), it may be possible to perform transport measurements while modulating the density by gating or by doping.

Finally, the methods developed in this dissertation could be applied to the growth of other Half Heuslers with novel functionality, such as half metals and topological insulators, as well as the growth of Heusler heterostructures. For example, topological insulators are currently of great interest due to their “protected” metallic surface states; however an outstanding challenge is minimizing the bulk carriers such that topological states can clearly be distinguished from bulk states. MBE growth of topological insulator candidates PtLuSb or PtLuBi in an adsorption limited regime, combined with the Sb (or Bi) capping techniques developed here for ARPES measurements, could be a powerful approach for growing and characterizing Half Heusler topological insulators. Some work in our group has already begun exploring these compounds [192]. Additionally, in the past two years several new properties of semiconducting Half Heuslers have been predicted, including piezoelectricity in the cubic Half Heuslers and ferroelectricity in the related hexagonal Half Heuslers [193, 194]. At first glance these properties are surprising, as they are normally associated with good insulators and not intermetallics. The ability to grow semiconducting Half Heuslers with low carrier density by MBE enables these new properties and many others to be investigated.

Appendix A

XPS layer intensity modeling

This Appendix section describes the use of layer photoemission intensity modeling the quantify the composition of films measured by XPS. The XPS core level peak intensities can be calculated by approximating the total photoemission intensity as the sum of the attenuated intensities generated from each atomic layer [195].

$$I_{x,total} = \sum_{i=1}^{N} I_{x,i} \tag{A.1}$$

where x denotes the elemental core level of interest and i indexes the atomic layer, where i runs from 1 (the surface) to N (the total number of layers). Here the intensity generated from elemental core level x in the i^{th} layer is given by

$$I_{x,i} = f_x \sigma_x n_{x,i} \prod_{i=1}^{N} \alpha_{x,i} \tag{A.2}$$

where f_x is an elemental instrument factor, σ_x is the photoionization cross-section of elemental core level x, $n_{x,i}$ is the planar atomic density of element x in layer i, and $\prod_{i=1}^{N} \alpha_{x,i}$ is an attenuation term that accounts for electron scattering effects from all layers above i. The individual attenuation terms are given by

$$\alpha_{x,i} = exp(\frac{-d_i}{\lambda_{x,i} cos\phi}) \tag{A.3}$$

where d_i is the interlayer spacing, ϕ is the emission angle of the electrons relative to normal, and $\lambda_{x,i}$ is the attenuation length of the photoelectrons through layer i. In our experiments $\phi = 55°$. This attenuation length is calculated from an elastic correction to the empirical Tanuma, Powell, and Penn (TPP-2M) model for the inelastic mean free path, where

$$\lambda_{x,i} = \lambda_{IMFP,x,i}(1 - 0.028Z_i^2)[0.501 + 0.068ln(E_x)] \tag{A.4}$$

and

$$\lambda_{IMFP,x,i} = E_x/\{\epsilon_i^2[\beta_i ln(\gamma_i E_i) - C_i/E_i + D_i/E_x^2]\} \tag{A.5}$$

where E_x is the kinetic energy of the photoemitted core electrons and γ_i, C_i, and D_i are element specific materials parameters as noted elsewhere.

We now apply this to the CoTiSb(001) surface in order to quantify the amount of excess Sb at the surface for (1 × 4) reconstruction. Following the (001) Half Heusler stacking sequence, we treat CoTiSb(001) as alternating atomic layers of Co ($n_{Co,Co} = 2/a_0^2$) and TiSb ($n_{Ti,TiSb} = n_{Sb,TiSb} = 2/a_0^2$) with interlayer spacing $d_i = a_0/4$ ($a_0 = 5.88$ Å is the lattice constant). Since the (2 × 1) surface reconstruction is stable upon annealing with excess Sb and also with explicit TiSb termination in the MBE, we let the stack terminate with TiSb at the surface (i.e. TiSb / Co / TiSb / Co ...). This is also consistent with the MnSb termination observed for the similar MBE-grown Half Heusler NiMnSb(001) [145]. Since density functional theory calculations suggest that Sb dimers are unstable on a 1:1 stoichiometric TiSb surface, we also consider the case where the top TiSb layer is Ti deficient (i.e. Sb / Co / TiSb / Co / TiSb ...).

To generate the total intensity, each layer is attenuated by the layers above it such that for the (2×1) CoTiSb reconstruction, the top TiSb layer is unattenuated, the next Co layer is attenuated by $\alpha_{x,TiSb}$, the next TiSb layer is attenuated by $\alpha_{x,TiSb}\alpha_{x,Co}$, the next Co layer by $(\alpha_{x,TiSb})^2\alpha_{x,Co}$, etc. The total intensity for elemental core level x for the (2×1) reconstruction then becomes

$$\begin{aligned}
I_{x,(2\times1)} =& I_{x,CoTiSb} \\
=& f_x[(\sigma_x n_{x,TiSb}) + (\sigma_x n_{x,Co}\alpha_{TiSb}) \\
& + (\sigma_x n_{x,TiSb})\alpha_{x,TiSb}\alpha_{x,Co} + (\sigma_x n_{x,Co})(\alpha_{x,TiSb}\alpha_{x,Co})\alpha_{x,TiSb} \\
& + (\sigma_x n_{x,TiSb})(\alpha_{x,TiSb}\alpha_{x,Co})^2 + (\sigma_x n_{x,Co})(\alpha_{x,TiSb}\alpha_{x,Co})^2\alpha_{x,TiSb} + ...] \\
=& f_x[(\sigma_x n_{x,TiSb}) + (\sigma_x n_{x,Co})\alpha_{x,TiSb}]\left(\frac{1}{1-\alpha_{x,TiSb}\alpha_{x,Co}}\right)
\end{aligned}$$

where we have rewritten the sum of attenuation terms using the result for an infinite geometric series since the total thickness of the CoTiSb is much larger than the attenuation length.

We then model the (1×4) reconstruction as having N monolayers of Sb on top of the

	$\frac{\left(I^{Sb}/I^{Ti}\right)_{(1\times4)}}{\left(I^{Sb}/I^{Ti}\right)_{(2\times1)}}$	$\frac{\left(I^{Sb}/I^{Co}\right)_{(1\times4)}}{\left(I^{Sb}/I^{Co}\right)_{(2\times1)}}$	$\frac{\left(I^{Ti}/I^{Co}\right)_{(1\times4)}}{(I^{Ti}/I^{Co})_{(2\times1)}}$
measured	1.68	1.62	0.97
model, 1.5 ML Sb	1.56	1.69	1.09

Table A.1. Measured XPS core level intensity ratios and comparison to the atomic layer model.

CoTiSb(001) surface, i.e. (N ML Sb) / TiSb/Co/TiSb/Co... The total intensity is

$$I_{x,(1\times4)} = I_{x,CoTiSb}(\alpha_{x,adlayer})^N + f_x\sigma_x n_{x,adlayer}\left[\frac{1-(\alpha_{x,adlayer})^N}{1-\alpha_{x,adlayer}}\right] \tag{A.6}$$

In order to remove the elemental instrument factors f_x we take the ratio of one elemental core level intensity to another core level intensity for the (1×4), and then divide by the corresponding ratio for the (2×1) reconstruction, e.g. $\{(I_{Sb}/I_{Ti})_{(1\times4)}\}/\{(I_{Sb}/I_{Ti})_{(2\times1)}\}$. In the calculations we let the attenuation for the alternating Co and TiSb layers take on the averaged values for CoTiSb, i.e. $\alpha_{x,TiSb} = \alpha_{x,Co} = \alpha_{x,CoTiSb}$ Table A.1 shows measured and calculated values of the double ratios, using the Sb 3d, Co 2p, and Ti 2p integrated intensities. Good agreement with the model is found for an excess (1×4) Sb coverage of 1.5 ML (Table A.1).

Appendix B

NiTi shape memory alloys

NiTi is a technologically important alloy that shows the shape memory effect and superelasticity. Its martensitic phase transformations have been widely studied in the bulk and in polycrystalline films. In previous publications [196, 197] we demonstrated the first MBE growths of single crystalline epitaxial NiTi films on MgO(001) and GaAs(001) substrates. We showed that despite the substrate constraint, the films undergo reversible martensitic phase transformations, and the results suggested that the transformation occurs by an in-plane shear that does not disturb the lattice coherence at the film/substrate interfaces. In this Appendix we provide further details of the growth and temperature dependent X-ray diffraction (XRD) measurements.[1]

Samples were grown by MBE in a modified VG V80 system that is dedicated for metals growth. This is the same system that was used for growths of the Half Heuslers NiTiSn and CoTiSb. For bulk NiTi, the high temperature austenite phase is a cubic

---

[1] Some of the work presented in this chapter has previously appeared in the following publications: [196, 197].

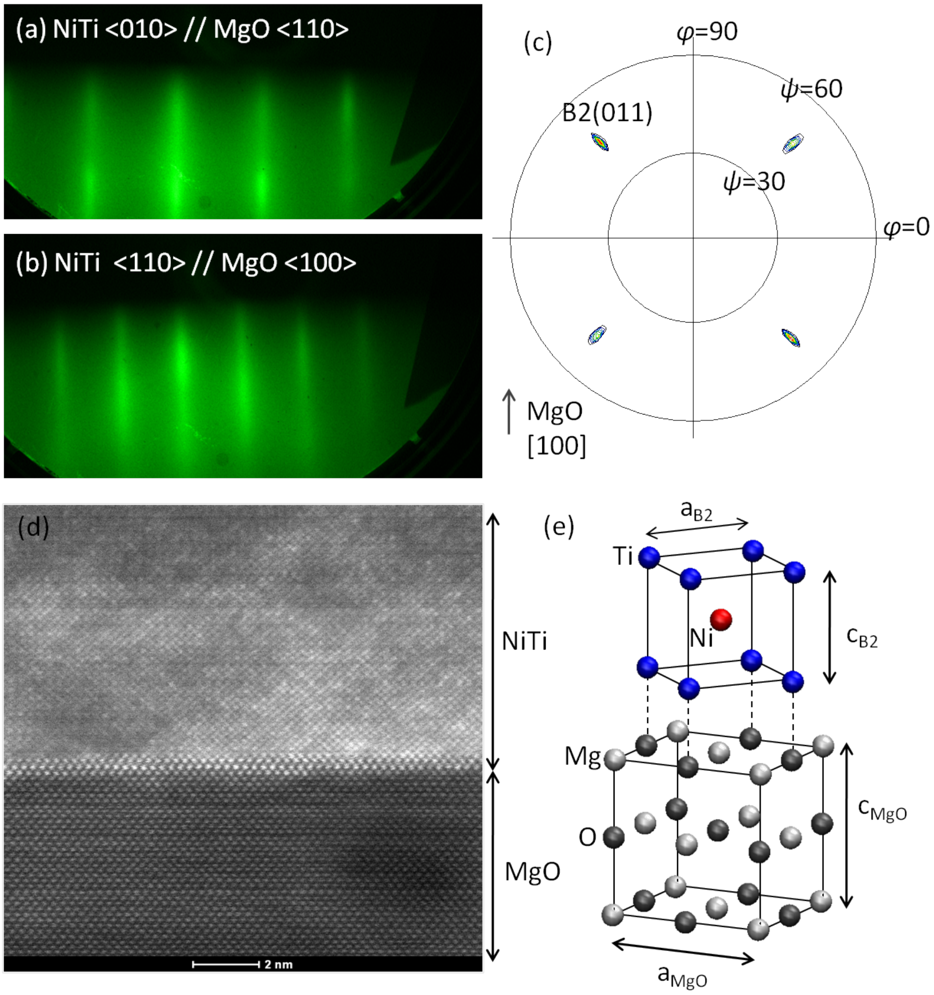

Figure B.1. (a,b) RHEED patterns for a 35 nm NiTi sample grown on MgO(001) at 560°C. (c) Pole figure of the NiTi (011) reflection, demonstrating that the NiTi film is rotated 45 degrees with respect to the MgO(001) substrate. (d) High-angle annular dark field (HAADF) cross sectional TEM image of NiTi on MgO(001), courtesy of Stefan Kramer. (e) Schematic of the NiTi/MgO(001) epitaxial relationship.

B2 while the low temperature martensite is a monoclinic B19'. Two substrates have been used for NiTi growth: MgO(001) and GaAs(001). MgO(001) was chosen because it is chemically stable with many intermetallic compounds and has a fairly small lattice mismatch with NiTi: $a_{NiTi,B2} = 3.015$ Å, $a_{MgO} = 4.212$ Å, mismatch of 1.3% for cube-on-cube alignment rotated 45 degrees around the c axis [Figure B.1(e)]. GaAs(001) was chosen because it is a commonly used substrate for III-V semiconductor devices and hence could be used for epitaxial integration of shape memory alloys with III-V devices. However, the lattice mismatch between NiTi and GaAs(001) is considerably larger: 6.7% for cube-on-cube growth with 2×2 NiTi B2 unit cells per GaAs zincblende unit cell.

For growths on MgO(001), after loading into UHV the substrates were annealed at 500°C to produce a (1×1) RHEED pattern. On some samples a 10 nm MgO buffer layer was then grown by electron beam evaporation of MgO. NiTi films were then grown by simultaneous deposition from elemental Ni and Ti sources. Cell fluxes were calibrated Rutherford Backscattering Spectrometry measurements of calibration NiTi samples grown on Si. By this method compositions could be controlled to approximately 1 atomic percent. Films were grown to a thickness of 35 nm at a rate of 11 nm/hr. Figure B.1(a,b) shows RHEED patterns of a 35 nm NiTi sample grown on MgO(001) at 560°C. During growth samples showed a streaky (1×1) pattern indicating two-dimensional growth, and XRD pole figure measurements of the NiTi B2 (011) reflections [Figure B.1(c)] confirm a 45 degree rotated cube-on-cube relationship with the substrate [Figure B.1(e)].

To investigate ordering in the films, XRD 2θ measurements (Cu $K\alpha$) were performed

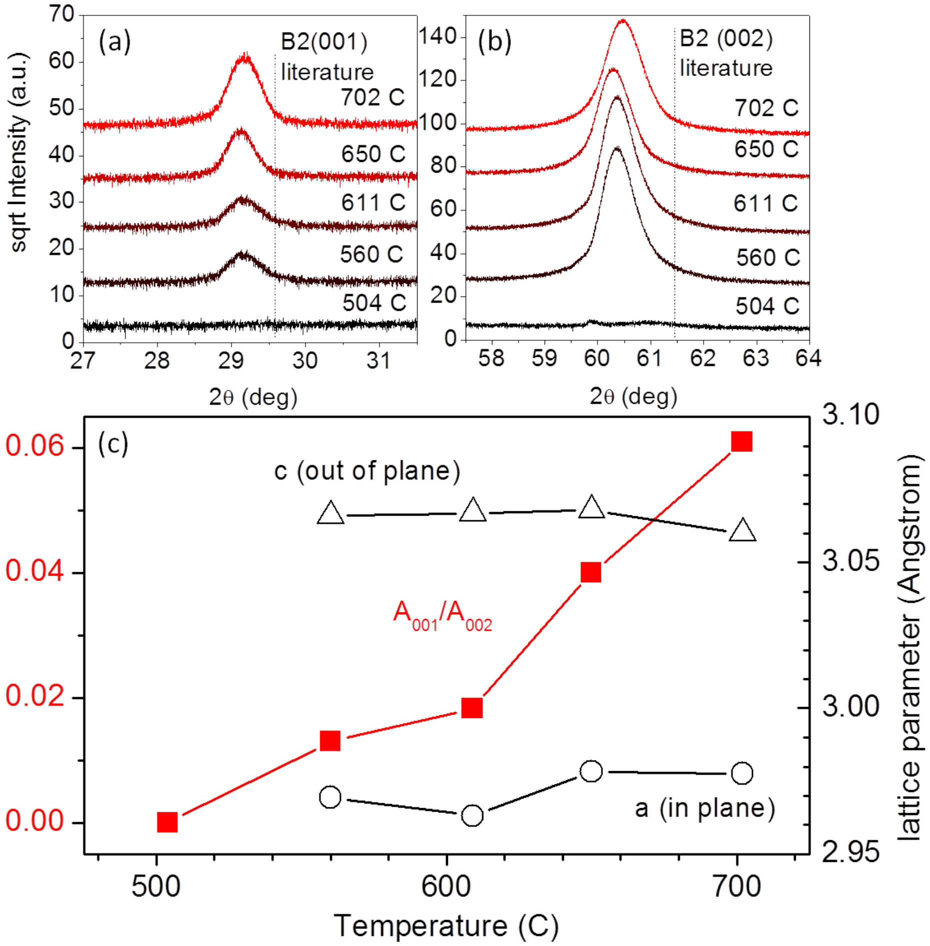

Figure B.2. Order parameter and lattice constants for 35 nm NiTi films grown on MgO(001). (a) XRD 2θ measurements of the NiTi B2(001) reflection using Cu $K\alpha$ radiation. The peak increases in intensity with increasing growth temperature. (b) B2(002) reflection. The (002) magnitude stays relatively constant. (c) Plot of the order parameter A_{001}/A_{002} versus growth temperature, and plot of the measured out-of-plane and calculated in-plane (assuming constant cell volume) lattice parameters versus growth temperature calculated from the angles in (a) and (b). We see an increase in order of the B2 superstructure, while both the in-plane and out-of-plane lattice parameters remain constant.

on a series of 35 nm stoichiometric NiTi films grown on MgO substrates at various temperatures. Figure B.2(a,b) show the B2 (001) and (002) film reflections respectively. For all samples the (001) and (002) reflections appear at lower angle, suggesting pseudomorphic growth and an expansion in the out-of-plane lattice parameter with respect to the bulk. With increasing growth temperature the magnitude of the (001) reflection increases while the magnitude of (002) remains roughly constant. We define a B2 ordering parameter as the ratio of the intensities of the (001) and (002) peaks: for B2 ordering this A_{001}/A_{002} ratio is finite while for a disordered BCC structure the ratio would tend towards zero because the (001) is not an allowed peak for BCC. Figure B.2(c) shows a plot of this order parameter along with the in-plane and out-of-plane lattice parameters versus growth temperature. The order parameter increases with increasing growth temperature suggesting best quality NiTi on MgO(001) is grown at or above 700°C. Growths were not performed much above 700°C due to substrate heater limitation.

For growths on GaAs(001) substrates, after desorption of the native oxide under As flux, III- V buffer layers were first grown in a separate III-V VG V80H MBE system that is connected to the metals V80 system through UHV. Buffer layer sequences typically consisted of ErAs(5 nm)/GaAs(50 nm)/$Al_{0.7}Ga_{0.3}As$(500 nm)/GaAs(500 nm)/GaAs(001). Here the AlGaAs serves as an etch stop for the processing of free standing NiTi films, while the ErAs serves as a diffusion barrier to prevent interfacial reactions between the NiTi and GaAs. Due to the high reactivity of Ni with GaAs, direct growth of NiTi on GaAs was not attempted. After buffer layer growth, samples were then transferred through UHV to the metals MBE system for growth of NiTi. NiTi growths on the

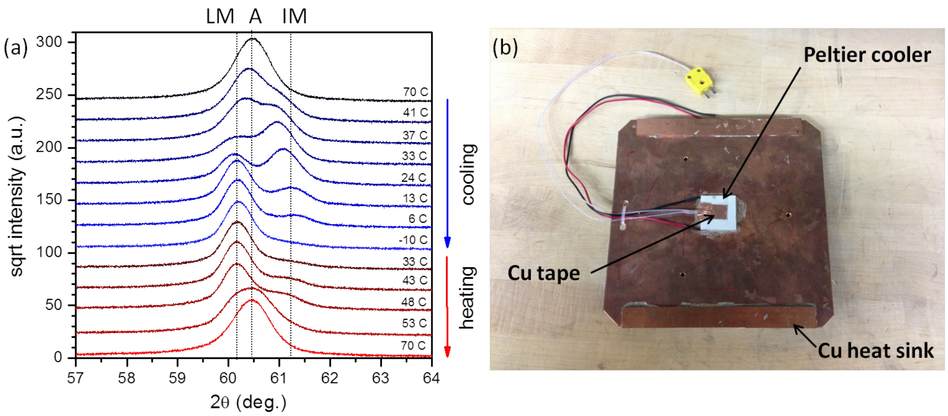

Figure B.3. (a) Temperature dependent XRD 2θ measurement of the (002) reflection of a Ni$_{0.49}$Ti$_{0.51}$. At high temperatures the NiTi is in the B2 Austenite phase (A). Upon cooling the film transforms into an intermediate martensite (IM), followed by a low temperature martensite (LM). The austenite is recovered upon heating. (b) Picture of heater assembly used for the temperature dependent XRD measurements. Samples were mounted to a Peltier cooler using thermally conductive copper tape. The back of the Peltier cooler was mounted to a large copper block which serves as a heat sink, and the entire heater assembly is mounted in the diffractometer. For measurement near and below 0°C the sample was covered with Kapton foil and dry nitrogen was continuously blown on the sample surface to prevent water vapor condensation on the sample.

ErAs/GaAs buffer layer structure were typically performed at a slightly lower temperature of 600°C as opposed to 700°C for growths on MgO. It was found that for some growths of NiTi on ErAs/GaAs at 700°C the RHEED pattern began to fade presumably due to interfacial reactions. But it is suspected that for some of these samples the ErAs diffusion barrier was thinner than expected and may have had pinholes to the GaAs buffer.

For studies of the martensitic phase transitions, temperature depended XRD measurements were performed in a Rigaku Smartlab Diffractometer using Cu $K\alpha$ radiation. For temperature control we assembled a heating stage which consists of a Peltier cooler that is glued with thermal epoxy to a large copper block [Figure B.3(b)]. It was found that this copper heat sink was needed in order to achieve stable temperatures. The assembly also has a thermocouple and the temperatures were controlled using a Eurotherm and DC power supply. The samples are mounted on the Peltier cooler using conductive Cu tape. This heater assembly could be mounted directly onto the horizontal sample stage of the Rigaku Diffractometer. For measurements at low temperature, in order to prevent water condensation on the sample we covered the sample with Kapton foil and blew the surface continuously with dry nitrogen. Figure B.3(a) shows temperature dependent measurements of the (002) reflection for a 35 nm NiTi sample on MgO(001) with stoichiometry 51 at.% Ti. At high temperature the austenite phase (A) is observed, and upon cooling the film transforms into an intermediate martensite (IM) and a low temperature martensite (LM). The austenite is recovered upon heating. We emphasize that these measurements were performed on an unprocessed film that is still clamped to the substrate. Further temperature dependent reciprocal space maps of the (011) reflection suggest that the transformation occurs by shearing parallel to the film plane, such that the lattice registry at the NiTi/MgO interface remains coherent [197].

Appendix C

MATLAB code for ARPES bulk dispersions using free electron like final states

The following MATLAB code converts ARPES normal emission energy dispersion curves (EDCs) at varying photon energy to a k perpendicular scale using a model of free-electron-like final states, i.e.

$$k_{\perp} = \sqrt{\frac{2m^{*}}{\hbar^{2}}} \left(E_{kin} cos^{2}\theta + U_{0}\right)^{1/2}. \tag{C.1}$$

For scans at normal emission $cos^{2}\theta = 1$. In the code, the inner potential U_0 can be used as an adjustable parameter to match the periodicity of the measured bands. The inputs to the code are 'normalGX.txt' (matrix whose columns are the energy dispersion curves at each photon energy), the photon energies, the inner potential, the workfunction, and the range of binding energies. After calculating $k_\perp$ for each point in the photoemission intensity matrix, it uses MATLAB's mesh command to plot the intensity versus binding energy and $k_\perp$. An example for the CoTiSb(001) surface is shown in Figure C.1.

```
A=importdata('normalGX.txt'); %photoemission intensity matrix
Ephoton=[[14:1:40],[42:2:90],[94:4:178]]; %vector of photon energies in eV
U0 = 12; %inner potential in eV
phi = 4.5; %workfunction in eV

%assemble vector containing binding energies
Eblow = -2.80625; %binding energy minimum in eV
Ebhigh  = 0.15625; %binding energy maximum in eV
Nebinding = length(A.data(:,1));
Nephoton = length(A.data(1,:));
dEbinding = (Ebhigh-Eblow)/(Nebinding-1);
Ebinding = [Eblow:dEbinding:Ebhigh];

%assemble matrix of binding energies. Ematrix has same dimensions as A.data
Ematrix=zeros(Nebinding,Nephoton);
for i=1:Nephoton
    Ematrix(:,i)=Ebinding;
end

%assemble matrix of kperpendicular values.
%kperp has same dimensions as A.data
kperp=zeros(Nebinding,Nephoton);
for i=1:Nephoton
    for j=1:Nebinding
        kperp(j,i) = 0.512*sqrt(Ephoton(i)+Ebinding(j)-phi+U0);
    end
end

%plot intensity matrix A.data versus kperp and binding energy
figure
hold on
mesh(kperp,Ematrix,A.data)
view(2)
colormap gray
xlabel('k_z (Angstrom^{-1})')
ylabel('Energy (eV)')
```

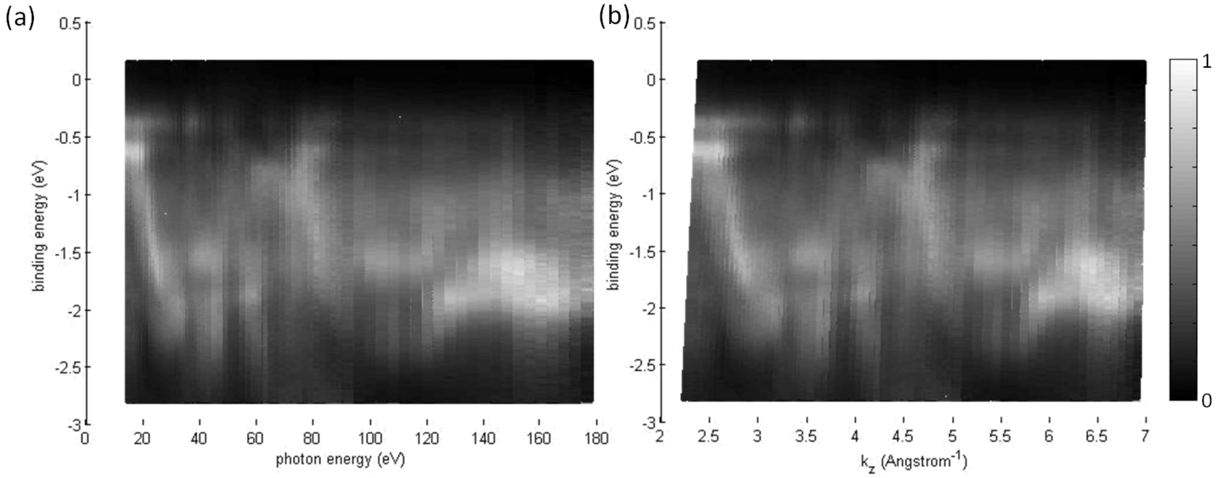

Figure C.1. (a) Plot of the photoemission intensity versus binding energy and photon energy for normal emission measurements of a CoTiSb(001) surface. Each vertical slice is an energy dispersion curve (EDC) of photoemission intensity versus binding energy. This is the input to the MATLAB code. (b) Plot of the photoemission intensity versus binding energy and the perpendicular component of momentum k_z, which was calculated using the MATLAB code.

Appendix D

MATLAB code numerical solutions to the Schrödinger equation

The following code solves the Schrödinger equation for an arbitrary potential using finite differences. This code was used to find the ground state energies for electrons and holes in ErAs subject to a confinement potential. The example potential shown below and in Figure D.1 is for the 1D harmonic oscillator.

```
%inputs
N=500;      %N by N mesh
xmax=30;    %outer bound for x
hbar=1; %hbar=m=1 for units of hartree
m=1;

dx=xmax/N;
x=[-xmax/2+dx:dx:xmax/2];

%harmonic oscillator potential
U=1/2*x.^2;

% assemble the Hamiltonian matrix
H=zeros(N,N);
```

```
t0=hbar^2/(2*m*dx^2);
for i=1:N
    for j=1:N
        if i==j+1
            H(i,j)=-t0;
        elseif i==j-1
            H(i,j)=-t0;
        elseif i==j
            H(i,j)=U(i)+2*t0;
        end
    end
end

%diagonalize the matrix
%En(n,n) is the energy
%Psi(:,n) is the corresponding wavefunction
[Psi,En]=eig(H);

%plot
figure
hold on
plot(x,U,'k')
norm=max(U)/max(abs(Psi(:,1)))/5;
plot(x,Psi(:,1)*norm+E0*10)
plot(x,Psi(:,2)*norm+En(2,2)*10,'r')
plot(x,Psi(:,3)*norm+En(3,3)*10,'g')
plot(x,Psi(:,4)*norm+En(4,4)*10,'m')
xlabel('x')
ylabel('energy')

legend('U(x)',['\Psi_{0}(x), E_0 = ',num2str(E0)],
['\Psi_{1}(x), E_1 = ',num2str(En(2,2))],
['\Psi_{2}(x), E_2 = ',num2str(En(3,3))],
['\Psi_{3}(x), E_3 = ',num2str(En(4,4))])
```

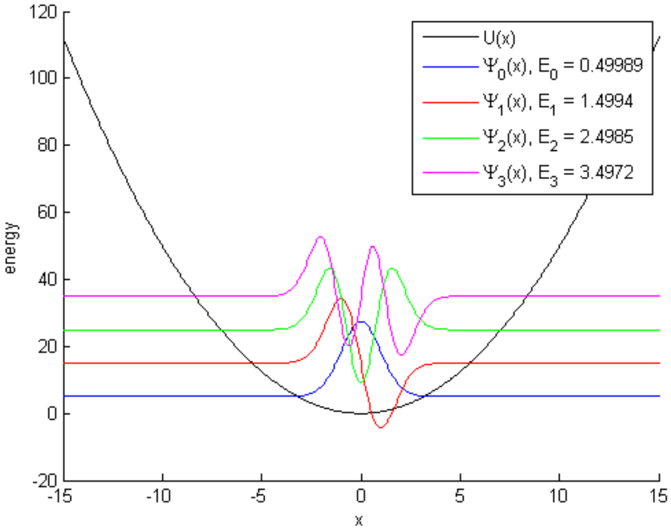

Figure D.1. Solutions for the 1D harmonic oscillator solved numerically in MATLAB using finite differences. Energy units are in Hartree.

Bibliography

[1] K. von Klitzing, G. Dorda, and M. Pepper. New method for high-accuracy determination of the fine-structure constant based on quantized hall resistance. *Phys. Rev. Lett.*, 45:494–497, Aug 1980. doi:10.1103/PhysRevLett.45.494. URL `http://link.aps.org/doi/10.1103/PhysRevLett.45.494`.

[2] D.C. Tsui, H.L. Stormer, and A.C. Gossard. Two-dimensional magnetotransport in the extreme quantum limit. *Phys. Rev. Lett.*, 48(22):1559–1562, 1982. URL `http://link.aps.org/doi/10.1103/PhysRevLett.48.1559`.

[3] D. G. Schlom. *Molecular beam epitaxial growth of cuprate superconductors and related phases*. PhD thesis, Stanford University, 1990. URL `http://snowboard.stanford.edu/thesis/Schlom.pdf`.

[4] H. Kroemer. Nobel Lecture: Quasielectric fields and band offsets: teaching electrons new tricks. *Reviews of Modern Physics*, 73(July), 2001. doi:10.1103/RevModPhys.73.783.

[5] R. Dingle, H. L. Stormer, A. C. Gossard, and W. Wiegmann. Electron mobilities in modulation-doped semiconductor heterojunction superlattices. *Applied*

Physics Letters, 33(7):665–667, 1978. URL http://ieeexplore.ieee.org/xpls/abs_all.jsp?arnumber=4847708.

[6] J. Tobola, J. Pierre, S. Kaprzyk, R. V. Skolozdra, and M. A. Kouacou. Crossover from semiconductor to magnetic metal in semi-Heusler phases as a function of valence electron concentration. *Journal of Physics: Condensed Matter*, 10:1013, 1998. URL http://iopscience.iop.org/0953-8984/10/5/011.

[7] R. A. de Groot, F. M. Mueller, P. G. van Engen, and K. H. J. Buschow. New class of materials: Half-metallic ferromagnets. *Phys. Rev. Lett.*, 50:2024–2027, Jun 1983. doi:10.1103/PhysRevLett.50.2024. URL http://link.aps.org/doi/10.1103/PhysRevLett.50.2024.

[8] J. Winterlik, G. H. Fecher, and C. Felser. Electronic and structural properties of palladium-based Heusler superconductors. *Solid State Communications*, 145(9-10):475–478, March 2008. ISSN 00381098. doi:10.1016/j.ssc.2007.12.020. URL http://linkinghub.elsevier.com/retrieve/pii/S0038109807008794.

[9] P. C. Canfield, J. D. Thompson, W. P. Beyermann, a. Lacerda, M. F. Hundley, E. Peterson, Z. Fisk, and H. R. Ott. Magnetism and heavy fermion-like behavior in the RBiPt series. *Journal of Applied Physics*, 70(10):5800, 1991. ISSN 00218979. doi:10.1063/1.350141. URL http://link.aip.org/link/JAPIAU/v70/i10/p5800/s1&Agg=doi.

[10] J. W. Dong. Shape memory and ferromagnetic shape memory effects in single-crystal Ni_2MnGa thin films. *Journal of Applied Physics*, 95(5):2593, 2004. ISSN

00218979. doi:10.1063/1.1643199. URL http://link.aip.org/link/?JAP/95/2593/1&Agg=doi.

[11] S. Chadov, X. Qi, J. Kübler, G. H. Fecher, C. Felser, and S. C. Zhang. Tunable multifunctional topological insulators in ternary Heusler compounds. *Nature Materials*, 9(7):541–5, July 2010. ISSN 1476-1122. doi:10.1038/nmat2770. URL http://www.ncbi.nlm.nih.gov/pubmed/20512154.

[12] H. Lin, L. Wray, Y. Xia, S. Xu, S. Jia, R. Cava, A. Bansil, and M. Hasan. Half-Heusler ternary compounds as new multifunctional experimental platforms for topological quantum phenomena. *Nature Materials*, 9(7):546, July 2010. ISSN 1476-1122. doi:10.1038/nmat2771. URL http://www.ncbi.nlm.nih.gov/pubmed/20512153.

[13] C. J. Palmstrom. Epitaxial heusler alloys: New materials for semiconductor spintronics. *MRS Bulletin*, 28:725–728, 10 2003. ISSN 1938-1425. doi:10.1557/mrs2003.213. URL http://journals.cambridge.org/article_S088376940001931X.

[14] S. Ouardi, G. Fecher, B. Balke, X. Kozina, G. Stryganyuk, C. Felser, S. Lowitzer, D. Ködderitzsch, and H. Ebert. Electronic transport properties of electron- and hole-doped semiconducting $C1_b$ Heusler compounds : $\mathrm{NiTi}_{1x}\mathrm{M}_x\mathrm{Sn}$ (M = Sc, V). *Phys. Rev. B.*, 82:085108, 2010. doi:10.1103/PhysRevB.82.085108.

[15] R. Ohyama, T. Koyanagi, and K. Matsubara. Magneto-optical Kerr effect of rf-sputtered PtMnSb thin films. *Journal of Applied Physics*, 61(6):2347, 1987. ISSN

00218979. doi:10.1063/1.337948. URL http://link.aip.org/link/JAPIAU/v61/i6/p2347/s1&Agg=doi.

[16] K. Ahilan, M. Bennett, M. Aronson, N. Anderson, P. Canfield, E. Munoz-Sandoval, T. Gortenmulder, R. Hendrikx, and J. Mydosh. Magnetotransport in single-crystal half-Heusler compounds. *Phys. Rev. B.*, 69(24):245116, June 2004. ISSN 1098-0121. doi:10.1103/PhysRevB.69.245116. URL http://link.aps.org/doi/10.1103/PhysRevB.69.245116.

[17] J. R. Arthur. Interaction of Ga and As2 Molecular Beams with GaAs Surfaces. *Journal of Applied Physics*, 39(8):4032–4034, 1968. doi:http://dx.doi.org/10.1063/1.1656901. URL http://scitation.aip.org/content/aip/journal/jap/39/8/10.1063/1.1656901.

[18] A. Y. Cho. Gaas epitaxy by a molecular beam method: Observations of surface structure on the (001) face. *Journal of Applied Physics*, 42(5):2074–2081, 1971. doi:http://dx.doi.org/10.1063/1.1660490. URL http://scitation.aip.org/content/aip/journal/jap/42/5/10.1063/1.1660490.

[19] R. F. C. Farrow. *Molecular beam epitaxy: applications to key materials*. Noyes Publications, Park Ridge, NJ, 1995.

[20] A.Y. Cho and J.R. Arthur. Molecular beam epitaxy. *Progress in Solid State Chemistry*, 10, Part 3(0):157 – 191, 1975. ISSN 0079-6786. doi:http://dx.doi.org/10.1016/0079-6786(75)90005-9. URL http://www.sciencedirect.com/science/article/pii/0079678675900059.

[21] A. Cho. *Molecular Beam Epitaxy*. Key Papers in Applied Physics. Springer Verlag, 1994. ISBN 9781563961328. URL `http://books.google.com/books?id=5zcbAQAAIAAJ`.

[22] J. Y. Tsao. *Materials Fundamentals of Molecular Beam Epitaxy*. Elsevier Science, 1993. ISBN 9780080571355. URL `http://books.google.com/books?id=1kgfS1JKhi4C`.

[23] G. Binnig, H. Rohrer, Ch. Gerber, and E. Weibel. Surface studies by scanning tunneling microscopy. *Phys. Rev. Lett.*, 49:57–61, Jul 1982. doi:10.1103/PhysRevLett.49.57. URL `http://link.aps.org/doi/10.1103/PhysRevLett.49.57`.

[24] G. Binnig, H. Rohrer, Ch. Gerber, and E. Weibel. Tunneling through a controllable vacuum gap. *Applied Physics Letters*, 40(2):178–180, 1982. doi:http://dx.doi.org/10.1063/1.92999. URL `http://scitation.aip.org/content/aip/journal/apl/40/2/10.1063/1.92999`.

[25] G. Binnig, H. Rohrer, Ch. Gerber, and E. Weibel. 7x7 Reconstruction on Si(111) Resolved in Real Space. *Phys. Rev. Lett.*, 50:120–123, Jan 1983. doi:10.1103/PhysRevLett.50.120. URL `http://link.aps.org/doi/10.1103/PhysRevLett.50.120`.

[26] Rainer Timm. *Formation , atomic structure , and electronic properties of GaSb quantum dots in GaAs*. PhD thesis, TU Berlin, 2007.

[27] Pedram Roushan. Visualizing Surface States of Topological Insulators with Scanning Tunneling Microscopy. *Princeton Ph.D. Thesis*, (September), 2011.

[28] Dawn Bonnell. *Scanning Tunneling Microscopy and Spectroscopy: Theory, Techniques and Applications*. Wiley, 1993.

[29] Roland Wiesendanger. *Scanning Probe Microscopy and Spectroscopy: Methods and Applications*. Cambridge University Press, Cambridge, UK, 1994.

[30] Wikipedia. Scanning tunneling microscope, May 2014. URL `http://en.wikipedia.org/wiki/Scanning_tunneling_microscope`.

[31] Herbert Kroemer. *Quantum mechanics: for engineering, materials science, and applied physics*. Prentice Hall, 1994.

[32] J. Bardeen. Tunnelling from a many-particle point of view. *Phys. Rev. Lett.*, 6:57–59, Jan 1961. doi:10.1103/PhysRevLett.6.57. URL `http://link.aps.org/doi/10.1103/PhysRevLett.6.57`.

[33] J. Tersoff and D. R. Hamann. Theory and application for the scanning tunneling microscope. *Phys. Rev. Lett.*, 50:1998–2001, Jun 1983. doi:10.1103/PhysRevLett.50.1998. URL `http://link.aps.org/doi/10.1103/PhysRevLett.50.1998`.

[34] J. Tersoff and D. R. Hamann. Theory of the scanning tunneling microscope. *Phys. Rev. B*, 31:805–813, Jan 1985. doi:10.1103/PhysRevB.31.805. URL `http://link.aps.org/doi/10.1103/PhysRevB.31.805`.

[35] R. M. Feenstra, Joseph A. Stroscio, J. Tersoff, and A. P. Fein. Atom-selective imaging of the gaas(110) surface. *Phys. Rev. Lett.*, 58:1192–1195, Mar 1987. doi:10.1103/PhysRevLett.58.1192. URL `http://link.aps.org/doi/10.1103/PhysRevLett.58.1192`.

[36] Jennifer Eve Hoffman. A Search for Alternative Electronic Order in the High Temperature Superconductor $Bi_2Sr_2CaCuO_{8+\delta}$ by Scanning Tunneling Microscopy. *Ph.D. Thesis*, 2001.

[37] J E Hoffman, K McElroy, D-H Lee, K M Lang, H Eisaki, S Uchida, and J C Davis. Imaging quasiparticle interference in $Bi_2Sr_2CaCu_2O_{8+\delta}$. *Science (New York, N.Y.)*, 297(5584):1148–51, August 2002. ISSN 1095-9203. doi:10.1126/science.1072640.

[38] Pedram Roushan, Jungpil Seo, Colin V Parker, Y S Hor, D Hsieh, Dong Qian, Anthony Richardella, M Z Hasan, R J Cava, and Ali Yazdani. Topological surface states protected from backscattering by chiral spin texture. *Nature*, 460(7259):1106–9, August 2009. ISSN 1476-4687. doi:10.1038/nature08308.

[39] R. M. Feenstra. Tunneling spectroscopy of the (110) surface of direct-gap III-V semiconductors. *Phys. Rev. B*, 50:4561–4570, Aug 1994. doi:10.1103/PhysRevB.50.4561. URL `http://link.aps.org/doi/10.1103/PhysRevB.50.4561`.

[40] Stefan Hufner. *Photoemission Spectroscopy: Principles and Applications 3rd Ed.* Springer, Berlin, 2003.

[41] Jose Avila, Ivy Razado-Colambo, Stehane Lorcy, Bruno Lagarde, Jean-Luc Gior-

getta, Franois Polack, and Maria C Asensio. Antares, a scanning photoemission microscopy beamline at soleil. *Journal of Physics: Conference Series*, 425(19): 192023, 2013. URL `http://stacks.iop.org/1742-6596/425/i=19/a=192023`.

[42] S. D. Kevan. *Angle-Resolved Photoemission: Theory and Current Applications*. Elsevier, Amsterdam, 1992.

[43] E. W. Plummer and W. Eberhardt. *Angle-Resolved Photoemission as a Tool for the Study of Surfaces*, volume 49, pages 533–656. John Wiley & Sons, Inc., 1982. ISBN 9780470142691. doi:10.1002/9780470142691.ch8. URL `http://dx.doi.org/10.1002/9780470142691.ch8`.

[44] Philip Hofmann. *Surface Physics: An Introduction*. Philip Hofmann, Aarhus, DK, 2013. ISBN 978-87-996090-0-0.

[45] D. P. Woodruff and T. A. Delchar. *Modern Techniques of Surface Science*. Cambridge University Press, Cambridge, UK, 1994.

[46] C. N. Berglund and W. E. Spicer. Photoemission studies of copper and silver: Theory. *Phys. Rev.*, 136:A1030–A1044, Nov 1964. doi:10.1103/PhysRev.136.A1030. URL `http://link.aps.org/doi/10.1103/PhysRev.136.A1030`.

[47] F J Himpsel. Experimental determination of bulk energy band dispersions. *Applied Optics*, 19(23):3964–70, December 1980. ISSN 0003-6935. doi:10.1364/AO.19.003964.

[48] Philip Hofmann. Synchrotron-radiation studies of topological insulators. *Magnetism and Synchrotron Radiation: Towards the Fourth Generation Light Sources*,

151:211–238, 2013. doi:10.1007/978-3-319-03032-6_7. URL http://link.springer.com/chapter/10.1007/978-3-319-03032-6_7.

[49] S Alcock, M Everard, C Nicklin, J Taylor, C Norris, and S Bennett. An investigation of the growth and removal of protective antimony caps for antimonide epilayers. *Thin Solid Films*, 514(1-2):198–203, August 2006. ISSN 00406090. doi:10.1016/j.tsf.2006.02.083. URL http://linkinghub.elsevier.com/retrieve/pii/S0040609006003415.

[50] J. K. Kawasaki, B. D. Schultz, H. Lu, A. C. Gossard, and C. J. Palmstrom. Surface-Mediated Tunable Self-Assembly of Single Crystal Semimetallic ErSb/GaSb Nanocomposite Structures. *Nano letters*, 13(6):2895–2901, May 2013. ISSN 1530-6992. doi:10.1021/nl4012563. URL http://pubs.acs.org/doi/full/10.1021/nl4012563http://pubs.acs.org/doi/abs/10.1021/nl4012563http://www.ncbi.nlm.nih.gov/pubmed/23701166.

[51] J. K. Kawasaki, B. D. Schultz, and C. J. Palmstrom. Size effects on the electronic structure of ErSb nanoparticles embedded in the GaSb(001) surface. *Phys. Rev. B.*, 87(3):035419, January 2013. ISSN 1098-0121. doi:10.1103/PhysRevB.87.035419. URL http://link.aps.org/doi/10.1103/PhysRevB.87.035419.

[52] J. K. Kawasaki, R. Timm, K. Delaney, E. Lundgren, A. Mikkelsen, and C. J. Palmstrom. Local Density of States and Interface Effects in Semimetallic ErAs Nanoparticles Embedded in GaAs. *Phys. Rev. Lett.*, 107(3):036806, July 2011.

ISSN 0031-9007. doi:10.1103/PhysRevLett.107.036806. URL http://link.aps.org/doi/10.1103/PhysRevLett.107.036806.

[53] J. K. Kawasaki, R. Timm, T. E. Buehl, E. Lundgren, A. Mikkelsen, A. C. Gossard, and C. J. Palmstrom. Cross-sectional scanning tunneling microscopy and spectroscopy of semimetallic ErAs nanostructures embedded in GaAs. *J. Vac. Sci. Tech. B.*, 29(3):03C104, 2011. ISSN 10711023. doi:10.1116/1.3547713. URL http://link.aip.org/link/JVTBD9/v29/i3/p03C104/s1&Agg=doi.

[54] Woochul Kim, Suzanne L Singer, Arun Majumdar, Joshua M O Zide, Dmitri Klenov, Arthur C Gossard, and Susanne Stemmer. Reducing thermal conductivity of crystalline solids at high temperature using embedded nanostructures. *Nano letters*, 8(7):2097–9, July 2008. ISSN 1530-6984. doi:10.1021/nl080189t. URL http://www.ncbi.nlm.nih.gov/pubmed/18507477.

[55] Hong Lu, Daniel G. Ouellette, Sascha Preu, Justin D. Watts, Benjamin Zaks, Peter G. Burke, Mark S. Sherwin, and Arthur C. Gossard. Self-assembled ersb nanostructures with optical applications in infrared and terahertz. *Nano Letters*, 14(3):1107–1112, 2014. doi:10.1021/nl402436g. URL http://pubs.acs.org/doi/abs/10.1021/nl402436g.

[56] A Guivarc'h, A Le Corre, P Auvray, B Guenais, J Caulet, Y Ballini, R Guerin, S Deputier, M. C. Le Clanche, G Jezequel, B Lepine, A Quemerais, and D. Sebilleau. Growth by molecular beam epitaxy of (rare-earth group V element)/III-V semiconductor heterostructures. *J. Mater. Res.*, 10(8), 1995.

URL http://journals.cambridge.org/production/action/cjoGetFulltext?fulltextid=8162191.

[57] Hong Lu, Peter G. Burke, Arthur C. Gossard, Gehong Zeng, Ashok T. Ramu, Je-Hyeong Bahk, and John E. Bowers. Semimetal/Semiconductor Nanocomposites for Thermoelectrics. *Advanced Materials*, 23(20):2377–2383, May 2011. ISSN 09359648. doi:10.1002/adma.201100449. URL http://doi.wiley.com/10.1002/adma.201100449.

[58] Jane G. Zhu, C. Barry Carter, Chris J. Palmstrom, and Suzanne Mounier. Microstructure of epitactically grown gaas/eras/gaas. *Applied Physics Letters*, 56 (14):1323–1325, 1990. doi:http://dx.doi.org/10.1063/1.102506. URL http://scitation.aip.org/content/aip/journal/apl/56/14/10.1063/1.102506.

[59] R. Bogaerts, F. Herlach, De Keyser A., F. M. Peeters, F. DeRosa, C. J. Palmstrom, D. Brehmer, and S. J. Allen. Experimental determination of the Fermi surface of thin Sc1-xErxAs epitaxial layers in pulsed magnetic fields. *Phys. Rev. B.*, 53(23): 15951–15963, June 1996. ISSN 0163-1829. URL http://prb.aps.org/abstract/PRB/v53/i23/p15951_1.

[60] Dmitri O. Klenov, Daniel C. Driscoll, Arthur C. Gossard, and Susanne Stemmer. Scanning transmission electron microscopy of ErAs nanoparticles embedded in epitaxial In[sub 0.53]Ga[sub 0.47]As layers. *Applied Physics Letters*, 86(11):111912, 2005. ISSN 00036951. doi:10.1063/1.1885172. URL http://link.aip.org/link/APPLAB/v86/i11/p111912/s1&Agg=doi.

[61] Laura E. Cassels, Trevor E. Buehl, Peter G. Burke, Chris J. Palmstrom, Art C. Gossard, Gilles Pernot, Ali Shakouri, Chelsea R. Haughn, Matthew F. Doty, and Joshua M. O. Zide. Growth and characterization of tbas:gaas nanocomposites. *Journal of Vacuum Science & Technology B*, 29(3):03C114, 2011. doi:http://dx.doi.org/10.1116/1.3555388. URL `http://scitation.aip.org/content/avs/journal/jvstb/29/3/10.1116/1.3555388`.

[62] J. Zide, D. Vashaee, Z. Bian, G. Zeng, J. Bowers, a. Shakouri, and a. Gossard. Demonstration of electron filtering to increase the Seebeck coefficient in $In_{0.53}Ga_{0.47}AsIn_{0.53}Ga_{0.28}Al_{0.19}As$ superlattices. *Physical Review B*, 74(20):1–5, November 2006. ISSN 1098-0121. doi:10.1103/PhysRevB.74.205335. URL `http://link.aps.org/doi/10.1103/PhysRevB.74.205335`.

[63] J. M. Zide, D. O. Klenov, S. Stemmer, a. C. Gossard, G. Zeng, J. E. Bowers, D. Vashaee, and a. Shakouri. Thermoelectric power factor in semiconductors with buried epitaxial semimetallic nanoparticles. *Applied Physics Letters*, 87(11):112102, 2005. ISSN 00036951. doi:10.1063/1.2043241. URL `http://link.aip.org/link/APPLAB/v87/i11/p112102/s1&Agg=doi`.

[64] E. Brown, A. Bacher, D. Driscoll, M. P. Hanson, C. Kadow, and A.C. Gossard. Evidence for a Strong Surface-Plasmon Resonance on ErAs Nanoparticles in GaAs. *Phys. Rev. Lett.*, 90(7):17–20, February 2003. ISSN 0031-9007. doi:10.1103/PhysRevLett.90.077403. URL `http://link.aps.org/doi/10.1103/PhysRevLett.90.077403`.

[65] M. P. Hanson, D. C. Driscoll, J. D. Zimmerman, A. C. Gossard, and E. R. Brown. Subpicosecond photocarrier lifetimes in GaSb/ErSb nanoparticle superlattices at 1.55 μm. *Appl. Phys. Lett.*, 85(15):3110, 2004. ISSN 00036951. doi:10.1063/1.1805711. URL `http://link.aip.org/link/APPLAB/v85/i15/p3110/s1&Agg=doi`.

[66] J. M. O. Zide, A. Kleiman-Shwarsctein, N. C. Strandwitz, J. D. Zimmerman, T. Steenblock-Smith, A. C. Gossard, A. Forman, A. Ivanovskaya, and G. D. Stucky. Increased efficiency in multijunction solar cells through the incorporation of semimetallic ErAs nanoparticles into the tunnel junction. *Appl. Phys. Lett.*, 88(16):162103, 2006. ISSN 00036951. doi:10.1063/1.2196059. URL `http://link.aip.org/link/APPLAB/v88/i16/p162103/s1&Agg=doi`.

[67] W. R. L. Lambrecht, A. G. Petukhov, and B. T. Hemmelman. Schottky barrier formation at ErAs/GaAs interfaces: a case of Fermi level pinning by surface states. *Solid state communications*, 108(6):361–365, 1998. URL `http://www.sciencedirect.com/science/article/pii/S0038109898003561http://linkinghub.elsevier.com/retrieve/pii/S0038109898003561`.

[68] B. D. Schultz, H. H. Farrell, M. M. R. Evans, K. Ludge, and C. J. Palmstrom. ErAs interlayers for limiting interfacial reactions in Fe/GaAs(100) heterostructures. *Journal of Vacuum Science & Technology B: Microelectronics and Nanometer Structures*, 20(4):1600, 2002. ISSN 0734211X. doi:10.1116/1.1491994. URL `http://link.aip.org/link/JVTBD9/v20/i4/p1600/s1&Agg=doi`.

[69] S. J. Allen, N. Tabatabaie, C. J. Palmstrom, S. Mounier, G. W. Hull, T. Sands, F. DeRosa, H. L. Gilchrist, and K. C. Garrison. Magneto-transport in ultrathin ErAs epitaxial layers buried in GaAs. *Surf. Sci.*, 228(1):13–15, 1990. URL `http://www.sciencedirect.com/science/article/pii/0039602890902476`.

[70] V. B. Sandomirskii. Quantum size effect in a semimetal film. *Soviet Journal of Experimental and Theoretical Physics*, 25:101, 1967. URL `http://adsabs.harvard.edu/abs/1967JETP...25..101S`.

[71] L Ilver, J Kanski, C Wigren, Uo Karlsson, and Pr Varekamp. Quantum Size Effects in Epitaxial ErAs on GaAs(001). *Physical Review Letters*, 77(24):4946–4949, December 1996. ISSN 1079-7114. URL `http://www.ncbi.nlm.nih.gov/pubmed/10062674`.

[72] M. A. Scarpulla, J. M. O. Zide, J. M. LeBeau, C. G. Van De Walle, A. C. Gossard, and K. T. Delaney. Near-infrared absorption and semimetal-semiconductor transition in 2 nm ErAs nanoparticles embedded in GaAs and AlAs. *Appl. Phys. Lett.*, 92(17):173116, 2008. ISSN 00036951. doi:10.1063/1.2908213. URL `http://link.aip.org/link/APPLAB/v92/i17/p173116/s1&Agg=doi`.

[73] L. Bolotov, T. Tsuchiya, a. Nakamura, T. Ito, Y. Fujiwara, and Y. Takeda. Semimetal to semiconductor transition in ErP islands grown on InP(001) due to quantum-size effects. *Physical Review B*, 59(19):12236–12239, May 1999. ISSN 0163-1829. doi:10.1103/PhysRevB.59.12236. URL `http://link.aps.org/doi/10.1103/PhysRevB.59.12236`.

[74] P. Hidalgo, B. Mendez, J. Piqueras, J. Plaza, and E. Dieguez. Scanning tunneling spectroscopy study of erbium doped GaSb crystals. *J. Appl. Phys.*, 86(3):1449, 1999. ISSN 00218979. doi:10.1063/1.370910. URL `http://link.aip.org/link/JAPIAU/v86/i3/p1449/s1&Agg=doi`.

[75] KA Jackson and JD Hunt. Lamellar and rod eutectic growth. *AIME MET SOC TRANS*, 1966.

[76] B. D. Schultz and C. J. Palmstrom. Embedded assembly mechanism of stable metal nanocrystals on semiconductor surfaces. *Phys. Rev. B.*, 73(24):1, June 2006. ISSN 1098-0121. doi:10.1103/PhysRevB.73.241407. URL `http://link.aps.org/doi/10.1103/PhysRevB.73.241407`.

[77] B. D. Schultz, S. G. Choi, and C. J. Palmstrom. Embedded growth mode of thermodynamically stable metallic nanoparticles on III-V semiconductors. *Applied Physics Letters*, 88(24):243117, 2006. ISSN 00036951. doi:10.1063/1.2213201. URL `http://link.aip.org/link/APPLAB/v88/i24/p243117/s1&Agg=doi`.

[78] A Guivarc'h, Y Ballini, Y Toudic, M Minier, P Auvray, B Guenais, J Caulet, B Le Merdy, B Lambert, and A Regreny. ErSb/GaSb(001) and GaSb/ErSb/GaSb(001) heterostructures and [ErSb,GaSb] superlattices: Molecular beam epitaxy growth and characterization. *J. Appl. Phys.*, 75(6):2876, 1994. doi:http://dx.doi.org/10.1063/1.356181.

[79] Takashi Komesu, Hae-Kyung Jeong, Jaewu Choi, C. Borca, P. Dowben, A. Petukhov, B. D. Schultz, and C. J. Palmstrom. Electronic structure

of ErAs(100). *Phys. Rev. B.*, 67(035104), January 2003. ISSN 0163-1829. doi:10.1103/PhysRevB.67.035104. URL `http://link.aps.org/doi/10.1103/PhysRevB.67.035104`.

[80] K. Shiraishi. Ga adatom diffusion on an As-stabilized dimer rows: First-principles calculation GaAs (001) surface via missing As. *Appl. Phys. Lett.*, 60(11):1363–1365, 1992. URL `http://apl.aip.org/resource/1/applab/v60/i11/p1363_s1`.

[81] H. E. Cline. Shape instabilities of eutectic composites at elevated temperatures. *Acta Metallurgica*, 1971. URL `http://www.sciencedirect.com/science/article/pii/0001616071900022`.

[82] J. W. Cahn and R. E. Hanneman. (111) surface tensions of III-V Compounds and their relationship to spontaneous ending of thin crystals. *Surf. Sci.*, 1:387–398, December 1964. doi:10.1016/0039-6028(64)90006-8.

[83] W. Liu, X. Liu, W.T. Zheng, and Q. Jiang. Surface energies of several ceramics with NaCl structure. *Surf. Sci.*, 600(2):257–264, January 2006. ISSN 00396028. doi:10.1016/j.susc.2005.10.035. URL `http://linkinghub.elsevier.com/retrieve/pii/S0039602805011805`.

[84] P.F. Miceli and C.J. Palmstrom. X-ray scattering from rotational disorder in epitaxial films: An unconventional mosaic crystal. *Physical Review B*, 51(8):5506–5509, 1995. URL `http://prb.aps.org/abstract/PRB/v51/i8/p5506_1`.

[85] A. J. Young, B. D. Schultz, and C. J. Palmstrom. Lattice distortion in single crystal rare-earth arsenide/gaas nanocomposites. *Applied Physics Letters*, 104(7):

073114, 2014. doi:http://dx.doi.org/10.1063/1.4865905. URL http://scitation.aip.org/content/aip/journal/apl/104/7/10.1063/1.4865905.

[86] T. E. Buehl, J. M. LeBeau, S. Stemmer, M. A. Scarpulla, C. J. Palmstrom, and A. C. Gossard. Growth of embedded ErAs nanorods on (411)A and (411)B GaAs by molecular beam epitaxy. *J. Cryst. Growth*, 312(14):2089, July 2010. ISSN 00220248. doi:10.1016/j.jcrysgro.2010.04.031. URL http://linkinghub.elsevier.com/retrieve/pii/S0022024810002757.

[87] T. E. Buehl, C. J. Palmstrom, and A.C. Gossard. Embedded ErAs nanorods on GaAs (n11) substrates by molecular beam epitaxy. *J. Vac. Sci. Tech. B.*, 29(3): 03C108, 2011. ISSN 10711023. doi:10.1116/1.3549888. URL http://link.aip.org/link/JVTBD9/v29/i3/p03C108/s1&Agg=doi.

[88] C. Domke, P. Ebert, M. Heinrich, and K. Urban. Microscopic identification of the compensation mechanisms in Si-doped GaAs. *Phys. Rev. B.*, 54(15):10288, October 1996. ISSN 0163-1829. URL http://www.ncbi.nlm.nih.gov/pubmed/9984805.

[89] C. J. Palmstrom and T. D. Sands. Stable and Epitaxial Contacts to III-V Compound Semiconductors. *Semiconductors*, pages 67–97, 1993. URL http://scholar.google.com/scholar?hl=en&btnG=Search&q=intitle:Stable+and+Epitaxial+contacts+to+III-V+compound+semiconductors#0http://scholar.google.com/scholar?hl=en&btnG=Search&q=intitle:Stable+and+Epitaxial+Contacts+to+III-V+Compound+Semiconductors#0.

[90] C. Kadow, J. Johnson, K. Kolstad, J.P. P Ibbetson, and A. Gossard. Growth and

microstructure of self-assembled ErAs islands in GaAs. *J. Vac. Sci. Tech. B.*, 18 (4):2197, 2000. ISSN 0734211X. doi:10.1116/1.1306299. URL `http://link.aip.org/link/JVTBD9/v18/i4/p2197/s1&Agg=doi`.

[91] Michael A. Scarpulla, Joshua M. O. Zide, James M. LeBeau, Chris G. Van de Walle, Arthur C. Gossard, and Kris T. Delaney. Near-infrared absorption and semimetal-semiconductor transition in 2nm ErAs nanoparticles embedded in GaAs and AlAs. *Applied Physics Letters*, 92(17):173116, 2008. ISSN 00036951. doi:10.1063/1.2908213. URL `http://link.aip.org/link/APPLAB/v92/i17/p173116/s1&Agg=doi`.

[92] D. C. Driscoll, M.P. P. Hanson, E. Mueller, and A.C. C. Gossard. Growth and microstructure of semimetallic ErAs particles embedded in an In0.53Ga0.47As matrix. *Journal of Crystal Growth*, 251(1-4):243–247, April 2003. ISSN 00220248. doi:10.1016/S0022-0248(02)02511-3. URL `http://linkinghub.elsevier.com/retrieve/pii/S0022024802025113`.

[93] Kris Delaney, Nicola Spaldin, and Chris Van de Walle. Theoretical study of the structural and electronic properties of strained ErAs. *Physical Review B*, 77(23): 1–7, June 2008. ISSN 1098-0121. doi:10.1103/PhysRevB.77.235117. URL `http://link.aps.org/doi/10.1103/PhysRevB.77.235117`.

[94] L. Pourovskii, K. T. Delaney, C. G. Van de Walle, N. Spaldin, and A. Georges. Role of Atomic Multiplets in the Electronic Structure of Rare-Earth Semiconductors and Semimetals. *Phys. Rev. Lett.*, 102(096401):2–5, March 2009. ISSN 0031-9007.

doi:10.1103/PhysRevLett.102.096401. URL `http://link.aps.org/doi/10.1103/PhysRevLett.102.096401`.

[95] Walter Lambrecht. Electronic structure and optical spectra of the semimetal ScAs and of the indirect-band-gap semiconductors ScN and GdN. *Physical Review B*, 62(20):13538–13545, November 2000. ISSN 0163-1829. doi:10.1103/PhysRevB.62.13538. URL `http://link.aps.org/doi/10.1103/PhysRevB.62.13538`.

[96] J. B. Xia, S. F. Ren, and Y. C. Chang. Electronic structures of GdAs/GaAs superlattices. *Physical Review B*, 43(2):1692, 1991. URL `http://prb.aps.org/abstract/PRB/v43/i2/p1692_1http://link.aps.org/doi/10.1103/PhysRevB.43.1692`.

[97] A G Petukhov, W R L Lambrecht, and B Segall. Electronic structure of rare-earth pnictides. *Physical Review B*, 53(8):4324–4339, 1996.

[98] Laura R. Vanderhoef, Abul K. Azad, Cory C. Bomberger, Dibakar Roy Chowdhury, D. Bruce Chase, Antoinette J. Taylor, Joshua M. O. Zide, and Matthew F. Doty. Charge carrier relaxation processes in tbas nanoinclusions in gaas measured by optical-pump thz-probe transient absorption spectroscopy. *Phys. Rev. B*, 89:045418, Jan 2014. doi:10.1103/PhysRevB.89.045418. URL `http://link.aps.org/doi/10.1103/PhysRevB.89.045418`.

[99] L. Bolotov, T. Tsuchiya, A. Nakamura, T. Ito, Y. Fujiwara, and Y. Takeda. Semimetal to semiconductor transition in ErP islands grown on InP(001) due

to quantum-size effects. *Phys. Rev. B.*, 59(19):12236–12239, May 1999. ISSN 0163-1829. doi:10.1103/PhysRevB.59.12236. URL `http://link.aps.org/doi/10.1103/PhysRevB.59.12236`.

[100] R. M. Feenstra. Electronic states of metal atoms on the gaas(110) surface studied by scanning tunneling microscopy. *Phys. Rev. Lett.*, 63:1412–1415, Sep 1989. doi:10.1103/PhysRevLett.63.1412. URL `http://link.aps.org/doi/10.1103/PhysRevLett.63.1412`.

[101] R M Feenstra, Y Dong, M P Semtsiv, and W T Masselink. Influence of tip-induced band bending on tunnelling spectra of semiconductor surfaces. *Nanotechnology*, 18(4):044015, January 2007. ISSN 0957-4484. doi:10.1088/0957-4484/18/4/044015. URL `http://stacks.iop.org/0957-4484/18/i=4/a=044015?key=crossref.cdaec18daad29af8489bd3ee8ad0c5ba`.

[102] R. M. Feenstra and P. Martensson. Fermi-level pinning at the Sb/GaAs (110) surface studied by scanning tunneling spectroscopy. *Phys. Rev. Lett.*, 61(4):447, 1988. URL `http://link.aps.org/doi/10.1103/PhysRevLett.61.447`.

[103] P. Chiaradia, M. Fanfoni, and C. Goletti. Nearly flat bands at the gap(110) surface. *Phys. Rev. B*, 52:10721–10724, Oct 1995. doi:10.1103/PhysRevB.52.10721. URL `http://link.aps.org/doi/10.1103/PhysRevB.52.10721`.

[104] T. M. Rossi, D. A. Collins, D. H. Chow, and T. C. McGill. p-type doping of gallium antimonide grown by molecular beam epitaxy using silicon. *Appl. Phys. Lett.*, 57

(21):2256–2258, 1990. URL http://ieeexplore.ieee.org/xpls/abs_all.jsp?arnumber=4862301.

[105] Kris T. Delaney, Nicola a. Spaldin, and Chris G. Van de Walle. Theoretical study of Schottky-barrier formation at epitaxial rare-earth-metal/semiconductor interfaces. *Physical Review B*, 81(16):1–11, April 2010. ISSN 1098-0121. doi:10.1103/PhysRevB.81.165312. URL http://link.aps.org/doi/10.1103/PhysRevB.81.165312.

[106] M. Said, C.M. Bertoni, A. Fasolino, and Stefano Ossicini. Electronic structure of rare earth arsenide/gallium arsenide superlattices. *Solid State Communications*, 100(7):477 – 480, 1996. ISSN 0038-1098. doi:http://dx.doi.org/10.1016/0038-1098(96)00453-X. URL http://www.sciencedirect.com/science/article/pii/003810989600453X.

[107] Peter G. Burke. *Molecular Beam Epitaxy Growth of Rare Earth Elements in III-V Semiconductors for Thermoelectrics*. PhD thesis, University of California Santa Barbara, 2013.

[108] E. M. Krivoy, H. P. Nair, a. M. Crook, S. Rahimi, S. J. Maddox, R. Salas, D. a. Ferrer, V. D. Dasika, D. Akinwande, and S. R. Bank. Growth and characterization of LuAs films and nanostructures. *Applied Physics Letters*, 101(14):141910, 2012. ISSN 00036951. doi:10.1063/1.4757605. URL http://link.aip.org/link/APPLAB/v101/i14/p141910/s1&Agg=doi.

[109] E. M. Krivoy, S. Rahimi, H. P. Nair, R. Salas, S. J. Maddox, D. J. Ironside,

Y. Jiang, V. D. Dasika, D. A. Ferrer, G. Kelp, G. Shvets, D. Akinwande, and S. R. Bank. Growth and characterization of single crystal rocksalt LaAs using LuAs barrier layers. *Applied Physics Letters*, 101(22):221908, 2012. ISSN 00036951. doi:10.1063/1.4766945. URL `http://link.aip.org/link/APPLAB/v101/i22/p221908/s1&Agg=doi`.

[110] J. K. Kawasaki, T. Neulinger, R. Timm, M. Hjort, A. A. Zakharov, A. Mikkelsen, B. D. Schultz, and C. J. Palmstrom. Epitaxial growth and surface studies of the Half Heusler compound NiTiSn (001). *J. Vac. Sci. Tech. B.*, 31(4):04D106, 2013. doi:10.1116/1.4807715. URL `http://scitation.aip.org/content/avs/journal/jvstb/31/4/10.1116/1.4807715`.

[111] J. K. Kawasaki, L. I. M. Johansson, B. D. Schultz, and C. J. Palmstrom. Growth and transport properties of epitaxial lattice matched Half Heusler CoTiSb/InAlAs/InP(001) heterostructures. *Appl. Phys. Lett.*, 104(2):022109, 2014. doi:10.1063/1.4862191.

[112] H. Kandpal, C. Felser, and R. Seshadri. Covalent bonding and the nature of band gaps in some half-Heusler compounds. *J. Phys. D.*, 39 (5):776, March 2006. ISSN 0022-3727. doi:10.1088/0022-3727/39/5/S02. URL `http://stacks.iop.org/0022-3727/39/i=5/a=S02?key=crossref.962c95bd187db0189c55d4c6b592fa4e`.

[113] Tanja Graf, Claudia Felser, and ParkinS. P. Simple Rules for the Understanding of Heusler Compounds. *Progress in Solid State Chemistry*, 39(1):1–50,

March 2011. ISSN 00796786. doi:10.1016/j.progsolidstchem.2011.02.001. URL `http://linkinghub.elsevier.com/retrieve/pii/S0079678611000021http://dx.doi.org/10.1016/j.progsolidstchem.2011.02.001`.

[114] S. Ogut and K.M. Rabe. Band gap and stability in the ternary intermetallic compounds NiSnM (M= Ti, Zr, Hf): A first-principles study. *Physical Review B*, 51 (16):10443, 1995. URL `http://prb.aps.org/abstract/PRB/v51/i16/p10443_1`.

[115] F. Heusler, W. Starck, and E. Haupt. Uber magnetische manganlegierungen. *Verhandlungen der Deutschen Physikalischen Gesellschaft*, 5:219, 1903.

[116] A. A. Knowlton and O. C. Clifford. The heusler alloys. *Trans. Faraday Soc.*, 8: 195–206, 1912. doi:10.1039/TF9120800195. URL `http://dx.doi.org/10.1039/TF9120800195`.

[117] Z. H. Liu, M. Zhang, Y. T. Cui, Y. Q. Zhou, W. H. Wang, G. H. Wu, X. X. Zhang, and Gang Xiao. Martensitic transformation and shape memory effect in ferromagnetic heusler alloy $\mathrm{ni_2fega}$. *Applied Physics Letters*, 82(3):424–426, 2003. doi:http://dx.doi.org/10.1063/1.1534612. URL `http://scitation.aip.org/content/aip/journal/apl/82/3/10.1063/1.1534612`.

[118] Jian Liu, Tino Gottschall, Konstantin P Skokov, James D Moore, and Oliver Gutfleisch. Giant magnetocaloric effect driven by structural transitions. *Nature materials*, 11(7):620–6, July 2012. ISSN 1476-1122. doi:10.1038/nmat3334. URL `http://www.ncbi.nlm.nih.gov/pubmed/22635044`.

[119] Jürgen Winterlik, Gerhard Fecher, Anja Thomas, and Claudia Felser. Super-

conductivity in palladium-based Heusler compounds. *Physical Review B*, 79(6): 1–9, February 2009. ISSN 1098-0121. doi:10.1103/PhysRevB.79.064508. URL `http://link.aps.org/doi/10.1103/PhysRevB.79.064508`.

[120] T. Klimczuk, C. H. Wang, K. Gofryk, F. Ronning, J. Winterlik, G. H. Fecher, J.-C. Griveau, E. Colineau, C. Felser, J. D. Thompson, D. J. Safarik, and R. J. Cava. Superconductivity in the Heusler family of intermetallics. *Physical Review B*, 85 (17):174505, May 2012. ISSN 1098-0121. doi:10.1103/PhysRevB.85.174505. URL `http://link.aps.org/doi/10.1103/PhysRevB.85.174505`.

[121] F.G. Aliev. Gap at fermi level in some new d- and f-electron intermetallic compounds. *Physica B: Condensed Matter*, 171(14):199 – 205, 1991. ISSN 0921-4526. doi:http://dx.doi.org/10.1016/0921-4526(91)90516-H. URL `http://www.sciencedirect.com/science/article/pii/092145269190516H`.

[122] D Jung, H.-J Koo, and M.-H Whangbo. Study of the 18-electron band gap and ferromagnetism in semi-heusler compounds by non-spin-polarized electronic band structure calculations. *Journal of Molecular Structure: {THEOCHEM}*, 527(13):113 – 119, 2000. ISSN 0166-1280. doi:http://dx.doi.org/10.1016/S0166-1280(00)00483-8. URL `http://www.sciencedirect.com/science/article/pii/S0166128000004838`.

[123] I. Galanakis, P. Dederichs, and N. Papanikolaou. Origin and properties of the gap in the half-ferromagnetic Heusler alloys. *Physical Review B*, 66(13):1–10, October

2002. ISSN 0163-1829. doi:10.1103/PhysRevB.66.134428. URL `http://link.aps.org/doi/10.1103/PhysRevB.66.134428`.

[124] K. Mastronardi, D. Young, C.-C. Wang, P. Khalifah, R. J. Cava, and a. P. Ramirez. Antimonides with the half-Heusler structure: New thermoelectric materials. *Applied Physics Letters*, 74(10):1415, 1999. ISSN 00036951. doi:10.1063/1.123596. URL `http://link.aip.org/link/APPLAB/v74/i10/p1415/s1&Agg=doi`.

[125] Jiong Yang, Huanming Li, Ting Wu, Wenqing Zhang, Lidong Chen, and Jihui Yang. Evaluation of Half-Heusler Compounds as Thermoelectric Materials Based on the Calculated Electrical Transport Properties. *Advanced Functional Materials*, 18(19):2880–2888, October 2008. ISSN 1616301X. doi:10.1002/adfm.200701369. URL `http://doi.wiley.com/10.1002/adfm.200701369`.

[126] S. Sakurada and N. Shutoh. Effect of Ti substitution on the thermoelectric properties of (Zr,Hf)NiSn half-Heusler compounds. *Applied Physics Letters*, 86(8):082105, 2005. ISSN 00036951. doi:10.1063/1.1868063. URL `http://link.aip.org/link/APPLAB/v86/i8/p082105/s1&Agg=doi`.

[127] Sung-Wng Kim, Yoshisato Kimura, and Yoshinao Mishima. High temperature thermoelectric properties of TiNiSn-based half-Heusler compounds. *Intermetallics*, 15(3):349–356, March 2007. ISSN 09669795. doi:10.1016/j.intermet.2006.08.008. URL `http://linkinghub.elsevier.com/retrieve/pii/S0966979506002482`.

[128] P J Brown, K U Neumann, P J Webster, and K R A Ziebeck. The magnetization distributions in some heusler alloys proposed as half-metallic ferromagnets. *Journal*

of Physics: Condensed Matter, 12(8):1827, 2000. URL `http://stacks.iop.org/0953-8984/12/i=8/a=325`.

[129] Iosif Galanakis, Marjana Ležaić, Gustav Bihlmayer, and Stefan Blügel. Interface properties of NiMnSb/InP and NiMnSb/GaAs contacts. *Physical Review B*, 71 (21):214431, June 2005. ISSN 1098-0121. doi:10.1103/PhysRevB.71.214431. URL `http://link.aps.org/doi/10.1103/PhysRevB.71.214431`.

[130] M Ležaić, I Galanakis, G Bihlmayer, and S Blügel. Structural and magnetic properties of the (001) and (111) surfaces of the half-metal NiMnSb. *Journal of Physics: Condensed Matter*, 17(21):3121–3136, June 2005. ISSN 0953-8984. doi:10.1088/0953-8984/17/21/008. URL `http://stacks.iop.org/0953-8984/17/i=21/a=008?key=crossref.214f9c575f8c7cc9be6e57521649621f`.

[131] S. Picozzi, A. Continenza, and A. J. Freeman. Spin injection at heusler/semiconductor interfaces: First-principles determination of potential discontinuity and half-metallicity. *Journal of Applied Physics*, 94(7):4723–4725, 2003. doi:http://dx.doi.org/10.1063/1.1608469. URL `http://scitation.aip.org/content/aip/journal/jap/94/7/10.1063/1.1608469`.

[132] Silvia Picozzi and Arthur J Freeman. Polarization reduction in half-metallic Heusler alloys: the effect of point defects and interfaces with semiconductors. *Journal of Physics: Condensed Matter*, 19(31):315215, August 2007. ISSN 0953-8984. doi:10.1088/0953-8984/19/31/315215. URL

http://stacks.iop.org/0953-8984/19/i=31/a=315215?key=crossref.3c6642eae8b47cabc52f7177c3621669.

[133] Chang Liu, Yongbin Lee, Takeshi Kondo, Eun Deok Mun, Malinda Caudle, Bruce N Harmon, Sergey L Bud, Paul C Canfield, Adam Kaminski, and Sergey Budko. Metallic surface electronic state in half-Heusler compounds RPtBi (R= Lu, Dy, Gd). *Phys. Rev. B.*, 1101(126):1–5, May 2011. ISSN 1098-0121. doi:10.1103/PhysRevB.83.205133. URL http://link.aps.org/doi/10.1103/PhysRevB.83.205133.

[134] P. Larson, S. D. Mahanti, Sandrine Sportouch, and M. G. Kanatzidis. Electronic structure of rare-earth nickel pnictides: narrow-gap thermoelectric materials. *Phys. Rev. B*, 59:15660–15668, Jun 1999. doi:10.1103/PhysRevB.59.15660. URL http://link.aps.org/doi/10.1103/PhysRevB.59.15660.

[135] P. Larson, S. Mahanti, and M. Kanatzidis. Structural stability of Ni-containing half-Heusler compounds. *Physical Review B*, 62(19):12754–12762, November 2000. ISSN 0163-1829. doi:10.1103/PhysRevB.62.12754. URL http://link.aps.org/doi/10.1103/PhysRevB.62.12754.

[136] Ting Wu, Wan Jiang, Xiaoya Li, Yanfei Zhou, and Lidong Chen. Thermoelectric properties of p-type Fe-doped TiCoSb half-Heusler compounds. *Journal of Applied Physics*, 102(10):103705, 2007. ISSN 00218979. doi:10.1063/1.2809377. URL http://link.aip.org/link/JAPIAU/v102/i10/p103705/s1&Agg=doi.

[137] K. Gofryk, D. Kaczorowski, T. Plackowski, J. Mucha, a. Leithe-Jasper, W. Schnelle,

and Yu. Grin. Magnetic, transport, and thermal properties of the half-Heusler compounds ErPdSb and YPdSb. *Physical Review B*, 75(22):224426, June 2007. ISSN 1098-0121. doi:10.1103/PhysRevB.75.224426. URL `http://link.aps.org/doi/10.1103/PhysRevB.75.224426`.

[138] F. G. Aliev, N. B. Brandt, V. V. Moshchalkov, V. V. Kozyrkov, R. V. Skolozdra, and A. I. Belogorokhov. Gap at the Fermi level in the intermetallic vacancy system RNiSn (R= Ti, Zr, Hf). *Z. Phys. B.*, 75(2):167–171, 1989. URL `http://www.springerlink.com/index/hpq37203374202j6.pdf`.

[139] Hiroaki Muta, Takanori Kanemitsu, Ken Kurosaki, and Shinsuke Yamanaka. High-temperature thermoelectric properties of Nb-doped MNiSn (M=Ti, Zr) half-Heusler compound. *Journal of Alloys and Compounds*, 469(1-2):50–55, February 2009. ISSN 09258388. doi:10.1016/j.jallcom.2008.02.041. URL `http://linkinghub.elsevier.com/retrieve/pii/S0925838808002739`.

[140] V. Ponnambalam, Paola N. Alboni, J. Edwards, Terry M. Tritt, Slade R. Culp, and S. Joseph Poon. Thermoelectric properties of p-type half-Heusler alloys $\mathrm{Zr}_{1x}\mathrm{Ti}_x\mathrm{CoSn}_y\mathrm{Sb}_{1y}$ ($0.0 < x < 0.5$; y=0.15 and 0.3). *Journal of Applied Physics*, 103(6):063716, 2008. ISSN 00218979. doi:10.1063/1.2896591. URL `http://link.aip.org/link/JAPIAU/v103/i6/p063716/s1&Agg=doi`.

[141] C Jacoboni, C Canali, G Otiaviani, and A Alberigi Quaranta. A review of some charge transport properties of silicon. *Solid-State Electronics*, 20:77–89, 1977. URL `http://www.sciencedirect.com/science/article/pii/0038110177900545`.

[142] L. Nowicki, a. Turos, a. Stonert, F. Garrido, L.W. Molenkamp, P. Bach, G. Schmidt, G. Karczewski, and a. Mücklich. Defect analysis of NiMnSb epitaxial layers. *Nuclear Instruments and Methods in Physics Research Section B: Beam Interactions with Materials and Atoms*, 240(1-2):356–359, October 2005. ISSN 0168583X. doi:10.1016/j.nimb.2005.06.161. URL `http://linkinghub.elsevier.com/retrieve/pii/S0168583X05010967`.

[143] Tino Jaeger, Christian Mix, Michael Schwall, Xeniya Kozina, Joachim Barth, Benjamin Balke, Martin Finsterbusch, Yves U. Idzerda, Claudia Felser, and Gerhard Jakob. Epitaxial growth and thermoelectric properties of TiNiSn and $Zr_{0.5}Hf_{0.5}NiSn$ thin films. *Thin Solid Films*, 520(3), August 2011. ISSN 00406090. doi:10.1016/j.tsf.2011.08.008. URL `http://linkinghub.elsevier.com/retrieve/pii/S0040609011014696`.

[144] X Dong, J Dong, J Xie, T. C. Shih, S. McKernan, and Palmstrom C. Leighton, C.J. Growth temperature controlled magnetism in molecular beam epitaxially grown Ni2MnAl Heusler alloy. *Journal of Crystal Growth*, 254:384–389, April 2003. ISSN 00220248. doi:10.1016/S0022-0248(03)01172-2. URL `http://linkinghub.elsevier.com/retrieve/pii/S0022024803011722`.

[145] P. Turban, S. Andrieu, E. Snoeck, B. Kierren, and C. Teodorescu. NiMnSb/MgO/NiMnSb heterostructures grown by MBE. *Journal of Magnetism and Magnetic Materials*, 240(1-3):427–429, February 2002. ISSN 03048853. doi:10.1016/S0304-8853(01)00883-6. URL `http://linkinghub.elsevier.com/retrieve/pii/S0304885301008836`.

[146] Siham Ouardi, Gerhard Fecher, Claudia Felser, Michael Schwall, S. Naghavi, Andrei Gloskovskii, Benjamin Balke, Jaroslav Hamrle, Kamil Postava, Jaromír Pištora, Shigenori Ueda, and Keisuke Kobayashi. Electronic structure and optical, mechanical, and transport properties of the pure, electron-doped, and hole-doped Heusler compound CoTiSb. *Physical Review B*, 86(4):045116, July 2012. ISSN 1098-0121. doi:10.1103/PhysRevB.86.045116. URL `http://link.aps.org/doi/10.1103/PhysRevB.86.045116`.

[147] J. Q. Xie, J. W. Dong, J. Lu, C. J. Palmstrom, and S. McKernan. Epitaxial growth of ferromagnetic Ni_2MnIn on (001) InAs. *Applied Physics Letters*, 79(7):1003, 2001. ISSN 00036951. doi:10.1063/1.1392968. URL `http://link.aip.org/link/APPLAB/v79/i7/p1003/s1&Agg=doi`.

[148] P. Bach, A. S. Bader, C. Ruster, C. Gould, C. R. Becker, G. Schmidt, L. W. Molenkamp, W. Weigand, C. Kumpf, E. Umbach, R. Urban, G. Woltersdorf, and B. Heinrich. Molecular-beam epitaxy of the half-Heusler alloy NiMnSb on (In,Ga)As/InP (001). *Applied Physics Letters*, 83(3):521, 2003. ISSN 00036951. doi:10.1063/1.1594286. URL `http://link.aip.org/link/APPLAB/v83/i3/p521/s1&Agg=doi`.

[149] Siham Ouardi, Gerhard H. Fecher, Claudia Felser, Jaroslav Hamrle, Kamil Postava, and Jaromir Pistora. Transport and optical properties of the gapless Heusler compound PtYSb. *Applied Physics Letters*, 99(21):211904, 2011. ISSN 00036951. doi:10.1063/1.3663569. URL `http://link.aip.org/link/APPLAB/v99/i21/p211904/s1&Agg=doi`.

[150] A. Lahav, M. Eizenberg, and Y. Komem. Interfacial reactions between Ni films and GaAs. *Journal of Applied Physics*, 60(3):991–1001, 1986. doi:http://dx.doi.org/10.1063/1.337343. URL `http://scitation.aip.org/content/aip/journal/jap/60/3/10.1063/1.337343`.

[151] C. D. Theis, J. Yeh, D. G. Schlom, M. E. Hawley, G. W. Brown, J. C. Jiang, and X. Q. Pan. Adsorption-controlled growth of $Bi_4Ti_3O_{12}$ by reactive MBE. *Applied Physics Letters*, 72(22):2817–2819, 1998. doi:http://dx.doi.org/10.1063/1.121468. URL `http://scitation.aip.org/content/aip/journal/apl/72/22/10.1063/1.121468`.

[152] Charles M. Brooks, Rajiv Misra, Julia A. Mundy, Lei A. Zhang, Brian S. Holinsworth, Kenneth R. O'Neal, Tassilo Heeg, Willi Zander, J. Schubert, Janice L. Musfeldt, Zi-Kui Liu, David A. Muller, Peter Schiffer, and Darrell G. Schlom. The adsorption-controlled growth of $LuFe_2O_4$ by molecular-beam epitaxy. *Applied Physics Letters*, 101(13):132907, 2012. doi:http://dx.doi.org/10.1063/1.4755765. URL `http://scitation.aip.org/content/aip/journal/apl/101/13/10.1063/1.4755765`.

[153] J. F. Ihlefeld, A. Kumar, V. Gopalan, D. G. Schlom, Y. B. Chen, X. Q. Pan, T. Heeg, J. Schubert, X. Ke, P. Schiffer, J. Orenstein, L. W. Martin, Y. H. Chu, and R. Ramesh. Adsorption-controlled molecular-beam epitaxial growth of $BiFeO_3$. *Applied Physics Letters*, 91(7):071922, 2007. doi:http://dx.doi.org/10.1063/1.2767771. URL `http://scitation.aip.org/content/aip/journal/apl/91/7/10.1063/1.2767771`.

[154] Bharat Jalan, Pouya Moetakef, and Susanne Stemmer. Molecular beam epitaxy of $SrTiO_3$ with a growth window. *Applied Physics Letters*, 95(3):032906, 2009. doi:http://dx.doi.org/10.1063/1.3184767. URL `http://scitation.aip.org/content/aip/journal/apl/95/3/10.1063/1.3184767`.

[155] B. J. Boyle, E. G. King, and K. C. Conway. Heats of formation of nickel and cobalt oxides (nio and coo) of combustion calorimetry. *Journal of the American Chemical Society*, 76(14):3835–3837, 1954. doi:10.1021/ja01643a072. URL `http://pubs.acs.org/doi/abs/10.1021/ja01643a072`.

[156] GL Humphrey and CJ O'Brien. Heats of Formation of Stannic and Stannous Oxides from Combustion Calorimetry. *Journal of the American Chemical Society*, 75(12):2805–2806, 1953. URL `http://pubs.acs.org/doi/abs/10.1021/ja01108a003`.

[157] Hugh J. McDonald and Harry. Seltz. The Heat Capacities of Titanium Dioxide from 68-298K. The Thermodynamic Properties of Titanium Dioxide. *Journal of the American Chemical Society*, 61(9):2405–2407, 1939. doi:10.1021/ja01878a040. URL `http://pubs.acs.org/doi/abs/10.1021/ja01878a040`.

[158] Koji Miyamoto, Akio Kimura, Kazuaki Sakamoto, Mao Ye, Yitao Cui, Kenya Shimada, Hirofumi Namatame, Masaki Taniguchi, Shin-ichi Fujimori, Yuji Saitoh, Eiji Ikenaga, Keisuke Kobayashi, Junichi Tadano, and Takeshi Kanomata. In-gap Electronic States Responsible for the Excellent Thermoelectric Properties of Ni-based Half-Heusler Alloys. *Applied Physics Express*, 1:081901, July 2008. ISSN 1882-

0778. doi:10.1143/APEX.1.081901. URL http://apex.ipap.jp/link?APEX/1/081901/.

[159] Peter Y. Yu and Manuel Cardona. *Fundamentals of Semiconductors: Physics and Materials Properties*. Springer, New York, 3rd edition, 2005. ISBN 978-3-662-03850-5. doi:10.1007/978-3-662-03848-2. URL http://www.springerlink.com/index/10.1007/978-3-662-03848-2.

[160] M. S. Lund, J. W. Dong, J. Lu, X. Y. Dong, C. J. Palmstrom, and C. Leighton. Anomalous magnetotransport properties of epitaxial full Heusler alloys. *Applied Physics Letters*, 80(25):4798, 2002. ISSN 00036951. doi:10.1063/1.1489081. URL http://link.aip.org/link/APPLAB/v80/i25/p4798/s1&Agg=doi.

[161] Patrick A. Lee and TV Ramakrishnan. Disordered electronic systems. *Reviews of Modern Physics*, 57(2):287–337, April 1985. ISSN 0034-6861. doi:10.1103/RevModPhys.57.287. URL http://rmp.aps.org/abstract/RMP/v57/i2/p287_1http://link.aps.org/doi/10.1103/RevModPhys.57.287.

[162] D. Schmidt, A. G. Petukhov, M. Foygel, J. P. Ibbetson, and S. J. Allen. Fluctuation Controlled Hopping of Bound Magnetic Polarons in ErAs:GaAs Nanocomposites. *Phys. Rev. Lett.*, 82(4):823–826, January 1999. ISSN 0031-9007. doi:10.1103/PhysRevLett.82.823. URL http://link.aps.org/doi/10.1103/PhysRevLett.82.823.

[163] B. Kramer and A. MacKinnon. Localization: theory and experiment. *Re-*

ports on Progress in Physics, 56(12):1469, 1993. URL http://stacks.iop.org/0034-4885/56/i=12/a=001.

[164] Akihiro Ohtake. Surface reconstructions on GaAs(001). *Surface Science Reports*, 63(7):295–327, July 2008. ISSN 01675729. doi:10.1016/j.surfrep.2008.03.001. URL http://linkinghub.elsevier.com/retrieve/pii/S0167572908000198.

[165] M. D. Pashley. Electron counting model and its application to island structures on molecular-beam epitaxy grown GaAs (001) and ZnSe (001). *Physical Review B*, 40 (15):10481, 1989. URL http://prb.aps.org/abstract/PRB/v40/i15/p10481_1.

[166] H. Kolev, G. Rangelov, J. Braun, and M. Donath. Reduced surface magnetization of NiMnSb(001). *Physical Review B*, 72(10):1–7, September 2005. ISSN 1098-0121. doi:10.1103/PhysRevB.72.104415. URL http://link.aps.org/doi/10.1103/PhysRevB.72.104415.

[167] S. Hashemifar, Peter Kratzer, and Matthias Scheffler. Preserving the Half-Metallicity at the Heusler Alloy Co2MnSi(001) Surface: A Density Functional Theory Study. *Physical Review Letters*, 94(9):096402, March 2005. ISSN 0031-9007. doi:10.1103/PhysRevLett.94.096402. URL http://link.aps.org/doi/10.1103/PhysRevLett.94.096402.

[168] C N Borca, D Ristoiu, H-K Jeong, Takashi Komesu, a N Caruso, J Pierre, L Ranno, J P Nozières, and P a Dowben. Epitaxial growth and surface properties of half-metal NiMnSb films. *Journal of physics. Condensed matter : an Institute of Physics journal*, 19(31):315211, August 2007. ISSN 0953-8984. doi:10.1088/0953-

8984/19/31/315211. URL http://stacks.iop.org/0953-8984/19/i=31/a=315211?key=crossref.e2c02770032fb9723e17eee39623bb51http://www.ncbi.nlm.nih.gov/pubmed/21694111.

[169] Q. D. Gibson, L. M. Schoop, a. P. Weber, Huiwen Ji, S. Nadj-Perge, I. K. Drozdov, H. Beidenkopf, J. T. Sadowski, a. Fedorov, a. Yazdani, T. Valla, and R. J. Cava. doi:10.1103/PhysRevB.88.081108.

[170] Xie-gang Zhu and Philip Hofmann. Topological surface states on $Bi_{1-x}Sb_x$: Dependence on surface orientation, surface termination and stability. *arXiv-condmat*, (1402.5751), 2014. URL http://arxiv.org/abs/1402.5751.

[171] Hsin Lin, Tanmoy Das, Yoshinori Okada, Mike C Boyer, W Doug Wise, Michelle Tomasik, Bo Zhen, Eric W Hudson, Wenwen Zhou, Vidya Madhavan, Chung-Yuan Ren, Hiroshi Ikuta, and Arun Bansil. Topological Dangling Bonds with Large Spin Splitting and Enhanced Spin Polarization on the Surfaces of Bi_2Se_3. *Nano letters*, April 2013. ISSN 1530-6992. doi:10.1021/nl304099x. URL http://www.ncbi.nlm.nih.gov/pubmed/23614400.

[172] Dieter Wolf. Reconstruction of NaCl surfaces from a dipolar solution to the Madelung problem. *Physical review letters*, 68(22):3315–3319, 1992. URL http://link.aps.org/doi/10.1103/PhysRevLett.68.3315.

[173] Joachim Barth, Benjamin Balke, Gerhard H Fecher, Hryhoriy Stryhanyuk, Andrei Gloskovskii, Shahab Naghavi, and Claudia Felser. Thermoelectric properties of CoTiSb based compounds. *Journal of Physics D: Applied*

Physics, 42(18):185401, September 2009. ISSN 0022-3727. doi:10.1088/0022-3727/42/18/185401. URL `http://stacks.iop.org/0022-3727/42/i=18/a=185401?key=crossref.8703d648adc9cd98f8f845d3d9e00666`.

[174] P. Turban, S. Andrieu, B. Kierren, E. Snoeck, C. Teodorescu, and A. Traverse. Growth and characterization of single crystalline NiMnSb thin films and epitaxial NiMnSb/MgO/NiMnSb(001) trilayers. *Physical Review B*, 65(134417), March 2002. ISSN 0163-1829. doi:10.1103/PhysRevB.65.134417. URL `http://link.aps.org/doi/10.1103/PhysRevB.65.134417`.

[175] P. Leicht, A. Laptev, M. Fonin, Y. Luo, and K. Samwer. Microstructure and atomic configuration of the (001)-oriented surface of epitaxial NiMnGa thin films. *New Journal of Physics*, 13(3):033021, March 2011. ISSN 1367-2630. doi:10.1088/1367-2630/13/3/033021. URL `http://stacks.iop.org/1367-2630/13/i=3/a=033021?key=crossref.e3a15b1a4bc153e73595a0bd5def43ea`.

[176] P. K. Larsen, J. H. Neave, J. F. van der Veen, P. J. Dobson, and B. A. Joyce. GaAs(001)-c(4x4): A chemisorbed structure. *Phys. Rev. B*, 27:4966–4977, Apr 1983. doi:10.1103/PhysRevB.27.4966. URL `http://link.aps.org/doi/10.1103/PhysRevB.27.4966`.

[177] A. Kotani and Y. Toyozawa. Photoelectron spectra of core electrons in metals with an incomplete shell. *Journal of the Physical Society of Japan*, 37 (4), 1974. URL `http://journals.jps.jp/doi/pdf/10.1143/JPSJ.37.912http://journals.jps.jp/doi/abs/10.1143/JPSJ.37.912`.

[178] JF Van der Veen, PK Larsen, J. H. Neave, and B. A. Joyce. The GaAs (001) - c(4 4) and (2 4) reconstructions: A comparative photoemission study. *Solid State Communications*, 49(7):659–662, 1984. URL http://www.sciencedirect.com/science/article/pii/0038109884902151.

[179] R. M. Feenstra. Scanning tunneling spectroscopy. *Surface Science*, 299-300(7):965–979, January 1994. ISSN 00396028. doi:10.1016/0039-6028(94)90710-2. URL http://linkinghub.elsevier.com/retrieve/pii/0039602894907102http://link.aps.org/doi/10.1103/PhysRevB.50.4561.

[180] H. W. Nesbitt, D. Legrand, and G. M. Bancroft. Interpretation of Ni2p XPS spectra of Ni conductors and Ni insulators. *Physics and Chemistry of Minerals*, 27(5):357–366, May 2000. ISSN 0342-1791. doi:10.1007/s002690050265. URL http://www.springerlink.com/openurl.asp?genre=article&id=doi:10.1007/s002690050265.

[181] Yu. Stadnyk and RV Skolozdra. Isothermal Section of the Ti-Ni-Sn System. *Izv. Akad. Nauk SSSR, Neorg. Mater.*, 27(10):2209, 1991.

[182] Aaron Bostwick and Eli Rotenberg. Zooming in on Electronic Structure: NanoARPES at SOLEIL and ALS. *Synchrotron Radiation News*, 25(5):19–25, 2012. URL http://www.tandfonline.com/doi/abs/10.1080/08940886.2012.720162.

[183] Emmanouil Frantzeskakis, José Avila, and Maria C. Asensio. Chemical imaging and angle-resolved photoemission study of well-ordered thermally reduced $SrTiO_3$(100). *Physical Review B*, 85(12):125115, March 2012. ISSN 1098-

0121. doi:10.1103/PhysRevB.85.125115. URL `http://link.aps.org/doi/10.1103/PhysRevB.85.125115`.

[184] G Jeffrey Snyder and Eric S Toberer. Complex thermoelectric materials. *Nature materials*, 7(2):105–14, February 2008. ISSN 1476-1122. doi:10.1038/nmat2090. URL `http://www.ncbi.nlm.nih.gov/pubmed/18219332`.

[185] Woochul Kim, Joshua Zide, Arthur Gossard, Dmitri Klenov, Susanne Stemmer, Ali Shakouri, and Arun Majumdar. Thermal Conductivity Reduction and Thermoelectric Figure of Merit Increase by Embedding Nanoparticles in Crystalline Semiconductors. *Phys. Rev. Lett.*, 96(4):045901, February 2006. ISSN 0031-9007. doi:10.1103/PhysRevLett.96.045901. URL `http://link.aps.org/doi/10.1103/PhysRevLett.96.045901`.

[186] V.V. Romaka, P. Rogl, L. Romaka, Yu. Stadnyk, N. Melnychenko, A. Grytsiv, M. Falmbigl, and N. Skryabina. Phase equilibria, formation, crystal and electronic structure of ternary compounds in TiNiSn and TiNiSb ternary systems. *Journal of Solid State Chemistry*, 197(0):103 – 112, 2013. ISSN 0022-4596. doi:http://dx.doi.org/10.1016/j.jssc.2012.08.023. URL `http://www.sciencedirect.com/science/article/pii/S0022459612005269`.

[187] Yaw Wang Chai and Yoshisato Kimura. Nanosized precipitates in half-Heusler TiNiSn alloy. *Applied Physics Letters*, 100(3):033114, 2012. ISSN 00036951. doi:10.1063/1.3679377. URL `http://link.aip.org/link/APPLAB/v100/i3/p033114/s1&Agg=doi`.

[188] Julien P. A. Makongo, Dinesh K. Misra, Xiaoyuan Zhou, Aditya Pant, Michael R. Shabetai, Xianli Su, Ctirad Uher, Kevin L. Stokes, and Pierre F. P. Poudeu. Simultaneous large enhancements in thermopower and electrical conductivity of bulk nanostructured half-heusler alloys. *Journal of the American Chemical Society*, 133 (46):18843–18852, 2011. doi:10.1021/ja206491j. URL `http://pubs.acs.org/doi/abs/10.1021/ja206491j`.

[189] Jason E. Douglas, Christina S. Birkel, Mao-Sheng Miao, Chris J. Torbet, Galen D. Stucky, Tresa M. Pollock, and Ram Seshadri. Enhanced thermoelectric properties of bulk tinisn via formation of a $\mathrm{tini_2sn}$ second phase. *Applied Physics Letters*, 101(18): 183902, 2012. doi:http://dx.doi.org/10.1063/1.4765358. URL `http://scitation.aip.org/content/aip/journal/apl/101/18/10.1063/1.4765358`.

[190] J. Q. Xie, J. Lu, J. W. Dong, X. Y. Dong, T. C. Shih, S. McKernan, and C. J. Palmstrom. Effects of growth temperature on the structural and magnetic properties of epitaxial $\mathrm{Ni_2MnIn}$ thin films on InAs (001). *Journal of Applied Physics*, 97(7):073901, 2005. ISSN 00218979. doi:10.1063/1.1868857. URL `http://link.aip.org/link/JAPIAU/v97/i7/p073901/s1&Agg=doi`.

[191] Rachel Koltun, Jacqueline L. Hall, Thomas E. Mates, John E. Bowers, Brian D. Schultz, and Christopher J. Palmstrom. Thermoelectric properties of single crystal $\mathrm{Sc_{1x}Er_xAs}$:InGaAs nanocomposites. *Journal of Vacuum Science & Technology B*, 31(4):041401, 2013. doi:http://dx.doi.org/10.1116/1.4810961. URL `http://scitation.aip.org/content/avs/journal/jvstb/31/4/10.1116/1.4810961`.

[192] S. J. Patel, J. K. Kawasaki, J. Logan, B. D. Schultz, J. Adell, B. Thiagarajan, A. Mikkelsen, and C. J. Palmstrom. Surface and electronic structure of epitaxial ptlusb (001) thin films. *Applied Physics Letters*, 104(20):201603, 2014. doi:http://dx.doi.org/10.1063/1.4879475. URL `http://scitation.aip.org/content/aip/journal/apl/104/20/10.1063/1.4879475`.

[193] Anindya Roy, Joseph Bennett, Karin Rabe, and David Vanderbilt. Half-Heusler Semiconductors as Piezoelectrics. *Physical Review Letters*, 109(3):037602, July 2012. ISSN 0031-9007. doi:10.1103/PhysRevLett.109.037602. URL `http://link.aps.org/doi/10.1103/PhysRevLett.109.037602`.

[194] Joseph W. Bennett, Kevin F. Garrity, Karin M. Rabe, and David Vanderbilt. Hexagonal ABC Semiconductors as Ferroelectrics. *Physical Review Letters*, 109 (16):167602, October 2012. ISSN 0031-9007. doi:10.1103/PhysRevLett.109.167602. URL `http://link.aps.org/doi/10.1103/PhysRevLett.109.167602`.

[195] B. D. Schultz, H. H. Farrell, M. M. R. Evans, K. Ludge, and C. J. Palmstrom. ErAs interlayers for limiting interfacial reactions in Fe/GaAs(100) heterostructures. *Journal of Vacuum Science & Technology B: Microelectronics and Nanometer Structures*, 20(4):1600, 2002. ISSN 0734211X. doi:10.1116/1.1491994. URL `http://link.aip.org/link/JVTBD9/v20/i4/p1600/s1&Agg=doi`.

[196] J. Buschbeck, J. K. Kawasaki, T E Buehl, A C Gossard, and C. J. Palmstrom. Growth of epitaxial NiTi shape memory alloy films on GaAs(001) and evidence of martensitic transformation. *J. Vac. Sci. Tech. B.*, 29(3):1–5, 2011.

doi:10.1116/1.3556973. URL `http://avspublications.org/jvstb/resource/1/jvtbd9/v29/i3/p03C116_s1`.

[197] J. Buschbeck, J. K. Kawasaki, A. Kozhanov, R. D. James, and C. J. Palmstrom. Martensite transformation of epitaxial NiTi films. *Appl. Phys. Lett.*, 98(19):191901, 2011. ISSN 00036951. doi:10.1063/1.3589361. URL `http://link.aip.org/link/APPLAB/v98/i19/p191901/s1&Agg=doi`.